OBSERVATIONS OF THE IMPACT OF MESOSCALE CURRENTS ON INTERNAL TIDE PROPAGATION

A DISSERTATION SUBMITTED TO THE GRADUATE DIVISION OF THE
UNIVERSITY OF HAWAI‘I IN PARTIAL FULFILLMENT
OF THE REQUIREMENTS FOR THE DEGREE OF

DOCTOR OF PHILOSOPHY

IN

OCEANOGRAPHY

DECEMBER 2007

By
Cédric Chavanne

Dissertation Committee:

Pierre Flament, Chairperson
Eric Firing
John Learned
Doug Luther
Mark Merrifield

We certify that we have read this dissertation and that, in our opinion, it is satisfactory in scope and quality as a dissertation for the degree of Doctor of Philosophy in Oceanography.

DISSERTATION COMMITTEE

_____
Chairperson

_____

_____

_____

_____

A mes parents

A mes grands-parents

A Marion et Margot

“The principle of science, the definition, almost, is the following: the test of all knowledge is experiment. Experiment is the sole judge of scientific ’truth’.”

Richard Feynman

Acknowledgements

I thank my advisor, Pierre Flament, for his material and intellectual support, and the other members of my Ph.D. committee, Eric Firing, John Learned, Doug Luther and Mark Merrifield, for their help and feedback.

Thanks to Glenn Carter, Ivica Janeković, Rudolf Kloosterziel, Patrice Klein, Mike Kuzmić, Paola Malanotte-Rizzoli, Jeff Paduan, Pierre-Marie Poulain, Alexandre Stegner, and Ed Zaron for fruitful scientific discussions.

Jeff Book provided the ADCP data in the Adriatic. Yvonne Firing processed the ADCP data in Hawai‘i. Jérôme Aucan provided the temperature data at the A2 mooring in Hawai‘i. Glenn Carter and Ivica Janeković provided the numerical models data in Hawai‘i and the Adriatic, respectively.

Olivier Ali, François Ascani, Jérôme Aucan, Camille Bandet, Marion Bandet, Riccardo Barbanti, Joël Benito, Fabio Brunetti, Alessandro Bubbi, Roberto Cecco, Thomas Decloedt, Julie Degoulet, Sophie Delambert, Davide Deponte, Michele Deponte, Julie Deshayes, Adrien Desoria, Bénédicte Dousset, Pierre Dutrieux, Tania Dutrieux, Io Flament, Maël Flament, Klaus-Werner Gurgel, Monika Hamann, Thomas Helzel, Shaun Johnston, Matthias Kniephoff, Oliver Koshe, Paolo Mansutti, Elena Mauri, Kimball Millikan, Philip Moravcik, Giulio Notarstefano, Georges Peeters, Mitch Pinkerton, and Derek Young helped with radar installation and maintenance, and with data processing. The algorithms of Klaus-Werner Gurgel were used for HF-radio radial currents processing. Yves Barbin provided numerous suggestions on operating and calibrating the radars, and Pierre Broche processed some data with the MUSIC direction finding algorithm to compare with the least-square fit direction finding algorithm of Klaus-Werner Gurgel, with satisfactory results. The HF radar processing routines by Jeff Paduan and Mike Cook were adapted to compute the vector currents from the radial measurements. Administrative assistance was provided by Gina Constantini, Laura Glenn and Lance Samura. Schematic figures were prepared by Nancy Hulbirt.

Thanks also to the graduate students of UH for stimulating scientific discussions and feedback on this work, particularly François Ascani and Pierre Dutrieux.

And special thanks to my wife Marion for her encouragement and patience, and to my daughter Margot for changing my life for the better.

Support was obtained from the following funding agencies: the United States Office of Naval Research (grants N00014-02-1-0272 to P. Flament and N00014-03-1-0291 to P-M. Poulain), and the United States National Science Foundation (grants OCE-9724464 and OCE-0453848 to P. Flament, grant OCE-0426112 to E. Firing).

ABSTRACT

High-Frequency Radio Doppler surface current meters and Acoustic Doppler Current Profilers observations during the Hawaiian Ocean Mixing Experiment and the Dynamics of Localized Currents and Eddy Variability in the Adriatic programs were analyzed to describe the tidal and mesoscale currents and their interactions in two very different oceanographic settings.

The northwestern Adriatic Sea has a shallow seasonal thermocline in spring and summer, when fresh water spreads from the Po over the northern Adriatic, which disappears during fall and winter in the interior of the basin where the water column is mixed to the bottom by outbreaks of cold dry Bora winds, but persists near the Italian coast along which the Po outflow is confined. The two-year DOLCEVITA deployment was along the Italian coast of the northwestern Adriatic. In the middle of the basin, the M_2 and K_1 currents oscillate along the basin axis, but become more circular toward the Italian coast. Comparison with a 3-D finite-element numerical model of the tides show a good agreement, except in a 10-20 km wide strip along the Italian coast, where the laterally-sheared and intermittent Western Adriatic Current flows southeastward. Observations suggest that tides in this area have a strong baroclinic component, possibly affected by the mesoscale currents, which could account for the discrepancies between observations and model predictions.

In contrast, the ocean around the main Hawaiian islands is strongly stratified yearlong. The Hawaiian Ridge is an abrupt topographic feature, rising from depths of 5000 m to the surface within O(50 km). M_2 barotropic tides propagate nearly perpendicular to the ridge, generating strong internal tides over the ridge flanks. The 9-month HOME deployment was along the west shore of O‘ahu. The instruments covered the southern side of the Kauai Channel, one of the strongest internal tides generation site of the Hawaiian Ridge. Comparisons with 3-D finite-difference numerical models of the tides show good agreement for the phases, but the kinetic energy pattern and amplitude differ significantly. The models predict a surfacing area of energetic internal tidal beams 30-40 km from the ridge axis, which is 20 km further away and weaker in the observations. The mesoscale variability was dominated by eddies in Fall 2002, with Rossby numbers reaching one, and vorticity waves in Spring 2003, both surface intensified with strong vertical shears. The

interaction of the internal tides with the mesoscale currents is studied using a standard ray tracing model, whose results agree qualitatively with the observations, showing that the energy and phase of the tidal beams are modulated by the mesoscale fields near the surface. The net effect of mesoscale variability over long periods of time is to low-pass filter the vertical modes of internal tides, the resulting surface pattern resembling that one would obtain from the summation of only the first few lowest vertical modes. Significant energy is smeared out of the phase-locked tides, and energy transfers between internal tides and mesoscale currents occur near the surface, with implications on tidal energy budgets.

The dynamics of a strong submesoscale anticyclone west of O'ahu are also described. It was generated in October 2002, possibly as a barotropic instability of the flow associated with a cyclone south of O'ahu, with an initial surface vorticity of $\sim -0.8f$, where f is the inertial frequency. Within three days, the anticyclone reached an extremum vorticity of $\sim -1.5f$, possibly as a result of non-linear Ekman pumping by the trade winds, with a solid-body core of 17 km radius and azimuthal velocity of ~ 35 cm.s^{-1}. It then slowly decayed to less than f five days later, possibly as a result of centrifugal instability. It was in cyclogeostrophic balance to first order. During this period, the anticyclone was trapped between the coast, the cyclone to the south, and a larger cyclone to the west. A front developed between the western cyclone and the anticyclone, as warm water from the southwest was advected northward, and cold water from the northeast southward. The front was divergent ($\sim 0.2f$) and anticyclonic ($\sim -0.25f$) on its warm side, and convergent ($\sim -0.25f$) and cyclonic ($\sim 0.15f$) on its cold side, counteracting the production of density gradient by eddies straining the temperature field.

Contents

List of Tables

List of Figures

Chapter 1

Introduction

This work is an observational study of the interactions of internal tides with mesoscale currents. Tides are believed to provide almost half of the 2 TW (2×10^{12} W) required for the maintenance of the abyssal stratification, the rest coming from the winds (Munk and Wunsch, 1998). The energy pathways from the basin-scale barotropic tides to the centimeter-scale mixing of water properties are not fully understood, and not well parametrized in large-scale ocean circulation models, which is especially of concern for simulations of past and future climate (Wunsch and Ferrari, 2004; Kuhlbrodt et al., 2007). Direct energy dissipation by bottom drag is negligible in the deep ocean, where most of the energy lost by barotropic tides is converted into baroclinic tides at rough or abrupt bottom topography. The energy in high vertical modes is rapidly dissipated, enhancing dissipation levels above rough topography (Polzin et al., 1997; Naveira Garabato et al., 2004), while energy in low vertical modes is carried away over thousands of kilometers (Ray and Mitchum, 1996, 1997). The fate of the internal tides propagating in the ocean is therefore of crucial importance. Numerical modeling studies have traditionally neglected the background currents, a good approximation for barotropic tides, with group velocities much higher than ocean current velocities, but not for the slower internal tides.

High-Frequency (HF) radio measurements of surface currents during the Hawaiian Ocean Mixing Experiment (HOME, Rudnick et al. (2003)) and the Dynamics of Localized Currents and Eddy Variability in the Adriatic (DOLCEVITA, Lee et al. (2005)) program were analyzed to describe the tidal and mesoscale currents and their interactions

in two very different oceanographic settings. Each chapter is an article published or to be submitted. We describe below the main results and provide an overview of the dissertation.

The two-year DOLCEVITA experiment of the northwestern Adriatic Sea is described in chapter 2. In the middle of the basin, the M_2 and K_1 currents oscillate along the basin axis, but become more circular toward the Italian coast. Comparisons with a 3D finite-element non-linear numerical model of the tides show a good agreement for phases in the middle of the basin, although modeled currents amplitudes are overestimated. However, modeled phases lag observed phases by up to 50^o (1.7 hours) for M_2 and 100^o (6.7 hours) for K_1, and modeled amplitudes are underestimated, in a 10-20 km wide strip along the Italian coast. This shallow ($<$ 30 m deep) region is stratified by low-salinity surface water from the Po, and laterally sheared by the Western Adriatic Current, both absent from the model but possibly affecting tidal propagation. The model may also incompletely parametrize the combined effects of bottom friction and vertical mixing of momentum.

The HOME experiment was designed to improve our understanding of tidally-induced mixing and quantify the energy budget for an isolated deep-ocean abrupt topographic feature. About 20 GW (2×10^{10} W) of barotropic energy is lost at the Hawaiian ridge (Egbert and Ray, 2001). An intensive observational program was carried out in the Kaua‘i Channel, one of the strongest internal tides generation sites along the ridge (Merrifield et al., 2001). Two HF-radios and several moored Acoustic Doppler Current Profilers (ADCP) were deployed along the west shore of O‘ahu in 2002 and 2003 to establish the long-term surface and sub-surface context for the experiment. Observations of tidal currents are described in chapter 3. Comparisons of coherent (i.e. phase-locked) surface M_2 currents with 3D finite-difference numerical models of the M_2 tide show good agreement for the phases, indicating a low-mode propagation of internal tides away from the ridge, but kinetic energy patterns and amplitudes differ significantly. The models predict a surfacing area of energetic internal tidal beams 30-40 km from the ridge axis, consistent with the path of M_2 characteristics emanating from the ridge slope breaks. The surfacing area is 20 km further away and weaker in the observations. However, the ADCPs confirm the beamlike structure of energy along the characteristics below $\sim 200m$.

The discrepancies between observations and models in the Kauai Channel are attributed in chapter 4 to the effects of mesoscale variability onto the internal tides prop-

agation. Sub-inertial variability is dominated by surface-trapped mesoscale and submesoscale eddies and vorticity waves, with strong horizontal and vertical shears, absent from the models. The interaction of the internal tides with the mesoscale currents is studied using a standard ray tracing model, the results of which agree qualitatively with the observations. It shows that the energy and phase of the tidal beams are modulated by the mesoscale fields near the surface. The net effect of mesoscale variability over long periods of time is to low-pass filter the vertical modes of internal tides, the resulting surface pattern resembling that one would obtain from the summation of only the first few lowest vertical modes. Significant energy is smeared out of the phase-locked tides, and energy transfers between internal tides and mesoscale currents occur near the surface, with implications on tidal energy budgets.

Finally, the dynamics of mesoscale and submesoscale vortices observed near O‘ahu are described in chapter 5, to document their key elements for introducing them into models, before their effects on internal tides propagation can be addressed numerically. Observations of surface currents by high-frequency radio current meters, and satellite altimeters, scatterometers and radiometers, are used to document the generation and evolution of a strong submesoscale anticyclone west of O‘ahu. It was generated in October 2002, possibly as a barotropic instability of the flow associated with a cyclone south of O‘ahu, with an initial surface vorticity of $\sim -0.8f$. Within three days, the anticyclone reached an extremum vorticity of $\sim -1.5f$, possibly as a result of non-linear Ekman pumping by the trade winds, with a solid-body core of 17 km radius and azimuthal velocity of ~ 35 cm.s^{-1}. It slowly decayed to less than f five days later, possibly as a result of centrifugal instability. It was in cyclogeostrophic balance to first order. During this period, the anticyclone was trapped between the coast, the cyclone to the south, and a larger cyclone to the west. A front developed between the western cyclone and the anticyclone, as warm water from the southwest was advected northward, and cold water from the northeast southward. The front was divergent ($\sim 0.2f$) and anticyclonic ($\sim -0.25f$) on its warm side, and convergent ($\sim -0.25f$) and cyclonic ($\sim 0.15f$) on its cold side, counteracting the production of density gradient by eddies straining the temperature field. Finally, as the western cyclone drifted westward, the front disappeared and the anticyclone broadened and weakened. Submesoscale processes are associated with strong vertical motions, and may

affect the oceanic primary production (Lévy et al., 2001; Lapeyre and Klein, 2006), and the upper ocean stratification (Lapeyre et al., 2006).

The main conclusions are summarized in chapter 6, and numerical experiments are proposed to address the issues raised by this study, namely what would be the net effect of mesoscale variability on tidal energy budgets for the Hawaiian ridge. Data processing and validation, and ray tracing equations are described in the appendices. Another mesoscale feature, namely vorticity waves, was observed during Spring 2003. Their analysis is still preliminary, and it is suggested in Appendix E that they are vortex Rossby waves associated with a large cyclone that was stalled south of Kauai during Spring 2003.

Chapter 2

Tidal Currents in the Northwestern Adriatic

Where it is shown that in a shallow basin, well-mixed half of the year, the mainly barotropic tides are accurately predicted by a non-stratified 3-D numerical model, except in an area where stratification is present yearlong and horizontally sheared background currents are energetic.

2.1 Introduction

The Adriatic tides have been interpreted as co-oscillations with the Ionian and Mediterranean seas, forced through the straight of Otranto (Defant, 1914; Cushman-Roisin et al., 2001; Cushman-Roisin and Naimie, 2002; Janeković and Kuzmić, 2005). The semi-diurnal tide consists of two oppositely traveling Kelvin waves, one incoming from the Ionian sea along the eastern coast, the other traveling back along the western coast after reflection at the northern end of the Adriatic. Their superposition results in an amphidrome centered on the basin axis (Taylor, 1921). The diurnal tide is attributed to a topographic wave propagating across the Adriatic sea (Malačič et al., 2000). The four major semi-diurnal (M_2, S_2, N_2, K_2) and the three major diurnal (K_1, O_1, P_1) constituents exhibit similar intra-group behavior, patterned after the M_2 and K_1 responses (Janeković and Kuzmić, 2005).

While the observed tidal elevation patterns are well explained theoretically, relatively little is known about tidal currents due to scarcity of observations. They are weak,

less than 15 cm/s, compared to baroclinic and wind-driven currents reaching 50 cm/s (Orlić et al., 1992; Poulain, 2001; Ursella et al., 2007). Separating them is difficult, especially for short time series typical of shipboard ADCP and moored current meter observations.

From a year-long repeated ADCP surveys, Ursella and Gačić (2001) confirmed the interpretation of the M_2 pattern as a superposition of Kelvin waves, and the K_1 pattern as resulting from a topographic wave. Their vertically-averaged tidal patterns differ between winter and summer, suggesting that baroclinic tides were not entirely removed by vertical averaging. Cushman-Roisin and Naimie (2002) found good qualitative agreement between these observations and their 3-D finite element model.

Moored current meters deployed in the northern Adriatic between 44^oN and 45^oN by Michelato (1983) have been used to benchmark several models. Cavallini (1985), using a spectral model, reported good agreement for the orientation of the M_2 ellipses, but over-estimated their major axis amplitude by 2.3 cm/s on average. Mosetti (1986), using a semi-analytical model, also found good agreement, consistent with the Kelvin wave description of M_2. Cushman-Roisin and Naimie (2002) were able to reproduce both amplitudes and orientations, except at two shallow stations.

Finally, Janeković and Kuzmić (2005) validated the predictions of their 3-D finite element model with current meter observations at 9 locations in the northeastern Adriatic. There was good agreement for the semi-diurnal currents, but the diurnal currents were generally over-estimated.

We present here the harmonic analysis of two-year time series of currents from high frequency radars deployed along the Italian coast between the Po delta and Pesaro. The observed surface tidal currents are compared with the numerical model of Janeković and Kuzmić (2005). The experimental setting and numerical model are described in section 2.2 and 2.3, respectively. Tidal currents are described and compared in section 2.4, followed in section 2.5 by a brief description of low-frequency currents to provide the mesoscale context for tidal propagation. The differences between model predictions and observations are discussed in section 2.6 and summarized in the conclusion. The data processing techniques are described in Appendix A.

2.2 Experimental setting

Three high frequency radars were deployed from October 2002 to October 2004 along the Italian coast of the northwestern Adriatic, south of the Po delta (Fig. 2.1), to monitor the surface circulation during the multi-investigator DOLCEVITA experiment (Dynamics of Localized Currents and Eddy Variability in the Adriatic, Lee et al. (2005)). The FMCW (frequency-modulated continuous-wave) Doppler radars were operated at 16 MHz with 100 kHz chirp width, yielding a range resolution of 1.5 km (Gurgel et al., 1999). A chirp length of 0.34 s, averaging time of 11.6 min and repeat cycle of 1 hour were programmed, each site transmitting while the others were quiet.

HF radars infer the radial current component from the Doppler-shift of radio waves back-scattered by surface gravity waves of half their electromagnetic wavelength (Bragg scattering), or 9.35 m at 16 MHz. Slower wave speeds in shallow water introduce a negligible error (less than 1 cm/s in water deeper than 5 m). Vector currents were estimated on a 5-km Cartesian grid by least-square fitting zonal and meridional components to radial measurements from at least two sites within a 5 km search radius. Poorly constrained estimations were discarded (see Fig. 2.2 and Appendix A).

The northernmost site at Faro di Goro, the southern mouth of the Po ($44^o47.4$'N, $12^o23.7$'E), was operated in beam-forming mode with a linear array of 16 receive antennas oriented at 46^o clockwise from north, yielding an azimuthal resolution of $\sim$ 7 degrees (Gurgel et al., 1999). The intermediate site at Punta Marina, Ravenna ($44^o26.8$'N, $12^o17.6$'E), and the southernmost site at Monte San Bartolo, Pesaro ($43^o56.6$'N, $12^o50.6$'E), were both operated in direction-finding mode with 4 receive antennas in a square array.

The transmit antennas array formed a beam toward the ocean, and a null in the direction of the receive antennas, to reduce the direct path energy. This also reduced the range away from the beam axis, as seen in Fig. 2.1. Ranges increased by $\sim$ 10 km at night, presumably due to diurnal variations of ionospheric propagation and absorption. This resulted in periodically missing observations at long ranges. While this does not affect the least-square analysis of constituents not synchronous to S_1, it biases that of S_2 and K_1, which differs from S_1 by only 1 cycle / year (see Table 2.1), and the estimation of power spectra. To alleviate this problem, missing data segments shorter than 16 hours

were interpolated (see Appendix A). Temporal coverages of the individual sites and of the vector currents estimations are shown in Fig. 2.3. Data were recorded about 80% of the time.

Data quality can be visualized by the correlation between radial currents from pairs of sites. As shown in Appendix B, the correlation should approach -1 along the baseline joining the two sites, where the radials are in opposite directions, and +1 far offshore, where the radials are almost collinear. If along-baseline and across-baseline current components were uncorrelated with equal variance, the correlation pattern would follow that of the cosine of the angle between the two sites. This relationship is well verified for pairs of sites including the beam-forming radar in Goro (top and middle panels in Fig. 2.4), but degrades for the pair of direction-finding sites (bottom panels in Fig. 2.4), reflecting the lower reliability of the direction finding method.

2.3 Numerical model

The finite element model of Janeković and Kuzmić (2005) is based on the 3-D, nonlinear, shallow water equations (Lynch et al., 1996) with no stratification. The 2.5-level turbulence-closure scheme of Mellor and Yamada (1982) is used with the improvements of Galperin et al. (1988). The horizontal diffusion parametrization scheme follows Smagorinsky (1963). A free-slip condition is imposed along the coast. Bottom stress is estimated by a quadratic drag law using a coefficient of 0.003. A bathymetry-following coordinate system is used in the vertical, with 21 non-uniformly spaced nodes, providing increased resolution in the surface and bottom layers. The near-surface resolution is 1 m, approximately the effective depth of HF-radars measurements (Stewart and Joy, 1974). The finite element grid covers the entire Adriatic sea from the strait of Otranto at 40^oN, with nodal distances ranging from 500 m in coastal areas to 44 km in deep water.

The model is forced by a time-varying sea level boundary condition along 40^oN, synthesized for the seven major tidal constituents (M_2, S_2, N_2, K_2, K_1, O_1, P_1) with a 3-D linearized model assimilating coastal sea level observations. This approach is justified by Janeković et al. (2003), who confirmed that direct astronomical forcing has a minor effect

compared to dominant co-oscillations forced by the Ionian sea. No observations of currents were used in the assimilation.

The tidal currents parameters were bi-linearly interpolated from the finite-element grid onto the HF radars polar and Cartesian grids, for comparisons with the harmonic analysis of the radar currents.

2.4 Tidal currents

The most energetic currents for periods shorter than 5 days are tidal and inertial. Fig. 2.5 shows the average rotary power spectrum over 61 grid points with more than 75% data return. Spectral smearing due to missing observations was minimized (see Appendix A).

The semi-diurnal peaks are centered on M_2 and S_2. For M_2, the counterclockwise energy dominates slightly, resulting in highly eccentric counterclockwise current ellipses. On the contrary, for S_2, the clockwise energy dominates. The diurnal peaks are centered on K_1, and a much weaker O_1, both strongly dominated by clockwise energy, resulting in less eccentric clockwise ellipses. The clockwise inertial frequency band (centered on $f_i = (17\ hr)^{-1}$) is unusually broad, possibly frequency-shifted by the vorticity of sub-inertial currents (Weller, 1982; Kunze, 1985); the intermittent forcing by strong Bora wind events is also noted (Lee et al., 2005).

Harmonic analyses of current components (radial, zonal and meridional) were performed with the T-tide Matlab package (Pawlowicz et al., 2002). Only the 7 tidal constituents modeled by Janeković and Kuzmić (2005) were least-square fitted to the observations, along with a constant and a linear trend; using more constituents degraded the correlation with the model. Nodal corrections were applied for consistency with the model. The 95% confidence intervals were computed by a bootstrap method.

Maps of observed and modeled tidal current ellipses, major axis amplitudes and phases, and their differences are shown in Fig. 2.6 for M_2 and Fig. 2.7 for K_1, and scatterplots of modeled vs. observed ellipse parameters are shown in Fig. 2.8. The other modeled constituents have similar patterns within each group, but the observed ones differ from each other. This is due to low signal-to-noise ratios for the weaker constituents (amplitudes are

less than 2 cm/s for N_2, K_2, O_1 and P_1). The observed S_2 pattern is similar to the M_2 pattern, but their direction of rotation differs, as noted above.

In the basin interior, M_2 ellipses degenerate into oscillations along the Adriatic axis, consistent with their description as a superposition of Kelvin waves traveling in opposite directions (Hendershott and Speranza, 1971; Mosetti, 1986). Their inclination turns with the channel orientation near 44.6^oN. Evanescent Poincare waves are suggested by less eccentric ellipses within 20 km from the coast, about the e-folding scale of M_2 Poincare modes (Hendershott and Speranza, 1971). The mostly counterclockwise ellipses rotation is also consistent with Kelvin waves, away from the closed end of the channel (Taylor, 1921; Mosetti, 1986). Between Pesaro and Goro, the M_2 major axis amplitudes decrease toward the coast as in Malačič et al. (2000). The model underestimates the amplitudes by 2 cm/s near the coast and overestimates them by 1.5 cm/s in the interior. The M_2 phases are relatively uniform over the width of the basin, consistent with the observations of Ursella and Gačić (2001) and with the location of the amphidrome farther south (Lozano and Candela, 1995). In the interior, the observed phases lag the model phases by 5 to 10 degrees (10 to 20 min.). A peculiar feature of the model, not observed, is the sharp phase decrease within 10-20 km from the coast, where the model lags the observations by up to 50^o (1.7 hours).

Modeled K_1 ellipses, major axis amplitudes, and phases patterns mimic those of M_2, suggesting that in this part of the basin K_1 tides may be described as a superposition of Kelvin waves as well. The topographic wave model of Malačič et al. (2000) produces an increase of current amplitude toward shallower water, and a lag of the tide along the Italian compared to the Croatian coast. Both model and observations show the opposite here. The along-channel topographic slope is gentler in the northern part of the basin than in the southern part, allowing diurnal tides to propagate as Kelvin waves. The modeled amplitudes underestimate the observed ones by 2 cm/s along the coast and underestimate them by 1.5 cm/s in the interior. The modeled phases lag the observed ones by up to 100^o (6.7 hours) along the coast, except south of 44.2^oN where observations indicate a decrease in phase at the coast as well. Observed ellipses are less eccentric and veer counterclockwise by $\sim 13^o$, compared to the modeled ones.

The scatterplots of modeled vs. observed ellipse parameters (Fig. 2.8) summarize the comparison. Overall, there is a better agreement for M_2 than for the weaker K_1, as was

also noted for comparisons with moored current meters (Janeković and Kuzmić, 2005). All parameters are well correlated, except the minor axes amplitudes, which have low signal-to-noise ratios (see Table 2.2). This explains the differences in direction of rotation and eccentricity of the K_1 ellipses (Fig. 2.7). The slopes of the major axes amplitudes scatters are greater than 1, a consequence of the modeled values being weaker than the observed ones near the coast but stronger in the interior, as noted above.

Statistics for major axis amplitude and Greenwich phase are condensed in a phase-plane representation in Fig. 2.9 for M_2, K_1, S_2 and O_1. The agreement is good for M_2, S_2 and O_1, but the model lags on average the observations by 15^o for K_1. The standard deviations for the model are larger than for the observations, a result of the model behavior near the coast, except for the weaker O_1.

Ellipse parameters for M_2 and K_1 at two ACE (Adriatic Circulation Experiment) moorings (CP2 and CP3, see Fig. 2.1 for their locations) are given in Table 2.2, and illustrated in Fig. 2.10. Data from the bottom-mounted ACE ADCP's (operational from Sep 2002 to Apr 2003) were provided by Jeff Book, and analyzed with T-tide. There is an excellent agreement for M_2 between both instruments and the model at each mooring location, but it is less good for K_1, except for the phases. The radars ellipses are much less eccentric than the model and ADCP's ellipses, and Table 2.2 shows that the minor axes amplitudes are significantly different from zero at 95% confidence for the radars. This peculiar feature may be due to a biasing from the diurnal modulation of data coverage, as the moorings lie outside the 50% daytime coverage for Pesaro (Fig. 2.1).

Time series of modeled and observed tidal currents, and of observed total currents, are shown for the fortnight 01/01/2004 to 01/15/2004 in Fig. 2.11 at the grid points closest to moorings CP2 and E4. At CP2, modeled and observed tidal currents are similar in amplitude and phase, while at E4 the observed amplitude is consistently stronger than the modeled one, and the phases are slightly offset. At CP2, the observed current variability is well explained by the phase-locked tides, while at E4 the variability is still dominated by the tides but with stronger amplitudes and phase offsets. This suggests a contribution from non-phase locked internal tides at E4, where the water column is stratified by fresh surface water from the Po, whereas at CP2, lying in the basin interior, the water column is mixed from surface to bottom during winter (Rizzoli and Bergamasco, 1983).

The major differences between modeled and observed surface tidal currents are thus within a 20-km wide band along the Italian coast. This region is also along the baselines between pairs of radars, yielding poor estimation of the across-baseline (across-shore) current component (see Fig. 2.2). To show that the differences are not due to geometry, the modeled currents were projected onto the radial directions from the radars, and compared with the observed radial tidal currents.

Comparisons for M_2 radial amplitude and phase in the directions from Goro and Pesaro are shown in Fig. 2.12 and 2.13, respectively. The amplitudes decrease and the phases jump by 180^o as the radial direction approaches the minor axes orientation. The lag between modeled and observed phases near the coast is similar to the lag for the vector currents, showing that it is not an artifact of the geometric dilution of precision. Furthermore, since the radars resolved azimuth through beam-forming at Goro but direction finding at Pesaro, the phase lag is not an artifact of the method of azimuthal resolution.

2.5 Western Adriatic Current

Phase-locked tidal currents explain less than 2% of the total variance over the 2-year record. Low-frequency currents are stronger than tidal currents, and exhibit temporal and spatial variability that may interact with tidal propagation.

The mean circulation over the 2-year record (Fig. 2.14) consists of a southeastward coastal current, the Western Adriatic Current (WAC), and the northern limb of a cyclonic gyre following the 50 m isobath (Poulain, 2001), the Northern Adriatic Filament (NAF, Mauri and Poulain (2001)).

Profiles of the mean along-shore current along two cross-shore transects are shown in Fig. 2.15. Off Ravenna (northern section), the WAC is 40-km wide and reaches a maximum value of ~ 6 cm/s at 20 km from the coast. Off Pesaro (southern section), the WAC widens to 50 km and intensifies to 12 cm/s at 10 km from the coast. Its cross-shore profile is almost linear. These characteristics are consistent with those inferred from surface drifters (Poulain, 2001). Neglecting stratification, the mean southward transport at the northern section is ~ 0.04 Sv (1 Sv = $10^6 m^3/s$) and increases to ~ 0.08 Sv at the southern section, suggesting that as the NAF merges with the WAC, it brings ~ 0.04 Sv.

Temporal variability of the WAC is shown in Fig. 2.16. Southeastward currents are intensified during fall / winter and reduced or even reversed during spring / summer, as documented by Poulain et al. (2004) for summer 2003. This seasonal cycle is consistent with contemporary surface drifter observations (Ursella et al., 2007). There are strong high frequency fluctuations, current reversals occurring with periods as short as 3-4 days.

The tides propagate therefore in laterally sheared background currents with spatial scales smaller than tidal wavelengths, and temporal variability from a few days to seasonal.

2.6 Discussion

The differences between model and observations of tidal currents along the Italian coast are robust features that do not result from measurement limitations, and may be attributed to physical processes absent from the model, or incomplete parametrization of sub-grid scale processes, such as vertical mixing or bottom friction.

The drag coefficient parametrizing bottom friction is constant, but should vary between the smoother muddy bottom along the Italian coast, and the rougher sandy bottom along the Croatian coast (Brambati (1990), their Fig. 15). Friction may therefore be overestimated along the Italian coast, reducing the tidal energy there.

Stratification may also account for the differences between model and observations for the super-inertial M_2 tides, by allowing the generation and propagation of internal tides, as the flow oscillates over sloping topography. Even for the sub-inertial K_1 tides, stratification could be important, if forced baroclinic modes modify significantly the bottom currents, hence the effect of bottom friction. Stratification is strongest in spring and summer, when fresh water spreads from the Po over the northern Adriatic. It disappears during fall and winter in the interior of the basin where the water column is mixed to the bottom by outbreaks of cold dry Bora winds, but persists near the Italian coast along which the Po outflow is confined (Rizzoli and Bergamasco, 1983). This may explain why model and observations compare better in the interior than along the coast. Bottom-mounted ADCP's deployed off the Po delta may help evaluate the internal tides contribution.

Interactions between tidal and low-frequency currents are also absent in the model. Mesoscale currents in the Adriatic will affect the spatial structure and frequency of the normal modes of the basin, since they will affect the propagation of the free waves of the system. Therefore the response of the basin to the periodic tidal forcing at the open boundary should be sensitive to the presence of mesoscale currents, especially if the forcing frequency is very close to an eigenfrequency of the basin, leading to resonance. This is almost the case for the Adriatic, for which the principal modes have periods of 22 hrs and 11 hrs, which explains why the northern Adriatic tides are the second highest tides in the Mediterranean sea (Cushman-Roisin et al., 2001). Therefore a possible significant impact of low-frequency currents, even though they are small compared to Kelvin waves propagation speed, cannot be ruled out.

2.7 Conclusion

Surface tidal currents in the northwestern Adriatic were extracted from HF-radar time series, and compared with numerical model predictions. The good agreement in the basin interior gives confidence in the model simulations there.

However M_2 and K_1 modeled amplitudes are underestimated by 2 cm/s, and modeled phases significantly lag observed phases in a narrow strip along the coast. This region, less than 30-m deep, is stratified by low-salinity water from the Po outflow, and laterally sheared by the Western Adriatic Current, both absent from the model but possibly affecting tidal propagation. The model may also incompletely parametrize the combined effects of bottom friction and vertical mixing of momentum.

	O_1	P_1	S_1	
	13.7	182.6	365.3	K_1
S_2	14.8	14.8	14.2	O_1
N_2	27.6	9.6	365.2	P_1
K_2	13.7	182.6	9.1	
	M_2	S_2	N_2	

Table 2.1: Periods (in days) corresponding to the frequency difference between pairs of diurnal (upper triangle) and semi-diurnal (lower triangle) tidal constituents.

		M_2				K_1			
		maj	min	inc	pha	maj	min	inc	pha
CP2	R	5.9±0.3	0.4±0.4	134.2±3.0	167.8±3.7	3.1±0.5	-0.9±0.5	147.5±12.2	336.5±12.1
	A	5.7±0.5	0.2±0.5	142.4±5.3	174.1±5.7	2.3±0.9	-0.3±0.9	127.9±22.2	331.7±27.0
	M	6.3±0.1	0.3±0.1	135.2±0.8	171.0±0.8	2.9±0.1	-0.1±0.1	134.5±2.1	334.0±2.2
CP3	R	6.6±0.3	-0.2±0.3	135.5±2.4	169.2±2.6	3.4±0.6	-1.3±0.5	136.3±10.9	338.0±10.9
	A	7.6±0.3	-0.3±0.3	126.6±2.9	172.3±2.8	2.7±0.6	-0.3±0.6	113.9±10.4	329.0±14.5
	M	7.3±0.1	0.1±0.1	130.3±0.8	169.4±0.9	3.4±0.1	-0.2±0.1	127.4±1.8	333.6±2.2

Table 2.2: M_2 and K_1 major and minor axes amplitudes (cm/s), northern semi-major axis inclination (degrees counterclockwise from east), and Greenwich phase (degrees) at ACE moorings CP2 and CP3 (see Fig. 2.1 for their locations). R: radars observations, A: ADCP observations (at 3.4 m depth), M: model predictions near the surface. The 95% confidence intervals are indicated.

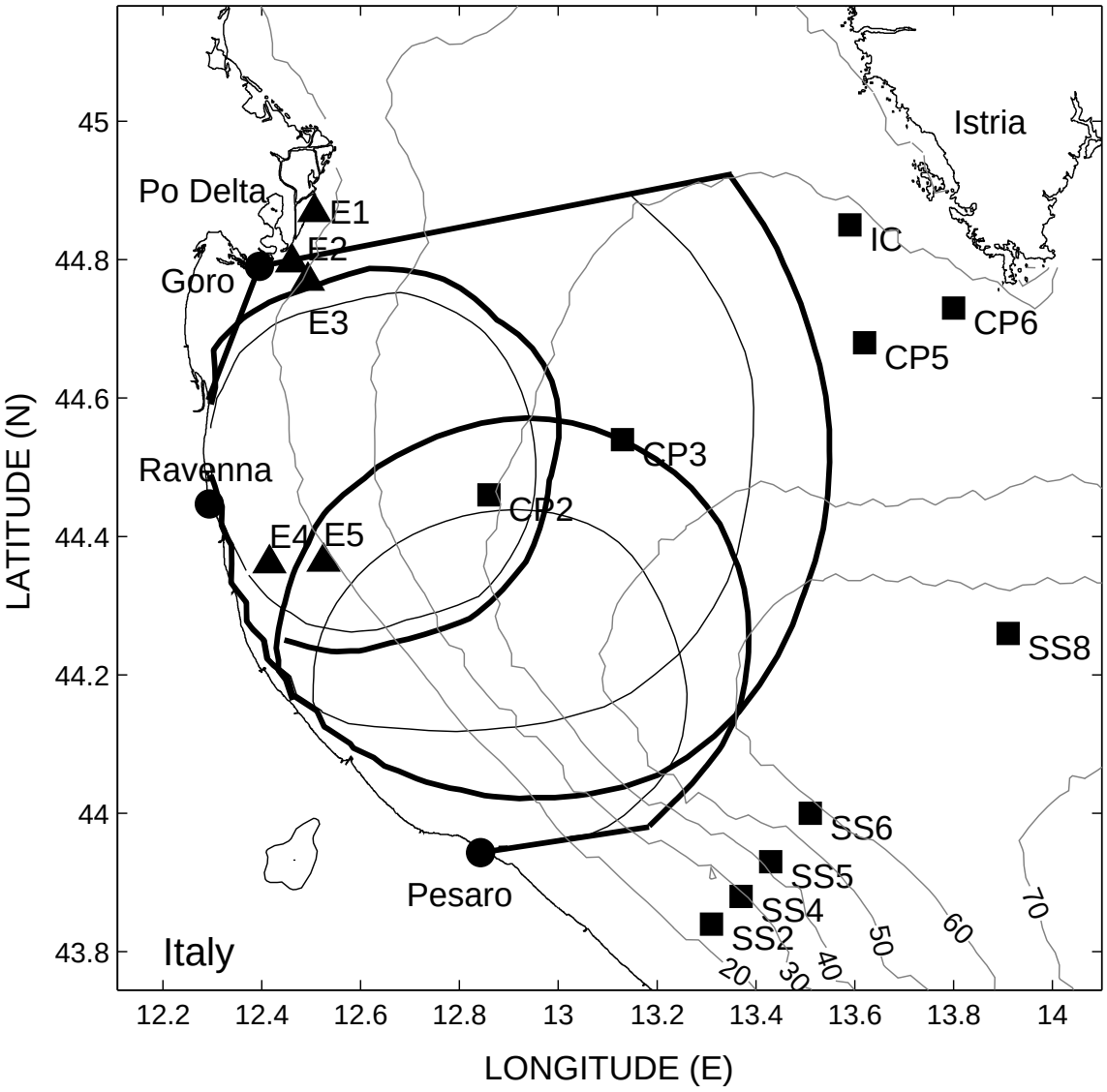

Figure 2.1: Bathymetry of the northwestern Adriatic (gray lines, in m) and the limits of 50% radars data coverage, thick lines for night time (10pm to 5am UTC) and thin lines for day time (6am to 9pm UTC). The maximum night/day time ranges are 102/90 km for Goro, 69/54 km for Pesaro, and 58/52 km for Ravenna. The locations of the radars (circles), EuroSTRATAFORM (triangles) and ACE (squares) moorings are indicated.

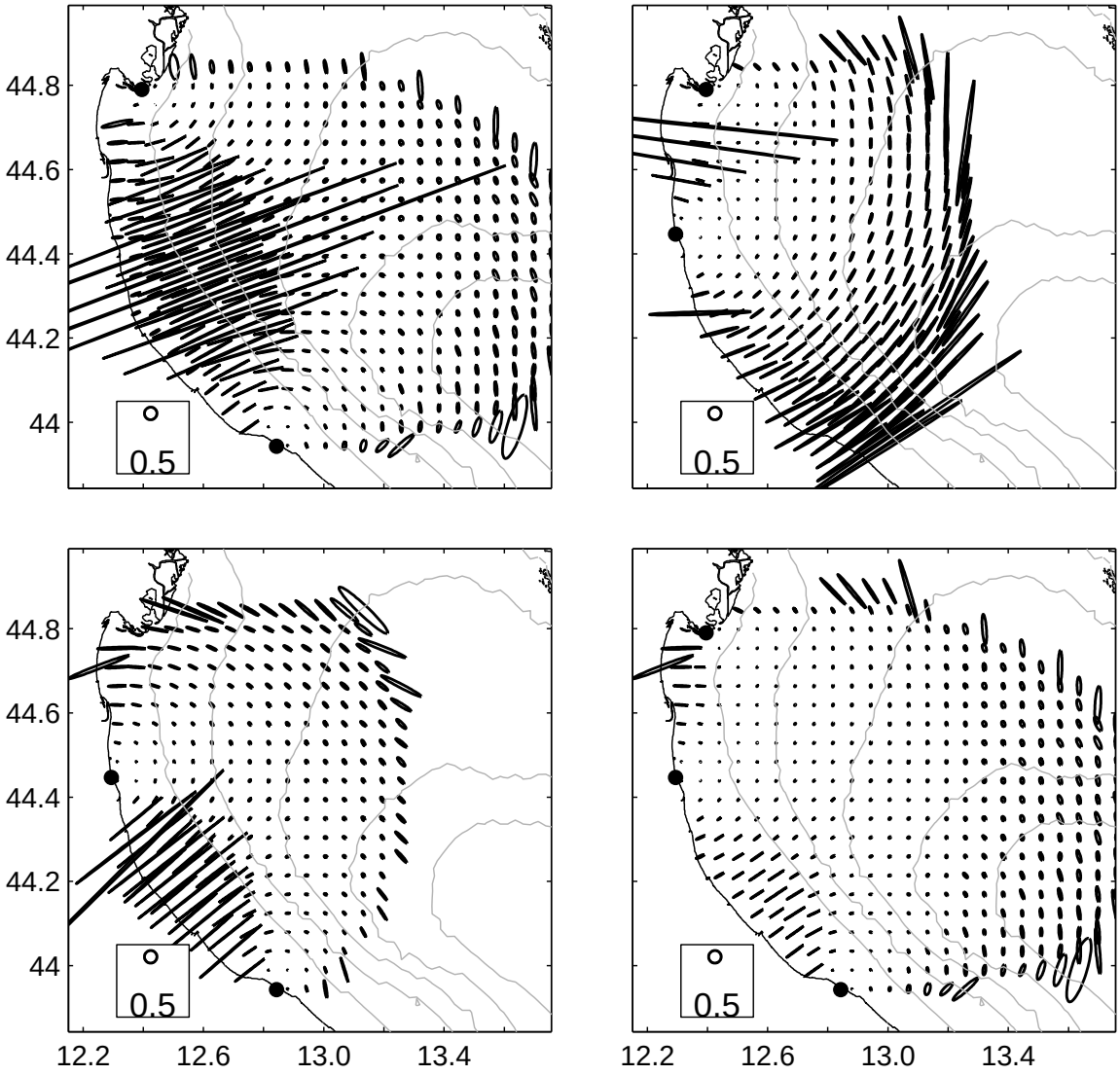

Figure 2.2: Geometric Dilution Of Precision (GDOP) ellipses for various geometric configurations: (top left) Goro and Pesaro only, (top right) Goro and Ravenna only, (bottom left) Ravenna and Pesaro only, (bottom right) Goro, Ravenna and Pesaro. The legend corresponds to the threshold value selected to discard vector currents poorly constrained.

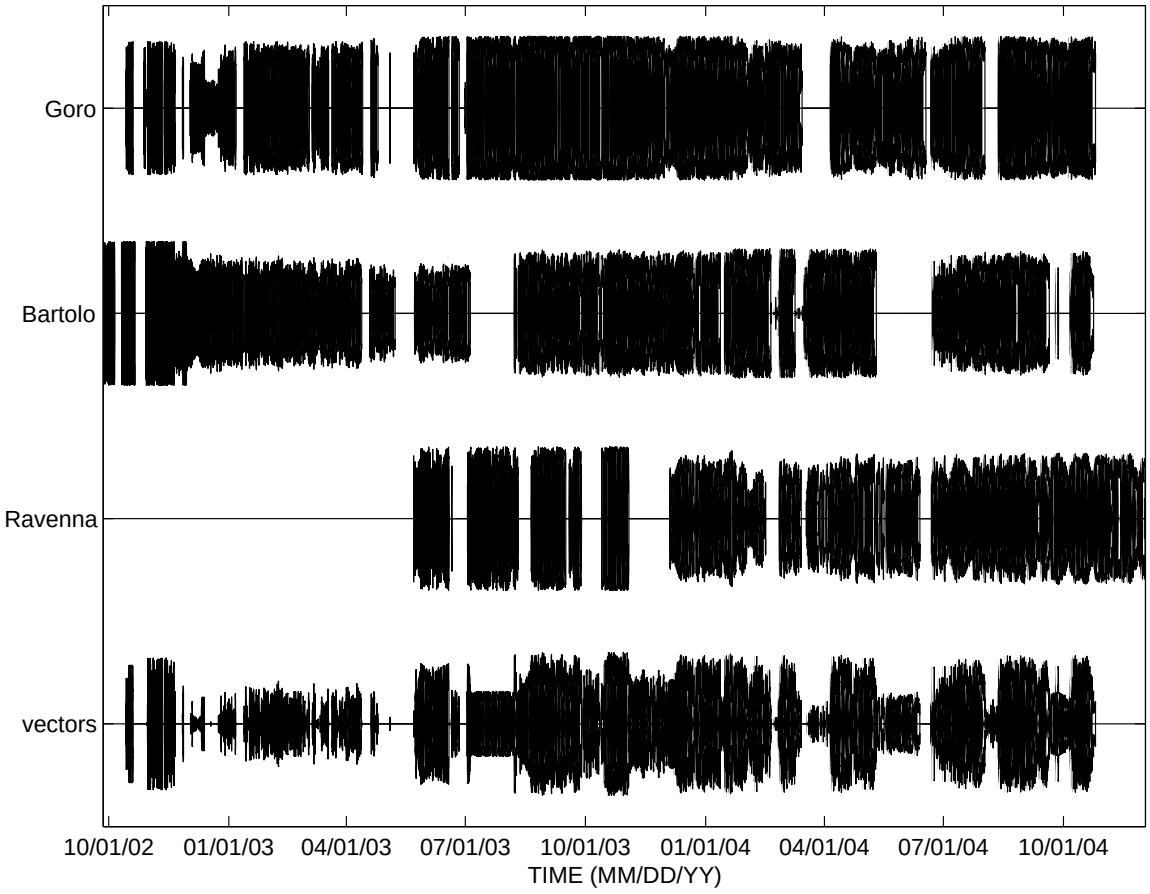

Figure 2.3: Temporal coverage of individual radar sites and of the combined vector currents. The thickness corresponds to the percentage of grid points with data. The fraction of time when there is some data over the operating periods is 83.8% for Goro, 79.5% for Pesaro, 80.1% for Ravenna, and 79.4% for the vector currents.

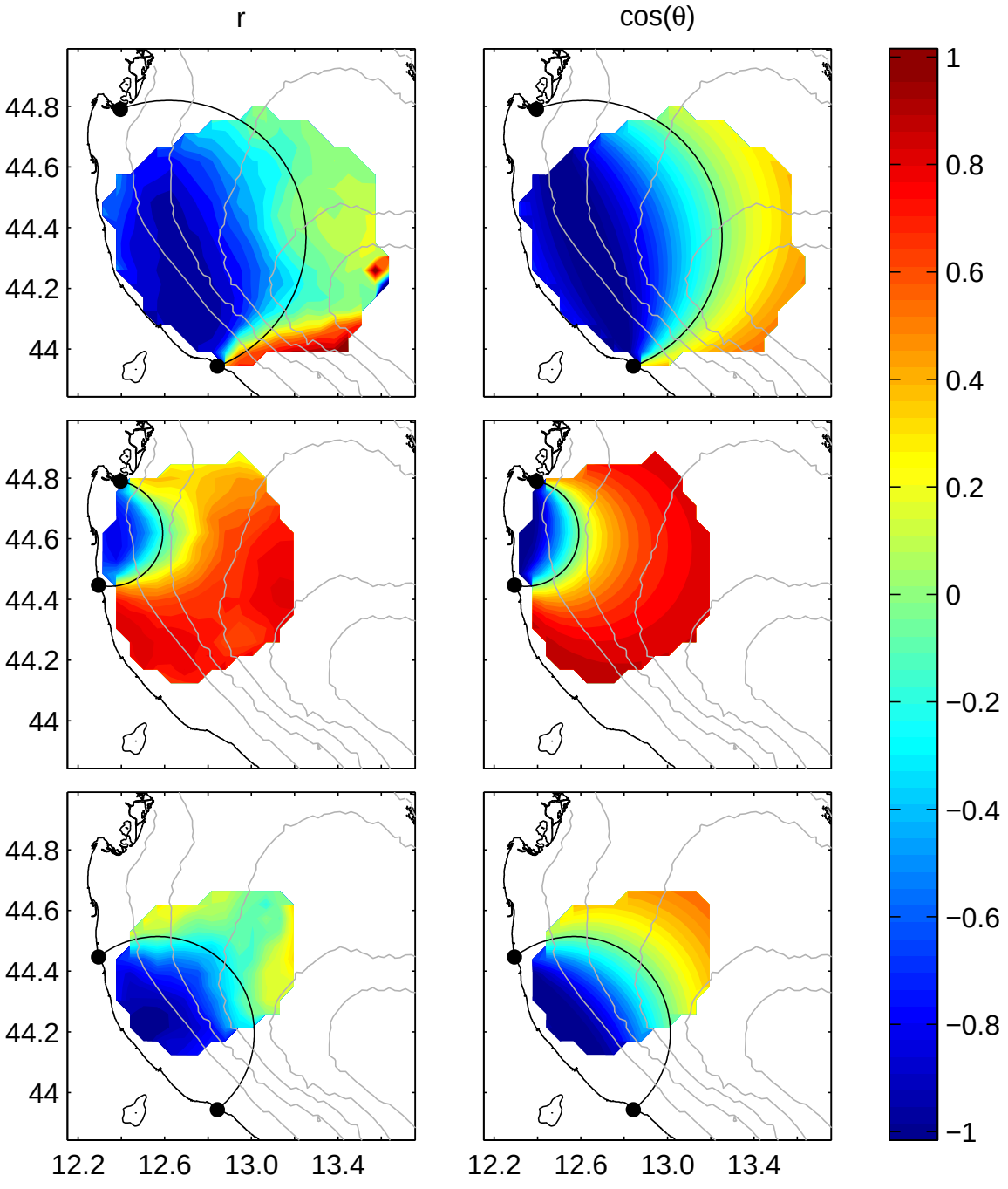

Figure 2.4: Cross-correlation between radial currents from pairs of sites (left column), and cosine of the angle between the sites (right column), for Goro and Pesaro (top row), Goro and Ravenna (middle row), and Pesaro and Ravenna (bottom row). The circle where the angle between the two sites is 90^o is shown for reference.

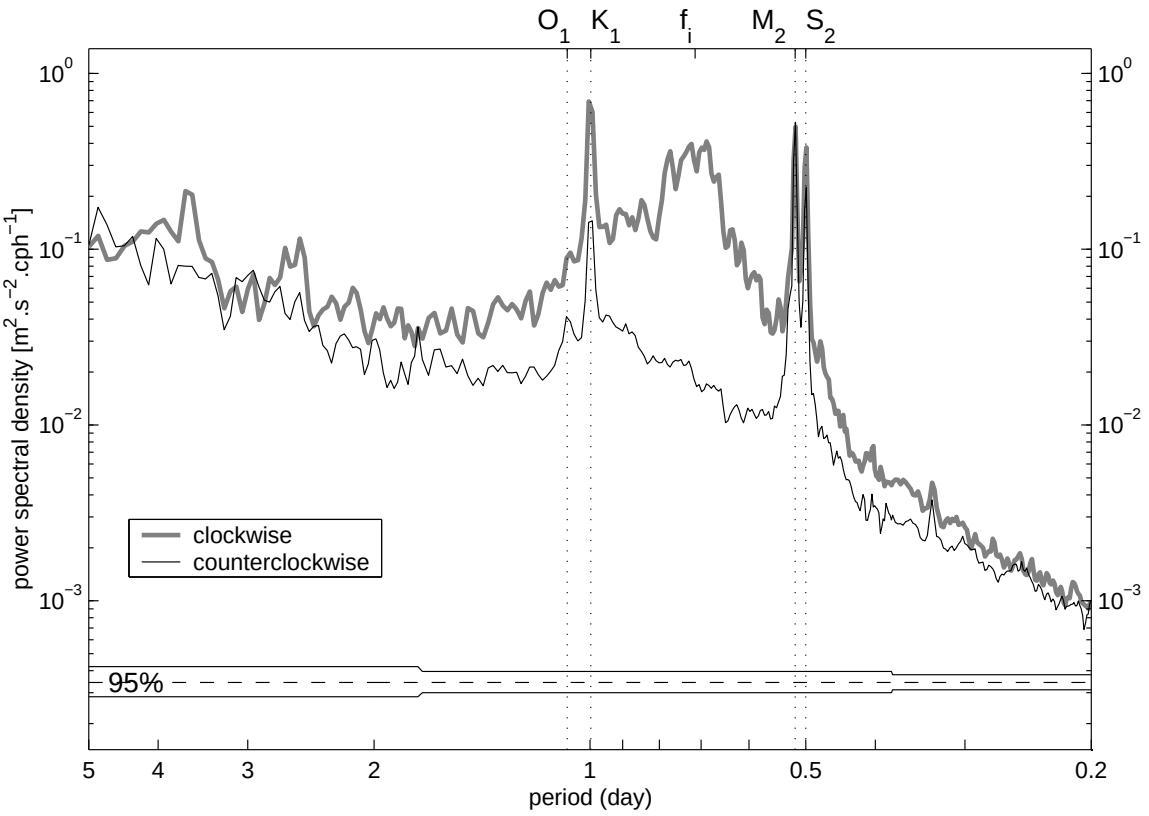

Figure 2.5: Rotary power spectrum averaged over 61 grid points with more than 75% temporal coverage. 95% confidence interval narrows at higher frequencies with the increased number of degrees of freedom used in the selected frequency ranges. Tidal constituents and inertial frequency f_i are indicated on the top x-axis.

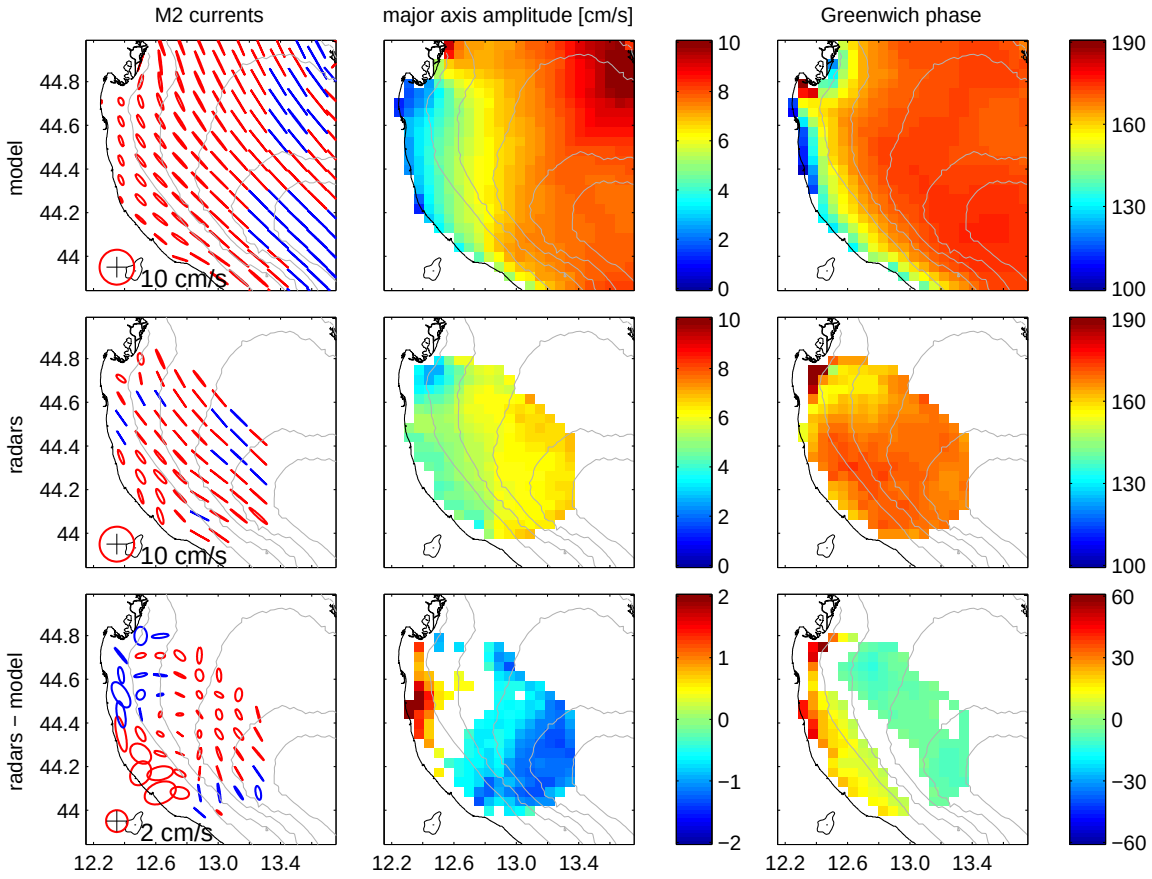

Figure 2.6: (left column) M_2 ellipses, (middle column) major axis amplitude, and (right column) Greenwich phase from (top row) the model , (middle row) the radars , and (bottom row) the difference radars - model (shown only where greater in absolute value than the combined 95% confidence intervals from the radars and model error analyses). Counterclockwise and clockwise ellipses are plotted in red and blue respectively. The phase is defined as the lag of the maximum current (along the northern semi-major axis) with respect to the astronomical phase of M_2 at 0^oE.

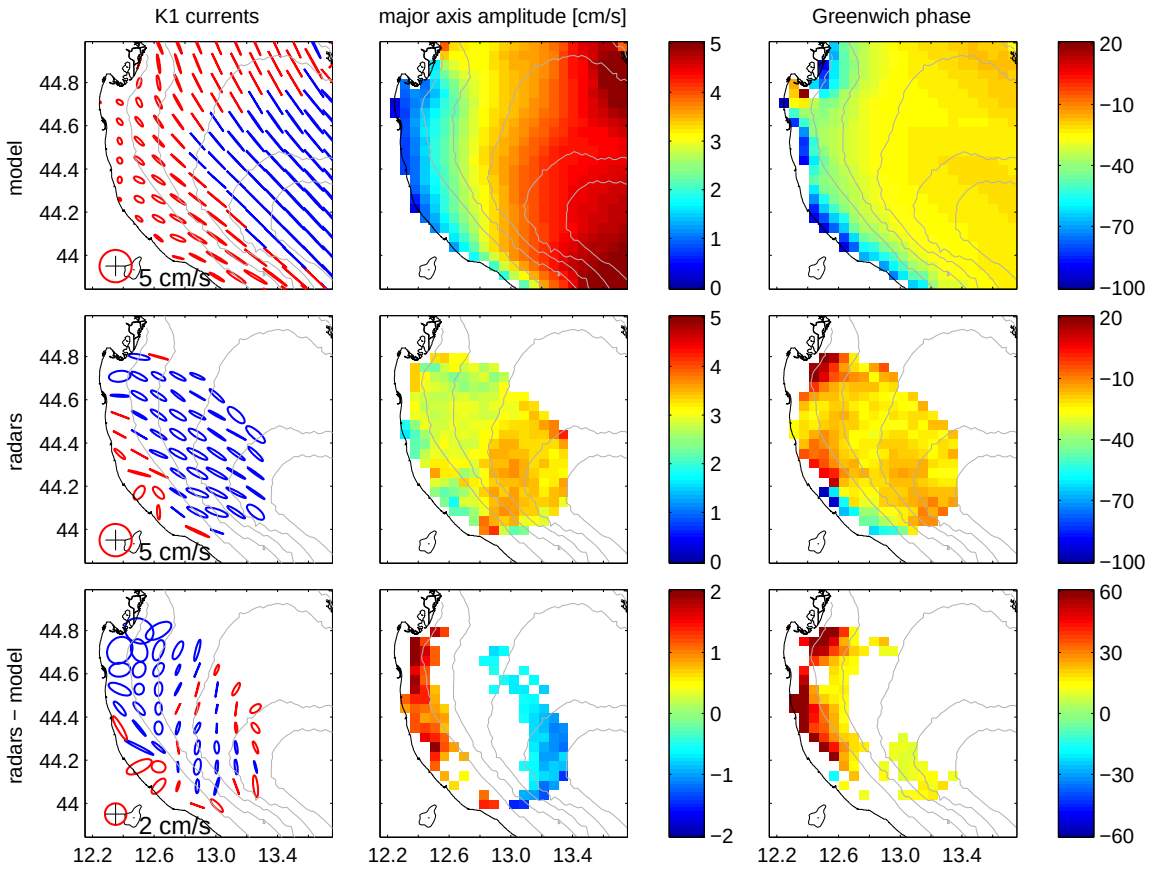

Figure 2.7: same as Fig. 2.6 for K_1.

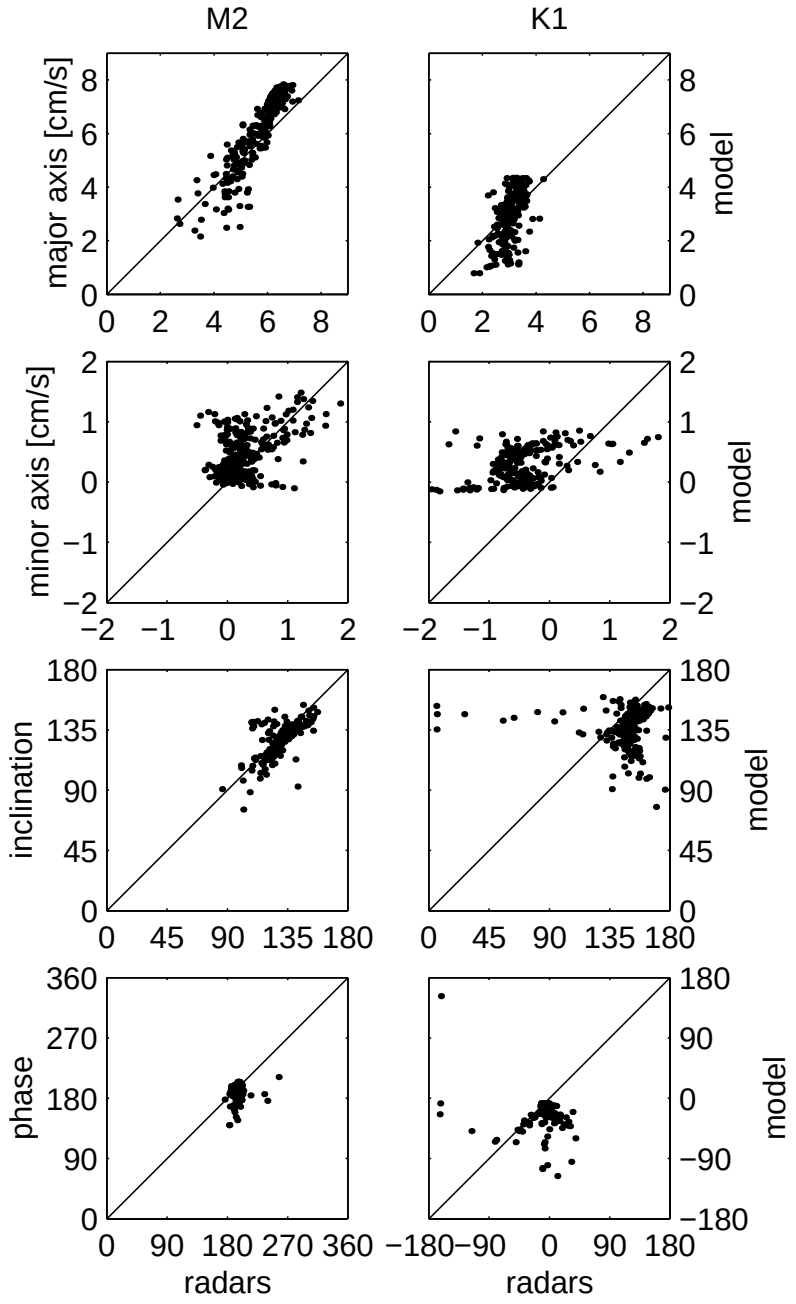

Figure 2.8: Scatterplots of model (vertical axes) versus radars (horizontal axes) tidal ellipse parameters: (top row) major axis amplitude (cm/s), (middle-top row) minor axis amplitude (cm/s, negative values indicate clockwise rotation), (middle-bottom row) inclination (degrees counterclockwise from east), and (bottom row) Greenwich phase (degrees) for M_2 (left column) and K_1 (right column) constituents.

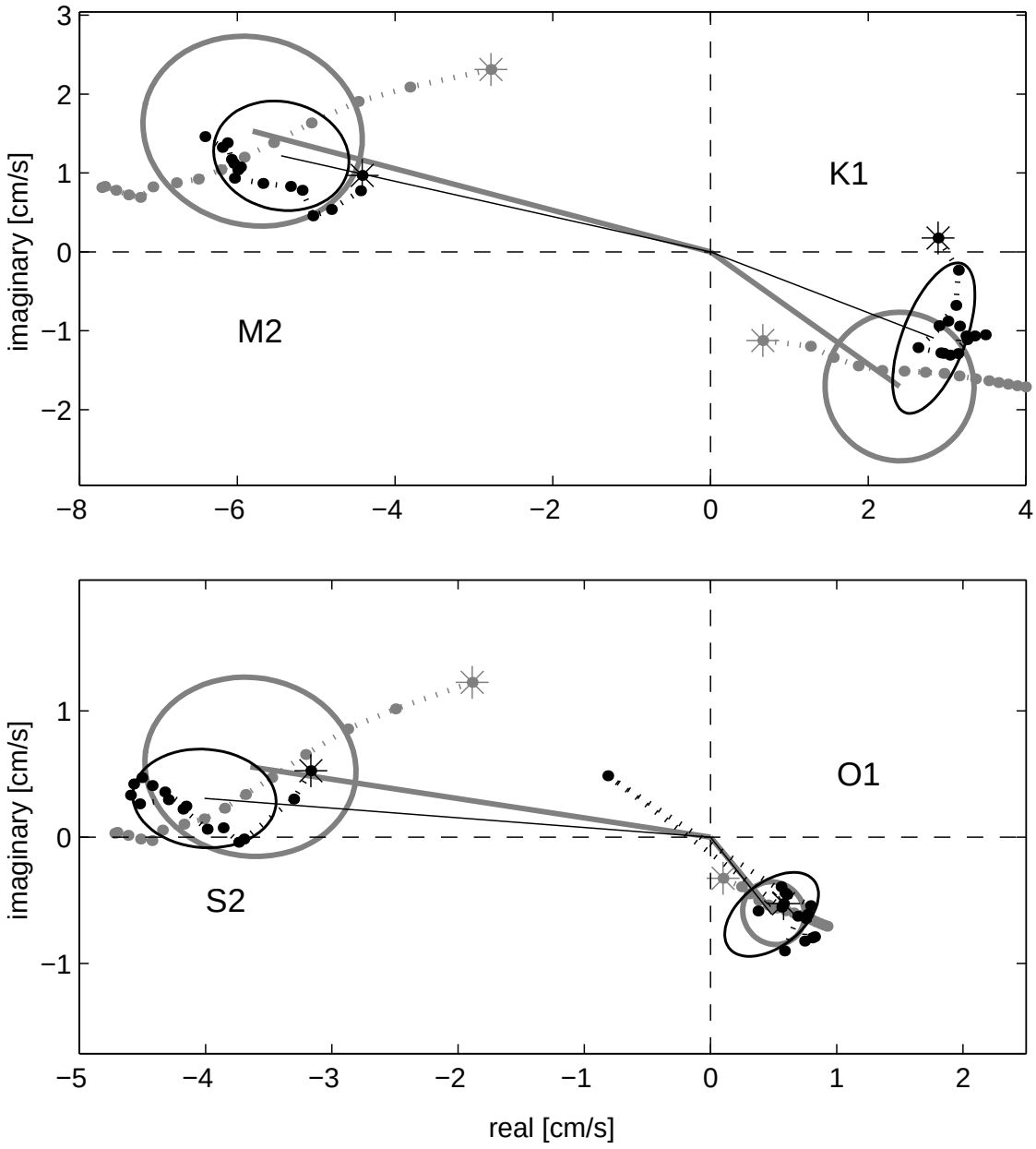

Figure 2.9: Statistics for the observed (black) and modeled (gray) major axis amplitude (radius) and Greenwich phase (angle) for the 4 major tidal constituents (top: M_2 and K_1, bottom: S_2 and O_1). The average and standard deviation of amplitudes and phases over the grid points with more than 4383 hourly observations (182.6 days) are represented by solid lines drawn from the origin and by ellipses, respectively. A zonal section along 44.3N is shown by dots, starting from the coast (star).

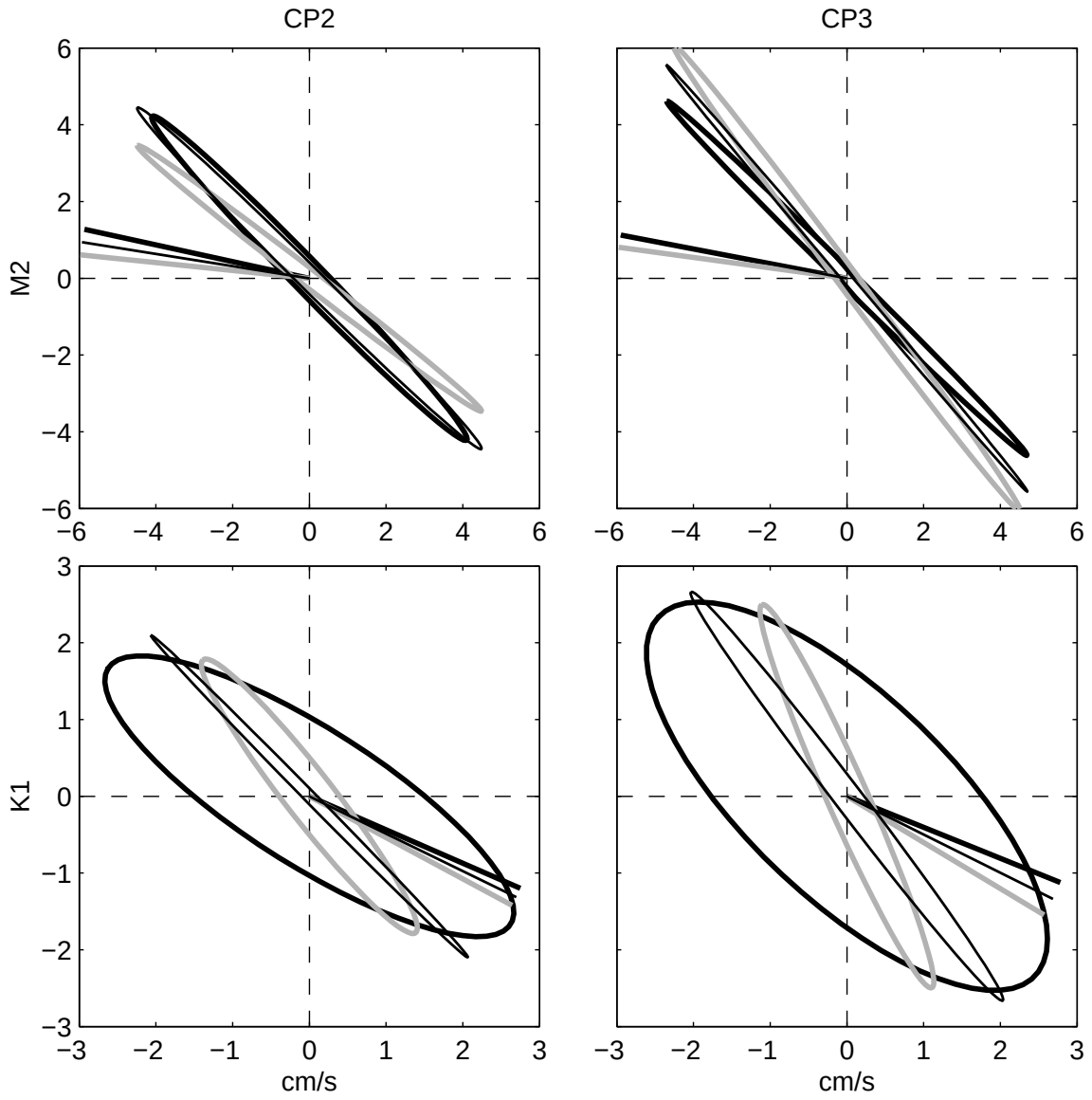

Figure 2.10: M_2 (top panels) and K_1 (bottom panels) current ellipses and Greenwich phases (represented by the angle of the straight lines relative to the x-axis) at the CP2 (left panels) and CP3 (right panels) mooring locations. Currents from radars (thick black lines), ADCP's at 3.4 m depth (thick gray lines), and model near the surface (thin black lines) are shown.

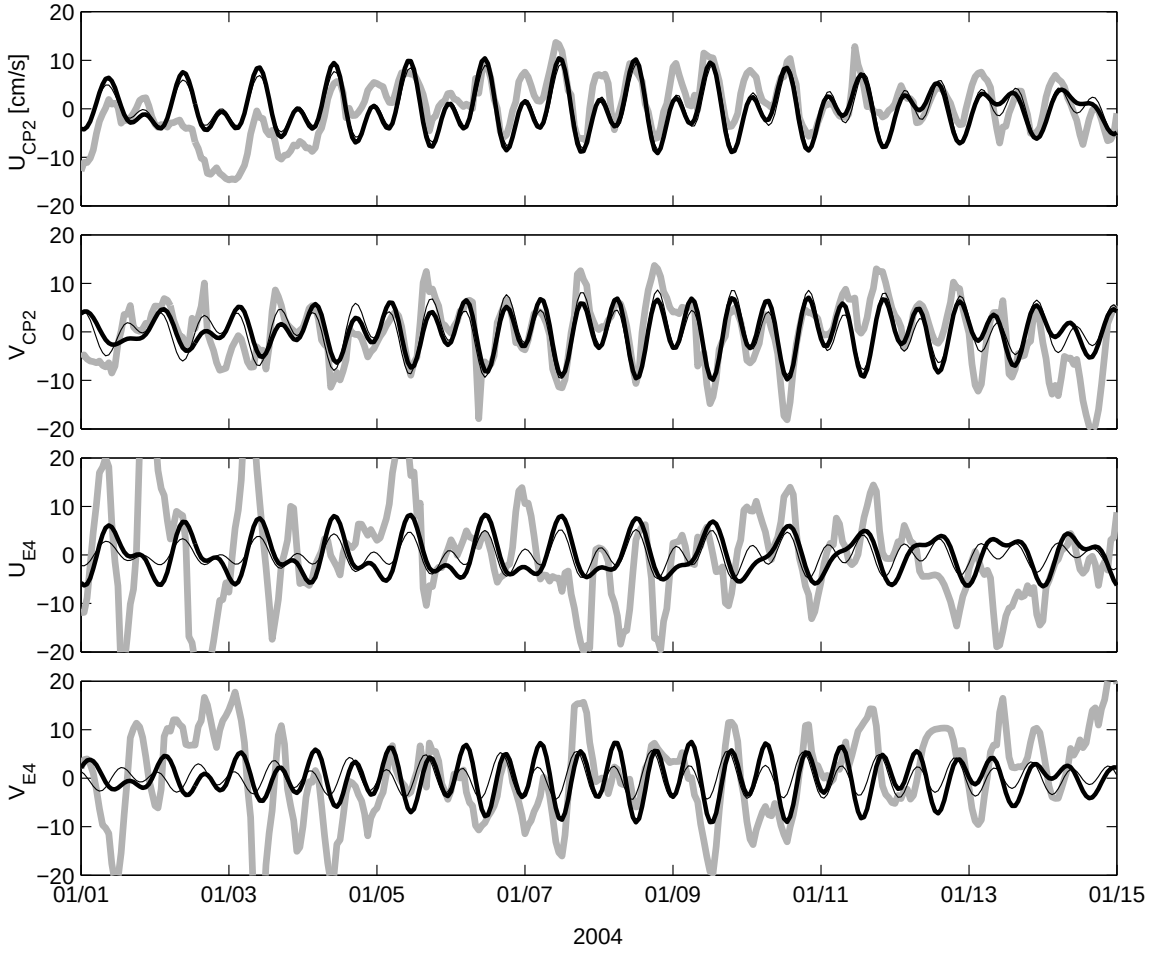

Figure 2.11: Time series of modeled (thin) and observed (thick black) tidal currents, as well as observed total currents (thick gray) at the grid points closest to moorings CP2 and E4. (top) zonal current at CP2, (middle-top) meridional current at CP2, (middle-bottom) zonal current at E4, (bottom) meridional current at E4. The mean over the fortnight has been removed from the total currents to improve the comparison.

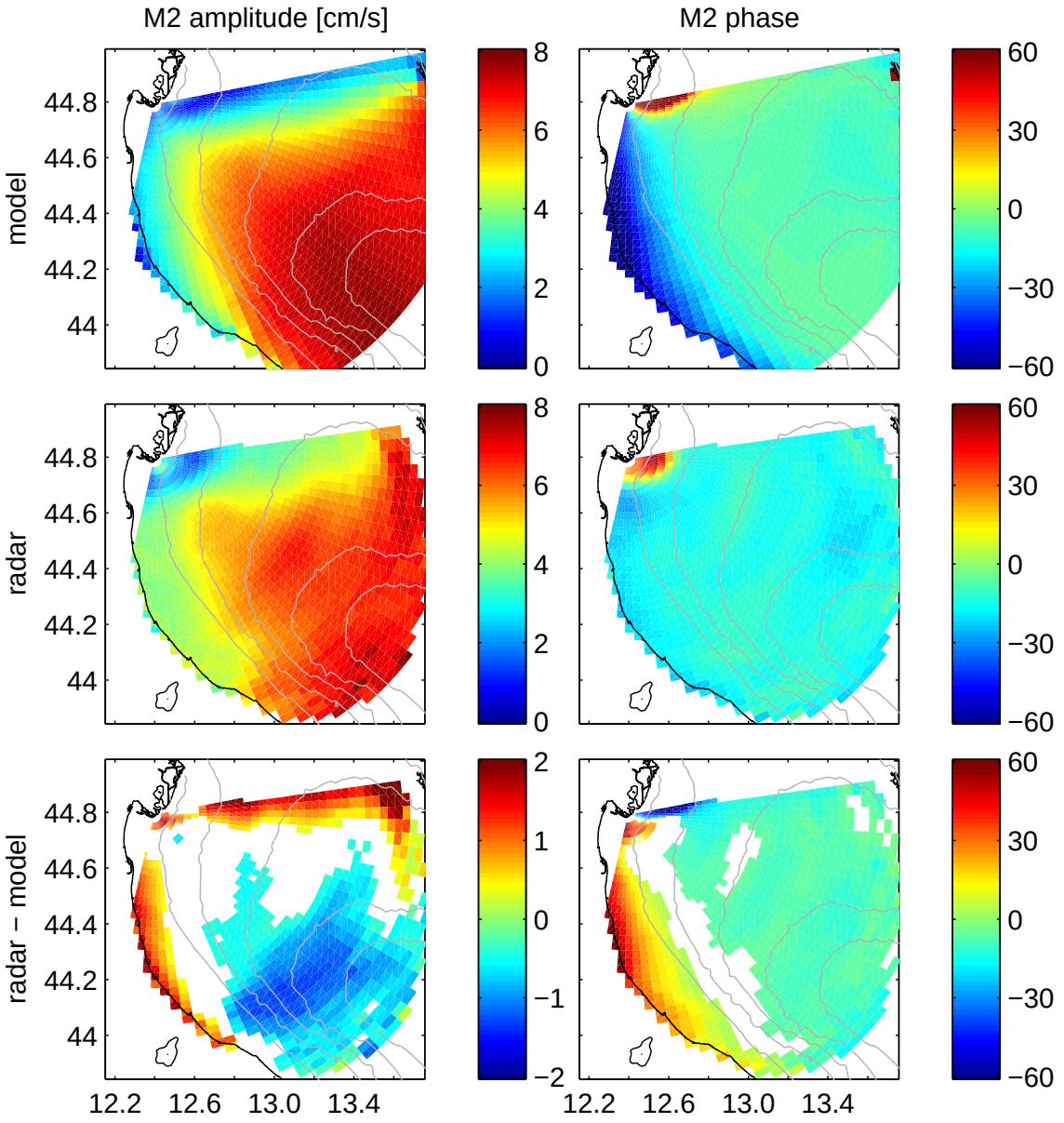

Figure 2.12: M_2 Goro radial currents amplitude (left column) and phase (right column) from the model (top row), the radars (middle row), and the difference radar-model (bottom row). The phase is defined as the lag of the maximum radial current with respect to the astronomical phase of M_2 at 0^oE.

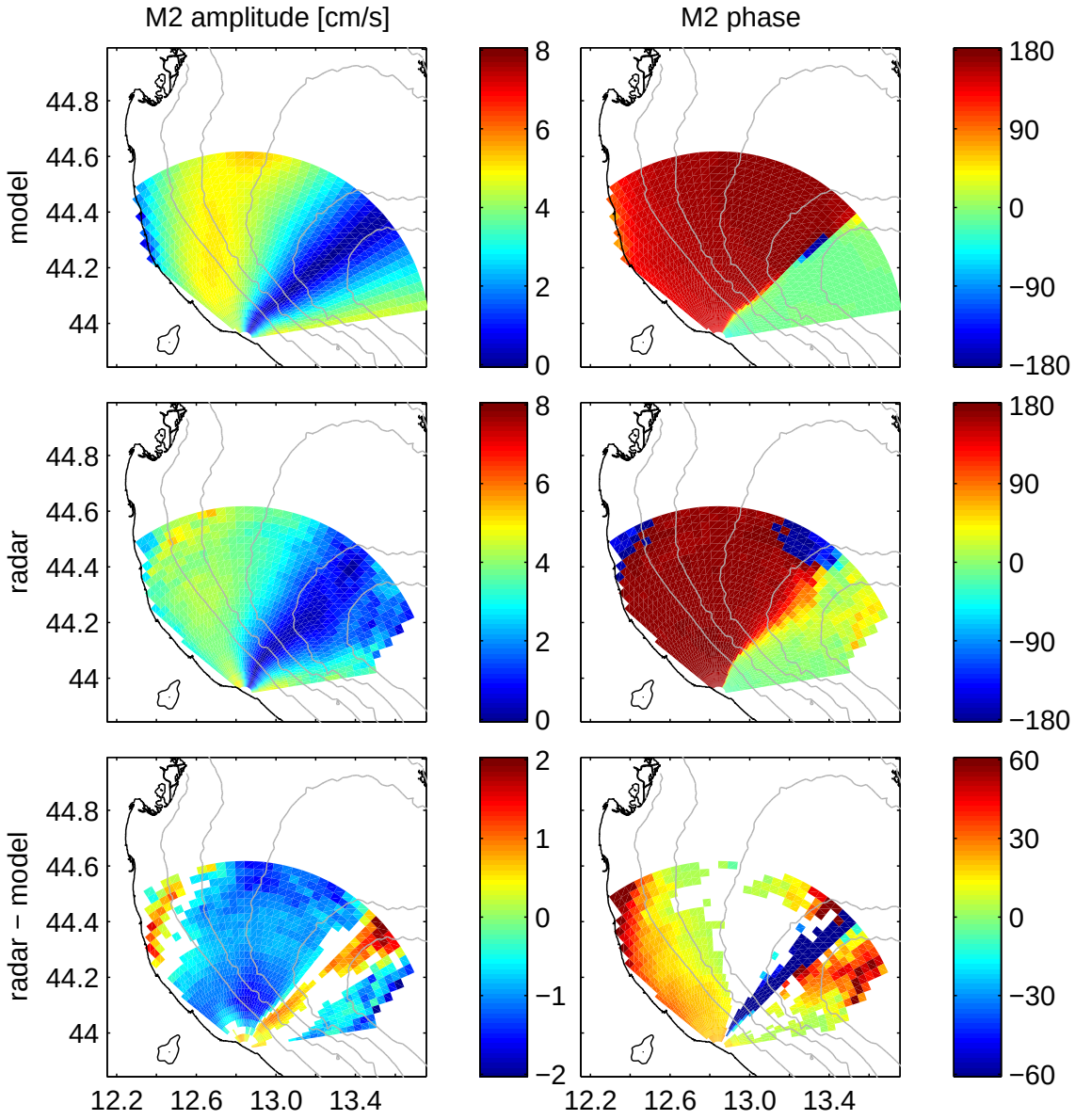

Figure 2.13: same as Fig. 2.12 for Pesaro.

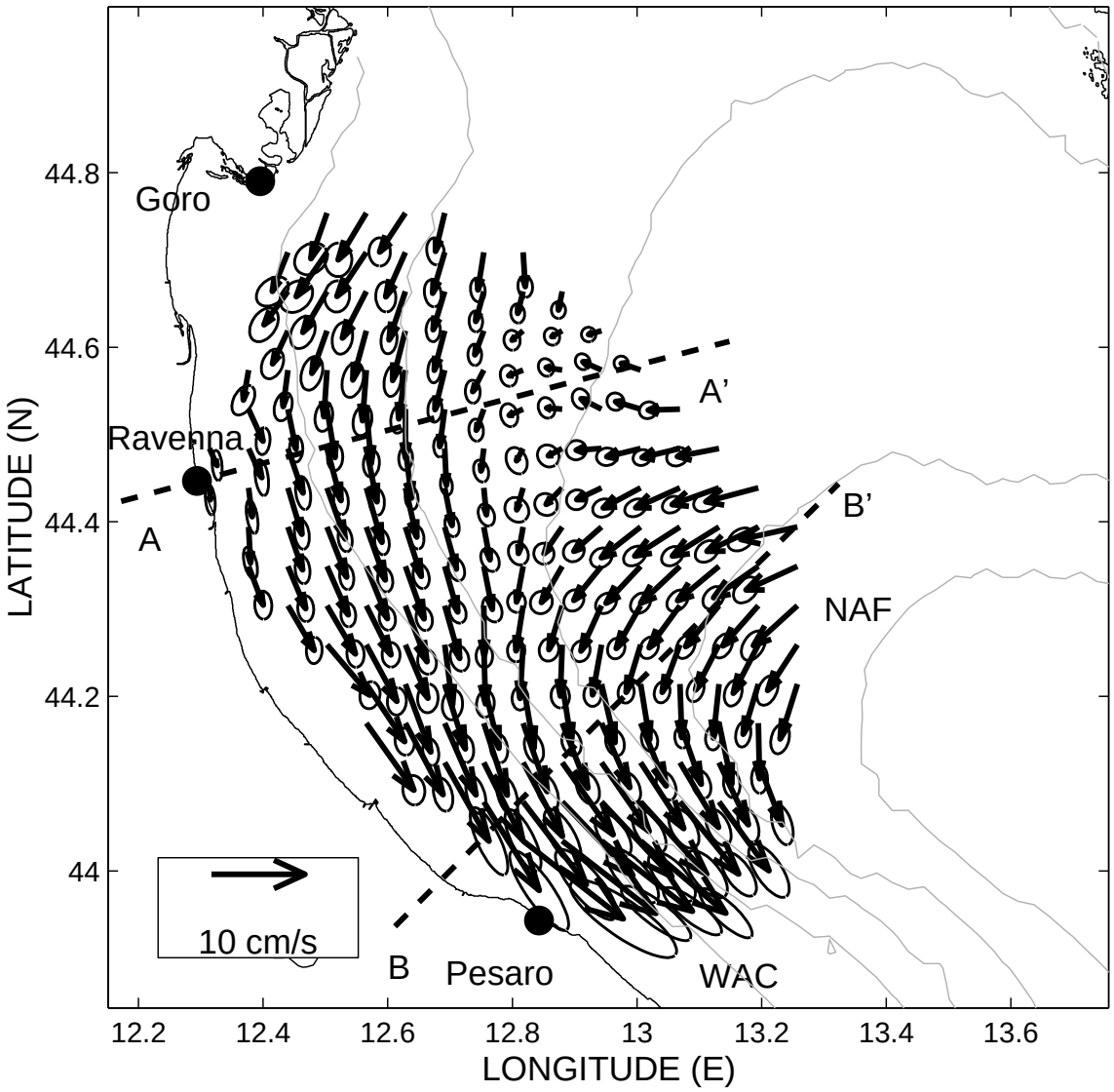

Figure 2.14: Mean flow over the 2-year record, along with 95% confidence ellipses, computed from the low-pass filtered currents variance scaled by the number of degrees of freedom estimated from the integral time scales of the time series. (Dashed lines) transects AA' and BB' along which mean flow profiles are shown in Fig. 2.15.

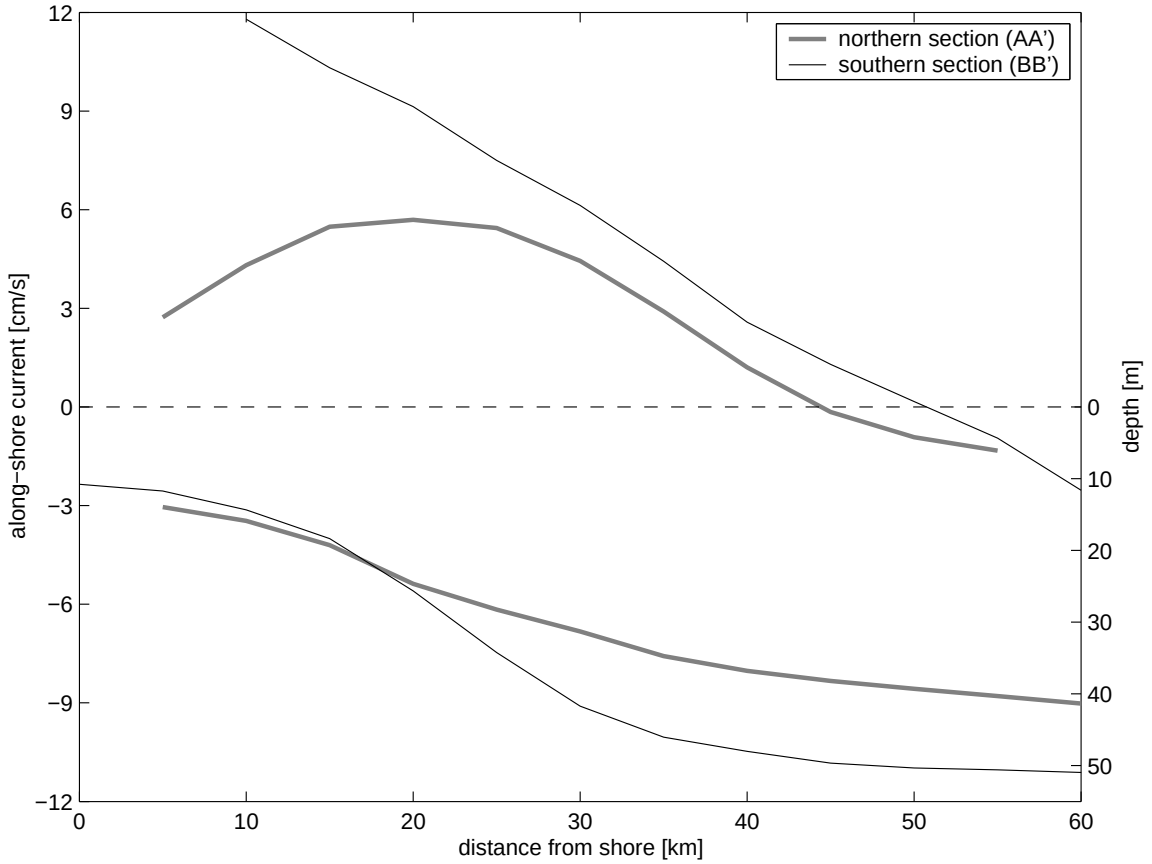

Figure 2.15: Along-shore component of the mean flow (top curves, left y-axis, positive values indicate flow toward the southeast), and bathymetry (bottom curves, right y-axis), along cross-shore transects AA' and BB' of Fig. 2.14.

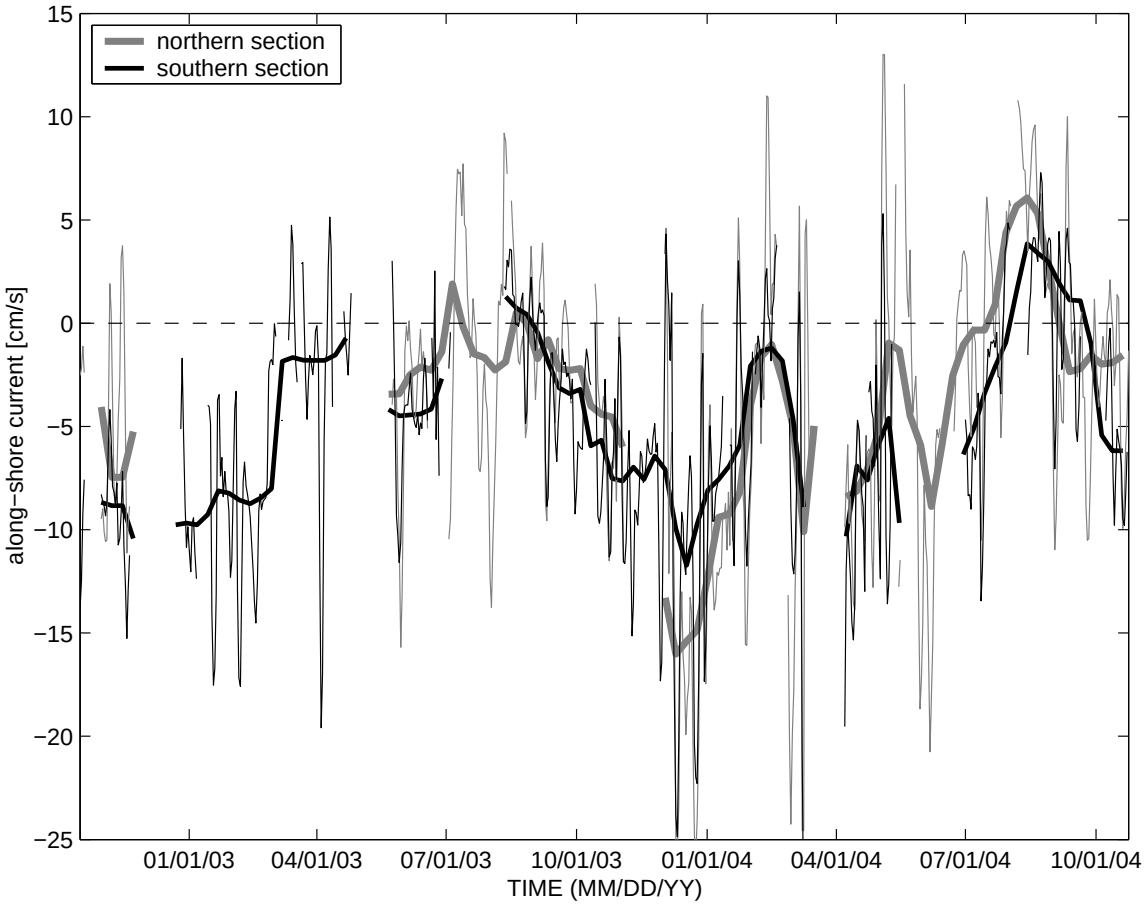

Figure 2.16: Time series of along-shore flow (negative values indicate flow toward the southeast) averaged over the cross-shore sections shown in Fig. 2.14 from the coast to the distance of no mean flow. Currents were detided and low-pass filtered with a 3-day running median (thin lines), and further low-pass filtered with a 30-day running median (thick lines).

Chapter 3

Tidal currents in the Kauai Channel, Hawai'i. Part I: observations and numerical model predictions

Where it is shown that in a stratified ocean, near abrupt topography, tides are not accurately predicted at the surface by stratified 3-D numerical models, which assume that they propagate in an ocean at rest, whereas surface-intensified energetic background currents affect their propagation, and act as a low-pass filter for vertical modes.

3.1 Introduction

The Hawai'i Ocean Mixing Experiment (HOME, Rudnick et al. (2003)) was designed to improve our understanding of tidally-induced mixing and quantify the energy budget for an isolated deep-ocean abrupt topographic feature. About 20 GW (2×10^{10} W) of barotropic energy is lost at the Hawaiian ridge (Egbert and Ray, 2001). An intensive observational program was carried out in the Kaua'i Channel, one of the strongest internal tides generation sites along the ridge (Merrifield et al., 2001). We report here on observations from two High-Frequency (HF) radio Doppler surface current meters and several moored Acoustic Doppler Current Profilers (ADCP) deployed in 2002 and 2003 to establish the long-term surface and sub-surface context for the experiment. Such long-term time-series are critical for placing the short-term dissipation measurements, often taken over one or two tidal cycles at a given location (Klymak et al., 2006; Carter et al., 2006;

Lee et al., 2006), or instantly along ship transects (Martin and Rudnick, 2007), into the context of tidal and mesoscale variability. They are also critical to estimate the amount of energy smeared out of the phase-locked signal (incoherent energy) by amplitude and phase modulation as the internal tides propagate through a varying medium (Chiswell, 2002), in order to adjust estimations from phase-locked observations (coherent energy), such as altimetry (Ray and Mitchum, 1997; Ray and Cartwright, 2001).

We compare our observations to the predictions of two different numerical models. Both compute the internal tides generation and propagation with realistic bathymetry and stratification in an ocean at rest, but they differ in their approach. One model (POM, Carter et al. (2007)) is nonlinear and uses a complex turbulent closure scheme, while the other (PEZHAT, Zaron and Egbert (2006b)) is linear with simple weak down-gradient diffusion. A companion paper, Zaron et al. (2008), presents an assimilative solution for PEZHAT, in order to infer the nonlinear and dissipative dynamics from the HF-radio data.

The paper is organized as follows: the experimental setting is described in section 3.2, the numerical models are described in section 3.3 and compared to the observations in section 3.4. The results are discussed in section 3.5 and summarized in section 3.6. Appendix A describes data processing and Appendix B compares the HF-radios and ADCPs observations.

3.2 Instruments and methods

Two 16 MHz HF-radio surface current meters were deployed along the west coast of O‘ahu, Hawai‘i (Fig. 3.1), from September 2002 to May 2003. HF-radios infer the radial component of surface currents from the Doppler-shift of radio waves Bragg-scattered by surface gravity waves of half the electromagnetic wavelength, or 9.35 m at 16 MHz. At least two sites are required to construct vector currents. The northern site was at Ka‘ena Point (21.57N, 158.26W), on top of a cliff 360 m above sea level. The southern site was at Ko‘Olina (21.33N, 158.12W), along the shore at sea level.

The FMCW (frequency-modulated continuous-wave) Doppler radios were operated with 100 kHz bandwidth, yielding a range resolution of 1.5 km. A chirp length of 0.34 s, averaging time of 9 min and repeat cycles of 20 min were programmed, each site

transmitting while the other was quiet. The transmit antenna arrays formed a beam toward the ocean, a null in the direction of the receive antennas to reduce the direct path energy, and a 22-dB rejection of the back signal (critical at Ka‘ena Point to attenuate the echoes from the northern side of the Kaua‘i channel). The instruments were operated in beam-forming mode with linear arrays of 16 receive antennas, oriented at 302^o clockwise from north at Ka‘ena and 355^o at Ko‘Olina, yielding an azimuthal resolution of ~ 7 degrees when steering the beam normal to the receive array, and degrading at higher incidence angles; above 60 degrees the sidelobes are too large to obtain uncontaminated measurements (Gurgel et al., 1999).

The maximum range of good measurements depends on the signal propagation conditions and on the ambient electromagnetic noise. During the experiment, there was a marked diurnal modulation of coverage (Fig. 3.1). The maximum day/night time ranges of 50% data return were 121/94 km for Ko‘Olina, and 127/106 km for Ka‘ena from September to November 2002. Presumably, the D-layer of the ionosphere, more dissipative, inhibits the propagation of distant electromagnetic signals in day time, but disappears at night, leaving the more reflective E-layer to propagate distant electromagnetic noise. To reduce the impact of this modulation on the analysis of tidal constituents, least-square fits were performed only if more than half of the data were available. It should be noted that M_2 will be less affected by a diurnal modulation of data availability than K_1 (separated from S_1 by only one cycle per year, see Table 2.1) or S_2.

Vector currents were mapped on a 5-km resolution Cartesian grid by least-square fitting the zonal and meridional components to radial measurements from both sites within a 5 km search radius. The range of useful data was limited by geometric dilution of precision (GDOP, see Fig. 3.2 and Appendix A). Vector current estimations with a GDOP greater than 1 were discarded.

ADCPs and temperature and salinity sensors were also deployed by other investigators (D. Luther, M. Merrifield, and M. Levine), on moorings A2 (1330m water depth), C1 (4700m water depth) and C2 (4010m water depth). Upward-looking 300 kHz ADCPs were deployed at $\sim 90m$ depths on each mooring, providing good data up to 12 m below the surface, with vertical resolution of 4 m, and 10-minute acquisitions at C1 and 20-minute acquisitions at C2 and A2. Upward-looking 75 kHz ADCPs were deployed at

$\sim 750m$ depths on each mooring with another one at $\sim 1300m$ on A2, with vertical resolution of 8 m, and 8-minute acquisitions at C1, 10-minute acquisitions at C2 and 16-minute acquisitions at A2. The two deepest ADCPs ranges at A2 were overlapping for a few depth bins. Visual inspection of the data prompted to discard the middle ADCP data in favor of the deeper ADCP where they overlapped. At all moorings, there were diurnally missing observations between 160 and 350 m due to a lack of scatterers twice a day. The same procedure as for the HF-radios was applied to minimize impacts on data processing. Finally, 36 irregularly-spaced temperature sensors on A2 covered the water column from 210 m to 1280 m. Clusters with instruments closer than 40 m from each other were averaged together. Temperatures were detided and low-pass filtered with a 3-day cutoff period.

Temporal coverages of the instruments are shown in Fig. 3.3. Failures occurred at both sites due to electrical power loss, cables damaged by surf run-up at Ko‘Olina and by high winds over Ka‘ena ridge, and by intermittent radio interference. Data was lost for periods of a few days to 2 months at Ka‘ena. Therefore, two 59-day periods (corresponding to four spring-neap cycles) of almost uninterrupted coverage were selected for analysis: Sep 11 to Nov 9, 2002 (period 1), and Mar 3 to May 1, 2003 (period 2). A quality check of the radial currents is provided by the correlation between measurements from both sites, which should mimic the cosine of the angle between the two sites if along-baseline and across-baseline current components were uncorrelated with equal variance (Appendix B). This is indeed well verified (Fig. 3.4), although the correlation is slightly lower at far ranges north of C1 than south during period 1, and in the middle of the sector during period 2. This is therefore more likely attributable to the violation of the above assumptions than to measurement errors.

Comparisons between HF-radios and ADCPs are presented in Appendix B. The instruments are consistent both at high and low frequencies. Rotary spectra of the surface currents, spatially averaged over grid points with more than 75% temporal coverage, are shown in Figure 3.5 for each period. The spectra are red, with the maximum energy at periods longer than 30 days during period 1, and at periods between 15 and 30 days during period 2. These low-frequency currents are described in Chapters 4 and 5 and Appendix E. The next strongest energy is at the semi-diurnal tides, while the diurnal tides energy is an order of magnitude smaller with barely defined peaks. Harmonics of M_2 are distinguishable

but weak. There is a small intertidal peak at 19.3hr during period 1 and 21.5hr during period 2, not far from the 20hr peak in sea level records from Honolulu and Mokuoloe described by Luther (1985). Most of the sub-inertial clockwise peaks fall close to idealized island-trapped wave frequencies, the fundamental eigenfrequency being very close to the inertial frequency (Merrifield et al., 2002) and therefore masking the inertial peak. They were computed for a circular island with vertical walls over a flat bottom ocean 4500m deep, with a radius of 29.4 km, representative of the circumference of O'ahu (Luther, 1985). Baroclinic modes equivalent depths were computed using stratification profiles, averaged over each period, from Station ALOHA, located 100 km north of O'ahu (Karl and Lukas, 1996). The first four vertical modes of the first azimuthal wave correspond very well to peaks during spring 2003. This is surprising and may be fortuitous for vertical modes higher than 2, since their shorter offshore decay scale make them more sensitive to bottom slope close to shore (Hogg, 1980). The peaks at 5.5 days during period 1 and at 8.4 days during period 2 are probably not associated with island trapped waves. The latter is close to the 8 days peak observed by a current meter moored at 41m depth offshore of Kahe Point (on the west shore of O'ahu) from Dec 1983 to Mar 1984 (Lumpkin (1995), his Fig. 14). We focus here on the main tidal frequencies (M_2, S_2, K_1, and O_1).

3.3 Numerical models

Two 3-D stratified numerical models of the tides are compared with our observations. These models have been validated with altimetry and moored ADCPs (Zaron and Egbert, 2007; Carter et al., 2007).

3.3.1 Description

PEZ-HAT (Primitive Equations Z-coordinate - Harmonic Analysis Tides, Zaron and Egbert (2006b)) is a primitive equation model based on the Geophysical Fluid Dynamics Laboratory Modular Ocean Model (GFDL MOM3, Pacanowski and Griffies (1999)), and a set of modules to implement the astronomical tidal forcing, open boundary conditions, and harmonic analysis of the solutions. In the present application, PEZ-HAT is

configured as a solver for the primitive equations linearized around a horizontally uniform background state. It is forced by the normal component of the M_2 barotropic transport on open boundaries, inferred from a larger-scale data-assimilating barotropic tidal model (Zaron and Egbert, 2006a), and by astronomical body forcing, which includes corrections for self-attraction and solid-earth loading (Zaron and Egbert, 2007).

The second model, POM (Princeton Ocean Model, Carter et al. (2007)), is a nonlinear primitive equation model with a second moment turbulent closure sub-model (Mellor and Yamada 2.5-level). It is forced by M_2 elevation and barotropic velocity on open boundaries, inferred from the Hawaii region TPXO6.2 inverse model (Egbert and Erofeeva, 2002). Therefore comparisons between the models should reveal the effects of tidal self-interactions and more complex turbulence mixing parametrization on the internal tides predictions.

The simulation domains encompass the main Hawaiian Islands, excluding the Island of Hawai‘i, which is not associated with large baroclinic energy fluxes (Merrifield and Holloway, 2002). The bathymetry is derived from multibeam sonar data (Eakins et al., 2003) smoothed and gridded to the model resolutions. The stratification is from temperature and salinity observations at Station ALOHA, averaged over 9-month (Sep 2002 - May 2003) for PEZHAT and 10 years for POM. They differ only slightly in the upper 300 m, with negligible effect on the lower vertical modes (Fig. 3.6): the surface values vary by less than 8% for the first three modes. Note that PEZHAT surface values are lower than POM. Other relevant parameters are listed in Table 3.1.

3.3.2 Results and comparisons

The M_2 kinetic energy and phase (phase is defined as the lag of the maximum current, along the northern semi-major axis, with respect to the astronomical phase of M_2 at 0^oE) of the barotropic and surface baroclinic currents for both models are shown in Fig. 3.7 and Fig. 3.8, respectively. Scatterplots of POM vs. PEZHAT values are shown in Fig. 3.9.

M_2 internal tides are generated as the barotropic tide encounters the Hawaiian ridge, propagating almost perpendicular to the ridge axis from the northwest (Larsen,

1977). The elongated structure of the ridge forces the barotropic currents to flow over the topography rather than around it (Fig. 3.7, top panels), inducing vertical velocities that advect isopycnals up and down along the ridge flanks. A resonance occurs when the topographic slope in the direction of the barotropic currents is equal to the internal tide characteristic slope. At these locations, the baroclinic energy is focused into beams radiating up and down the water column along the characteristics, reflecting subsequently off the sea surface and bottom (Merrifield and Holloway, 2002). This is illustrated in Fig. 3.10, which shows vertical sections of baroclinic M_2 kinetic energy and phase across the ridge and cutting through C1 and C2-A2.

The surface reflexion areas are clearly visible in Fig. 3.7 (bottom panels) as arcs of enhanced surface baroclinic currents on both sides of the ridge $\sim$ 30-40 km from the ridge axis. The phase of the surface baroclinic currents (Fig. 3.8, bottom panels) shows the propagation of the internal tides away from the ridge. Interference patterns with other generation areas are found west of Kauaʻi and east of Oʻahu. Notice also the complicated phase pattern right over the ridge, where internal tides generated on both sides of the ridge are superimposed. In contrast, the barotropic phases vary over larger scales, except around the islands where abrupt phase changes are found. The barotropic currents are less than $5cm/s$ in deep water, but can reach over 30 cm/s over the shallow parts of the ridge.

The barotropic currents are well correlated between both models, being mainly determined by the boundary conditions and the topography, but the amplitudes are stronger in PEZHAT compared to POM (Fig. 3.9a). The ratio of spatially averaged barotropic kinetic energy of PEZHAT over POM is 1.32 for the area displayed in Fig. 3.7. This can be attributed to the lack of body forcing in POM (open boundary conditions are similar for both models). In contrast, the surface baroclinic currents show much less correlation (Fig. 3.9b). The surface reflexions are at similar locations but are weaker in POM, probably as a result of the weaker barotropic currents, except for an area south of Kauaʻi, corresponding to the surface reflexion of internal tides generated between Kauaʻi and Niʻihau. The ratio of spatially averaged baroclinic kinetic energy of PEZHAT over POM is 1.27 for the area displayed in Fig. 3.7, close to the ratio of barotropic kinetic energy. Phases are in good agreement between both models (Fig. 3.9, bottom panels), although there is a stronger scatter for the baroclinic surface currents. POM phases have smaller scale structure than

PEZHAT phases, possibly due to nonlinear interactions. The median phase differences (POM minus PEZHAT) is -0.4^o and -10.2^o for the barotropic and surface baroclinic currents, respectively.

There are also differences in the vertical structure of baroclinic currents between both models (Fig. 3.10). At C1, the surface amplification is stronger in PEZHAT, but the subsurface maximum around 300-400 m is weaker, than in POM. Phases agree above 200 m and below 600 m, but differ by $\sim 130^o$ in-between. At C2, PEZHAT predicts a surface intensification absent from POM. This comes from a southward propagating beam generated at the northern branch of the ridge. Both models show a subsurface intensification, corresponding to the beam generated at the southern branch of the ridge, although offset by 120 m in the vertical, and twice as strong in PEZHAT. Finally at A2, there are 3 subsurface maxima, the 2 shallowest corresponding to the southward propagating beams while the deepest corresponds to a northward propagating beam generated at the southern branch of the ridge. They are offset in the vertical: the shallowest beam is deeper in PEZHAT by 65 m, while the middle and deeper beams are shallower by 80 m and 100 m than in POM, respectively. This may be a result of the different stratification (for the shallower beam) and vertical discretization, the 61 levels terrain-following coordinates of POM providing a better resolution over shallow topography than the 60 levels z-coordinates of PEZHAT.

3.4 Models and observations comparisons

HF-radios and ADCPs currents were harmonically analyzed using the T-tide Matlab package (Pawlowicz et al., 2002) over each 59-day period, during which both instruments recorded data (Fig. 3.3). Six tidal constituents (M_2,S_2,N_2,K_1,O_1,Q_1), a constant and a linear trend were least-square fitted to hourly smoothed observations. In addition, HF-radios were harmonically analyzed over the 9-month records using 8 tidal constituents (M_2,S_2,N_2,K_2,K_1,O_1,Q_1,P_1), for comparison with the numerical models.

3.4.1 M_2 constituent

Fig. 3.12 and Fig. 3.13 show the total (barotropic plus baroclinic) M_2 surface currents ellipses and phase, and radial components amplitude and phase in the direction of Ko‘Olina and Ka‘ena, respectively, from the HF-radios, ADCPs 12m bins and models. At C1, the HF-radios (models) major axis amplitude is smaller (larger) than the ADCP. The inclinations of the HF-radios and models ellipses differ by less than 6 degrees, but by up to 20^o from that of the ADCP. The phases all agree within 8^o (~ 15 minutes). Because of the significant geometric dilution of precision at C1 for the HF-radios vector currents (Fig. 3.2), it is better to compare the amplitude and phase of the radial currents in the direction of Ko‘Olina and Ka‘ena (Fig. 3.13, top panels). For these two directions, the observed amplitudes agree within the 95% confidence intervals, while the models are overestimating them. However, the HF-radios and models phases agree within the 95% confidence intervals, while the ADCPs and models phases are significantly different, reflecting the ellipse inclination differences. At C2 and A2, only the radial component in the direction from Ko‘Olina can be compared (Fig. 3.13, bottom panels). The observed currents amplitudes are not or barely significant at the 95% level, and observations and models amplitudes and phases all differ. Again the models overestimate the amplitudes.

Fig. 3.14 shows the kinetic energy and ellipses of total (barotropic plus baroclinic) M_2 surface currents and the amplitudes of the radial currents from the models and HF-radios. A comparison with Fig. 3.7 shows that the surface currents are dominated by the baroclinic component, except near Ka‘ena Point. Strikingly, the surface reflexion is not reproduced in the observations, except southwest of Ka‘ena Point. Instead there is an area of slightly enhanced energy further away from the ridge, centered at (158.5W, 21.15N), with circular ellipses. A comparison of the radial amplitudes shows more clearly that the HF-radios measure enhanced currents further away from the ridge by about 20 km and weaker than in the models.

Scatterplots of modeled versus observed M2 kinetic energy and radial amplitudes (Fig. 3.15) reflect the discrepancies and show the tendency of the models to overestimate the amplitudes, especially for the strongest values. The ratio of modeled over observed

spatially averaged surface kinetic energy for the area covered by the HF-radios is 2.67 for PEZHAT and 1.43 for POM.

Phases, on the other hand, show better agreement than amplitudes (Figs. 3.16 and 3.17). The direction of propagation of the baroclinic tides change near O‘ahu as the tides are refracted by the topography (this could also be due to generation areas over the shallow part of the ridge near Ka‘ena Point where the barotropic currents are aligned in the along-shore direction, see Fig. 3.7). The mean wavelength over the area of observations, computed from the gradients of the cosine and sine of phases, is 162 km from the HF-radios, slightly larger than the 150 km of the first baroclinic M_2 internal mode detected from altimetry data (Ray and Mitchum, 1996), and 103 km and 125 km for PEZHAT and POM, respectively, indicating the contribution of higher modes responsible for the beam-like structure of the internal tides in the models. The median differences between observed and modeled phases are 9.9^o for PEZHAT and 7.3^o for POM.

Comparisons of the vertical structure are provided by the moored ADCPs. They covered almost the whole water column at A2, so baroclinic currents were computed by subtracting depth-averaged currents. At C1 and C2, ADCPs only covered a small portion of the water column, so barotropic currents from PEZHAT were subtracted to obtain baroclinic currents. As C1 and C2 were moored in deep water, barotropic currents are weak and rather well predicted by numerical models. Fig. 3.10 shows the kinetic energy and phase for the models and ADCPs currents. The M_2 currents intensification corresponding to the locations of the beams are confirmed by the observations, except for the surface intensification at C2, although the observed amplitudes are weaker than the modeled amplitudes. At C1, the surface intensification starts just above 200 m in the models, while only above 100 m in the observations. POM phases follow the observed phase increase with depth, with some oscillations around the observed values associated with the location of the beam reflected from the sea surface, but PEZHAT phases differ from the observed values except near the surface. At C2 and A2, both models reproduce the observed phase variations. At A2, the three subsurface intensifications are present in the observations around 240 m, 600 m and just above the bottom at 1290 m. The latter is deeper in the observations than in the models, due to their limited vertical resolution.

3.4.2 S_2, K_1, and O_1 constituents

For these constituents, only POM runs are available, with a reduced domain. The modeled S_2 pattern is similar to that of M_2 (compare Fig. 3.14 and 3.18, and Fig. 3.16 and 3.19), but weaker. However, the observed S_2 pattern is different from the observed M_2 pattern, being more similar to the modeled M_2 pattern, with the surface reflexion at the same location than in the model. The observed mean horizontal wavelength is 143 km, the modeled being 103 km. The ratio of modeled over observed horizontally-averaged kinetic energy is 1.50, close to the M_2 ratio.

Observed and modeled diurnal tidal surface currents are very different, both in amplitude and phase (Fig. 3.20 and 3.21 for K_1, and 3.22 and 3.23 for O_1). Observed amplitudes are generally much stronger than modeled amplitudes. The ratio of observed over modeled horizontally-averaged kinetic energy is ~ 6 for K_1 and O_1. Modeled phases are very homogeneous, the domain being too small to resolve the propagation structure with wavelengths of ~ 400 km. Observed phases are less homogeneous, but do not show a clear propagation signal neither.

3.5 Discussions

Modeled and observed semidiurnal tidal currents have similar phases, with only differences in the inferred internal tide wavelength, but the amplitude patterns and magnitudes differ for M_2. This cannot be attributed to a particular model, since both models are more similar to each other than to the observations. A possible candidate for explaining the differences is the assumption in both models that the tides propagate in an ocean at rest. The ocean around the Hawaiian islands is not at rest. Mean currents flow along the ridge on both sides, and instantaneous currents are dominated by energetic mesoscale and submesoscale eddies (Patzert, 1969; Lumpkin, 1998; Qiu et al., 1997; Flament et al., 2001), described in Chapters 4 and 5 and Appendix E. Eulerian integral time scales computed from the HF-radios observations are typically 3 days only.

Spatial variations in stratification associated with mesoscale currents in thermal wind balance, combined to Doppler-shifting by the mesoscale currents, modify the propa-

gation paths and amplitude by refraction of the internal tides (Rainville and Pinkel, 2006b; Park and Watts, 2006). The associated modification in travel time from the generation area and the measurement locations modulate the phase of the observed signal (Chiswell, 2002; Alford et al., 2006). Phase and amplitude modulations lead to a leaking of energy into neighboring frequencies around the tidal frequencies (incoherent part of the energy), hence decreasing the amount of coherent energy, given by the harmonic analysis over the 9-month record. Colosi and Munk (2006) designed two methods to estimate the incoherent internal tide energy from the Honolulu and Hilo sea level records, the first in the frequency domain (spectral analysis) and the second in the time domain (complex demodulation). Our records lengths are much too short to apply their frequency analysis, since we can barely separate tidal constituents separated by 1 cycle per month. We will therefore apply their time domain analysis, after some modifications required by the short time scales of variability involved here.

The demodulation window length must be chosen no longer than the characteristic time scales of the mesoscale currents, hence should be three days at most. Therefore it is not possible to separate M2 from S2 and K1 from O1 by complex demodulation, and the demodulated amplitude and phase for M2 and K1 will show variations caused by the other tidal constituents. To separate them from variations caused by mesoscale variability, we also apply the complex demodulation to the phase-locked tidal currents obtained from the harmonic analysis over the 9-month record, which resolved the main tidal constituents in the diurnal and semi-diurnal groups. We choose a window length of 3 days to fully resolve M2 and K1 in the presence of noise and missing data, and move the window at daily time steps. A harmonic analysis is performed over each 3-day segment by least-square fitting a constant, a linear trend, and M2 and K1 sinusoids. The fit is not performed if more than 50% of data are missing.

Fig. 3.24 shows the complex-demodulated semi-diurnal major axis amplitude and phase at C1, for the HF-radios grid point closest to C1 and the ADCP 12-m depth bin. A large fraction of variability is due to the interference between different tidal constituents (spring-neap cycle and monthly modulations). However there remains a significant fraction of variability not attributable to these interferences. Most noticeable is the delay and increased strength of maximum currents for the first spring tide, which should have occurred

on Sep 22 according to the phase-locked tidal currents, but actually occurs on Sep 27-29 for the observed currents, 5-7 days later. It corresponds to the passage of a cyclone over the mooring location (see Chapter 4). Park and Watts (2006) showed that eddies in the South China Sea modify the propagation paths of mode 1 internal tides through refraction by varying stratification and currents. Trajectories are focused toward the center of cyclones, leading to an increased energy over the cyclone, while they are diverted away from the center of anticyclones. Using 3-D ray tracing, we show in Chapter 4 that the same is happening here for the internal tidal beams.

At other times, the mesoscale currents do not affect much the internal tides propagation, and the observed amplitude pattern resembles the modeled pattern, as shown in Fig. 3.25 on 11/05/2002. Interestingly, this only happens during spring tides, and may have constrained the observed S_2 pattern to be more similar to the modeled semi-diurnal patterns than the observed M_2 pattern.

To account for the incoherent energy lost by the 9-month harmonic analysis, we average the complex demodulated tidal surface currents kinetic energy over the observation area, and plot the resulting time variability in Fig. 3.26. The energy leaked to neighboring frequencies due to time variability of tidal amplitude and phase, caught by the complex demodulation but not by the 9-month harmonic analysis, results in higher kinetic energies for the "full" currents than for the phase-locked currents. Although we cannot separate the contributions from the different semi-diurnal constituents, if we assume that each looses the same relative amount of coherent energy (as supported by the similar ratios of modeled over observed horizontally-averaged kinetic energies), the ratio of temporally-averaged kinetic energies should reflect that of each constituent. The latter is 1.6 during fall 2002, slightly higher than the ratio of modeled over observed M_2 phase-locked energy for POM, but below that for PEZHAT, and only 1.1 during spring 2003, insufficient to account for the differences with the models. During spring 2003 there were not only times when the "full" energy was stronger than the phase-locked energy (e.g. around April 18), like during Fall 2002, but also times when it was weaker (e.g. around March 19). We show in Chapter 4 that this is due to the passage of mesoscale vorticity waves over the ridge, modulating the internal tides surface amplitude higher or lower, depending on the phase of the waves.

Another possible contribution to the lower energy level in Spring 2003 is that the barotropic to baroclinic energy conversion is modulated by the stratification changes associated with the vorticity waves. Holloway and Merrifield (1999) investigated numerically the internal tide generation by idealized seamounts and ridges with realistic stratification profiles. To investigate the effect of stratification variations, they compared the depth-integrated energy fluxes for two different stratification profiles for the same topographic feature, a Gaussian shaped ridge peaking at 200 m below sea level, with horizontal aspect ratio equal to 3. One profile was representing the annually averaged Hawaiian conditions, and the other had reduced values in the upper 1500 m. They found that the energy fluxes reached 50% higher values about 30 km from the ridge crest in the case of weaker stratification. Assuming that the barotropic tidal currents were not affected, they attributed it to the fact that the ratios of bottom slope to M_2 characteristic slope were closer to 1 in the supercritical depth range, which increased the area of near-critical slopes and therefore favored the barotropic to baroclinic energy conversion.

Similarly, Park and Watts (2006) suggested that stratification variability associated with mesoscale eddies was responsible for internal tides generation modulation in the Southwestern Japan/East Sea. They showed that basin averaged first-baroclinic mode M2 amplitudes seemed correlated with the difference between the M2 characteristics and bottom slopes averaged over the continental shelf-slope region.

The same could happen in our case when stratification is increased in the upper water column during the passage of the vorticity waves over the ridge (see Chapter 4). To investigate this possibility, we compute the M_2 characteristic slopes from the HOT stratification and from that associated with an idealization of the observed vorticity wave on March 19, 2003. Histograms of the ratio of bottom slope in the direction of maximum barotropic vertical velocity (computed from PEZHAT solution) over M_2 characteristic slope for depths shallower than 2000 m and areas of the ridge potentially affecting the HF-radios observation domain are shown in Fig. 3.27. We see that the changes are negligible, with only slightly fewer locations with ratios near one in the presence of the vorticity wave. This suggests that the internal tide generation is not significantly affected by stratification variability associated with mesoscale features passing over the ridge.

The strong stratification in the seasonal thermocline during Fall conditions (Fig. 3.6) could also affect the internal tides reaching the surface, through partial reflexion of energy at the stratification peak, which is not taken into account by the WKB approximation used in Chapter 4. Gerkema (2001) studied the propagation of internal waves in an ocean with an idealized stratification consisting of a mixed upper layer and a linearly stratified lower layer, with a density jump across the interface, which represented the thermocline. He showed that a strong thermocline was almost entirely reflecting upward propagating internal wave beams, while with a moderately strong thermocline some energy was leaking into the mixed layer, and with no thermocline the beams were reflecting off the sea surface. This would imply for us that the energy reaching the surface should be stronger in spring than in fall, contrary to our observations. This suggests that this phenomenon is not dominant here.

Rainville and Pinkel (2006b) showed that the effect of mesoscale variability on the propagation of internal tides generated in the Kaua‘i Channel increased with higher mode numbers, and could explain the decay of the coherent signal along Topex-Poseidon track 112 south of the ridge. The same phenomenon can explain our observations: the beam structure of the internal tides near the ridge requires many vertical modes to be superimposed coherently. The strong mesoscale currents observed near the ridge render the higher vertical modes incoherent with the barotropic forcing very close to their generation locations, so that at the first surface reflexion, the vertical structure results mainly from the lowest modes, yielding a weaker and broader area of enhanced energy, as shown in Fig. 3.28. Comparing Fig. 3.28 to the observations in Fig. 3.14a, we find a qualitative agreement, the weaker and broader area of increased energy in the observations being consistent with the contribution of only a few low modes. However, the location of this area still does not correspond to that in the low-modes summations from the POM model. The discrepancy could be attributed to several factors. First, this is a qualitative explanation only, since a quantitative analysis as in Rainville and Pinkel (2006b) would be complicated by the fact that vertical modes are coupled together in the case of variable topography (Griffiths and Grimshaw, 2007) and vertically-sheared currents (Mooers, 1975a). Therefore, computing vertical modes at each grid point of the model and projecting the currents on them is not expected to reproduce the evolution of the low modes as they propagate away

from the ridge. Second, the low modes can be affected by the mean currents, or be rectified by the mesoscale variability. Zaron et al. (2008) use the data-assimilating version of PEZHAT to assimilate the HF-radios observations and diagnose the structure of the mean currents that would explain the observations if the only missing physics in the model were the tides-mesoscale interactions. The result does not resemble the observed mean currents, suggesting that the rectification by the mesoscale variability is preponderant.

3.6 Conclusions

Observations of surface currents by High-Frequency radio current meters were compared with two 3D high resolution numerical models of the tides in the Kaua‘i Channel. Over the observed area, south of Ka‘ena ridge, the tidal surface currents are dominated by the baroclinic modes. An harmonic analysis over the 9-month record yields a good agreement for the phases, consistent with a southwestward propagation of low-mode internal tides refracted by topography. However, the amplitude or horizontal kinetic energy are not well reproduced by the models. They both predict a band of sharply enhanced energy between 30 and 40 km from the ridge crest, corresponding to the first surface reflexion of internal tidal beams generated at critical slopes on the flanks of the ridge. Instead, the observations show weaker and broader areas of increased energy: one extending southwestward from Ka‘ena Point, at the same location as in the models, and one centered at (158.5W, 21.15N), with circular current ellipses, ~ 20 km further away from the ridge than in the models.

Observations also show a strong temporal variability in the spatial pattern and amplitude of the semi-diurnal and diurnal currents, due to interference between the different tidal constituents and to interactions with mesoscale currents. The latter are surface-intensified and therefore mainly affect the tides in the upper 200 m of the water column (see Chapter 4). This explains why deeper observations from other HOME investigators agreed quite well with the POM model (Rainville and Pinkel, 2006a; Lee et al., 2006; Alford et al., 2006; Nash et al., 2006; Carter et al., 2006), while significant differences are found with our surface observations. The observed energy pattern can be explained as the superposition of only a few low modes, the higher modes coherent amplitudes being reduced by

the mesoscale variability. Accounting for the incoherent part of energy in the observations yields averaged values closer to the modeled values.

Parameter	PEZHAT	POM
Δx	2km	$\sim$ 1km (0.01^o)
Δz	60 z-levels unevenly spaced (30m near surface to 430m at 4000m)	61 σ-levels evenly spaced
A_V	$5 \times 10^{-4} m^2.s^{-1}$	Mellor-Yamada 2.5
K_V	$0.5 \times 10^{-4} m^2.s^{-1}$	0
A_H	$12 m^2.s^{-1}$	Smagorinsky
K_H	$12 m^2.s^{-1}$	0
T	14 M_2 periods	18 M_2 periods
T_{HA}	3 M_2 periods	6 M_2 periods

Table 3.1: Models parameters: Δx: approximate horizontal resolution, Δz: vertical resolution, A_V and K_V: vertical viscosity and diffusivity, A_H and K_H: horizontal viscosity and diffusivity, T: time of model integration, T_{HA}: time at the end of model integration used for harmonic analysis.

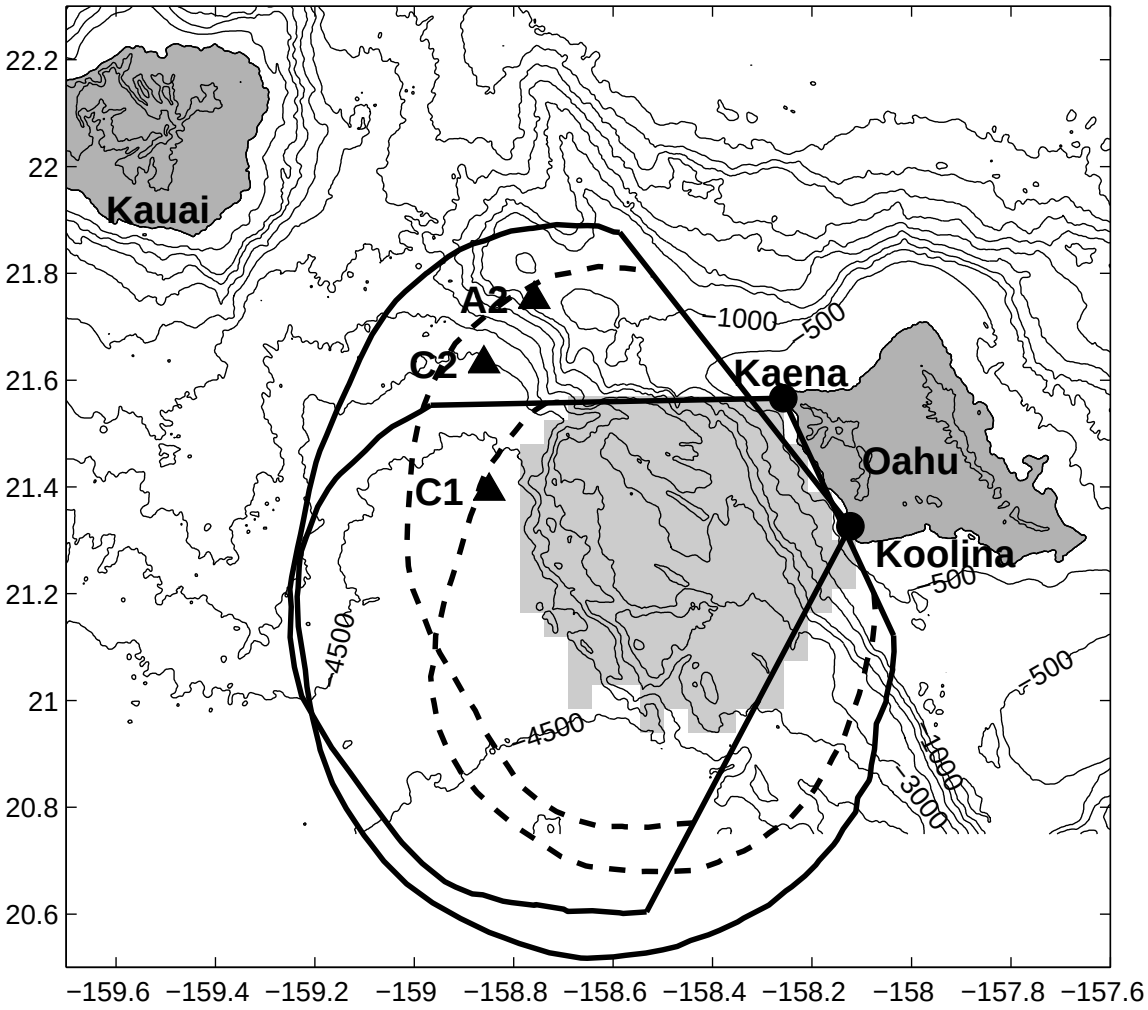

Figure 3.1: Bathymetry (from 150m resolution data, Eakins et al. (2003)) of the Kauai Channel (thin gray lines every 500 m, thick lines for 0 m) and the limits of 50% HF-radios data return over the period Sep 11 to Nov 9, 2002 for day time (4pm to 4am UTC, thick solid lines) and night time (4am to 4pm UTC, thick dashed lines). The area of 75% data return for vector currents is shaded in gray. The locations of the HF-radios (circles) and HOME moorings (triangles) are indicated.

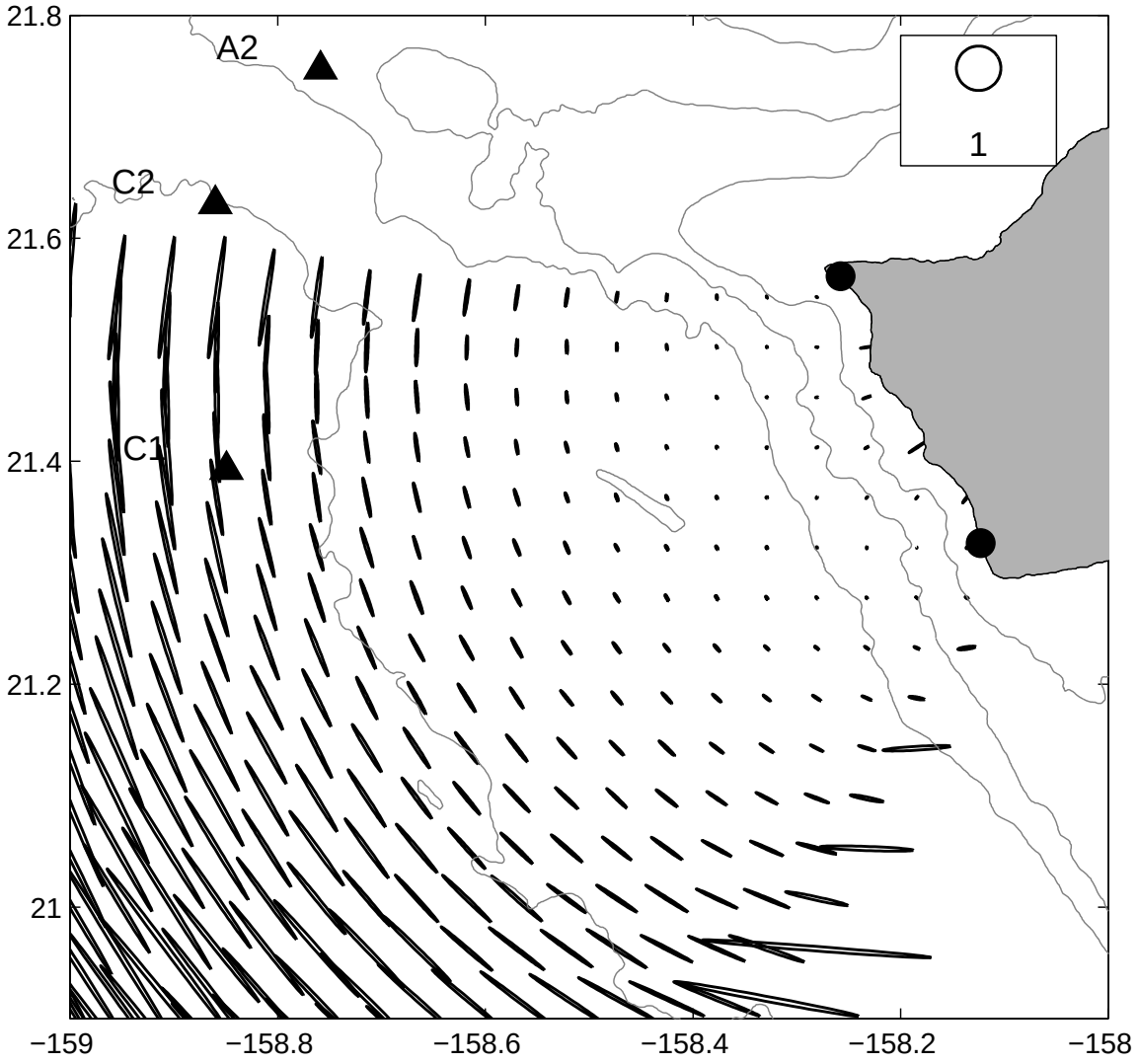

Figure 3.2: Geometric Dilution Of Precision (GDOP) ellipses. The legend corresponds to the threshold value selected to discard vector currents poorly constrained.

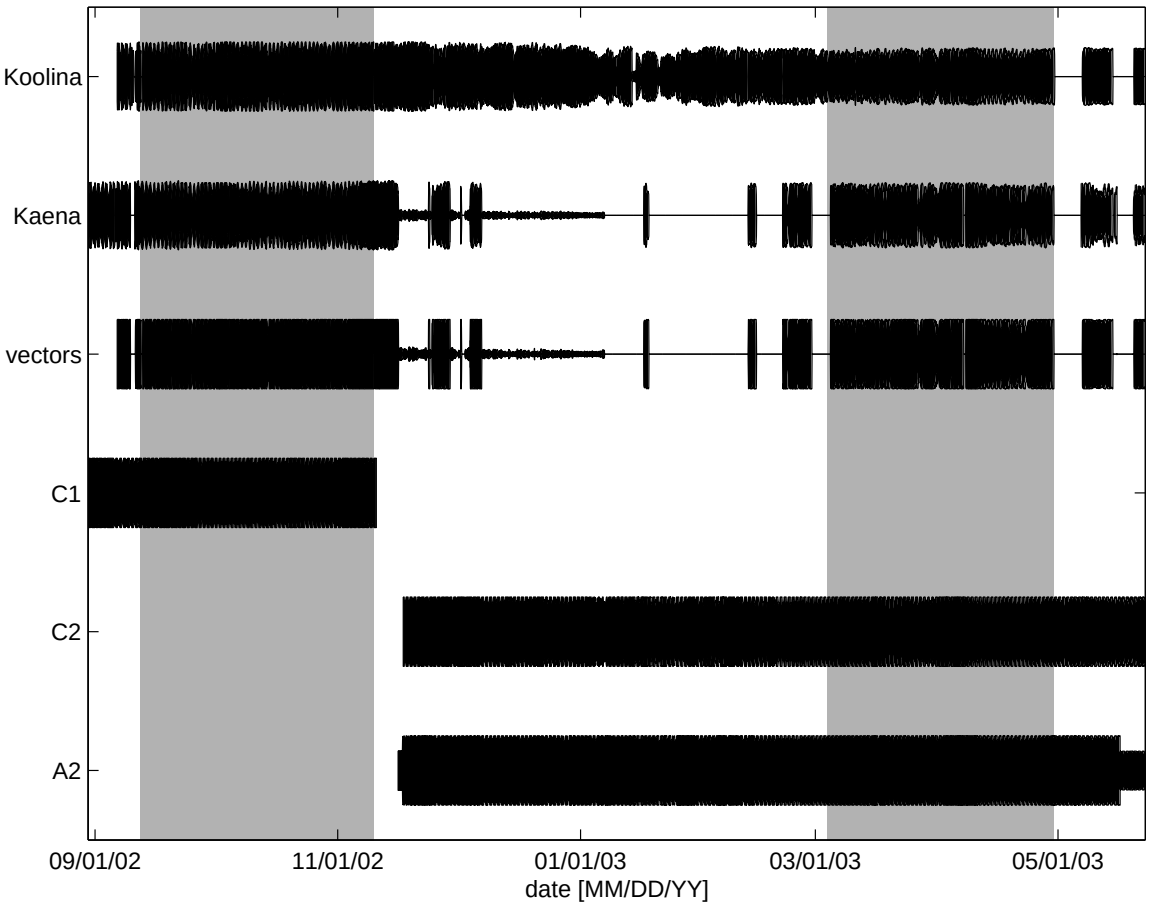

Figure 3.3: Temporal coverage of the two HF-radio sites, of the combined vector currents, and of the ADCPs. The lines thickness corresponds to the relative percentage of grid points with data. The two 59-day periods selected in this study are shaded in gray: Sep 11 to Nov 9, 2002 (period 1) and Mar 3 to May 1, 2003 (period 2).

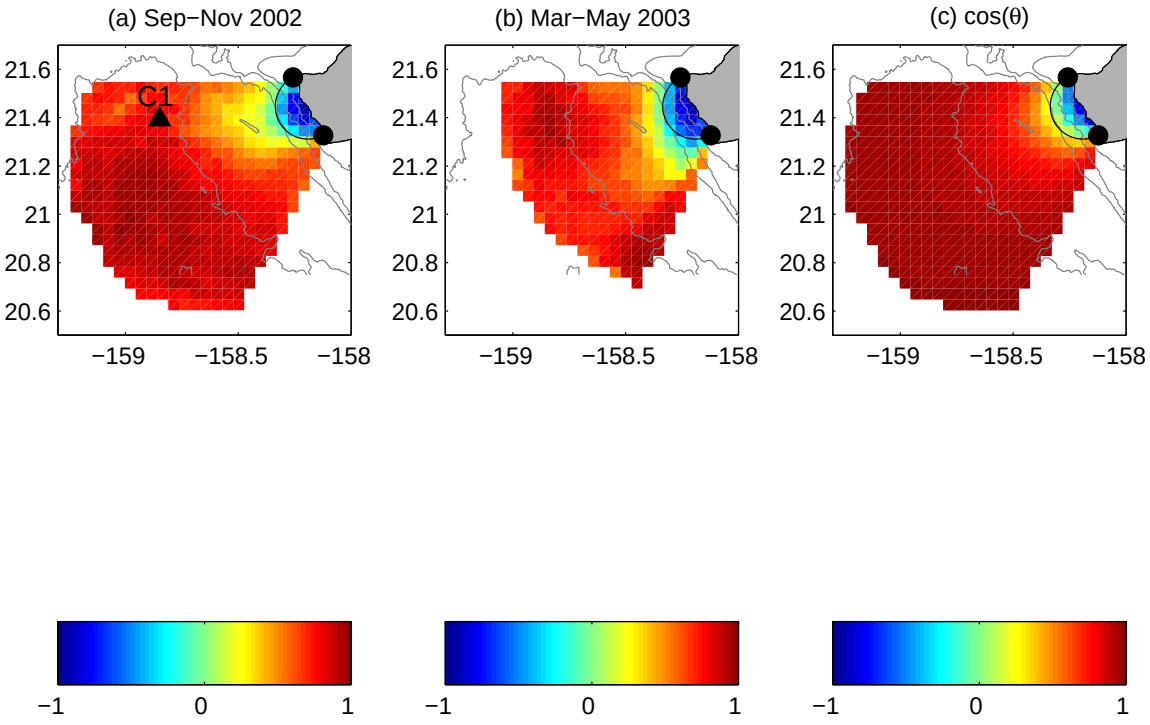

Figure 3.4: Correlation between Ko‘Olina and Ka‘ena radial currents for the first period (a) and the second period (b); and the cosine of the angle between the 2 sites (c). The circle where the angle between the two sites is 90^o is shown for reference.

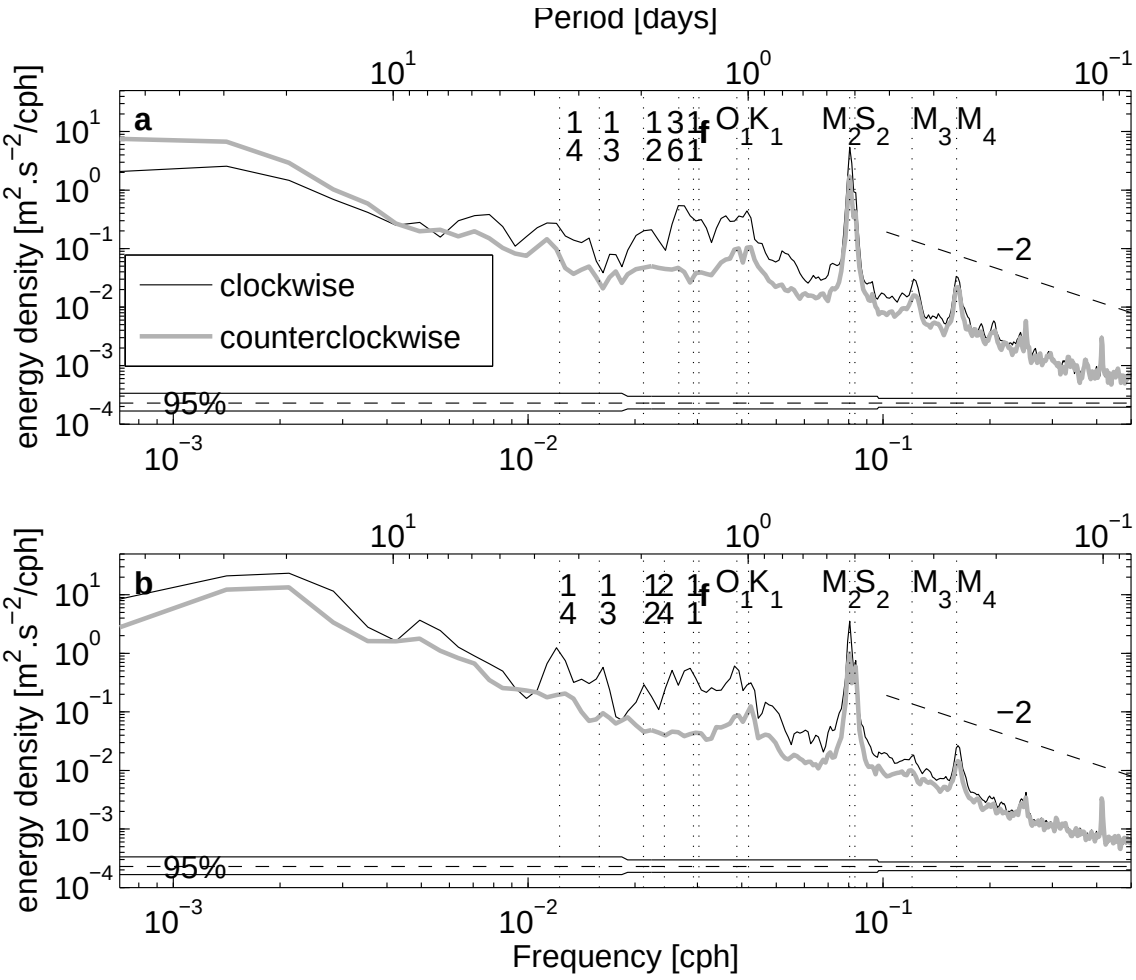

Figure 3.5: Rotary power spectra spatially-averaged over grid points with more than 75% data return (Fig. 3.1) for period 1 (a) and period 2 (b). Black thin lines for clockwise and gray thick lines for anticlockwise components. 95% confidence intervals, shown at the bottom of the panels, narrow at higher frequencies with the increased number of degrees of freedom used in the selected frequency ranges. Tidal constituents, inertial frequency f and island trapped waves frequencies (top number: azimuthal mode, bottom number: vertical mode) are indicated by vertical dotted lines and labeled at the top of the panels. The slanted dashed lines indicate a -5/3 slope in frequency.

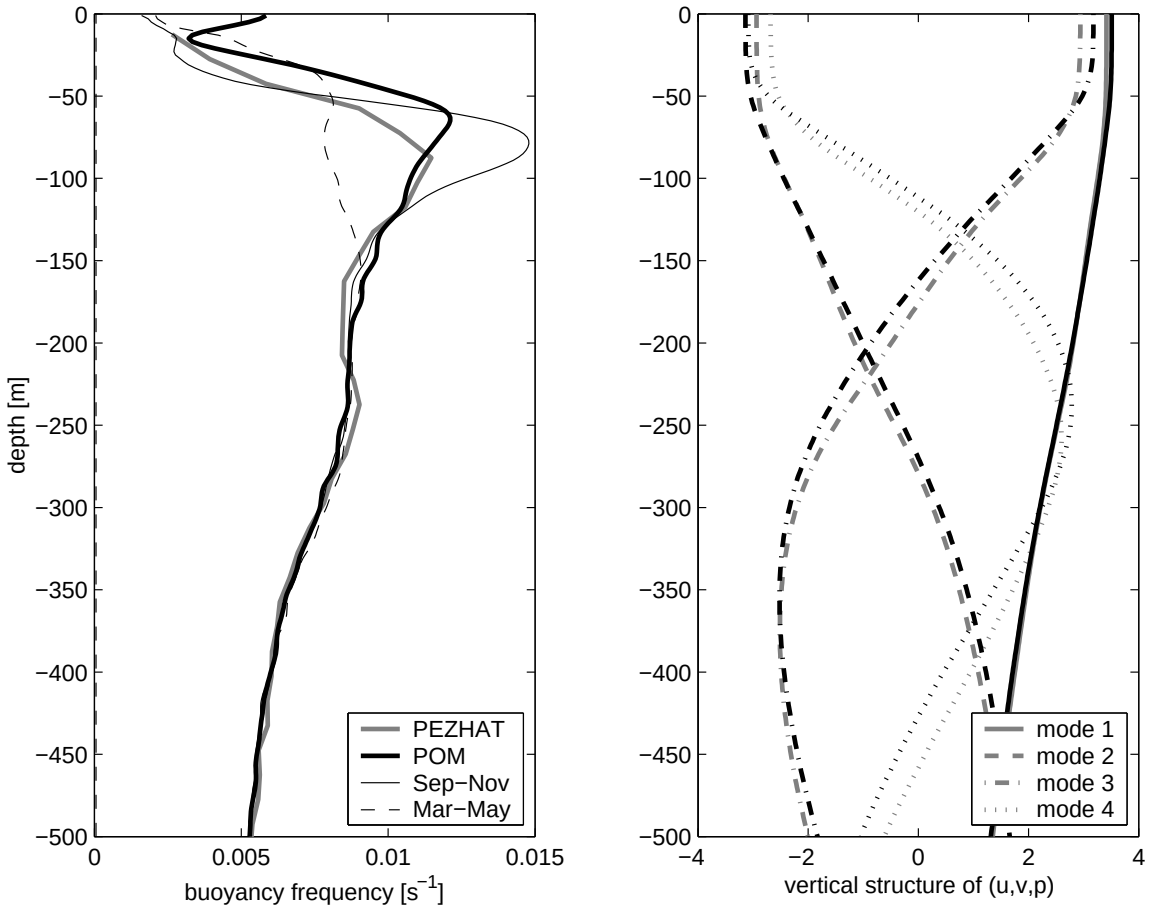

Figure 3.6: (a) Buoyancy frequency (s^{-1}) used in PEZHAT (thick gray line) and POM (thick black line), from temperature and salinity observations at Station Aloha. Also shown are climatologies for Sep-Nov (thin solid line) and Mar-May (thin dashed line). (b) Vertical structure for u, v or p for the first 4 modes for PEZHAT (gray lines) and POM (black lines).

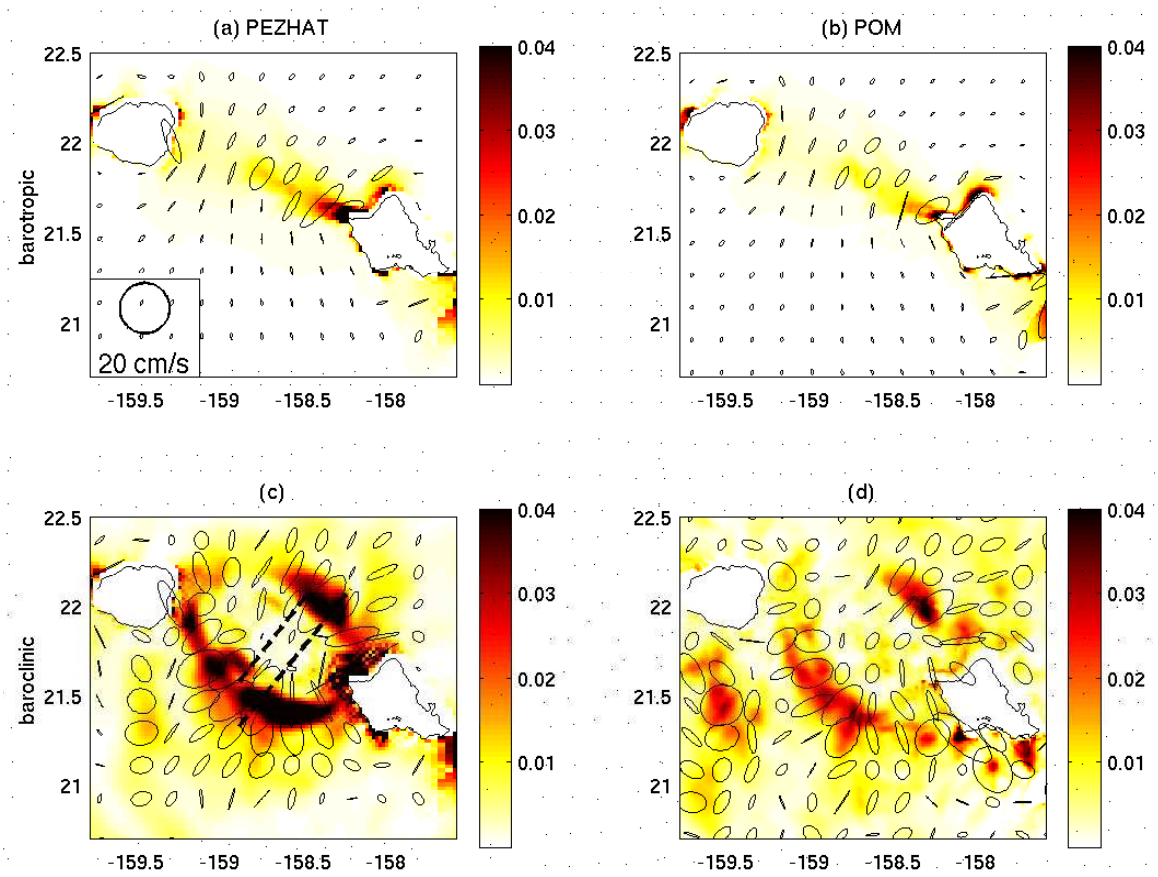

Figure 3.7: M_2 kinetic energy (color, $m^2.s^{-2}$) and ellipses (black) of the barotropic (top panels) and surface baroclinic (bottom panels) currents for PEZHAT (left panels) and POM (right panels). The white dashed lines in panel c indicate the locations of the vertical transects shown in Fig. 3.10.

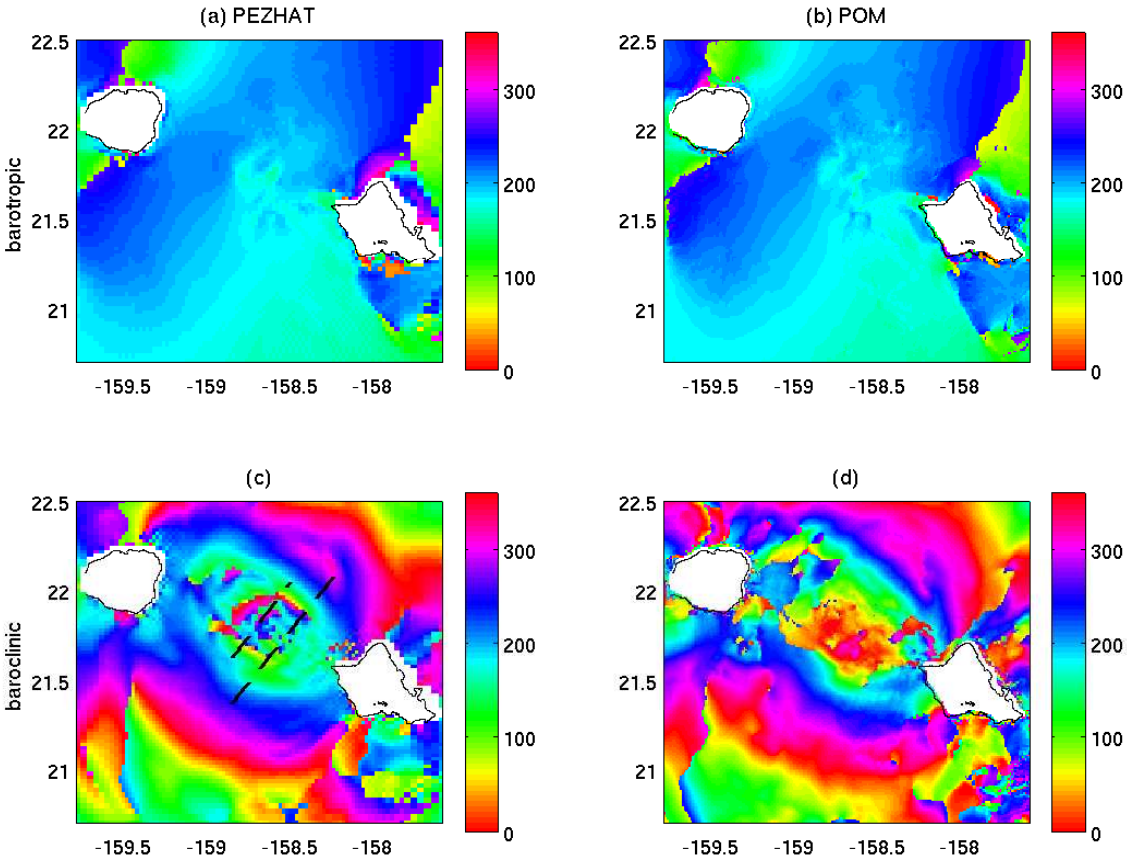

Figure 3.8: Same as in Fig. 3.7 for the phase.

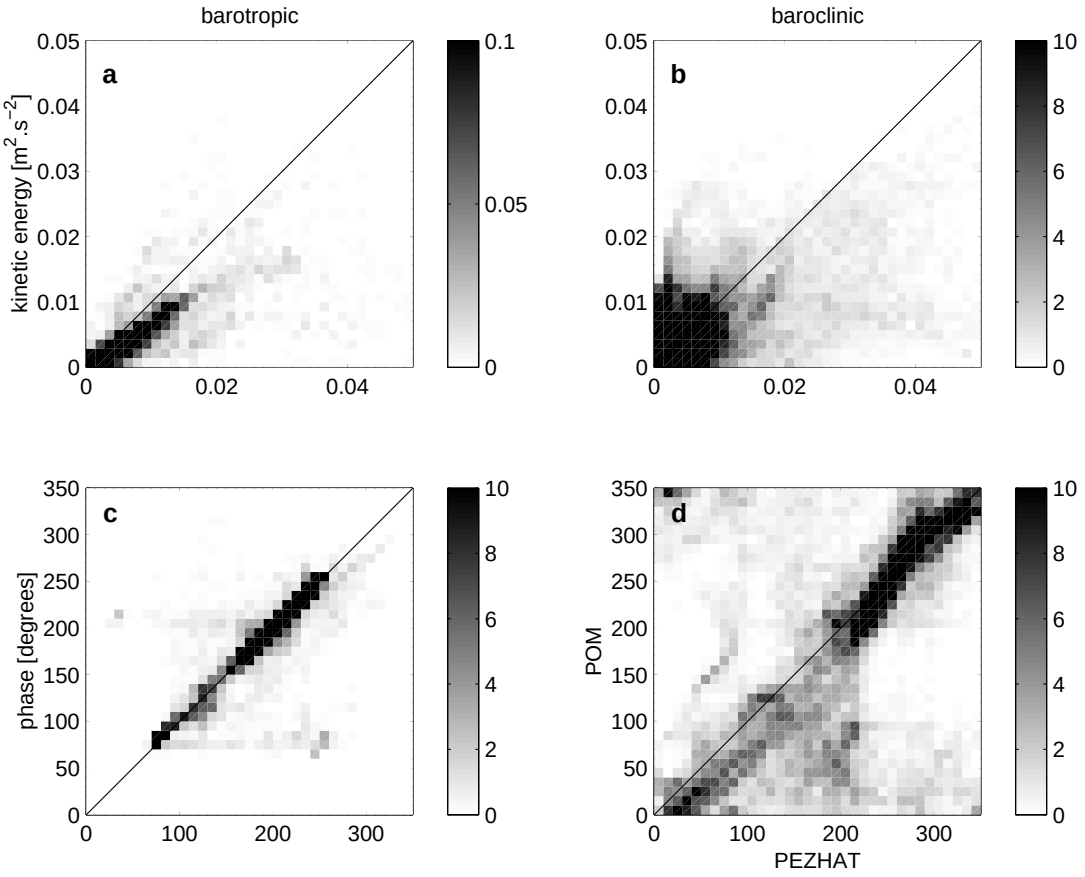

Figure 3.9: Scatterplots of POM (y-axes) vs. PEZHAT (x-axes) kinetic energy (top panels) and phase (bottom panels) of the barotropic (left panels) and surface baroclinic (right panels) M_2 currents. Gray scale represents the percentage of points falling into bins of $1.5 \times 10^{-3} m^2.s^{-2}$ for kinetic energy and 10 degrees for phase.

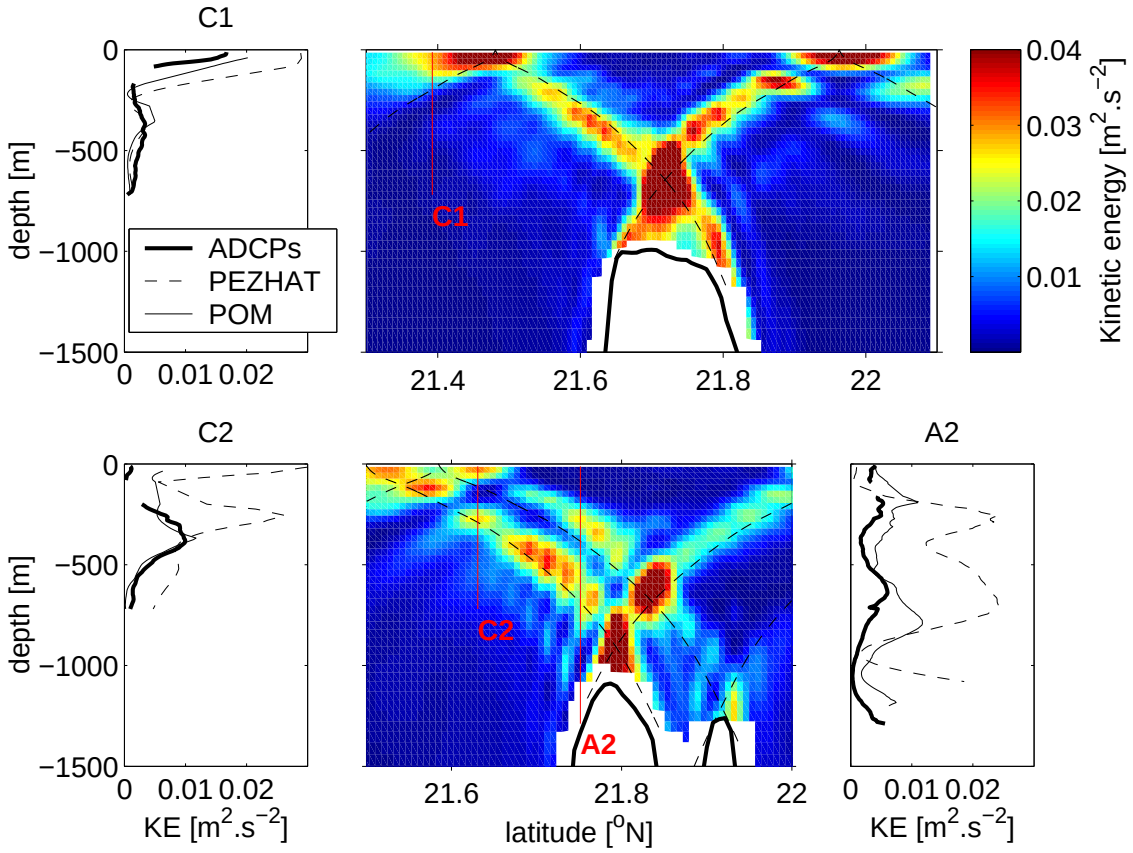

Figure 3.10: Vertical structure of the M_2 kinetic energy along the C1 (top panels) and C2-A2 (bottom panels) transects (see Fig. 3.7 for the transects locations) from PEZHAT. Vertical lines indicate the locations of the moorings, as well as the zero axis for the moorings profiles, shown in thick solid lines for the ADCPs, thin solid lines for PEZHAT and thin dashed lines for POM. M2 characteristics originating at critical slopes for the model topography are shown as dotted lines. The 150m resolution topography is shown in black thick lines.

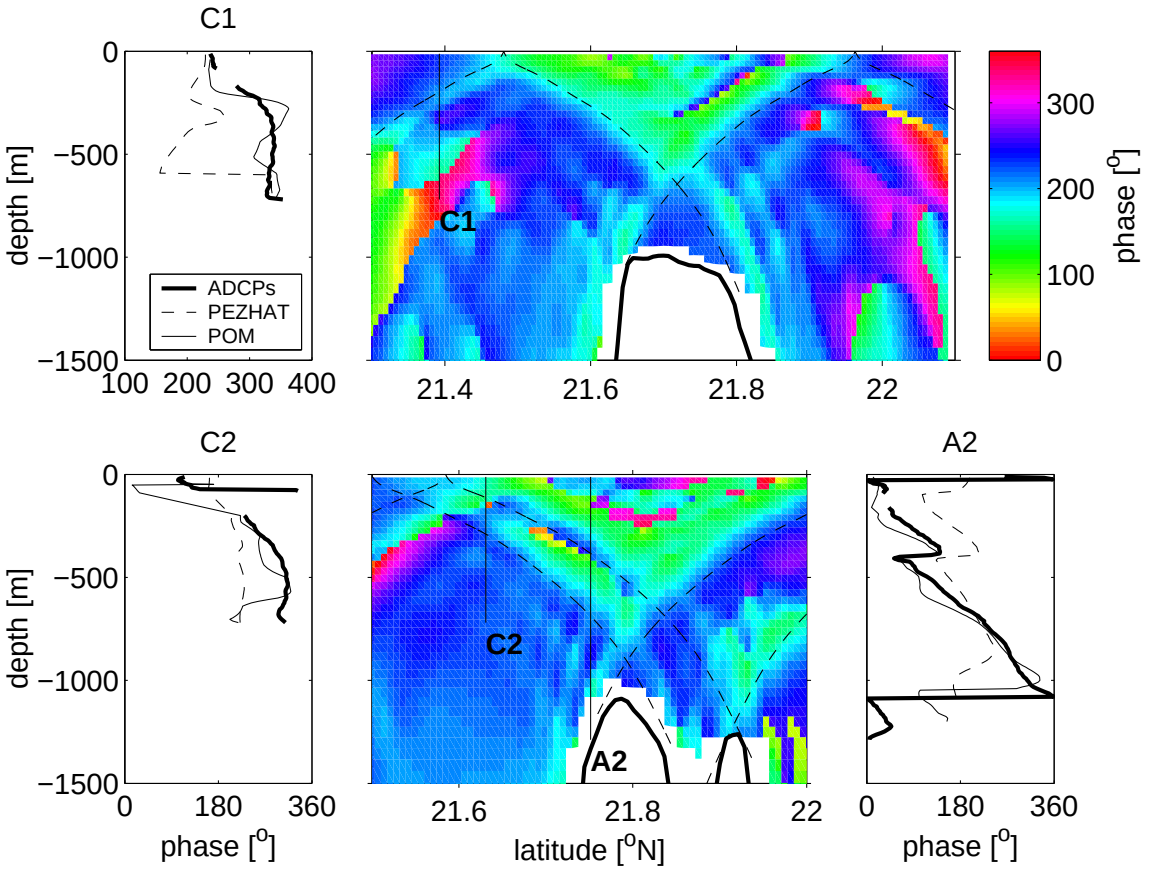

Figure 3.11: Same as Fig. 3.10 but for the phases.

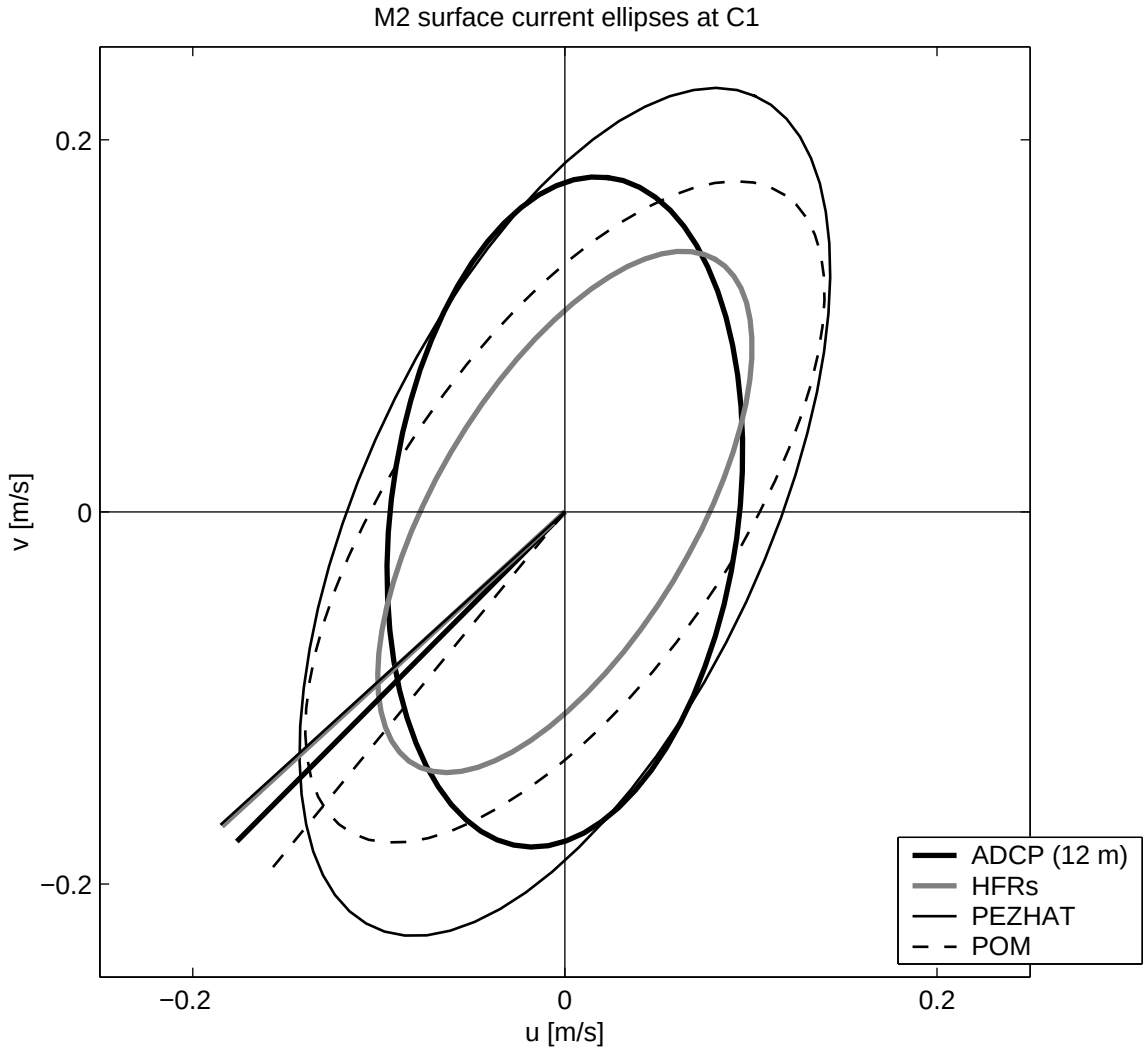

Figure 3.12: M_2 surface currents ellipses at C1 for ADCP's 12 m bin (thick solid line), HF-radios (thick gray line), PEZHAT (thin solid line) and POM (thin dashed line). Phases are represented by the angle ccw from the x-axis of the straight lines.

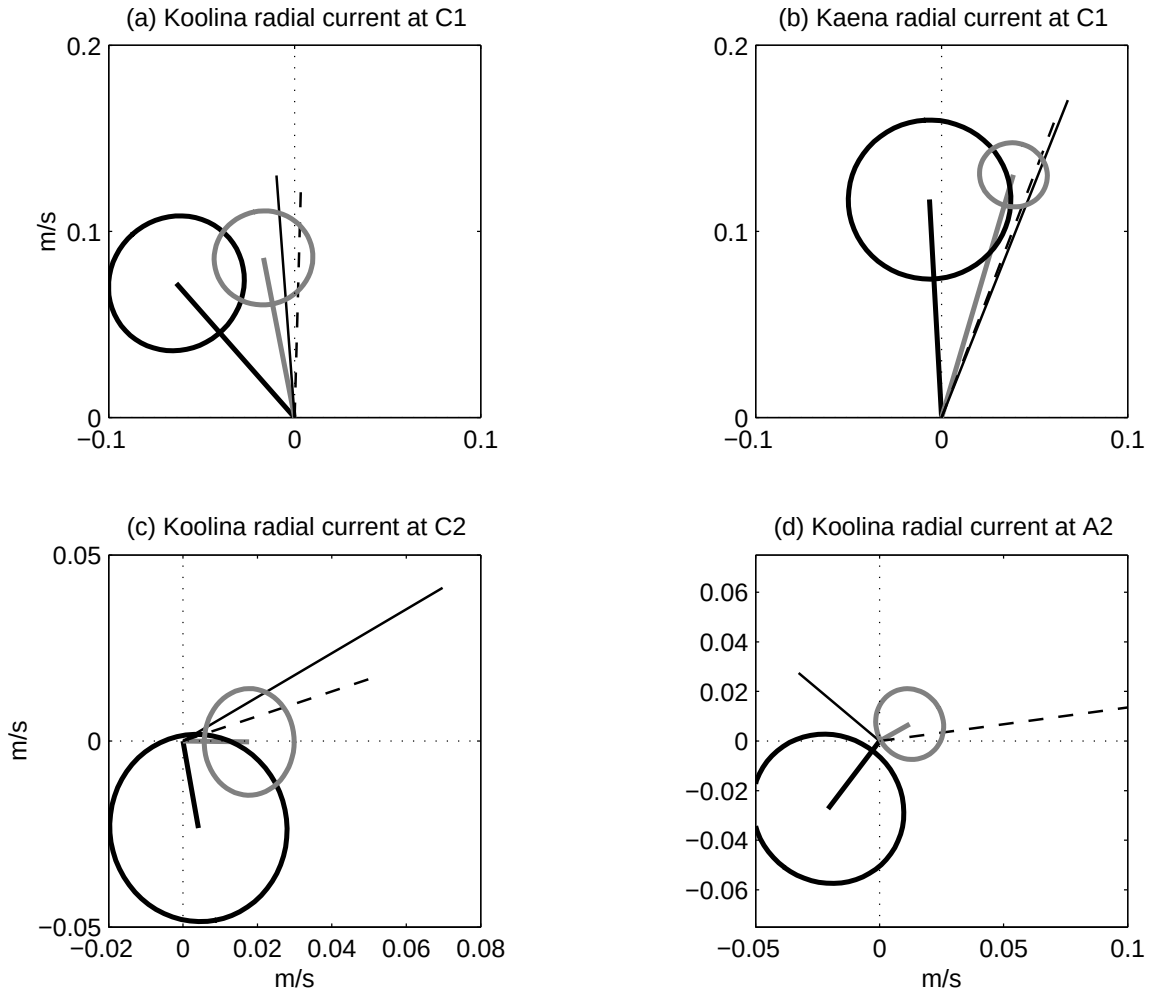

Figure 3.13: M_2 surface radial currents in the direction from Koolina (a) and Kaena (b) at C1 and in the direction from Koolina at C2 (c) and A2 (d). Legend is the same as for Fig. 3.12. Observed currents parameters were obtained from harmonic analyses on radial currents. Modeled currents parameters were obtained from a projection of the tidal ellipses on the radial directions. Phases are represented by the angle ccw from the x-axis and amplitudes by the length of the straight lines. 95% confidence intervals on amplitude and phase are shown by ellipses.

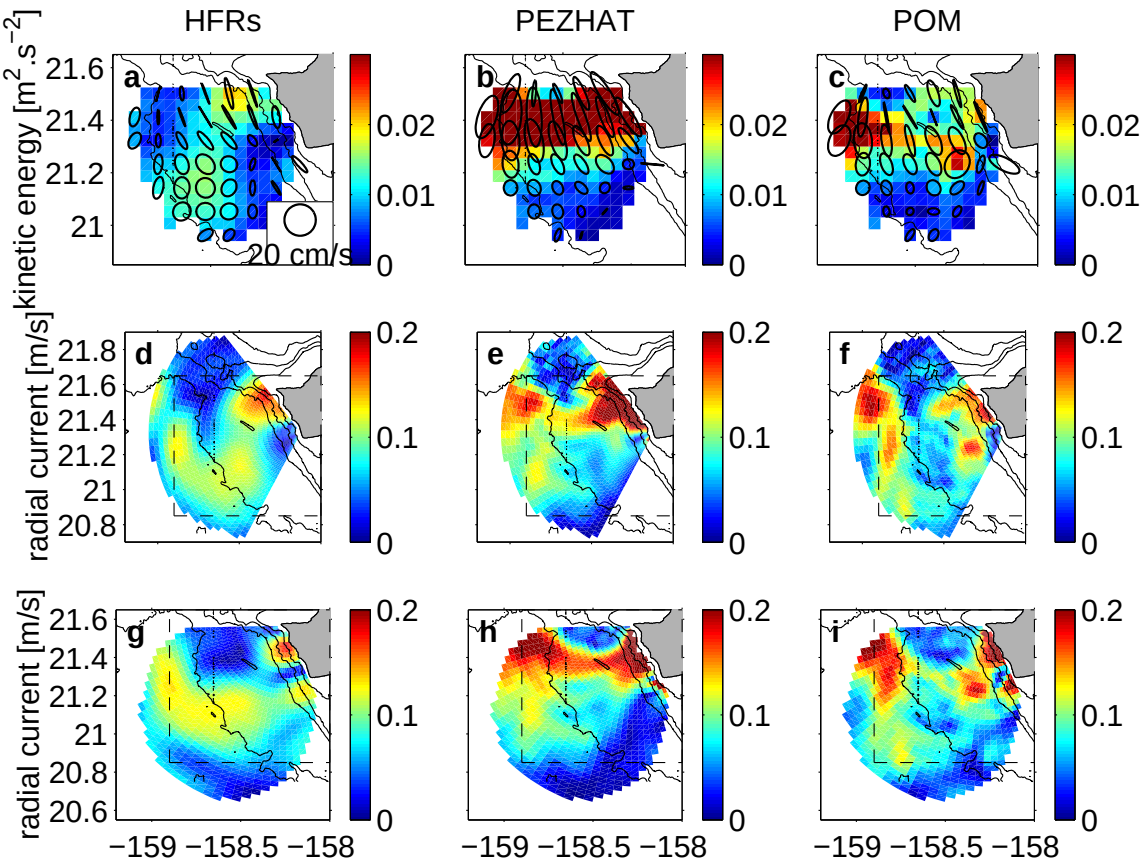

Figure 3.14: Kinetic energy and ellipses of total (barotropic plus baroclinic) M_2 surface currents (top panels), and amplitude of the radial currents in the direction from Koolina (middle panels) and Kaena (bottom panels), from HF-radios (left panels), PEZHAT (middle panels), and POM (right panels).

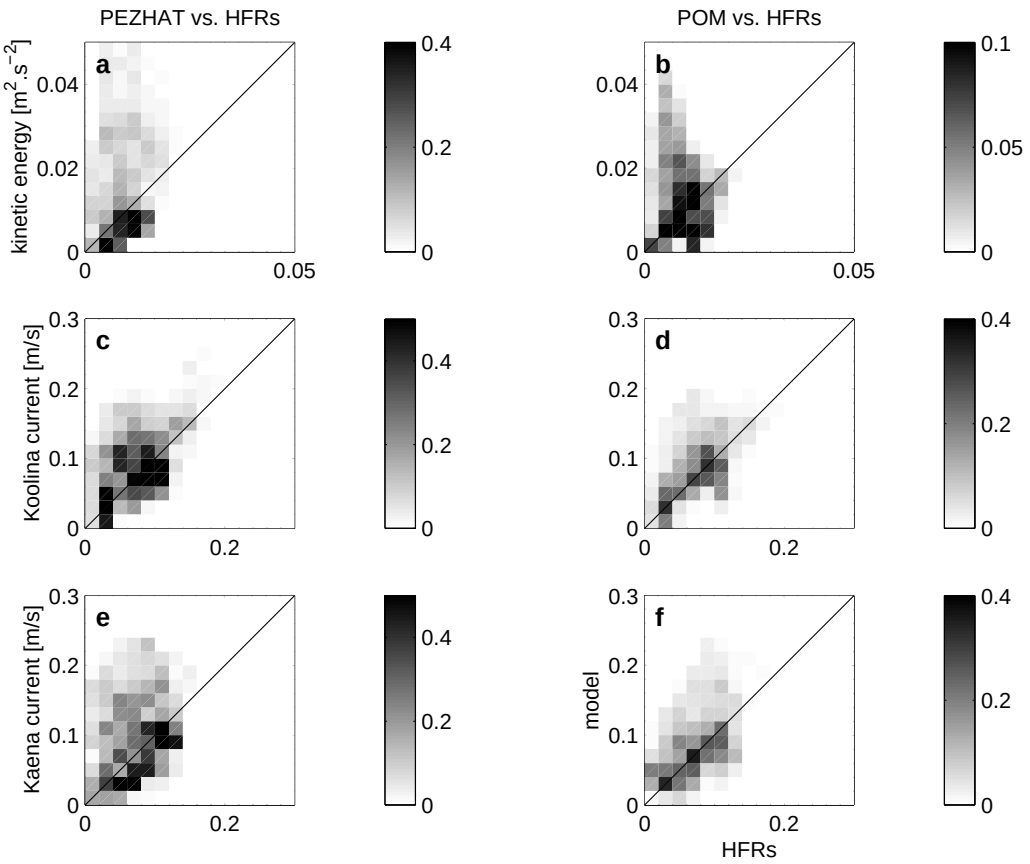

Figure 3.15: Scatterplots of M2 surface currents kinetic energy (top panels) and amplitude in the direction from Koolina (middle panels) and Kaena (bottom panels) for PEZHAT vs. HF-radios (left panels) and POM vs. HF-radios (right panels). Models values are on the y-axes and observations on the x-axes. Gray scale represents the percentage of points falling into bins of $3.3 \times 10^{-3} m^2.s^{-2}$ for kinetic energy and $2cm.s^{-1}$ for radial currents.

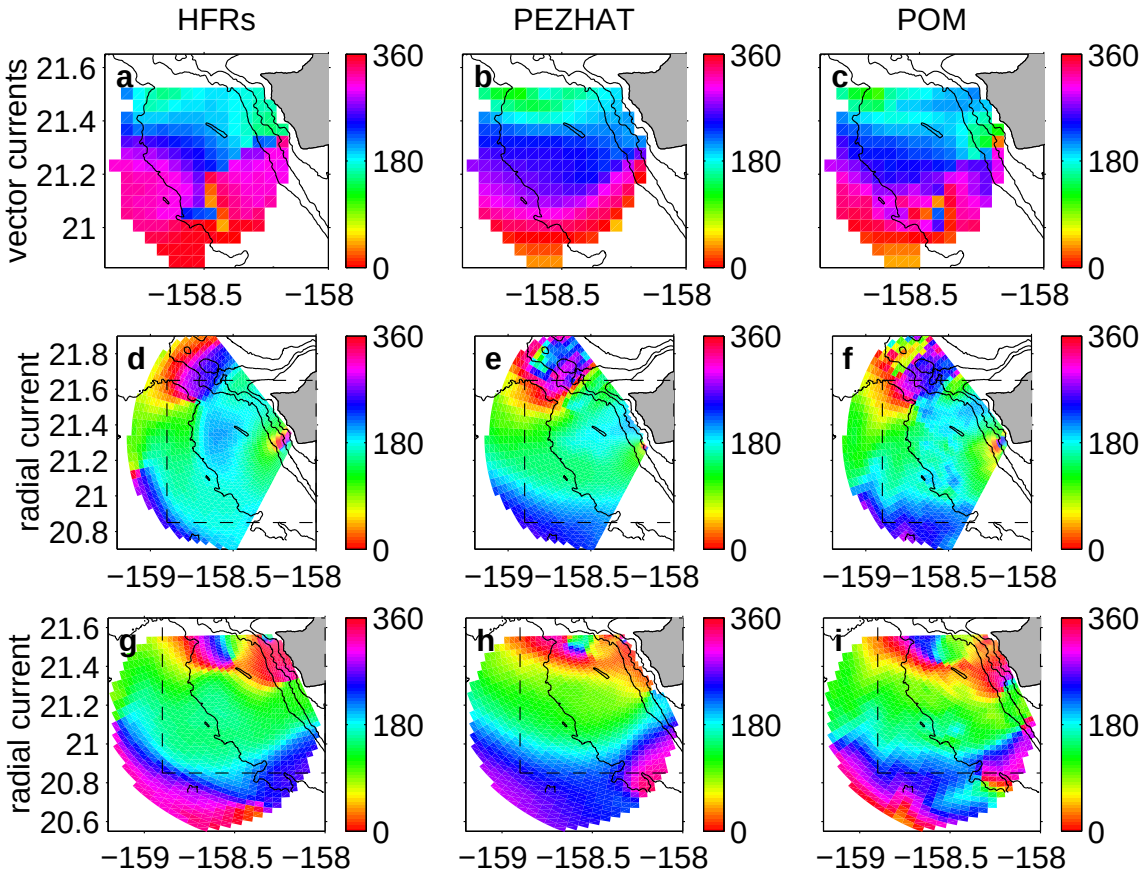

Figure 3.16: Same as Fig. 3.14, but for phases.

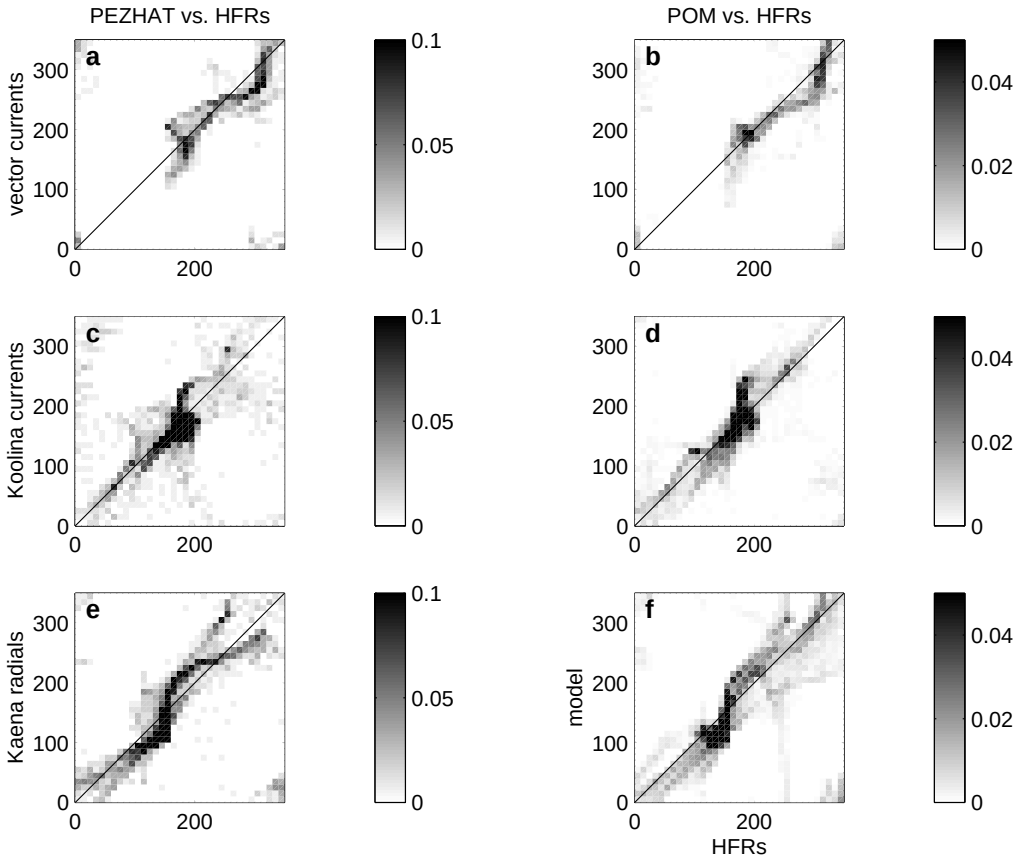

Figure 3.17: Same as Fig. 3.15, but for phases.

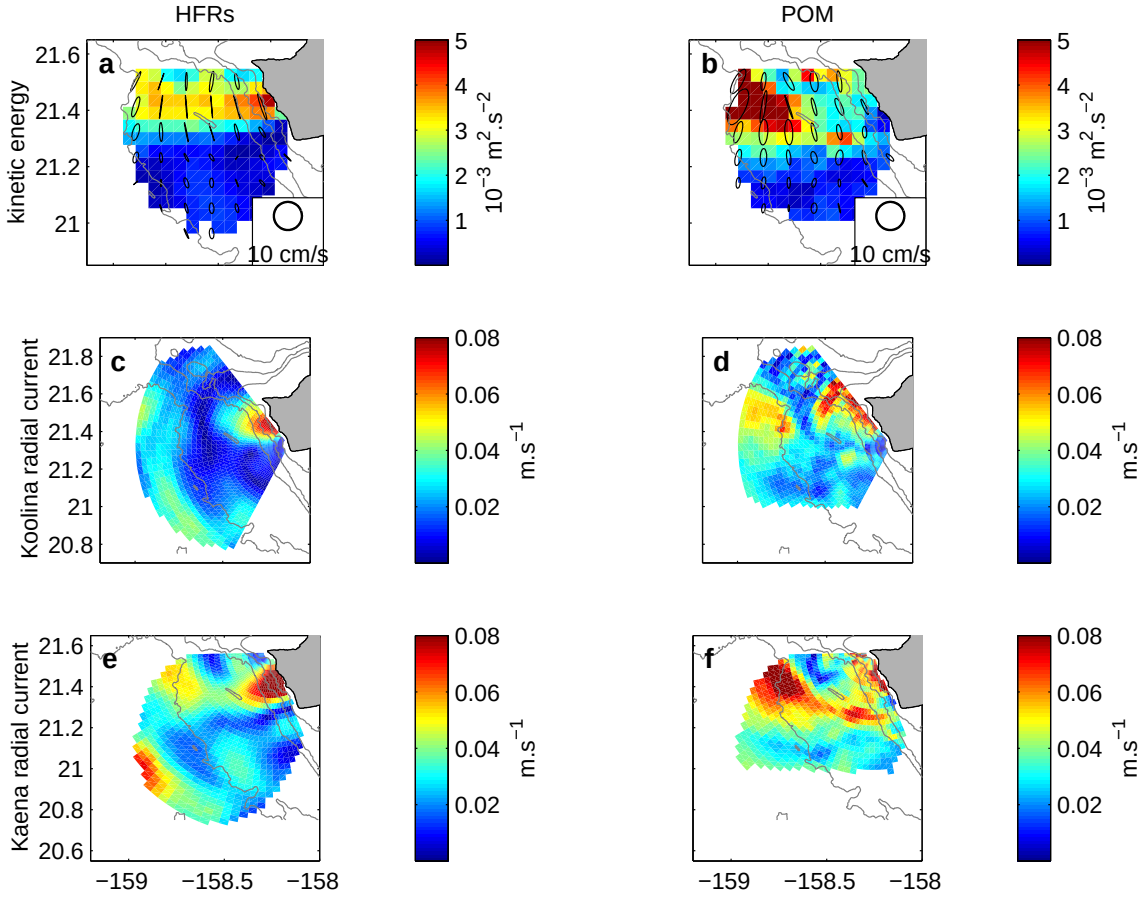

Figure 3.18: Kinetic energy and ellipses of total (barotropic plus baroclinic) S_2 surface currents (top panels), and amplitude of the radial currents in the direction from Koolina (middle panels) and Kaena (bottom panels), from HF-radios (left panels), and POM (right panels).

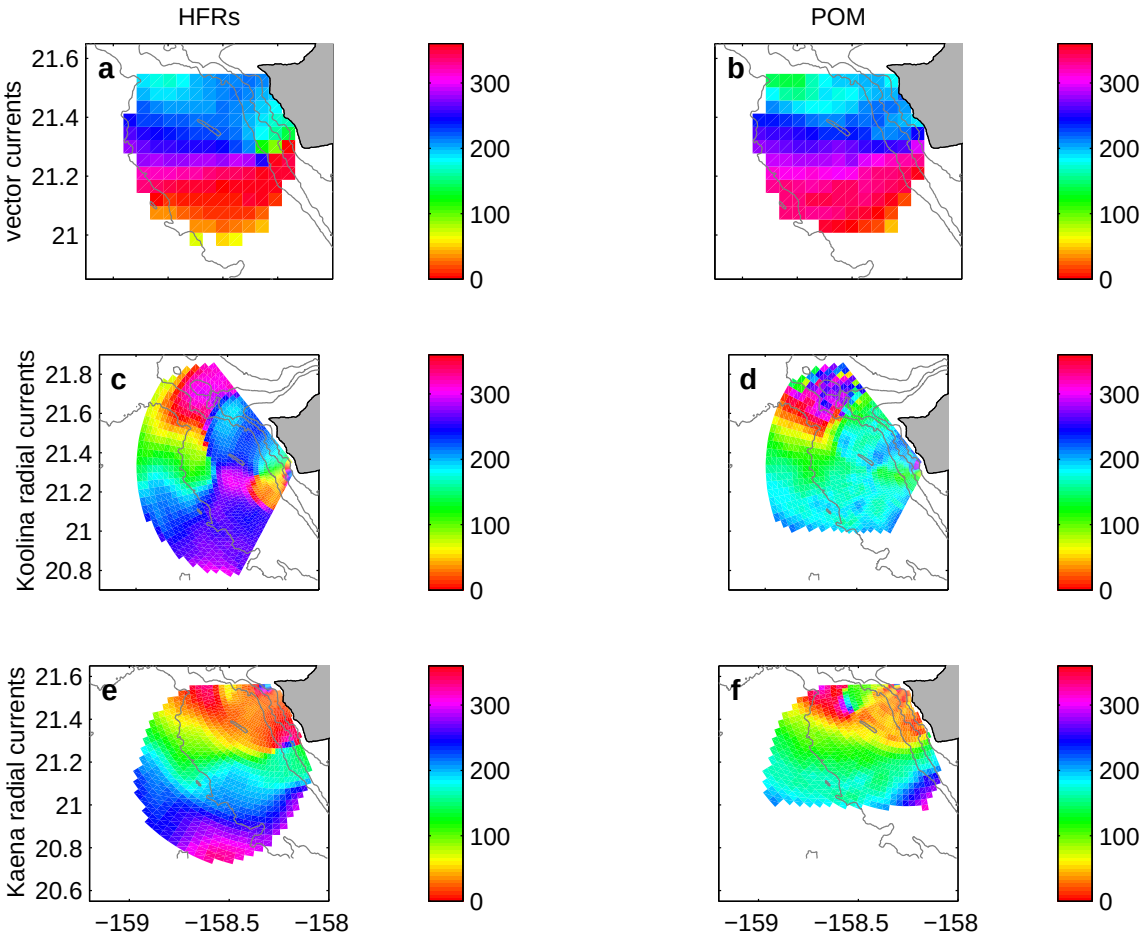

Figure 3.19: Same as Fig. 3.18, but for phases.

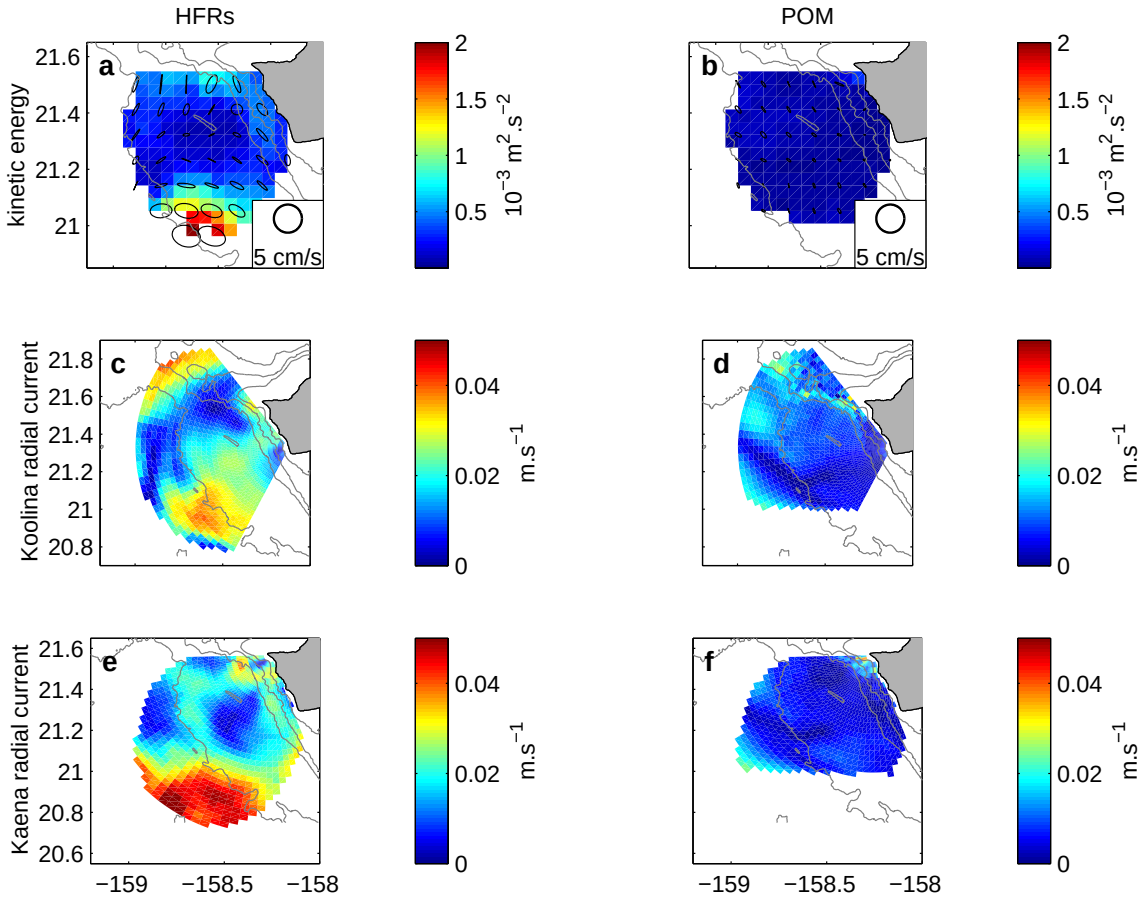

Figure 3.20: Same as Fig. 3.18, but for K_1.

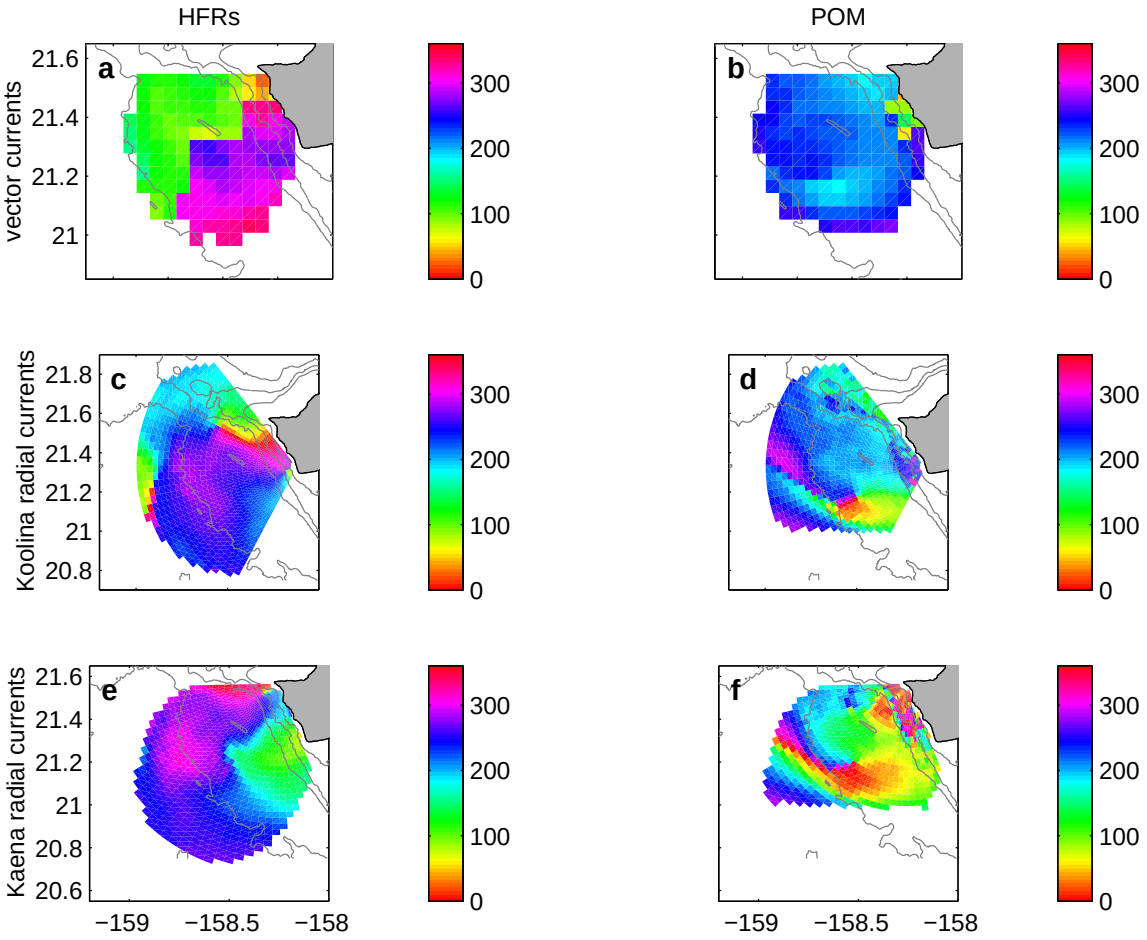

Figure 3.21: Same as Fig. 3.19, but for K_1.

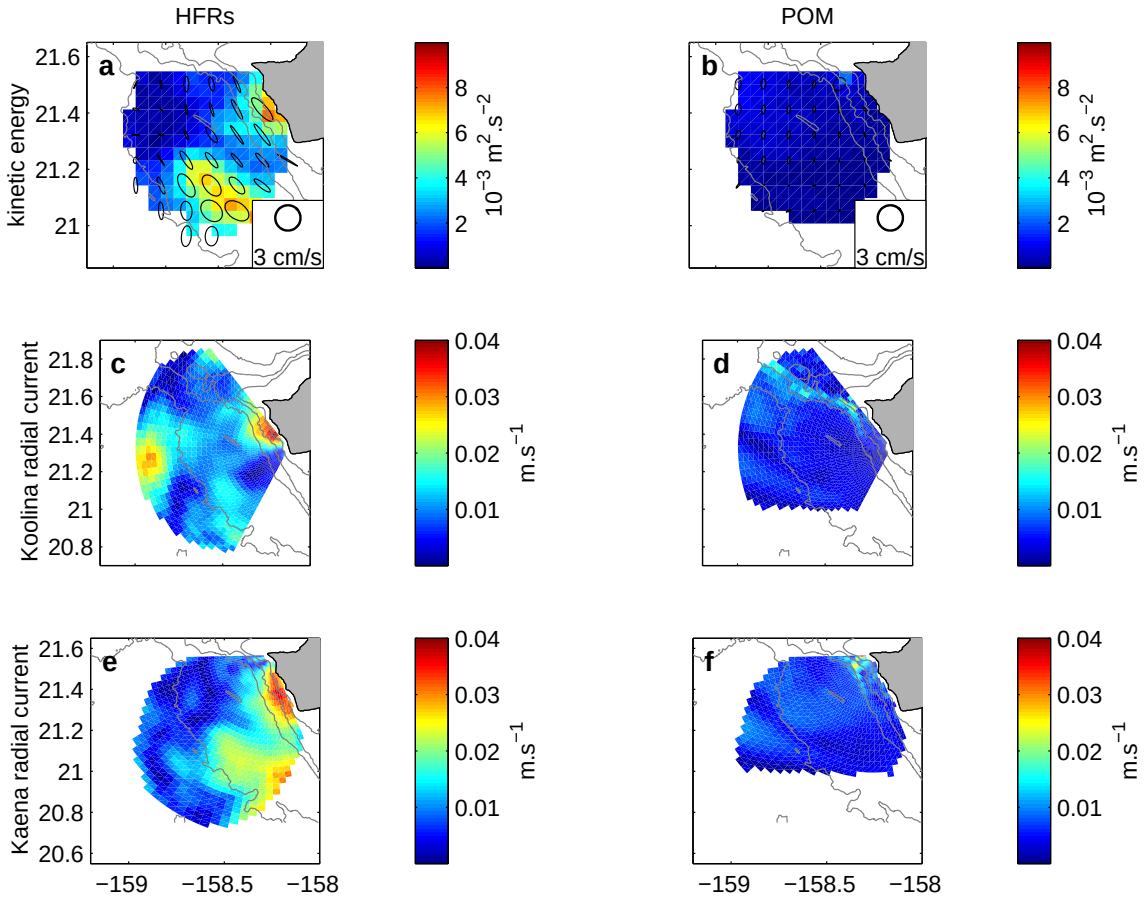

Figure 3.22: Same as Fig. 3.18, but for O_1.

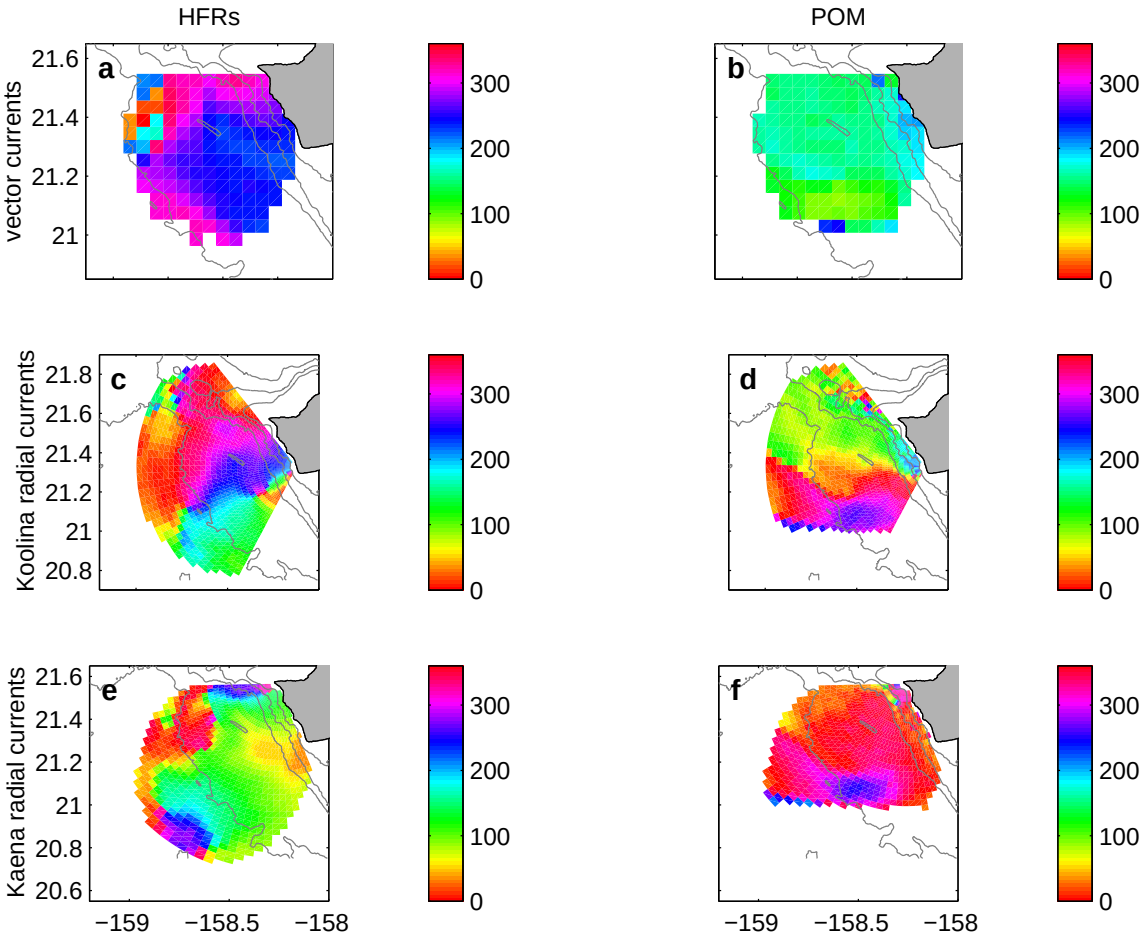

Figure 3.23: Same as Fig. 3.19, but for O_1.

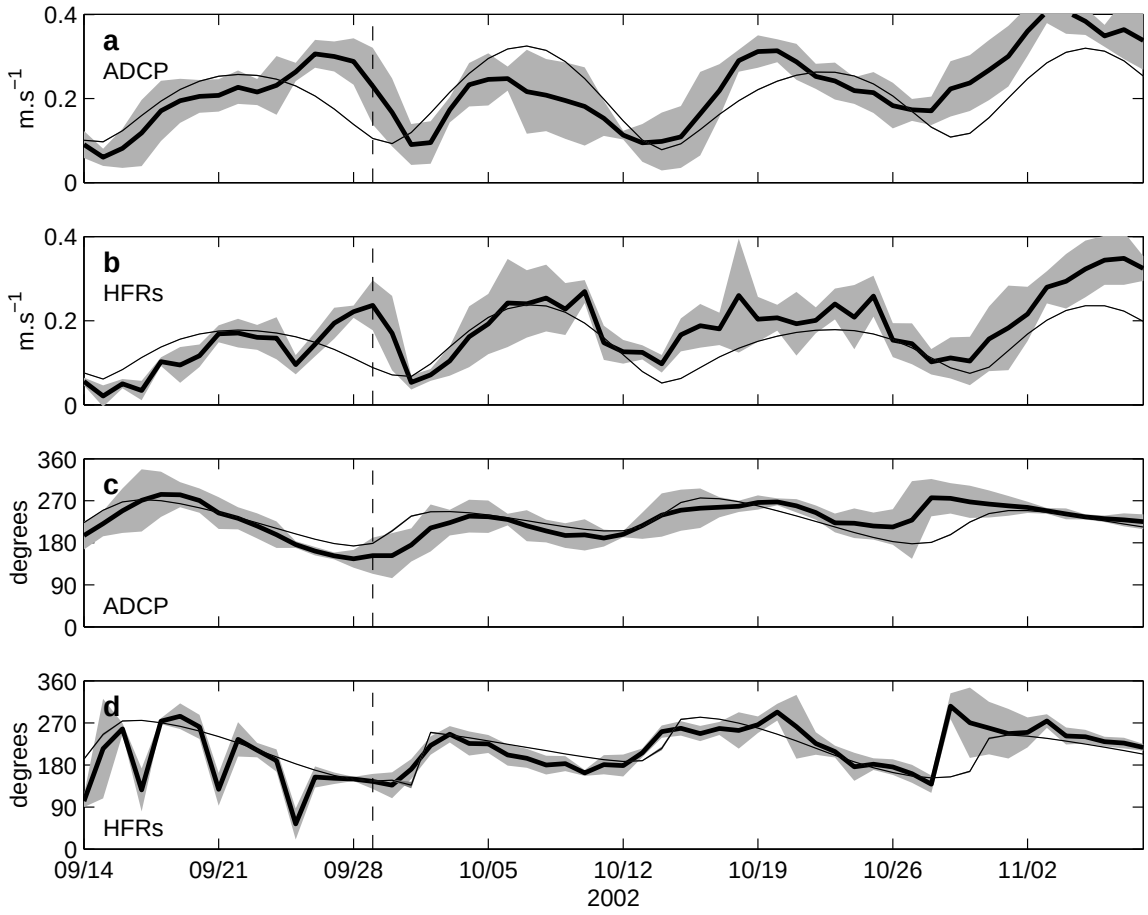

Figure 3.24: Complex-demodulated semi-diurnal major axis amplitude (a: ADCP, b: HF-radios) and Greenwich phase (c: ADCP, d: HF-radios) at C1. ADCP data are from the 12 m depth bin. HF-radios data are from the grid point closest to C1 (4.5 km away). Thick lines are for the "full" currents, thin lines are for the phased-locked currents. Shadings indicate 95% confidence intervals. The vertical dashed lines indicate the time of the snapshot in Figs. 4.2a and 4.9c.

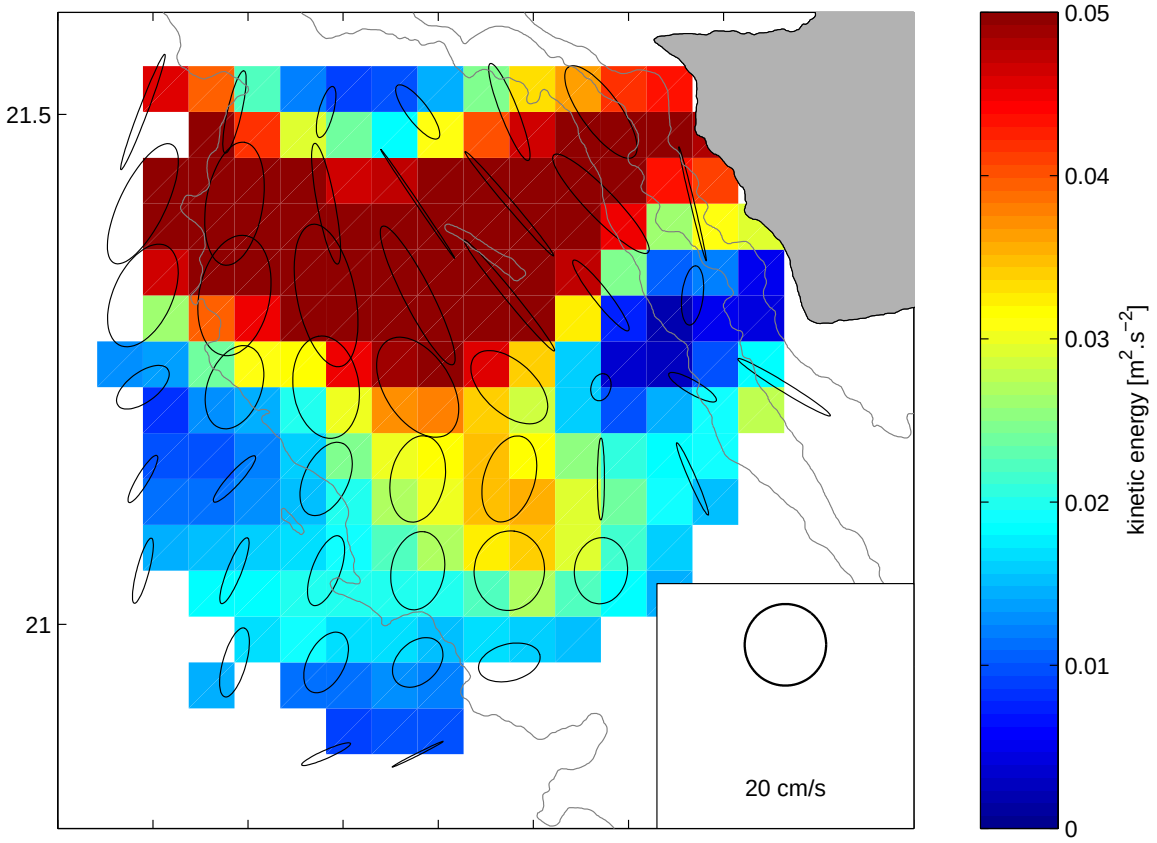

Figure 3.25: Complex demodulated semi-diurnal kinetic energy and ellipses on 11/05/2002.

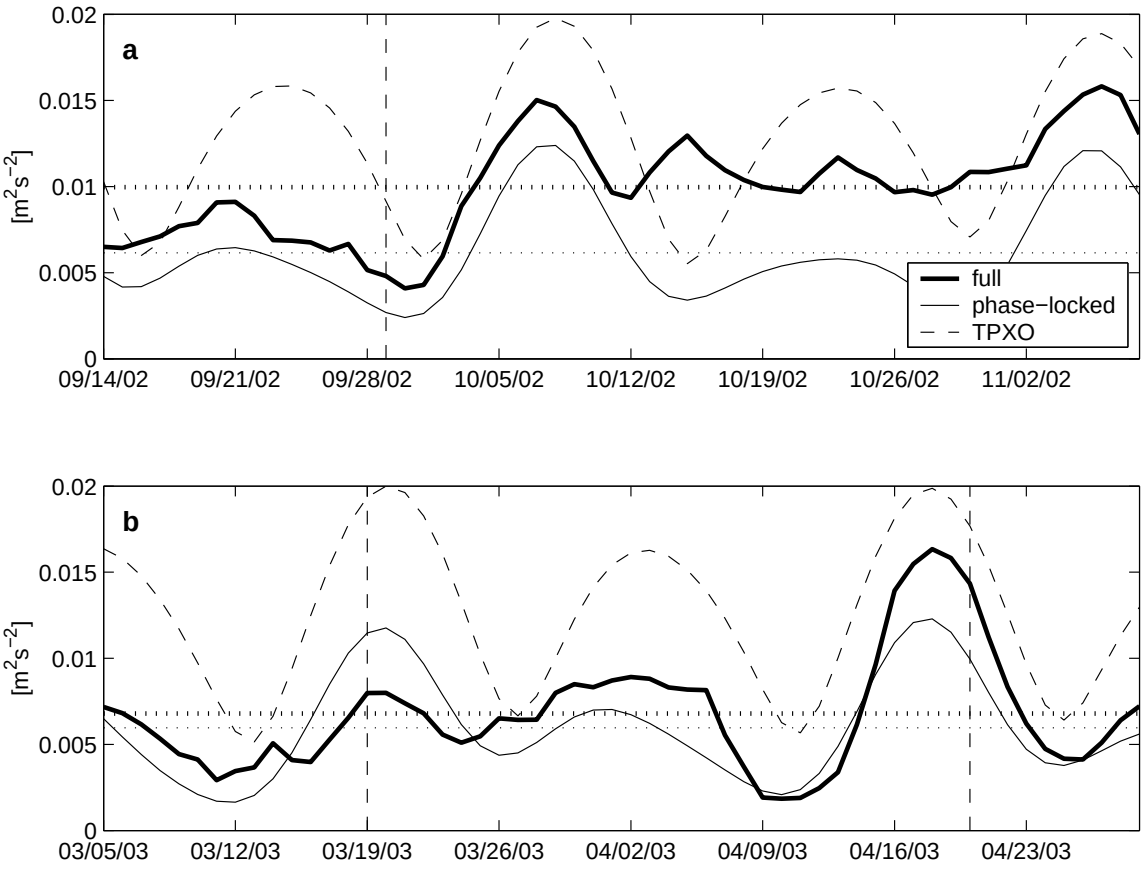

Figure 3.26: Time series of spatially-averaged complex-demodulated semi-diurnal kinetic energy during period 1 (a) and period 2 (b), for "full" (thick lines) and phase-locked (thin lines) currents. Barotropic forcing at A2 from the Hawai'i region TPXO6.2 inverse model (Egbert and Erofeeva, 2002) is shown by dashed lines (scaled to compare to the other curves). The temporal averages are shown as dotted lines. Vertical dashed lines indicate the time of the snapshots shown in Chapter 4.

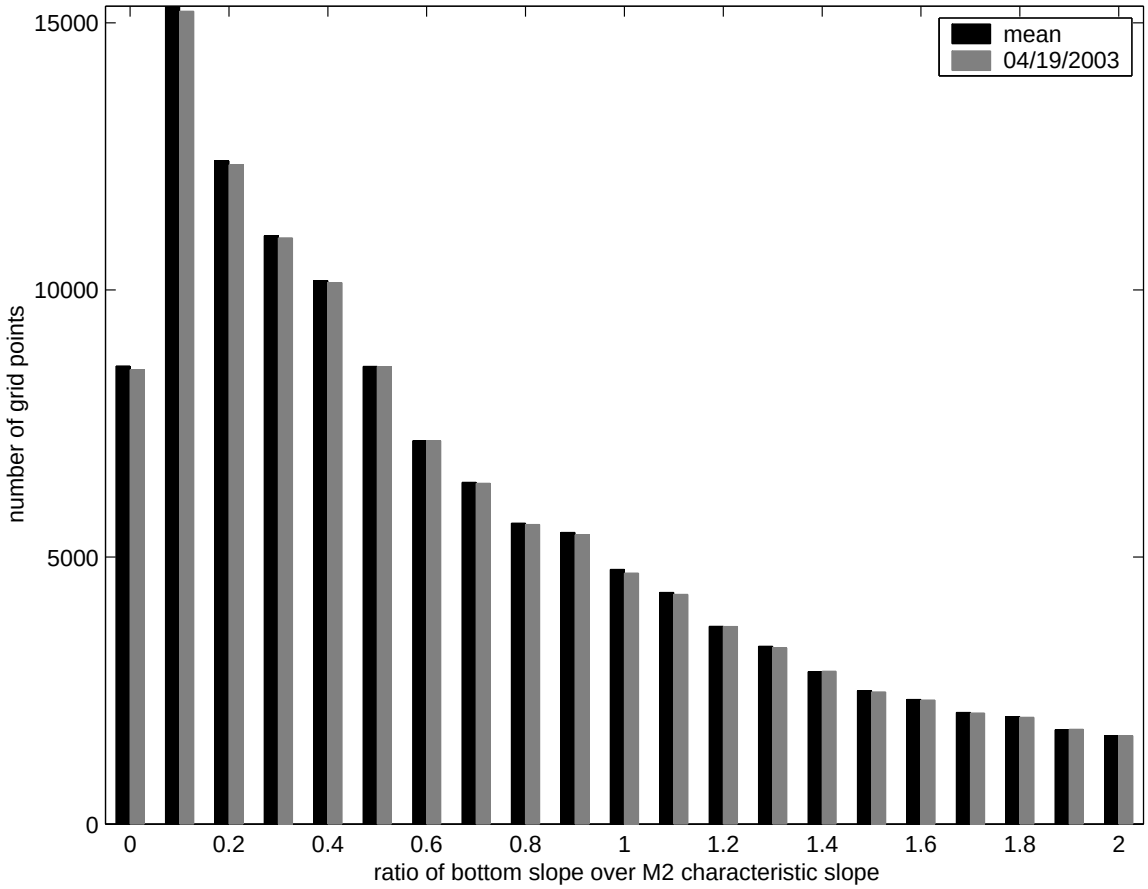

Figure 3.27: Histograms of ratio of bottom slope in the direction of maximum barotropic vertical velocity over M_2 characteristic slope for 10-year mean stratification (black) and that associated with the idealized vorticity wave on 03/19/2003 (gray).

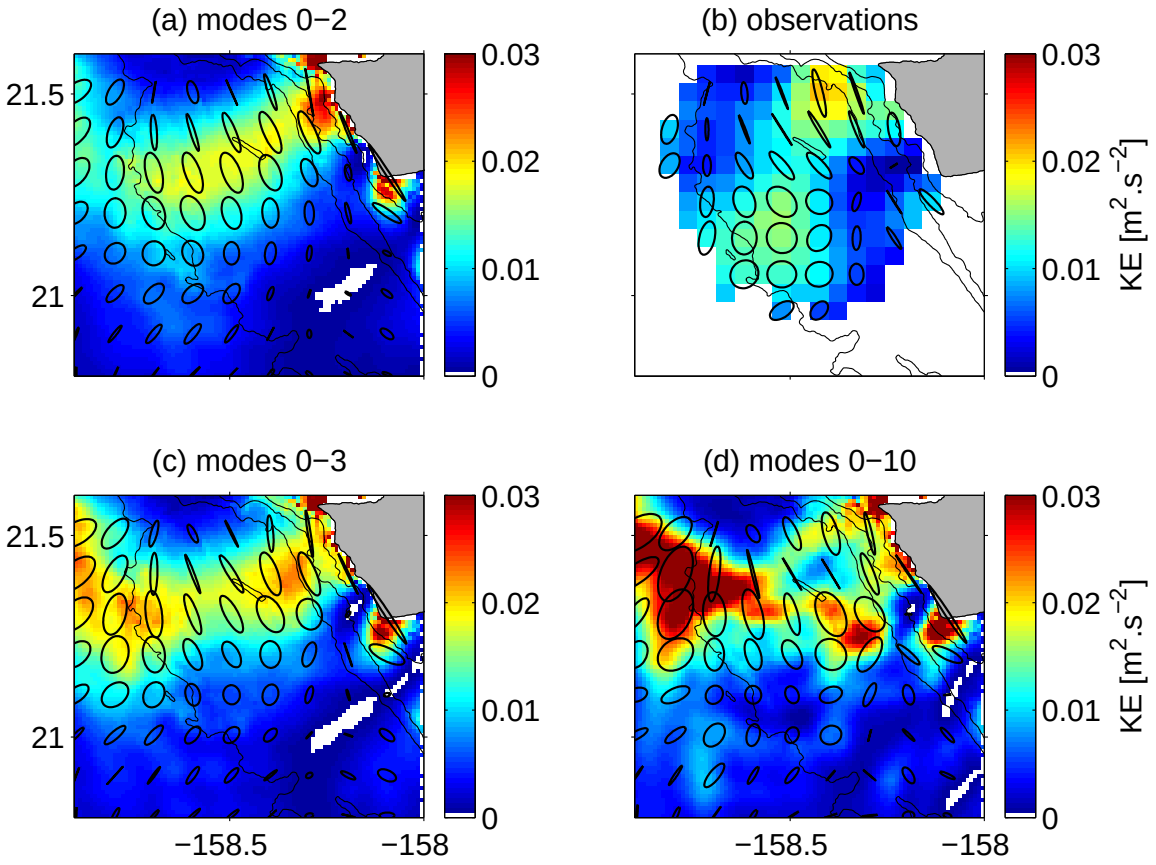

Figure 3.28: Horizontal kinetic energy of baroclinic surface currents reconstructed from a summation of a different number of modes for POM: (a) mode 1 only, (b) modes 1-2, (c) modes 1-3 and (d) modes 1-10. The modes were computed numerically at each grid point with the local bottom depth, and the vertical profiles of currents were projected onto the first 10 modes by least-square fit.

Chapter 4

Tidal currents in the Kauai Channel, Hawai'i. Part II: interactions with mesoscale currents

Where it is shown that strongly vertically and horizontally sheared background currents affect internal tides amplitude, phase and trajectories.

4.1 Introduction

Interactions of internal waves with mesoscale currents has traditionally been addressed by ray tracing, or Wentzel-Kramers-Brillouin (WKB), techniques (Bretherton, 1966; Jones, 1969; Müller, 1976; Olbers, 1981b; Edwards and Staquet, 2005; Moulin and Flór, 2006). This approximation is formally valid as long as the wavelengths are much smaller than the scales of background current variations, which is usually satisfied for high-frequency internal waves in the atmosphere and ocean. For internal waves at tidal frequencies, or internal tides, and at near-inertial frequencies, the wavelength can be on the order of or larger than the scales of variations of the background currents. Although this violates the WKB assumptions, Kunze (1985) showed that ray tracing results agreed qualitatively with exact numerical solutions for idealized cases of near-inertial waves propagating through horizontally and vertically sheared currents, provided flow scales were not much smaller than waves scales. This approach neglects scattering effects (Olbers, 1981a). Young and Ben Jelloul (1997) developed an approximation for near-inertial frequencies

to avoid the scale separation requirement of WKB. They found the same result as Kunze (1985), namely that refraction by sheared currents shifts the local frequency by $\zeta/2$, where ζ is the vorticity of the mesoscale currents. However, they noted that when the current scales where much smaller than the waves scales, their effects were averaged over the wavelength, so the waves were affected by the averaged background eddy kinetic energy instead of the vorticity.

We want here to interpret observations of currents in the Kauai Channel, Hawai'i (see Chapter 3), as internal tides generated on the Hawaiian ridge propagate through energetic mesoscale currents, with scales on the order of the internal tides wavelengths. Tidal frequencies are too far from the inertial frequency at this latitude to be able to apply the method of Young and Ben Jelloul (1997). We will follow instead Park and Watts (2006) and Rainville and Pinkel (2006b), who used ray tracing to study the propagation of internal tides through mesoscale currents in the Japan/East Sea and Hawaiian archipelago, respectively, and were able to explain qualitatively their observations. They both used a 2-D ray tracing approach, to study the effect of mesoscale currents on the horizontal propagation of vertical modes, assuming that each mode could propagate independently from the others.

However, our observations are just over the Hawaiian ridge, where the strong bottom topography variations couple the vertical modes together. Even away from the ridge, vertically sheared background currents couple the modes together (Mooers, 1975a). For this reason, Rainville and Pinkel (2006b) only considered barotropic currents, and Park and Watts (2006) only considered the advective effect of mesoscale currents averaged through the thermocline on the mode 1 tide propagation. Here, the beam-like structure of the internal tides close to the ridge (cf Fig. 3.10) warrants the use of a 3-D ray tracing approach.

We describe some properties of observed mesoscale currents relevant to internal tides propagation in section 4.2. We then compare ray tracing predictions with observations in section 4.3. The main results are summarized in section 4.4. The ray tracing equations are recalled in Appendix C, and the idealized mesoscale current structures used for ray tracing are described in Appendix D.

4.2 Mesoscale currents

We describe here some properties of mesoscale currents relevant to internal tides propagation. The currents were detided using the Matlab package T_Tide (Pawlowicz et al., 2002) and averaged over 3-day windows, and daily subsampled.

4.2.1 Horizontal structure

The average low-pass filtered currents over the 9-month record are shown in Fig. 4.1. The circulation is northwestward, with maximum speed of 30 $cm.s^{-1}$ farther from the island, decreasing and changing direction toward the coast. This corresponds to the Hawaiian Lee Current (Lumpkin, 1998), a mean current flowing along the western shores of the main Hawaiian islands. An anticyclonic circulation, with vorticity reaching $-0.3f$, is located off the southwest corner of the island, where anticyclones are regularly generated (see Chapter 5 for a remarkable example). Vorticity reaches $+0.2f$ near the northwest corner of the island, where small cyclones are sometimes generated.

During Fall 2002, the low-frequency variability was dominated by mesoscale and submesoscale vortices. We will not investigate the effect of submesoscale vortices, such as the one described in Chapter 5, on the internal tides since their scales are smaller than the tides scales. We will instead focus on the largest vortices observed, such as the cyclone shown in Fig. 4.2a on September 29, which have scales closer to the tides scales ($\sim 55km$ diameter, compared to a wavelength of $\sim 45km$ for M_2 tides observed on Kaena ridge by Nash et al. (2006)). It drifted northward then westward, and never got further inside the observational domain, so is only partially sampled. Velocity reached $60cm.s^{-1}$, and vorticity $0.4f$, but the strongest vorticity inside the core was not sampled. Its center location was estimated from the current curvature field, and currents were interpolated onto a polar grid with the origin at the estimated center. Azimuthal currents were azimuthally averaged, and an idealized profile (Eq. D.0.23 in Appendix D) was chosen as a good visual fit to the observations. The resulting idealized vortex is shown in Fig. 4.2b. Its radius is $28km$, with maximum azimuthal velocity of $57cm.s^{-1}$, maximum vorticity of $1.2f$ inside the core, and minimum vorticity of $-0.2f$ outside the core.

During Spring 2003, the low-frequency variability was dominated by vorticity waves, with northwestward and southeastward alternating currents, and a northeastward phase propagation (see Appendix E). Two different phases are shown in Fig. 4.3, on March 19 and April 20 (average currents from Mar 3 to May 1 have been removed). On March 19, velocity reached $40cm.s^{-1}$, and vorticity was negative in the entire observational domain (except in the coastal boundary layer), reaching $-0.4f$. The wave pattern was not rectilinear, with currents flowing northeastward in the Kauai Channel, but we idealize them as rectilinear for the purpose of ray tracing, neglecting also the influence of the coast, with a wavelength of 80 km (directly estimated from the snapshot on March 19), current amplitude of $24cm.s^{-1}$, and vorticity amplitude of $0.35f$. On April 20, velocity reached $30cm.s^{-1}$, and vorticity ranged from $-0.5f$ near the coast to $+0.3f$. The idealized wave has a wavelength of 90 km (directly estimated from the snapshot on April 20), current amplitude of $25cm.s^{-1}$, and vorticity amplitude of $0.3f$.

4.2.2 Vertical structure

Vertical profiles of currents at C1 are shown in Fig. 4.4. The mean currents at C1 are strongly sheared in the top 100 m, from $25cm.s^{-1}$ at the surface to less than $3cm.s^{-1}$ below 200 m, with an e-folding scale of $\sim 75m$. The currents do not turn with depth in the top 200 m. The currents associated with the cyclone, shown by a snapshot on September 29, 2002, are also strongly sheared in the top 250 m, from $45cm.s^{-1}$ at the surface to less than $4cm.s^{-1}$ below 250 m. The currents do not turn with depth in the top 250 m. Ray tracing results are sensitive to the second derivative of vertical currents (see Eq. D.0.24 and D.0.27), therefore we cannot utilize directly the observed structure, which is too noisy, and have to fit a smooth profile to the observations. The vertical profile is idealized for ray tracing by:

$$e^{-(z/H)^2} \tag{4.2.1}$$

with $H = 100m$, and no turning in vertical.

Temperature and current anomalies observed at mooring A2 show the passage of the vorticity waves over the ridge crest (Fig. 4.5). The alternating currents are associated with temperature anomalies reaching 1.5^oC at 200 m and extending to 350 m, below which

the temperature varies on longer time scales. The waves extend deeper in March than in April 2003. Vertical profiles of currents at C2 and A2 are shown in Fig. 4.6 and 4.7, respectively. The mean currents at C2 and A2 are slightly sheared, from $\sim 10cm.s^{-1}$ at the surface to less than $2cm.s^{-1}$ below 500 m at C2, but increase again to $6cm.s^{-1}$ around 800 m at A2, before dropping back to zero at the bottom. The currents turn by $\sim 35^o$ counterclockwise in the upper 100 m, and remain in the same direction over the next 300 m. To characterize the different vertical structures of the waves on March 19 and April 20, we performed empirical orthogonal function (EOF) analyses of the currents over two periods: March 14 to 30, and April 14 to 24, corresponding to the periods used to infer the horizontal structures of the waves in Appendix E. The first modes, which contain $\sim 90\%$ of the variance, represent the waves variability.

The currents associated with the vorticity waves are surface intensified. On March 19, 2003, the currents decrease from $20cm.s^{-1}$ at the surface to less than $10cm.s^{-1}$ below 200 m. The currents do not turn much with depth in the top 200 m at C2, but there is a counterclockwise rotation at A2. The vertical profile is idealized for ray tracing by Eq. 4.2.1, with $H = 200m$, and no turning in vertical.

On April 20, 2003, the currents decrease from $30cm.s^{-1}$ at the surface to less than $5cm.s^{-1}$ below 160 m at A2 (there is a deep local maximum of $20cm.s^{-1}$ around 200-250 m at C2, which we will not try to model here). The vertical profile is idealized for ray tracing by Eq. 4.2.1, with $H = 70m$, and no turning in vertical.

4.3 Propagation of internal tides through mesoscale currents

The background currents in which internal tides propagate are energetic near the surface, and strongly sheared both horizontally and vertically, with spatial scales of variation smaller than the horizontal and vertical wavelengths of low-mode internal tides. However, if we consider the propagation of energy as localized beams along tidal characteristics (see Chapter 3), then the scales of background currents become comparable to the scales of the internal tide packets, and we are (marginally) justified in using ray tracing techniques.

We adopt the standard WKB technique (Olbers, 1981b), in which the background variations are neglected to derive the dispersion relation (except for the vertical gradient of buoyancy), but are retained to compute the waves evolution (see Appendix C). The inclusion of the current shears and horizontal gradients of buoyancy in the dispersion relation (Mooers, 1975b; Kunze, 1985; Jones, 2001) is likely to modulate the effect of mesoscale currents, through modifications of the effective Coriolis and buoyancy frequencies. For example the effective Coriolis frequency (without approximation on the relative vorticity magnitude) is:

$$f_{eff} = \left[f^2 + f(\frac{\partial V}{\partial x} - \frac{\partial U}{\partial y}) - \frac{\partial V}{\partial x}\frac{\partial U}{\partial y} + \frac{\partial U}{\partial x}\frac{\partial V}{\partial y} \right]^{1/2} \tag{4.3.1}$$

Toward the idealized cyclone center, f can be modified by as much as 60 % higher. This could lead to wave energy absorption by the mean flow when the intrinsic frequency is Doppler shifted low (see below). These effects are not considered here. We furthermore use the hydrostatic approximation since $f_{M2}^2 \ll N^2$ in the upper 1500 m, and it simplifies the interpretation of the results.

4.3.1 Cyclone

It is necessary to estimate the stratification modifications associated with the mesoscale currents. Following Moulin and Flór (2006), we idealize the cyclone by assuming that it is axisymmetric with analytical radial and vertical profiles of azimuthal velocity, described in the previous section, and in gradient wind balance. The stratification at infinite radius is computed from temperature and salinity observations at Station ALOHA (Karl and Lukas, 1996), located 100 km north of O‘ahu, averaged over 10 years. This enables us to extrapolate the currents over the ridge (neglecting the effect of topography on the mesoscale currents) and to compute the 3D variations in stratification (see Appendix D and Fig 4.8). The upwelling associated with the cyclone increases the stratification near the surface by squeezing the isopycnals together, while decreasing it in the thermocline by stretching the isopycnals (Fig. 4.8d). Near the vortex center, the buoyancy frequency becomes negative, and was set to zero, between 100 and 150 m. Internal waves cannot propagate in this area, but the rays considered here never reached it.

Potential generation locations of internal tidal beams were selected over the topographic slopes surrounding O‘ahu. The initial directions of propagation were those maximizing the barotropic vertical currents (as predicted by a 3-D primitive equation numerical model of the tides, PEZHAT, cf Chapter 3), and the initial horizontal wavelengths were chosen to be 44 km, as observed by Nash et al. (2006) over the middle of Ka‘ena ridge (the wavelength is twice the distance between the generation locations on each side of the ridge, so it should vary along the ridge, but for simplicity we set it to a constant value). Ray tracing was carried out both in the absence and presence of currents, until each ray reached the sea surface. Energy evolution was inferred from wave action evolution:

$$\frac{dE}{dt} = -E\nabla.\mathbf{C_g} + \frac{E}{\omega_0}\frac{d\omega_0}{dt} \tag{4.3.2}$$

and kinetic energy at the surface was computed from the relation:

$$\frac{KE}{E} = \frac{1}{2}\frac{\omega_0^2 + f^2}{\omega_0^2} \tag{4.3.3}$$

The ratio of surface kinetic energy for ray tracing through currents over ray tracing without currents is shown in Fig. 4.9d. In the presence of the cyclone, the kinetic energy at the sea surface is increased as the beams get close to the eddy center, up to a factor of 16 near the cyclone center. For comparison, the surface kinetic energy for complex-demodulated semi-diurnal currents (see Chapter 3) is shown in Fig. 4.9a, and for phase-locked currents in Fig. 4.9b. Their ratio is shown in Fig. 4.9c. The pattern is similar to the ray tracing pattern, with increased energy near the vortex center reaching a factor of 16. Although the phase-locked tides are probably affected by the mean currents described in the previous section, and by rectification of the mesoscale variability, and could therefore differ from tides propagating in an ocean at rest (Chapter 3), the effects of particular mesoscale features such as the cyclone are filtered out (or at least attenuated) by harmonic analysis over a period of time (9 months) much longer than the time scales of the mesoscale features at a given location (about a week for the cyclone). Therefore the increase of energy over the cyclone area in Fig. 4.9c can be attributed to the presence of the cyclone, in light of the ray tracing predictions. Furthermore, the location and time of surfacing can vary, as shown in Fig. 4.10a,b. The ray with lowest Doppler shifting and the ray surfacing closest to the vortex center are shown as examples. The intrinsic frequency of the lowest Doppler

shifted ray (Fig. 4.10c) decreases strongly near the surface, but remains above f_{eff}, although barely so near 20 m depth. It is therefore possible that semi-diurnal internal tides encounter critical layers in the presence of slightly stronger cyclones. Since the frequency approaches f near the surface, the vertical propagation velocity is much reduced, and it takes longer for the wave to reach the surface (Fig. 4.10b), giving it time to be advected by the mesoscale currents (Fig. 4.10a). The surfacing in the presence of currents takes place 48 km away from where it would occur without currents, and 20 hours later. This illustrates that even as close to the ridge as the first surface reflexion occurs, M_2 internal tides at a fixed location can become incoherent with the astronomical forcing due to the presence of background variability.

In order to understand the mechanisms responsible for the energy increase associated with the cyclone, we compute the different terms of the energy balance equation 4.3.2, and show their evolution as a function of depth in Fig. 4.10d,e. In the absence of background currents, the energy variations are entirely due to vertical divergence or convergence of rays associated with vertical gradients of buoyancy frequency. Near the surface, the gradient of buoyancy frequency is strongly negative, so the rays diverge and the energy drops sharply. In the presence of background currents, the vertical profiles of stratification are modified (Fig. 4.8), and rays are refracted horizontally, both affecting ray divergence and therefore energy. For both rays, the stratification gradient near the surface is reversed, so energy increases by ray divergence near the surface (Fig. 4.10d,e, dashed curves). The energy transfer with the mesoscale currents modulates the balance: it is negative for the western ray, which propagates in the direction of the currents, but smaller than the contribution from ray divergence, resulting in a stronger energy at the surface than without currents; it is positive for the eastern ray, which propagates against the currents, reinforcing the effect of divergence and resulting also in a stronger energy at the surface than without currents. The fact that the strongest stratification gradients and currents are located near the surface results in the energy being significantly modified only close to the surface (in the top 200 m), as shown in Fig. 4.10f.

4.3.2 Vorticity waves

We idealize the vorticity waves as a parallel shear flow in the along-ridge direction varying only in the cross-ridge direction. Expressed in a reference frame rotated in the direction of propagation of the wave, the momentum dynamics, neglecting acceleration and eddy diffusion, are reduced to geostrophic balance, so we can derive the stratification associated with the wave through thermal wind balance (see Appendix D). Assuming that the stratification oscillates around the reference stratification used above, the buoyancy frequency can become negative near the surface at some locations, and was set to zero in those cases (Fig. 4.8e, thin solid line). Ray tracing was stopped when rays reached the depth where buoyancy frequency was equal to the intrinsic frequency. This happens very close to the mixed layer depth, where the vertical current shears disappear, so the surface values were taken as those at the depth where ray tracing was stopped.

The observations and results of ray tracing on 03/19/2003 are shown in Figs. 4.11 and 4.12. This is during a spring tide, and we see in the observations that the surface semi-diurnal currents are reduced near the ridge, but amplified in the south, compared to the phase-locked currents. This is qualitatively reproduced by the ray tracing model, where energy is reduced near the ridge (except right over the ridge, where energy is increased, contrary to the observations) and increased about a quarter wavelength of the vorticity wave away from the ridge. The increase of energy in the northwest and at the moorings is not reproduced, but the observed currents differ from the idealized currents there. We investigate again two particular rays shown in Fig. 4.12a. Ray surfacing is barely shifted in space and time, due to the fact that the tides propagate almost perpendicularly to the currents. For the western ray, ray divergence decreases energy at the surface, but some energy is gained from the currents, although not enough to cancel the divergence effect, so energy decreases at the surface compared to without currents (Fig. 4.12e,f). For the eastern ray, divergence increases the energy at the surface, but some energy is lost to the currents, but not sufficiently to cancel the divergence effect, so energy increases at the surface compared to without currents (Fig. 4.12d,f). The intrinsic frequency Doppler shift and effective Coriolis frequency shift are weak, so no critical layers can be encountered here.

As expected, things are different at another phase of the wave, as shown in Fig. 4.13 and 4.14 for 04/20/2003. This is also during a spring tide, but this time the surface semi-diurnal energy is increased near the ridge and reduced far from the ridge, compared to the phase-locked currents. This time, however, the contrary is produced by the ray tracing model, where energy is decreased near the ridge and increased about a quarter wavelength of the vorticity wave away from the ridge. This is due to the particular vertical structure chosen, where the gaussian profile results in stratification variations near the surface opposite to those below the thermocline (see Fig. 4.8), which translates into energy variations near the surface opposite to those below the thermocline (Fig. 4.14).

Using an exponential profile instead of a gaussian profile gives opposite results, as shown in Fig. 4.15 and 4.16. This time ray tracing results are qualitatively similar to observations. Using exponential profiles for the vorticity wave on 03/19/2003 and the cyclone on 09/29/2002 gives also opposite results to using gaussian profiles. While for the cyclone the gaussian profile clearly fits observations much better than the exponential profile, this is less evident for the vorticity waves, which have more complicated vertical profiles than either gaussian or exponential. Furthermore, we note that the results of ray tracing are sensitive to vertical variations of background fields that are significantly smaller than internal tides vertical wavelengths, and should therefore be considered with caution. Full 3D numerical modeling of internal tides propagation through vertically and horizontally sheared background currents should be undertaken to study the sensitivity of internal tides to the vertical and horizontal structures of the currents.

4.4 Conclusions

Despite the obvious limitation of ray tracing when background current scales are similar to wave scales, the qualitative agreement between observations of surface tidal currents and ray tracing predictions shows that ray tracing captures the main effects of mesoscale currents on internal tides propagation, with the caveat of the high sensitivity to the vertical structure of the currents near the surface. The kinetic energy is primarily modulated by vertical and horizontal refraction due to stratification variations associated with the mesoscale currents, and secondly by energy exchange between internal tides and

background currents. The fact that the strongest stratification gradients and currents are located near the surface results in the energy being significantly modified only close to the surface, in the top 200 m. There are additional effects due to modification of the effective Coriolis and buoyancy frequencies associated with horizontal and vertical current shear, not taken into account here, that may be important for critical layer absorption phenomena. Pereira et al. (2007) suggested that internal tides in the South Brazil Bight encounter critical layers due to the strongly sheared western boundary Brazil Current. Here, this could also happen for semi-diurnal tides in the presence of strong cyclones, and could happen for diurnal tides, whose frequencies are closer to f, even more frequently.

We used ray tracing as a convenient tool for interpreting our observations. For rigorous quantification of the effects of mesoscale and submesoscale currents on internal tides propagation, and the sensitivity to the vertical and horizontal structures of the currents, primitive equation numerical models of the tides should incorporate realistic background currents.

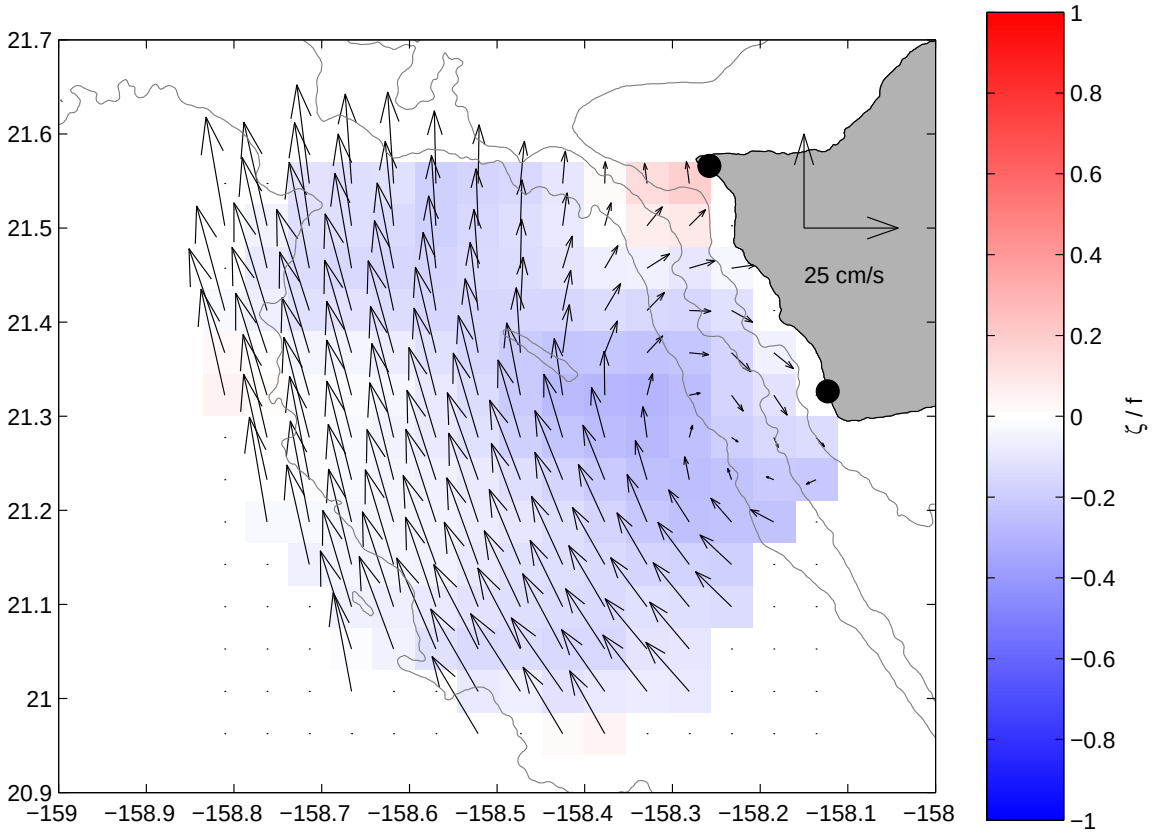

Figure 4.1: 9-month (September 2002 to May 2003) mean surface currents and vorticity (normalized by f) from HFRs. In this and subsequent figures, bathymetric contours are at 500, 1000, 2000 and 4000 m.

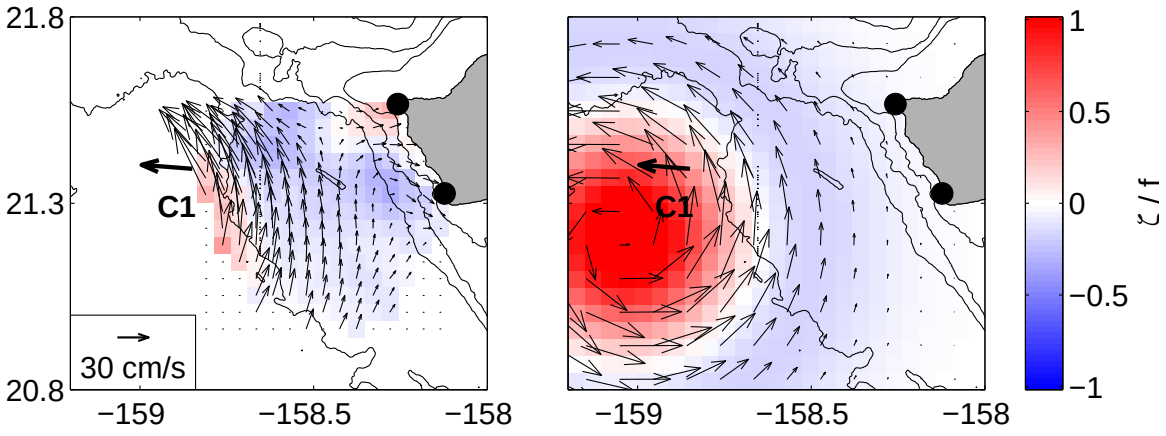

Figure 4.2: (a) Low-pass filtered surface currents and vorticity (normalized by f) from HFRs and ADCP (12-m depth, thick arrow), on September 29, 2002. (b) Idealized surface currents and vorticity, used for ray tracing.

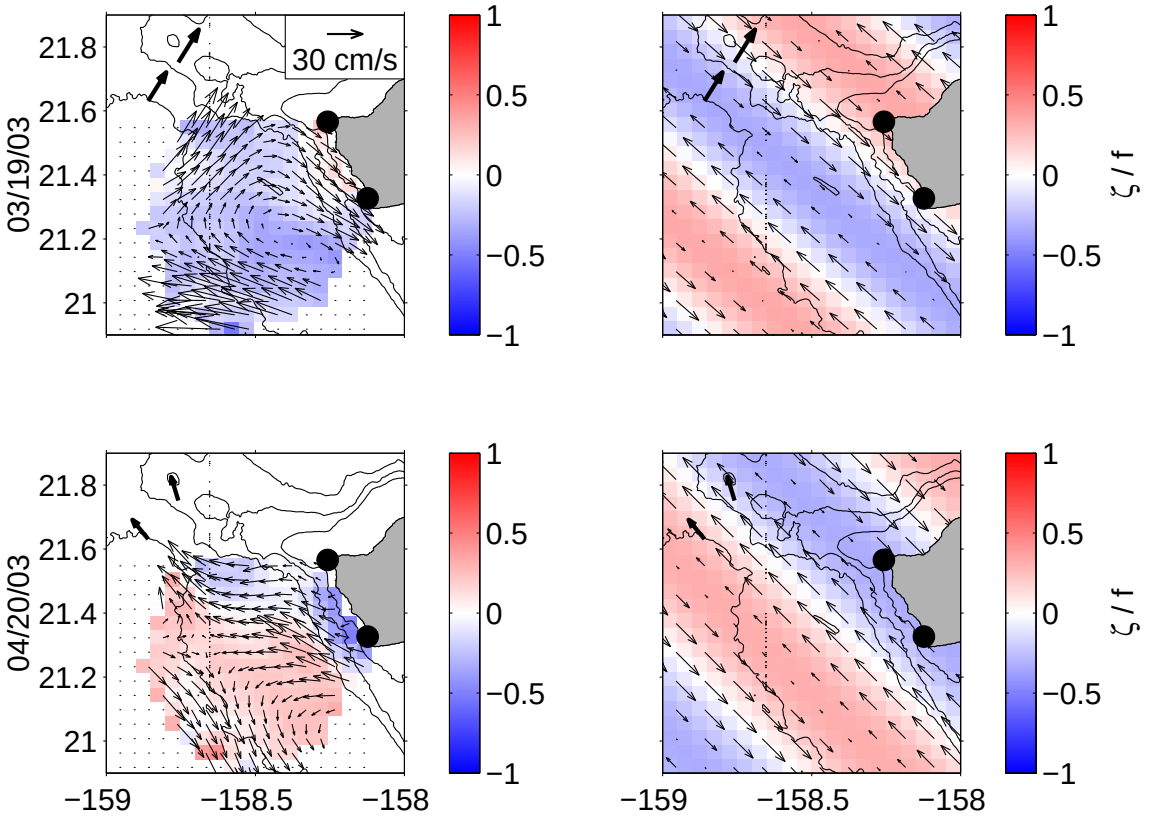

Figure 4.3: Observed (left panels) and idealized (right panels) low-pass filtered surface currents and vorticity (normalized by f) on March 19, 2003 (top panels) and April 20, 2003 (bottom panels). Observations are from HFRs and ADCPs (12-m depth, thick arrows).

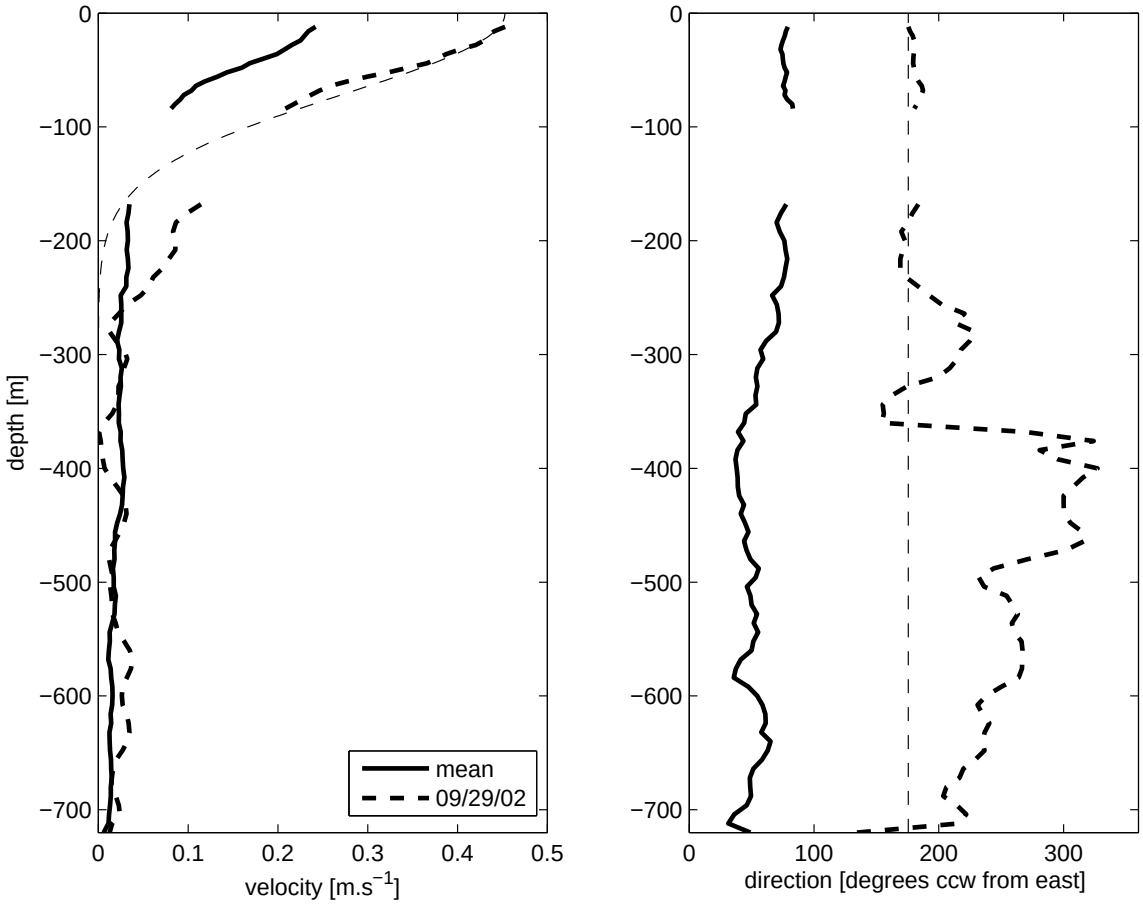

Figure 4.4: Vertical profiles of horizontal current velocity (a) and direction (b), measured by ADCPs at mooring C1. Average currents from August 16 to November 10, 2002 (thick solid lines) and low-pass filtered currents on September 29, 2002 (thick dashed lines) are shown. Idealized profiles for ray tracing are shown in thin lines.

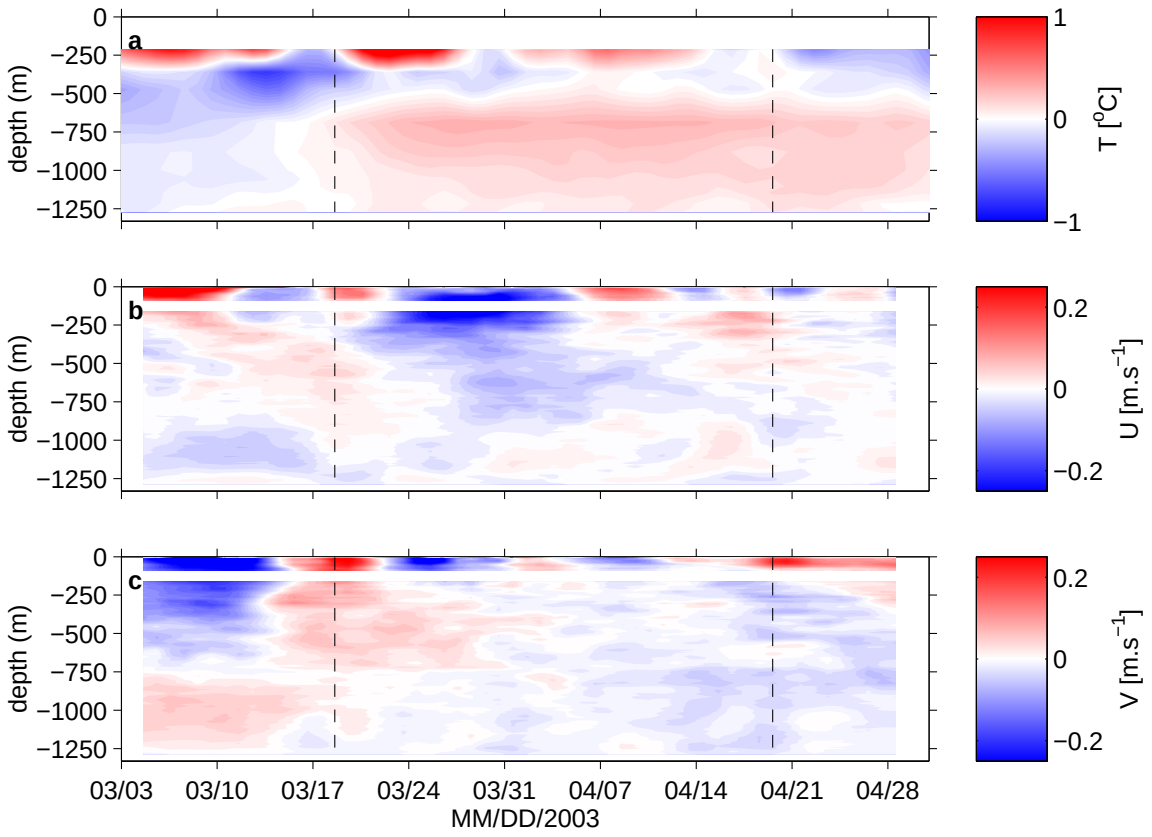

Figure 4.5: Low-pass filtered temperature (a) and zonal (b) and meridional (c) currents anomalies at mooring A2. The vertical dashed lines indicate the time of the snapshots in Figs. 4.3, 4.6 and 4.7.

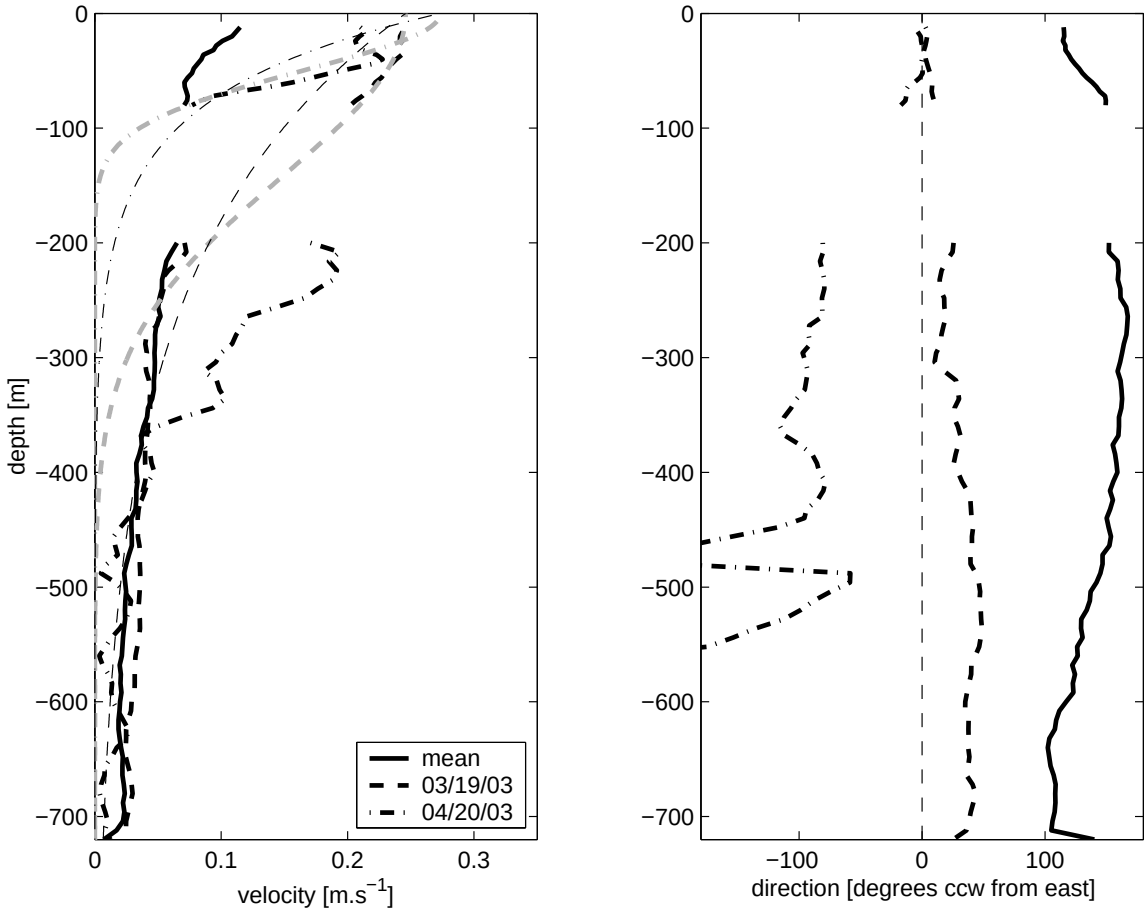

Figure 4.6: Vertical profiles of horizontal current velocity (a) and direction (b), measured by ADCPs at mooring C2. Average currents from November 17, 2002, to June 11, 2003 (thick solid lines) and first EOF of low-pass filtered currents during March 2003 (5-23, thick dashed lines) and April 2003 (5-24, thick dash-dotted lines) are shown. Directions for EOFs are relative to the surface direction. Idealized profiles for ray tracing are shown in thick gray lines for the gaussian profiles and in thin lines for the exponential profiles.

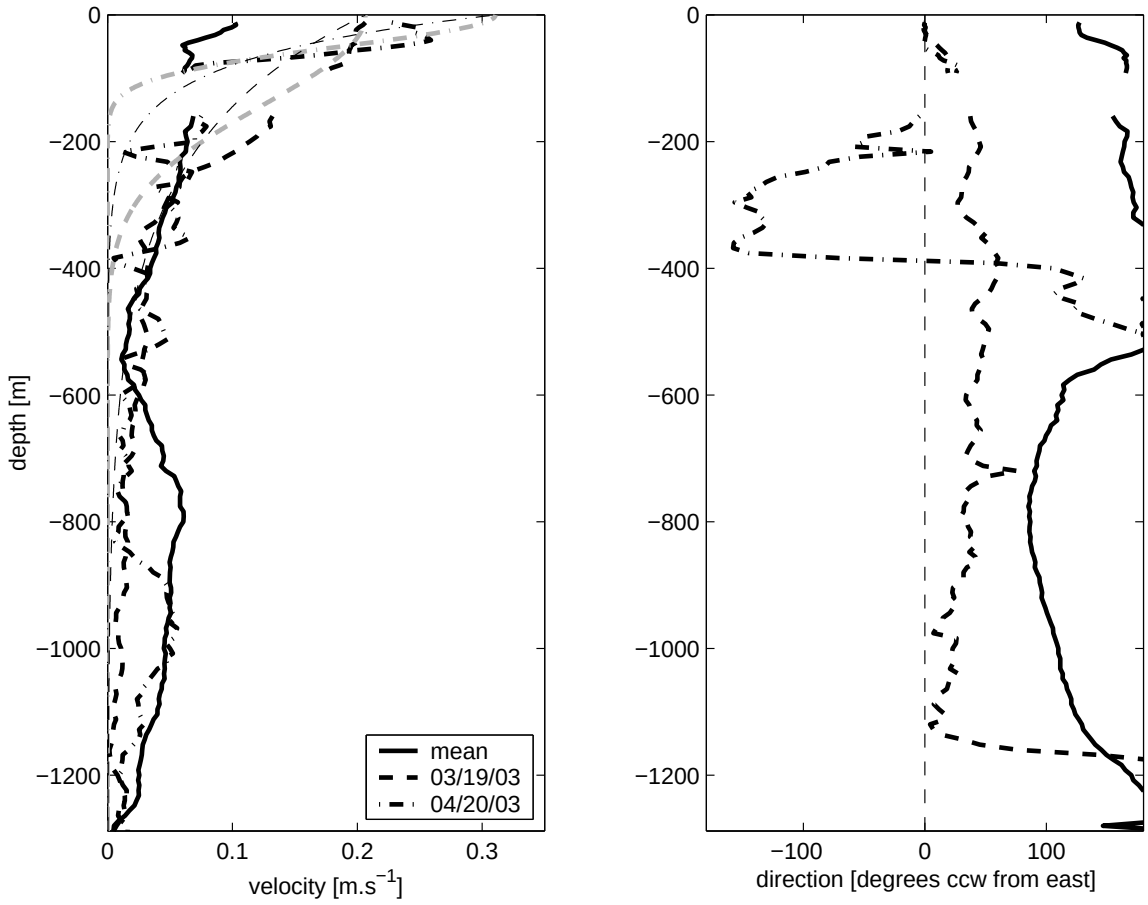

Figure 4.7: Same as Fig. 4.6 for mooring A2.

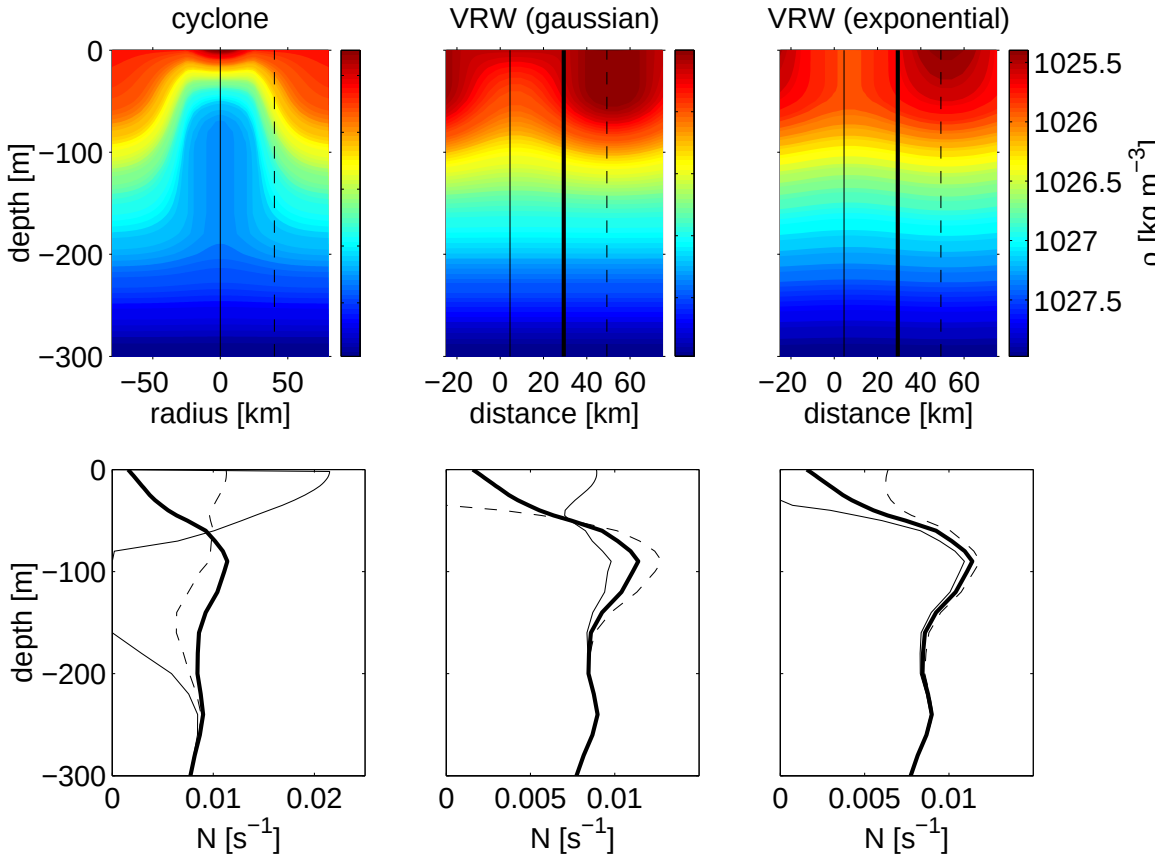

Figure 4.8: (top panels) Vertical section of density across the eddy center for the cyclone (a) and in the direction of propagation for the vorticity wave with gaussian vertical profile (b) and exponential vertical profile (c), assuming an arbitrary density of $1030 kg.m^{-3}$ at depth; (bottom panels) buoyancy frequency profiles at different locations indicated in the top panels (the thick solid line for the cyclone is for infinite radius).

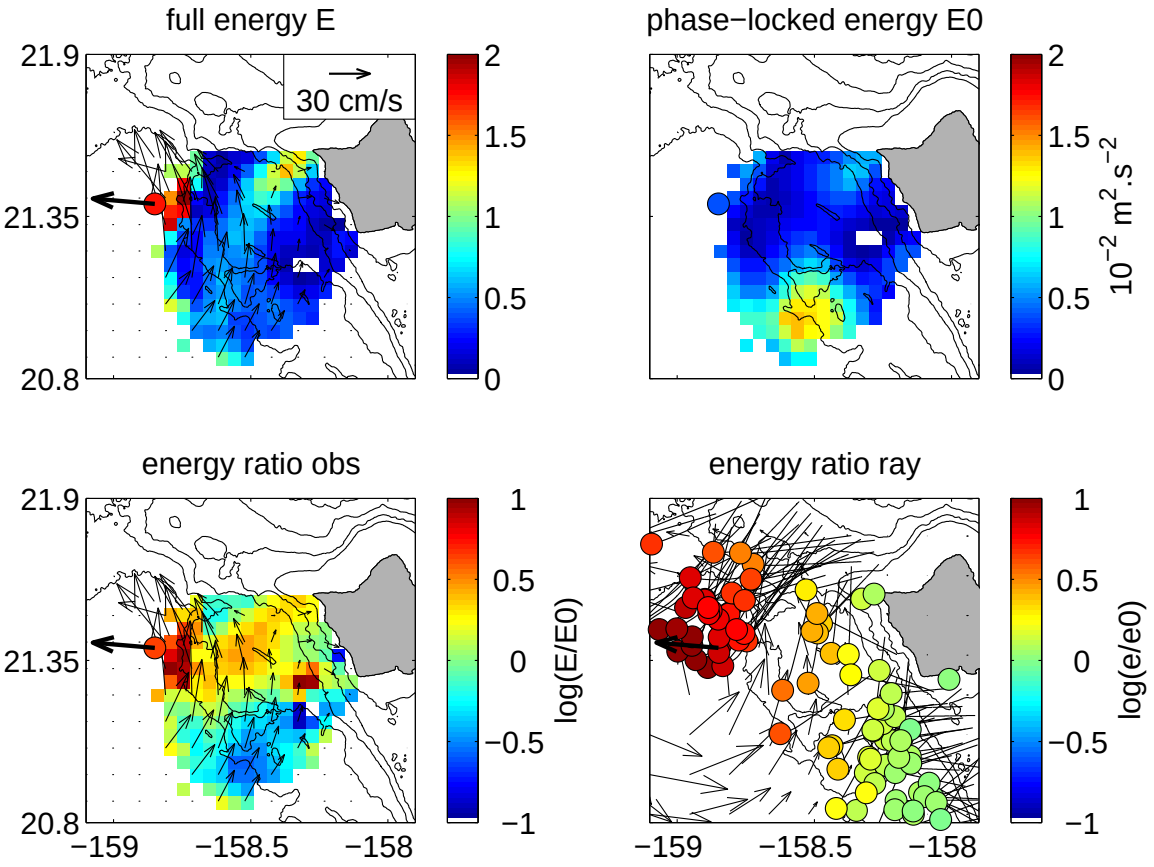

Figure 4.9: Complex-demodulated semi-diurnal surface currents kinetic energy on Sep 29, 2002, for (a) original and (b) phase-locked currents; logarithm of kinetic energy ratio for (c) original over phase-locked currents and (d) surface currents from ray tracing with mesoscale currents over ray tracing without currents. Mooring C1 location is indicated by a star. Mesoscale currents are superimposed.

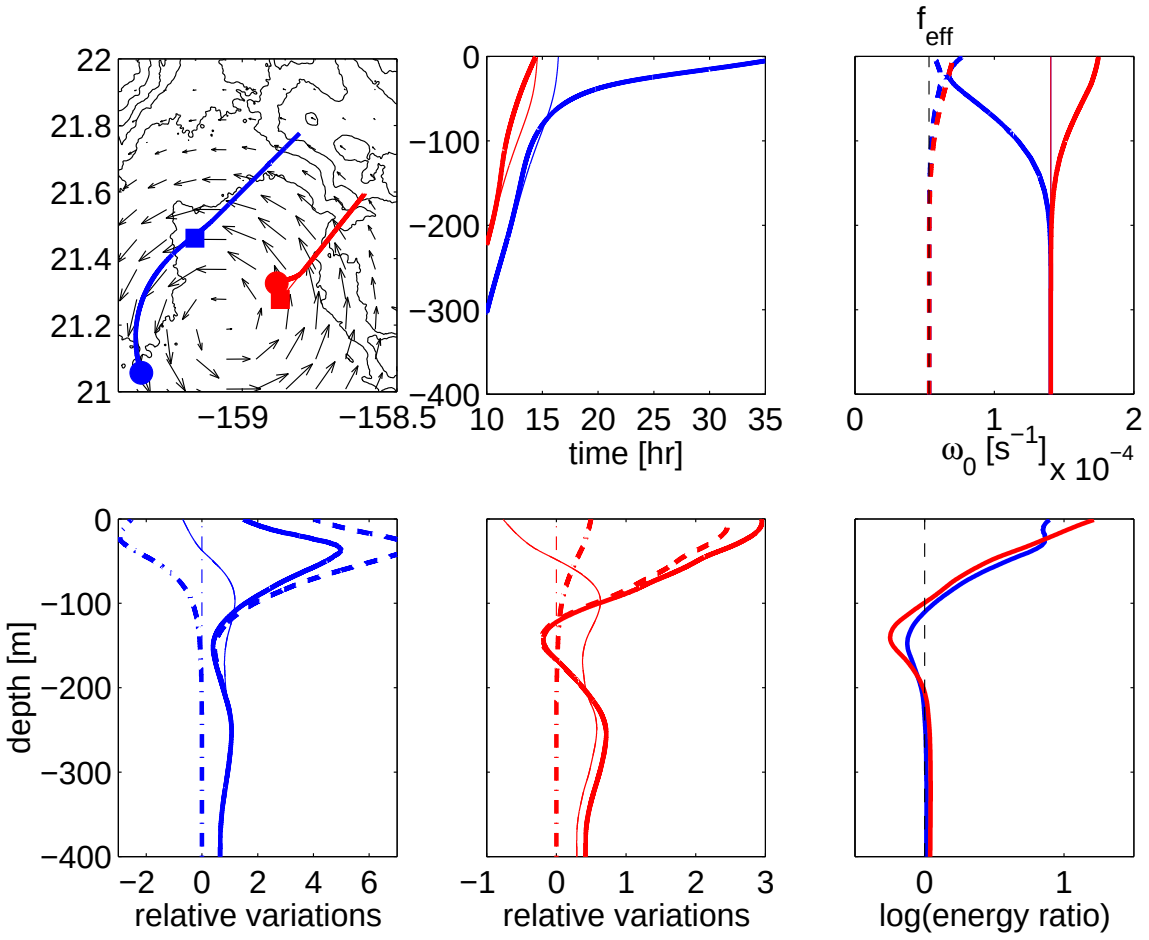

Figure 4.10: Ray tracing without (thin lines) and with (thick lines) mesoscale currents. (a) Horizontal trajectories. Rays originate at depth at a potential generation location of internal beams. The surface reflexion is indicated by a square (without currents) or a circle (with currents). Surface currents are shown by vectors. (b) Vertical trajectories as a function of time. (c) Intrinsic frequencies versus depth. The vertical dashed line indicate the inertial frequency. (d,e) Energy balance (Eq. 4.3.2) versus depth: normalized energy variations relative to the initial energy (solid lines), ray divergence contribution (dashed lines), and transfer with mesoscale currents contribution (dash-dot lines), for the western (d) and eastern (e) rays. (f) logarithm of energy ratio (currents over no currents) versus depth.

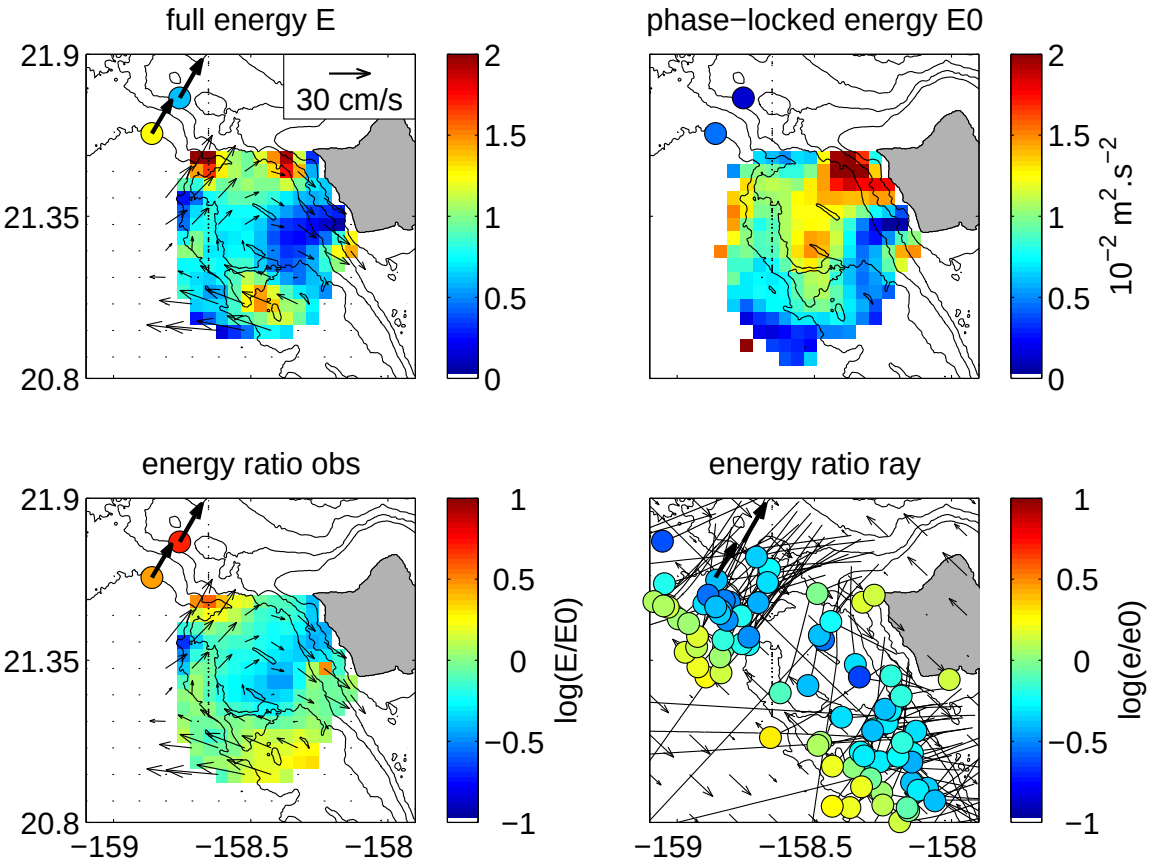

Figure 4.11: Same as Fig. 4.9 but for 03/19/2003.

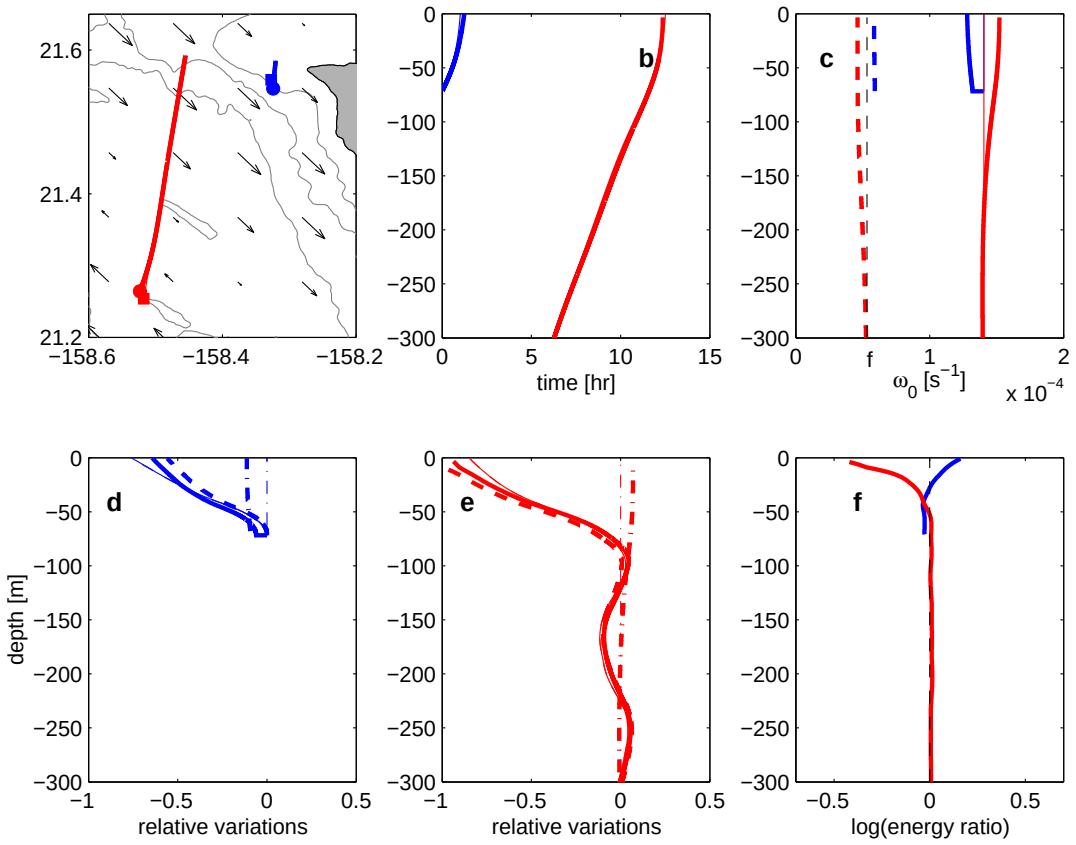

Figure 4.12: Same as Fig. 4.10 but for 03/19/2003. The eastern (western) ray energy balance is shown in panel d (e).

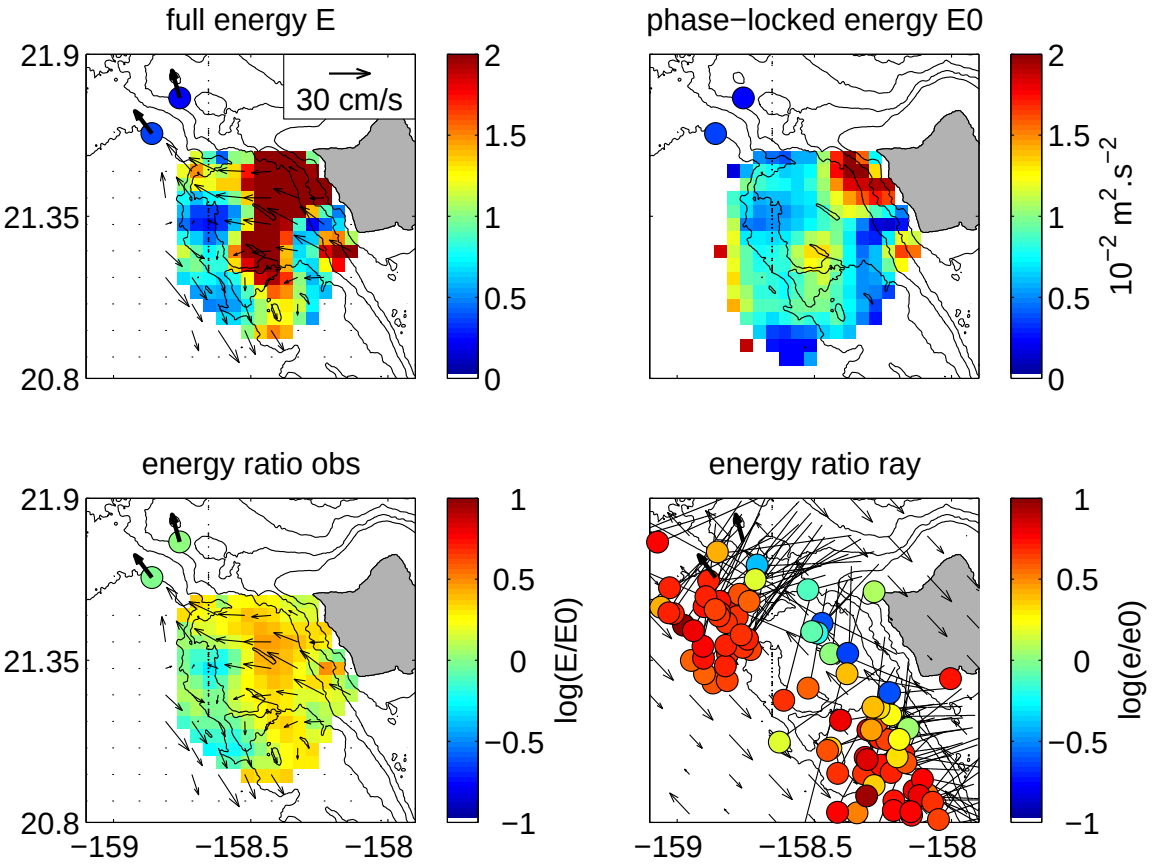

Figure 4.13: Same as Fig. 4.9 but for 04/20/2003 with gaussian vertical structure.

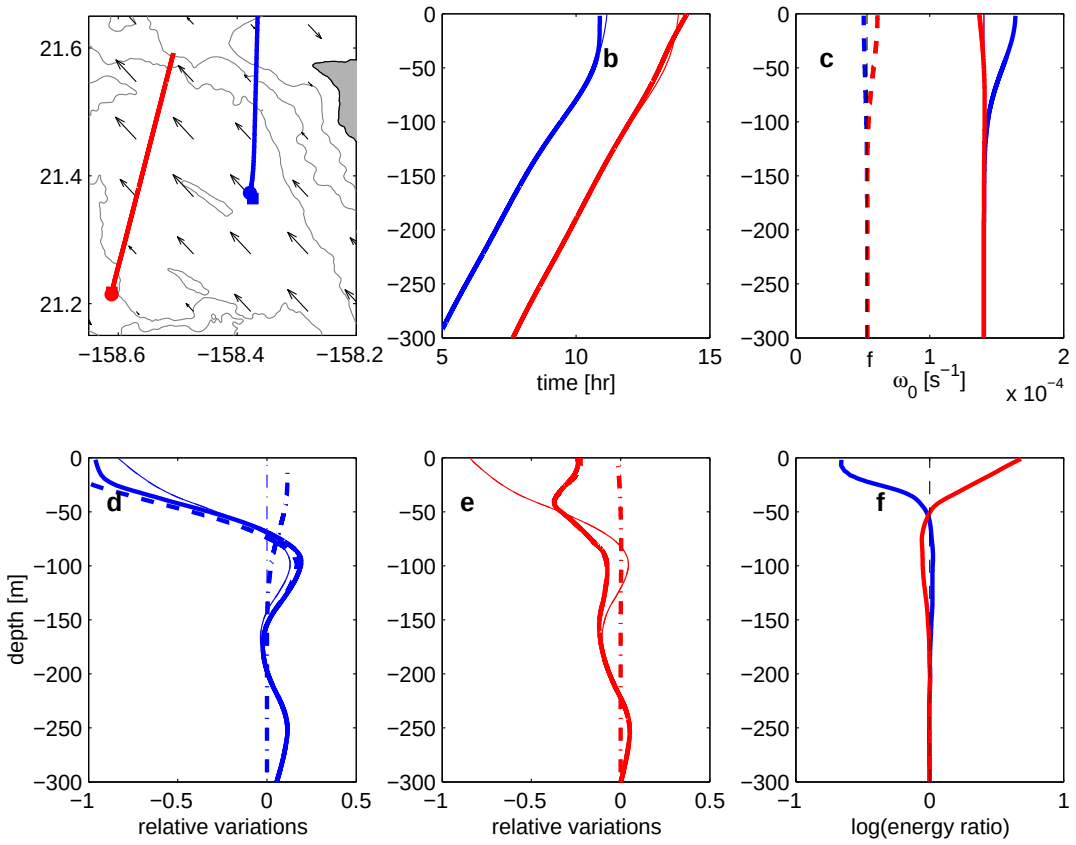

Figure 4.14: Same as Fig. 4.10 but for 04/20/2003 with gaussian vertical structure. The eastern (western) ray energy balance is shown in panel d (e).

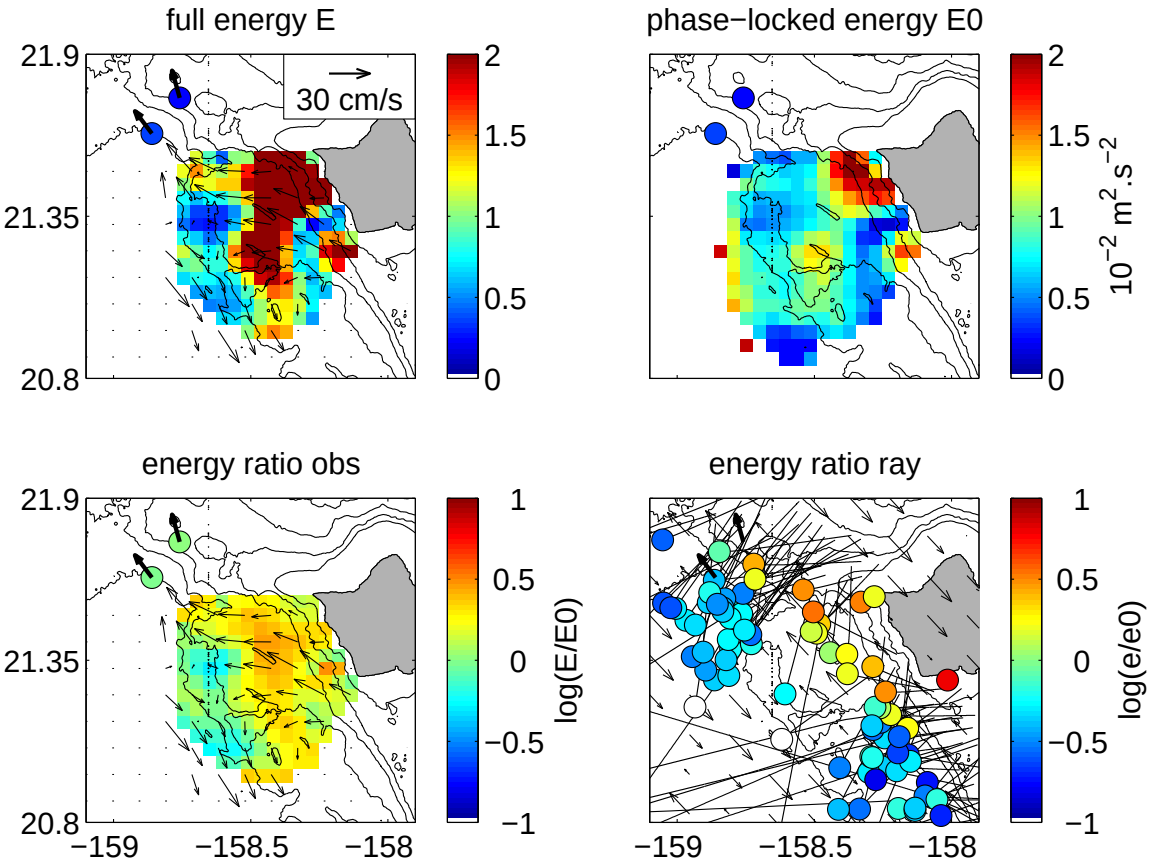

Figure 4.15: Same as Fig. 4.9 but for 04/20/2003 with exponential vertical structure.

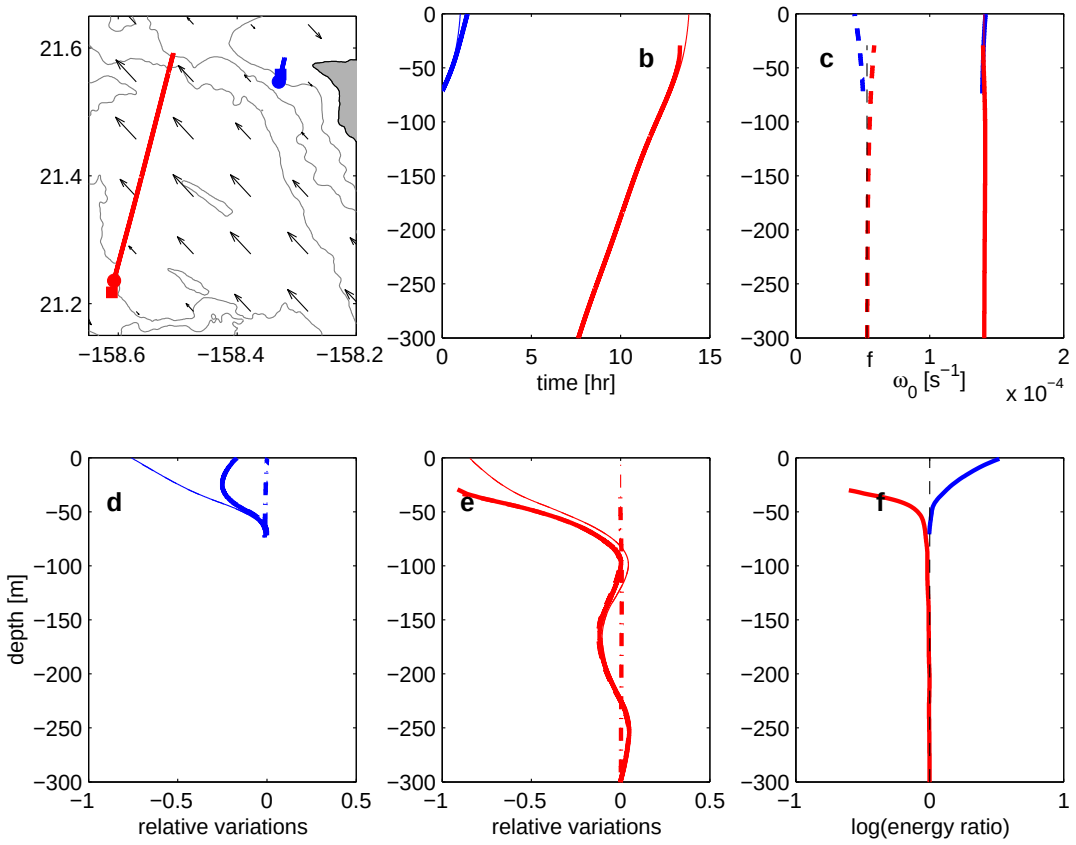

Figure 4.16: Same as Fig. 4.10 but for 04/20/2003 with exponential vertical structure. The eastern (western) ray energy balance is shown in panel d (e).

Chapter 5

Submesoscale anticyclone and frontogenesis

Where we present a case study of the generation and evolution of a strong submesoscale anticyclone west of O‘ahu, Hawai‘i, and the frontogenesis triggered by the interaction of the anticyclone with a cyclone south of Kaua‘i.

5.1 Introduction

Mesoscale and submesoscale variability is an important aspect of ocean circulation, affecting meridional heat transports (Qiu and Chen, 2005), the upper stratification (Lapeyre et al., 2006), as well as the oceanic primary production (McGillicuddy et al., 1998; Lapeyre and Klein, 2006). Horizontal resolution is a challenge both for numerical modelization (Siegel et al., 2001) and observations (Rudnick, 2001). The latter have often to make a compromise between spatial and temporal resolution. An exception are high-frequency (HF) radio current meters, which provide time series of 2D maps of surface currents with spatial resolutions ranging from 250 m to a few km and temporal resolutions of 20 minutes (e.g. Shay et al. (2000)). We document here 2-km resolution HF-radio observations of a strong submesoscale anticyclone and associated frontogenesis near the island of O‘ahu, Hawai‘i.

The Hawaiian archipelago is an ideal natural laboratory to study mesoscale and submesoscale vortices. It presents a barrier to the North Equatorial Current and the trade winds, generating an energetic wake of eddies through Ekman pumping and instability

of the North Equatorial Current (Patzert, 1969; Lumpkin, 1998; Flament et al., 2001). A typical example is shown in Fig. 5.1. The SST and geostrophic current fields reveal three mesoscale cyclones, centered at (159.4W, 21.3N) west of O‘ahu, (158.1W, 20.7N) west of Maui-Molokai-Lanai, and (156.9W, 20.1N) west of Hawai‘i. The cold cyclonic cores result from a combination of local upwelling (the cyclone west of Hawai‘i is colder than any surrounding water), and advection of colder water from the northeastern side of the ridge.

This picture is reminiscent of frontal instabilities observed at the Pacific Subtropical Front (Roden, 1981), located well north of the Hawaiian archipelago on average but with considerable variability in its position. However, additional forcing by Ekman pumping associated with island orographic effects on the trade winds (Patzert, 1969; Chavanne et al., 2002) may yield a more complex dynamics than the baroclinic instability of the front. Fig. 5.2 shows that each of the main islands (Hawai‘i, Maui-Molokai-Lanai, O‘ahu and Kauai) is associated with a dipole of wind stress curl in its atmospheric lee. The cyclones may have been spun up under positive wind stress curls near the islands, and subsequently drifted westward by the time of Fig. 5.1, except for the cyclone south of Kauai, which drifted northward. In addition, the hammerhead SST features between the cyclones suggest the presence of sub-mesoscale anticyclones just west of O‘ahu and southwest of Lanai, not resolved by the gridded altimetric currents (low-pass filtered with a wavelength cutoff of 200 km (Ducet et al., 2000).

Here, we will focus on the anticyclone west of O‘ahu and the associated SST front. We will show that (i) the anticyclone may have been generated by a barotropic instability of the cyclone south of O‘ahu, reinforced by wind forcing, (ii) its absolute vorticity reached negative values, possibly triggering centrifugal instability, and (iii) the SST straining by the anticyclone and cyclone west of O‘ahu lead to frontogenesis and the development of an ageostrophic secondary circulation across the SST front. We describe the instruments and methods in section 5.2, and the observations in section 5.3. The dynamics of the anticyclone and SST front are investigated in sections 5.4 and 5.5, and hypotheses about the anticyclone formation, growth and decay are discussed in section 5.6. Conclusions are summarized in section 5.7.

5.2 Instruments and methods

Two 16-MHz high-frequency radio surface current meters were deployed along the west shore of O‘ahu (Fig. 3.1), from September 2002 to May 2003. Each HF-radio measured the radial component of surface currents in the direction of the instrument at 1.5-km resolution, averaged over 9 minutes every 20 minutes. Vector currents were mapped on a 2-km resolution Cartesian grid by least-square fitting the zonal and meridional components to the radial observations in a 3-km search radius (Appendix A). The range of useful data was limited by geometric dilution of precision (GDOP), shown as ellipses in Fig. 3.2.

A 300-kHz and a 75-kHz ADCPs were moored upward-looking at 90-m and 750-m depth, respectively, in 4700-m water depth (labeled C1 in Fig. 3.1), with vertical resolutions of 4 m and 8 m, respectively, and 10-minutes acquisitions. To illustrate the GDOP effects, correlations between the 12m-depth bin of the upper ADCP and the closest HF-radio grid cell were 0.9 for the radial and zonal components, but dropped to 0.5 for the meridional component (still significant to 95% confidence, however).

Current observations were detided using T_Tide (Pawlowicz et al., 2002) and averaged, over 3-day windows, and 95% confidence intervals were computed as twice the variance of the detided 3-day time series, divided by the effective number of degrees of freedom (number of observations multiplied by the time step and divided by the integral time scale, computed from the autocorrelation of the detided time series).

Currents observations were complemented by 33-km resolution gridded geostrophic altimetric currents (Ducet et al., 2000), and 7-km resolution along-track sea level anomalies. Wind stress at 25-km resolution was obtained from QuikSCAT, (Liu and Tang, 1996), complemented by observations of 10-m wind at airports. Finally, 1-km resolution sea surface temperature (SST) and chlorophyll a concentrations were obtained from the Moderate Resolution Imaging Spectroradiometer (MODIS) onboard Aqua and Terra. SST images less than one day apart were composited to reduce the loss of coverage from clouds.

5.3 Description

Fig. 5.3 shows the evolution of the anticyclone at different stages of its life. Time series of the vortex extremum vorticity and velocity, and radius (defined as the range of extremum velocity from the vortex center, where velocity is minimum), are shown in Fig. 5.5, and the evolution of azimuthally-averaged profiles of velocity and vorticity are shown in Fig. 5.6.

On Oct 20 (Fig. 5.3, panels a, b, c), prior to the anticyclone generation, a cyclone was lying west of the observed area, as indicated by the positive vorticity on the edge of the domain and confirmed by a patch of relatively lower SST values centered at (159.0W, 21.3N). The associated northwestward flow decreased toward the coast, with vorticities reaching $\sim -0.5f$ near the coast. There was a band of convergence following the 2000 m isobath, with an associated band of high SST, and a patch of convergence in the northwest corner of the domain.

The anticyclone first appeared as a closed circulation with a radius of 11 km on Oct 24 (Fig. 5.3, panels d, e, f), centered ~ 9 km from the coast, embedded in a larger meander of the flow associated with the cyclone south of O'ahu, bringing colder water that remained separated from the other cyclone cold water by a meridional band of warm SST. The extremum vorticity value, of $-0.8f$, was not located in the anticyclone core, where the vorticity was $\sim -0.5f$, but on the inside edge of the meander. The vortex core was convergent, and there was strong divergence in the northwestern part of the domain.

Three days later, on Oct 27 (Fig. 5.3, panels g, h, i), the anticyclone reached its extremum vorticity value of $-1.45 \pm 0.2f$, located at the vortex center, which was no longer convergent, and ~ 22 km from the coast, . Its radius was 14 km and maximum azimuthal velocity was $35cm.s^{-1}$. A sharp meridional SST front had developed at 158.63W, flanked by negative vorticity and divergence on its warm side and positive vorticity and convergence on its cold side.

Five days later, on Nov 1 (Fig. 5.3, panels j, k, l), the anticyclone core vorticity dropped to $-f$, with the core almost in solid-body rotation at $v = -fr/2$ (Fig. 5.6). The radius increased to 19 km, but the extremum azimuthal velocity remained the same. The SST front had been advected around the anticyclone, which moved southward by ~ 15 km.

Only two days later, on Nov 3 (Fig. 5.3, panels m, n, o), the anticyclone had broadened and deformed, its vorticity now reaching only $-0.6f$ in the core rim, while the western cyclone had moved northwestward and the southern cyclone southward, freeing the anticyclone. It then kept broadening and weakening, and started to drift westward while becoming more elliptic, as suggested by the advection pattern of warm SST (Fig. 5.3, panels p, q, r).

Other similar cyclones and anticyclones (but not this one) drifted over the mooring C1, and their typical vertical structure is captured by the first empirical orthogonal function of the horizontal currents, shown in Fig. 5.7. They are surface trapped, with an exponential decay scale of ~ 100 m, much smaller than that of the first baroclinic mode, computed from 10-year averages of temperature and salinity observations at Station ALOHA (Karl and Lukas, 1996), located 100 km north of O‘ahu. The vertical shear is negligible in a surface mixed-layer ~ 20-m thick, and maximum at 35 m depth.

Two satellite tracks crossed the anticyclone near the time of its extremum vorticity, GFO track 13 on Oct 27 at 5 UTC, and Jason 1 track 223 on Oct 28 at 13 UTC (indicated in Fig. 5.1). Along-track sea level anomalies (SLA) along the GFO track are shown in Fig. 5.8. The sea level extremum associated with the anticyclone clearly stands out of the noise. Also shown are the sea level anomalies computed from the HFRs currents assuming cyclo-geostrophic balance. The Jason 1 observations were noisier, and did not show the sea level extremum.

Finally, chlorophyll a concentrations from Aqua MODIS are shown in Fig. 5.9. On Oct 26, the warm water advected northward by the eddies was relatively low in chlorophyll, and was well separated from richer waters associated with the eddies. The anticyclone was advecting coastal water rich in chlorophyll south of O‘ahu. Four days later (Oct 30), some lateral stirring had occurred over the warm water tongue, and chlorophyll concentration was building up in the anticyclone core, possibly as a result of advection.

5.4 Dynamical balance

Here, we investigate the dynamical balance of the anticyclone and associated front. We will assess the relative importance of the terms of the divergence equation. From the primitive equations on the f-plane:

$$\frac{D\mathbf{u_h}}{Dt} + f(\mathbf{k}\times\mathbf{u})_h = -\frac{1}{\rho_0}\nabla_\mathbf{h} p + \frac{1}{\rho_0}\nabla_\mathbf{h}.\tau_\mathbf{h} + \frac{1}{\rho_0}\frac{\partial \tau_\mathbf{v}}{\partial z} \quad (5.4.1)$$

$$0 = \frac{\partial p}{\partial z} + \rho g \quad (5.4.2)$$

$$\nabla_\mathbf{h}.\mathbf{u_h} + \frac{\partial w}{\partial z} = 0 \quad (5.4.3)$$

$$\frac{DT}{Dt} = -\nabla_\mathbf{h}.\mathbf{F_h} - \frac{\partial F_v}{\partial z} \quad (5.4.4)$$

where $D/Dt = \partial/\partial t + \mathbf{u_h}.\nabla_\mathbf{h} + w\partial/\partial z$ is the 3-D material derivative, subscripts h denote horizontal components, $\mathbf{u} = (u, v, w)$ is the 3-D velocity, $\mathbf{k}$ is the vertical unit vector, f is the Coriolis parameter, T is the potential temperature, $\tau_\mathbf{h} = -\rho_0\overline{u'_i u'_j}$ is the 2-D Reynolds stress tensor, representing the turbulent fluxes of horizontal momentum in the horizontal directions, $\tau_\mathbf{v} = -\rho_0\overline{u'_i w'}$ is the turbulent flux of horizontal momentum in the vertical direction, and $\mathbf{F_h} = \overline{\mathbf{u'_h} T'}$ and $F_v = \overline{w'T'}$ are the horizontal and vertical turbulent heat fluxes, respectively.

$\nabla_\mathbf{h}.(5.4.1)$ yields an equation for the 2-D divergence $\delta = \nabla_\mathbf{h}.\mathbf{u_h}$:

$$\frac{\partial\delta}{\partial t} + \nabla_\mathbf{h}.(\mathbf{u_h}.\nabla_\mathbf{h}\mathbf{u_h}) + \nabla_\mathbf{h} w.\frac{\partial \mathbf{u_h}}{\partial z} + w\frac{\partial\delta}{\partial z} - f\zeta = -\frac{1}{\rho_0}\nabla_h^2 p + \frac{1}{\rho_0}\nabla_\mathbf{h}.(\nabla_\mathbf{h}.\tau_\mathbf{h}) + \frac{1}{\rho_0}\frac{\partial \nabla_\mathbf{h}.\tau_\mathbf{v}}{\partial z} \quad (5.4.5)$$

where $\zeta = \mathbf{k}.\nabla\times\mathbf{u}$ is the relative vorticity.

If $\tau_\mathbf{v}$ decays linearly with depth, from the surface wind stress $\tau_\mathbf{h}^\mathbf{w}$, to zero at the base of the mixed layer h, if we neglect the contribution of the turbulent fluxes of horizontal momentum in the horizontal directions, and if $w = 0$ at the surface, the horizontal divergence equation for the surface currents results:

$$\frac{\partial\delta}{\partial t} + \nabla_\mathbf{h}.(\mathbf{u_h}.\nabla_\mathbf{h}\mathbf{u_h}) - f\zeta = -\frac{1}{\rho_0}\nabla_h^2 p + \frac{1}{\rho_0 h}\nabla_\mathbf{h}.\tau_\mathbf{h}^\mathbf{w} \quad (5.4.6)$$

The first, second, fourth and fifth terms of Eq. 5.4.6 are shown in Fig. 5.10, normalized by the third term. The wind stress is obtained from QuikSCAT, and the mixed

layer is taken to be 20 m thick. The pressure term is obtained as the resultant from all the other terms. The first and fifth terms are an order of magnitude smaller than the third term. Inside the anticyclone core, the balance is cyclo-geostrophic, with the advection term dominating over the pressure term near the center, where it reached $0.75 f\zeta$. The SST front is not in geostrophic balance, the advection term almost balancing the Coriolis term on the cold side, and reaching $-f\zeta$ on the warm side.

5.5 Frontogenesis

Fig. 5.11 shows the evolution of the SST front between Oct 23 and November 1, a period during which the front was meridional. SST was averaged meridionally between 21.2N and 21.4N. On Oct 23, the front corresponded to a band of warm SST flanked by colder SST to the west, associated with the western cyclone, and to the east, advected from the southern cyclone by the flow meander around the coast (Fig. 5.3d). Two days later (Oct 25), as the anticyclone was spinning up, the front had drifted westward by ~ 15 km, and the warm band had widened. Two days later (Oct 27), when the anticyclone reached its extremum vorticity, the front had not move but sharpened, reaching an eastward SST gradient of $-0.1^o C.km^{-1}$, twice its value on Oct 25. Two days later (Oct 29), the front was still as sharp and at the same location, but had moved eastward and decayed in amplitude as the warm SST was being advected toward the coast by the anticyclone.

There was a strong frontogenesis associated with the spinning up of the anticyclone between Oct 25 and 27. Taking $\nabla_{\mathbf{h}}(5.4.4)$ yields the equation for the evolution of the horizontal temperature gradient:

$$\frac{D\nabla_{\mathbf{h}}T}{Dt} = -\mathbf{G}.\nabla_{\mathbf{h}}T - \frac{\partial T}{\partial z}\nabla_{\mathbf{h}}w - \nabla_{\mathbf{h}}(\nabla_{\mathbf{h}}.\mathbf{F_h}) - \nabla_{\mathbf{h}}(\frac{\partial F_v}{\partial z}) \qquad (5.5.1)$$

where $\mathbf{G} = [\partial u_j/\partial x_i]$ is the 2-D velocity gradient tensor. The first term on the rhs of (5.5.1) is the frontogenetical $\mathbf{Q}$ vector (Hoskins et al., 1978), representing straining of temperature by the horizontal velocity field, the second term corresponds to straining by the vertical velocity, leading to a flattening or steepening of the isotherms, and the remaining terms represent the effects of turbulent heat fluxes on horizontal temperature gradients.

Fig. 5.12 shows that on Oct 27, $\mathbf{Q}$ is strong and westward along the front, leading to an increase (in absolute value) of the zonal SST gradient, of $\sim 0.2^oC.km^{-1}.day^{-1}$. This is ~ 8 times the observed SST gradient increase between Oct 25 and 27. Clearly, there must be a counteraction by the other terms on the rhs of (5.5.1). At the surface, where $w = 0$, the second term on the rhs of (5.5.1) is zero, so frontogenesis must be reduced by the effects of turbulent heat fluxes, as shown in the numerical simulations of Capet et al. (2007).

Below the surface, the second term on the rhs of (5.5.1) can play a frontolytical role too. Indeed, a secondary vertical circulation develops in response to the increase of density gradients due to horizontal straining by the horizontal velocity field, in order to restore the thermal wind balance (Hoskins et al., 1978). This secondary circulation acts to flatten the isopycnals (see Fig. 1 in Lapeyre et al. (2006) or Fig. 2 in Capet et al. (2007)), hence restratifying the upper ocean. The surface manifestation of this mechanism is present in our observations. Fig. 5.13 shows that there is surface divergence, hence upwelling on the warm side of the front, and surface convergence, hence downwelling on the cold side of the front. Therefore below the surface, the zonal vertical velocity gradient is negative, and since the vertical temperature gradient must be positive for hydrostatic stability (assuming there is not a strong negative vertical salinity gradient), the second term on the rhs of (5.5.1) is eastward, counteracting the effect of the straining of temperature by the horizontal velocity.

Furthermore, there is negative vorticity on the warm side of the front, and positive vorticity on its cold side. $\mathbf{k}.\nabla \times (5.4.1)$ yields the vorticity equation:

$$\frac{D\zeta}{Dt} = (\zeta + f)\frac{\partial w}{\partial z} + \frac{\partial(\mathbf{k} \times \mathbf{u})_h}{\partial z}.\nabla_{\mathbf{h}} w + \frac{1}{\rho_0}\mathbf{k}.\nabla \times (\nabla_{\mathbf{h}}.\tau_{\mathbf{h}}) + \frac{1}{\rho_0}\frac{\partial}{\partial z}\mathbf{k}.\nabla \times \tau_{\mathbf{v}} \quad (5.5.2)$$

where the continuity equation (5.4.3) has been used. Since near the front $|\zeta| < f$, $\zeta + f$ is positive, we see that the divergence pattern reinforces the vorticity pattern through the vortex stretching mechanism (first term on the rhs of Eq. (5.5.2)), hence accelerating the frontal jet to restore the thermal wind balance. There is an asymmetry between cyclonic and anticyclonic vorticity, the former being more accelerated than the latter for the same divergence values, which is also indicated in the observations.

5.6 Discussion

5.6.1 Vertical velocity

The higher divergence and convergence values, hence stronger vertical velocities, are found on the edges of the eddies, not in their cores. They are associated with secondary circulations that result from the straining of the density by the horizontal velocity field. In oligotrophic waters, such vertical velocities can make an important contribution to primary production, by pumping nutrients vertically into the euphotic layer (Lévy et al., 2001). Here, the chlorophyll content of the surface waters sensed by MODIS is controlled primarily by horizontal advection of chlorophyll-rich coastal water (Fig. 5.9).

5.6.2 Anticyclone growth

What processes could have generated the anticyclone ? One possibility is friction at the coast, which is the vorticity source in classic Von Karman streets. D'Asaro (1988) proposed this formation mechanism for anticyclonic submesoscale vortices observed in the Beaufort Sea. Vorticity less than $-f$ is generated on the inshore side of a coastally trapped current, which subsequently detaches from the coast where the latter makes a sharp change in direction, and becomes inertially unstable, generating anticyclonic $Ro = 1$ vortices. Flament et al. (2001) suggested the same mechanism was responsible for the generation of mesoscale anticyclones west of Hawai'i, where they observed $\sim -f$ vorticity 12 km downstream from the separation point of the North Equatorial Current.

Here, however, the strongest vorticity observed prior to the anticyclone formation was not near the coast, but within the anticyclonic side of the westward current associated with the cyclone south of O'ahu, where the vorticity reached $\sim -0.8f$ on Oct 24, the day the anticyclone appeared. The anticyclone could therefore have been generated by a barotropic instability of the northern rim current of the cyclone south of O'ahu. The radius of this cyclone can be estimated to be $R \sim 30$ km from SST (Fig. 5.3d), and its maximum azimuthal velocity is $V \sim 0.5 m.s^{-1}$, yielding a Rossby number $Ro = 2V/R \sim 0.6$. The first radius of deformation is $R_d \sim 60km$ (Chelton et al., 1998), yielding a Froude number $Fr = (R/Rd)^2 \sim 0.25$. This parameter regime has been investigated by Poulin and Flierl

(2003) for a parallel jet in a 1.5-layer shallow water model. For $Ro = 1$ and $Fr = 0.1$, the vorticity in the anticyclones developing on the anticyclonic side of the jet could grow temporarily stronger than that initially provided by the jet (their Fig. 9a). A similar scenario could be happening in our case, although it is not clear what mechanism is responsible for this transient growth. Potential vorticity conservation suggests that anticyclonic vorticity would decrease as the vortex moves away from the jet axis toward thicker water layer (in the 1.5-layer framework).

Another possibility is vortex squeezing by topography, or bottom frictional torques. However, if the anticyclone had a vertical structure similar to that shown in Fig. 5.7, it would not have felt much topography below 500 m depth. This isobath is too close to the coast (Fig. 3.1) to affect the vortex.

Yet another possibility for the vorticity growth beyond that provided by the unstable jet is wind forcing. Since the trade winds had been blowing steadily for at least two days prior to Oct 24 (Fig. 5.5), and since the Ekman flow develops typically over an inertial period (33 hrs), we assume that the Ekman transport is in equilibrium with the wind, and is given by:

$$\mathbf{u_E} = -\frac{(\mathbf{k} \times \tau^{\mathbf{w}})_h}{\rho_0(f + \zeta_0)} \tag{5.6.1}$$

where ζ_0 is the vorticity of the pre-existing flow (the anticyclone generated by the unstable jet). The Ekman flow feels the combined rotation of the Earth and of the pre-existing flow (Stern, 1965). This leads to increased (decreased) Ekman transports over anticyclonic (cyclonic) flows. The associated Ekman pumping velocity is:

$$w_E = \frac{\mathbf{k}.\nabla \times \tau^{\mathbf{w}}}{\rho_0(f + \zeta_0)} + \frac{(\mathbf{k} \times \tau^{\mathbf{w}})_h.\nabla_{\mathbf{h}}\zeta_0}{\rho_0(f + \zeta_0)^2} \tag{5.6.2}$$

Not only wind stress curl, but also wind blowing over vorticity gradients can generate Ekman pumping.

The response of the ocean interior (below the Ekman layer) is obtained by neglecting turbulent stresses and linearizing around the pre-existing flow (assumed to have no vertical velocity) in (5.5.2). To obtain an estimate of $\partial w/\partial z$, we assume that the interior vertical velocity w decays exponentially with depth from its surface value $-w_E$, where the

decay scale H is given by fitting an exponential profile to the horizontal currents observed at the mooring C1. This is a diagnostic computation, we do not seek to justify why the profile should be exponential.

$$\frac{D_0\zeta}{Dt} = \frac{\mathbf{k}.\nabla \times \tau^{\mathbf{w}}}{\rho_0 H} + \frac{(\mathbf{k} \times \tau^{\mathbf{w}})_h.\nabla_{\mathbf{h}}\zeta_0}{\rho_0 H(f+\zeta_0)} \tag{5.6.3}$$

where D_0/Dt is the material derivative following the pre-existing flow. The effect of the wind stress curl on the interior vorticity is not modified, because the interior fluid also feels the combined rotation of the Earth and of the pre-existing flow. Recalling (5.6.1), the second term on the rhs of (5.6.3) is merely the advection of interior vorticity by the Ekman velocity averaged over the depth scale of the interior flow. Since the Ekman transport depends on both the wind and the pre-existing vorticity, its effect on the vorticity evolution will depend on the relative configuration of the wind and pre-existing vorticity fields. Here, the wind is to the southwest over the entire vortex area (Fig. 5.2), so there will be a tendency for the vortex to drift northwestward. The wind is also stronger over the southern part of the vortex than over the northern part, more shielded from the upstream trades by the coastal mountains (Fig. 3.1), inducing an accumulation of vorticity in the middle of the vortex as the Ekman transport converges (in addition to the vorticity generated by vortex squeezing below the mixed layer).

The initial observed vorticity growth rate is $D\zeta/Dt = -1.75 \times 10^{-10}s^{-2}$. When estimating the order of magnitude of the second term on the rhs of (5.6.3), one should be careful that (5.6.1) was obtained for pre-existing flows with weak vorticities. Therefore one should approximate the second term on the rhs of (5.6.3) by $(\mathbf{k} \times \tau^{\mathbf{w}})_h.\nabla_{\mathbf{h}}\zeta_0/(\rho_0 H f)$ to avoid this term to become arbitrarily large when $\zeta_0 \to -f$. Non-linear effects come into play when ζ_0 in not small, but Thomas and Rhines (2002) showed that including them lead to an even faster anticyclonic vorticity growth due to the positive feedback of increasing anticyclonic vorticity onto the Ekman pumping. Therefore the above estimate should be a lower bound. Taking $H \sim 100m$, $\rho_0 \sim 10^3 kg.m^{-3}$, $\mathbf{k}.\nabla \times \tau^{\mathbf{w}} \sim 10^{-6}N.m^{-3}$, $|\tau^{\mathbf{w}}| \sim 0.1N.m^{-2}$, $\zeta_0 \sim -f$ and varying over $\sim 10km$, the first term on the rhs of (5.6.3) is $\sim 10^{-11}s^{-2}$ and the second term is $\sim 10^{-10}s^{-2}$, one order of magnitude stronger than the first term and of the same order as the observed vorticity growth. Therefore in the presence of an already established strong anticyclone, the important parameter for forcing

by the wind is not the wind stress curl but the magnitude of the wind stress and of the pre-existing vorticity gradient. Note, however, that wind stress curl estimated from QuikSCAT observations at 25 km resolution could be underestimated, since wind shear lines are very narrow behind the islands (Chavanne et al., 2002).

Using the previous scaling, the Ekman advection speed is $\sim 2cm.s^{-1}$ or $\sim 2km.day^{-1}$. The vortex drifted northwestward by $\sim 7km$ between Oct 25 and 27, slightly faster than predicted from Ekman advection, but subsequently stalled before drifting southward and finally westward. The Ekman advection is probably small compared to the effects of the coast or of the surrounding cyclones on the anticyclone motion. Since the trade winds kept blowing, although weaker, during the rest of the vortex evolution, and that the vortex remained at the same location for a few more days, one has to explain now why the vorticity did not keep growing after Oct 27.

5.6.3 Anticyclone decay

The negative absolute (relative + planetary) vorticity suggests that the vortex growth may have been limited by the development of centrifugal instability. An axisymmetric baroclinic vortex is unstable to axisymmetric perturbations if (Kloosterziel et al., 2008):

$$(\frac{2V}{r}+f)(\zeta+f) < (\frac{2V}{r}+f)^2 Ri^{-1} \tag{5.6.4}$$

where r is the radial distance from the vortex center, V is the azimuthal velocity, and $Ri = N^2/(\partial V/\partial z)^2$ is the Richardson number (N^2 is the buoyancy frequency). Since the rhs of (5.6.4) is always positive, a more stringent criterion is the modified Rayleigh criterion (Kloosterziel and van Heijst, 1991):

$$LQ < 0 \tag{5.6.5}$$

where $L = Vr + fr^2/2$ is the absolute angular momentum, and $Q = \zeta + f$ is the absolute vorticity. The radial profiles of L and Q are shown in Fig. 5.14 for Oct 27 and Nov 1. On Oct 27, both L and Q are negative for small ranges and positive for long ranges, but

they are of opposite sign between 9 and 13 km, where centrifugal instabilities can therefore develop. Five days later (Nov 1), both L and Q have become positive everywhere.

For barotropic vortices, the upper limit for the exponential growth rate of perturbations is $s_m = (max|\phi|)^{1/2}$, where $\phi = 2L/r^2Q$ is the Rayleigh discriminant (Kloosterziel et al., 2007). We obtain here $s_m = 0.6day^{-1}$, so the amplitude of axisymmetric perturbations can be multiplied by 2.7 in 1.7 days. For baroclinic vortices, the upper bound on the growth rate is even higher (Kloosterziel et al., 2008). Therefore it appears possible that centrifugal instabilities have developed and have redistributed angular momentum five days later to suppress the unstable conditions. Kloosterziel et al. (2007) predict that in the limit of infinite Reynolds number (inviscid fluid), the absolute angular momentum in the equilibrated vortex core would be exactly zero, up to the radius where the radial integral of the initial absolute angular momentum is zero, beyond what it will be identical to the initial profile (red solid curve in Fig. 5.14). Then the core absolute vorticity would be zero (red dashed curve in Fig. 5.14) and the core would be in solid-body rotation at $V = -fr/2$ (red dashed line in Fig. 5.6). Although the ocean has very high Reynolds numbers, the profiles on Nov 1 do not follow exactly the predictions, but appear to be a smoothed version of them, as one would expect due to frictional processes, and 3D perturbations not accounted for by Kloosterziel et al. (2007).

The later development of the vortex, with a very fast increase of its radius, and distortion of its shape, cannot be explained by centrifugal instability, and is probably the result of interactions with the surrounding vortices.

5.7 Conclusions

Our observations show energetic dynamical submesoscale O(10 km) structures, embedded within a field of mesoscale eddies, unresolved by gridded altimetric products, and barely resolved by unfiltered along-track altimetric observations. Negative absolute vorticity persisted for a week in the core of an oceanic anticyclone, before centrifugal instabilities eventually redistributed absolute angular momentum until the absolute vorticity was zero in the core, following the numerical predictions of Kloosterziel et al. (2007)). The anticyclone was in cyclogeostrophic balance to first order. Wind forcing was shown to be a

possible important contributor to the vorticity growth, and could play a role in many other areas where strong orographic wind stress curls are found, such as Cabo Verde (Chavanne et al., 2002), the Canary islands (Barton et al., 2000), the Southern California islands (Dong and McWilliams, 2007), the gulfs of Tehuantepec and Papagayo (McCreary et al., 1989) or the gulf of Aden (Fratantoni et al., 2006).

SST fronts developed in response to the straining of SST by the velocity field, triggering frontolytic secondary circulations to restore the thermal-wind balance. The front was divergent ($\sim 0.2f$) and anticyclonic ($\sim -0.25f$) on its warm side, and convergent ($\sim -0.25f$) and cyclonic ($\sim 0.15f$) on its cold side. Such processes may strongly affect the oceanic primary production (Lévy et al., 2001; Lapeyre and Klein, 2006) and the upper ocean stratification (Lapeyre et al., 2006). Submesoscale structures are widespread in the ocean (e.g. Flament et al. (1985); Munk et al. (2000)), yet they are not resolved by global ocean circulation models. More observational and numerical work is required to fully understand their dynamics and parametrize their effects on the oceanic and atmospheric circulations.

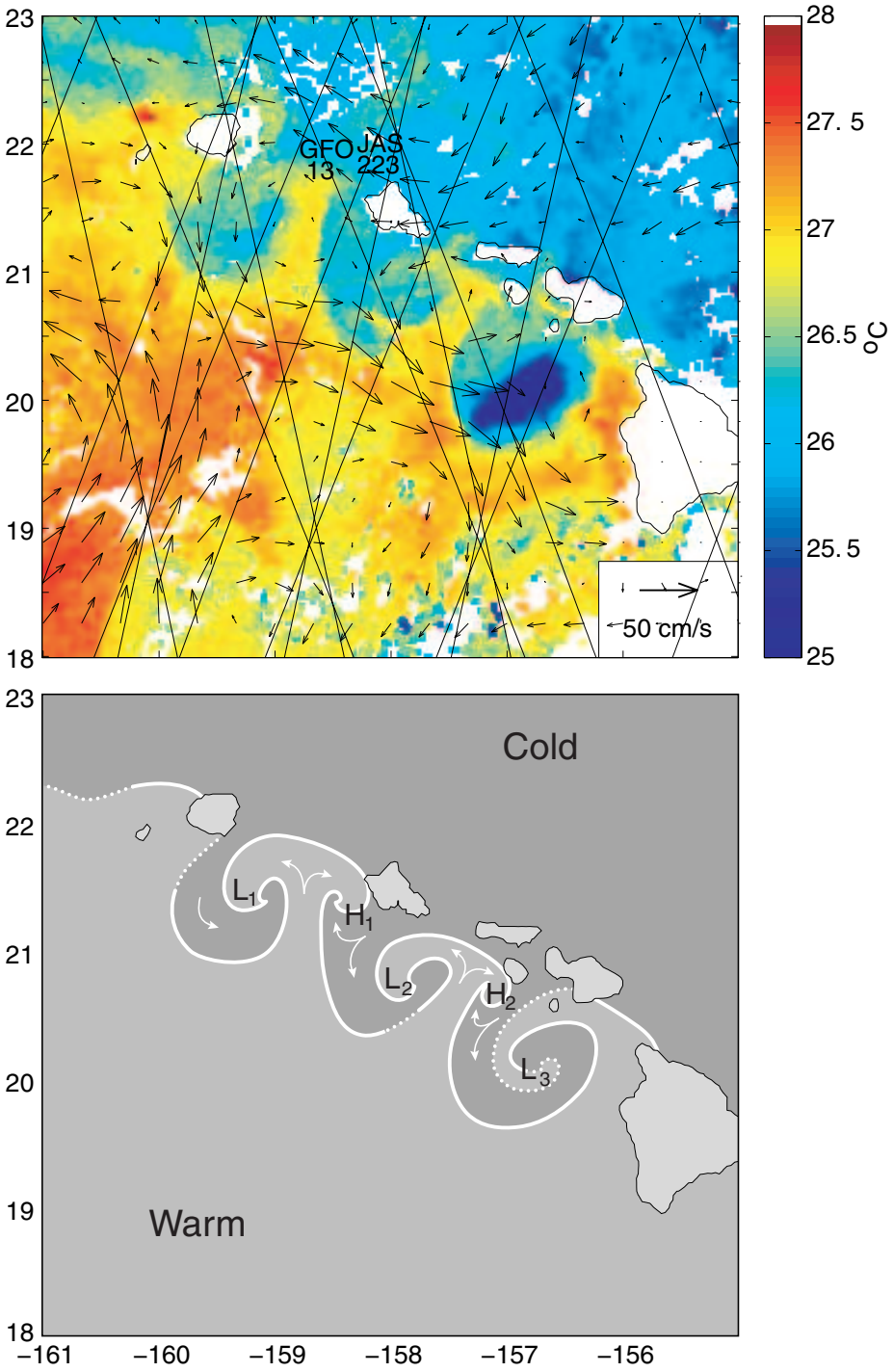

Figure 5.1: (a) AVISO surface geostrophic currents for October 23 to 30, 2002, overlaid on a composite of sea surface temperature from Aqua and Terra MODIS for October 26, 2002. The tracks of the Jason-1, ERS-2, GFO and Topex/Poseidon satellites used in AVISO processing are shown in black lines. (b) Sketch of the main SST and circulation features (H: anticyclones, L: cyclones).

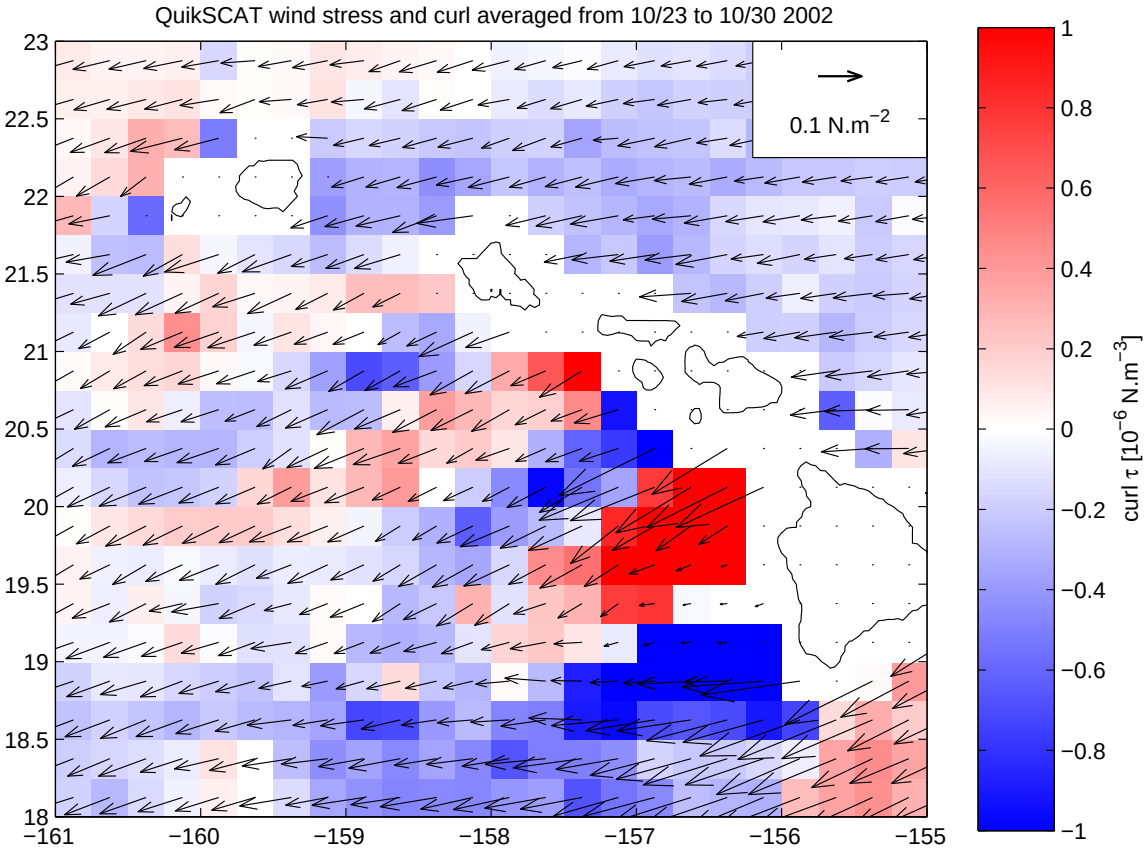

Figure 5.2: Wind stress vectors and curl from QuikSCAT at 25 km resolution, averaged from October 23 to 30, 2002.

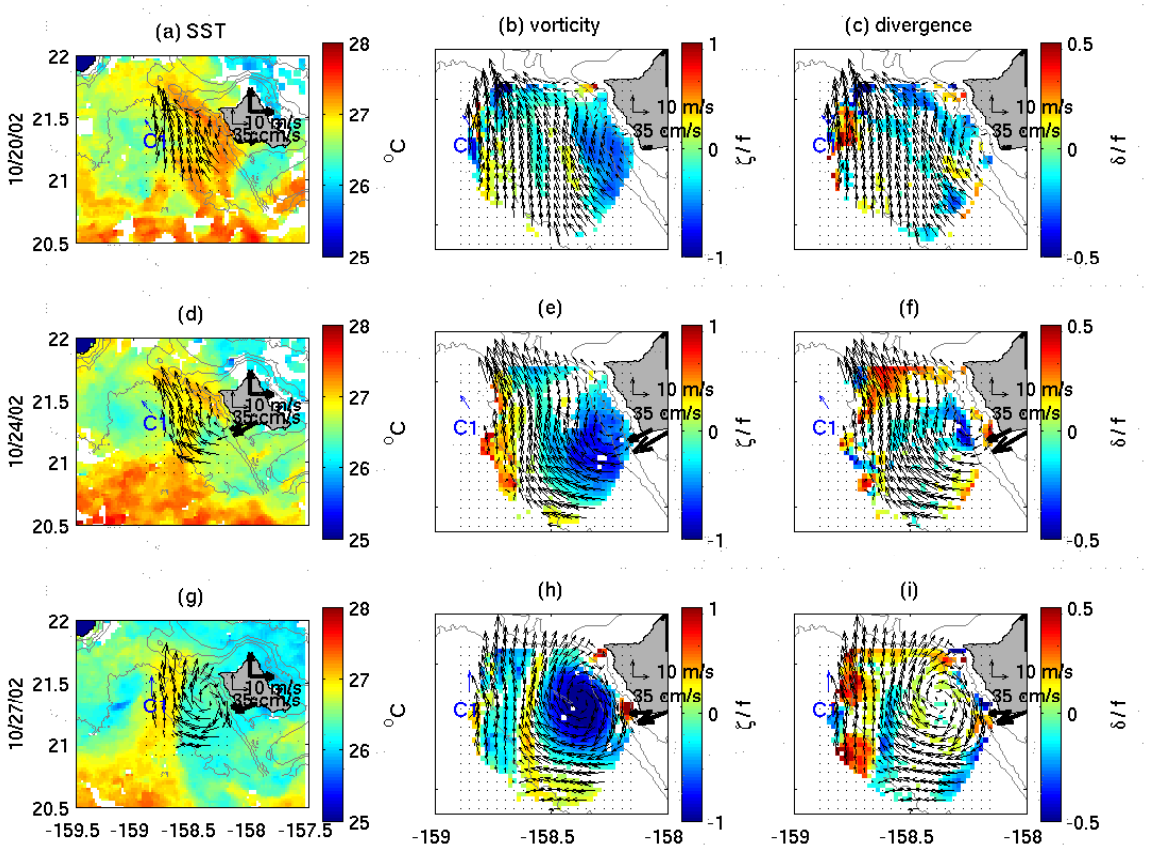

Figure 5.3: Snapshots of lowpass filtered currents (black: HFRs; blue: ADCP) and 10m-height wind at Honolulu (thick black), overlain on (left panels) sea surface temperature from MODIS, (middle panels) vorticity, and (right panels) divergence, shown only when above 95% confidence intervals and normalized by f, for (a, b, c) Oct 20, (d, e, f) Oct 24, (g, h, i) Oct 27, (j, k, l) Oct 31, (m, n, o) Nov 3, and (p, q, r) Nov 7. Gray lines are bathymetric contours at 500m, 1000m, 2000m and 4000m.

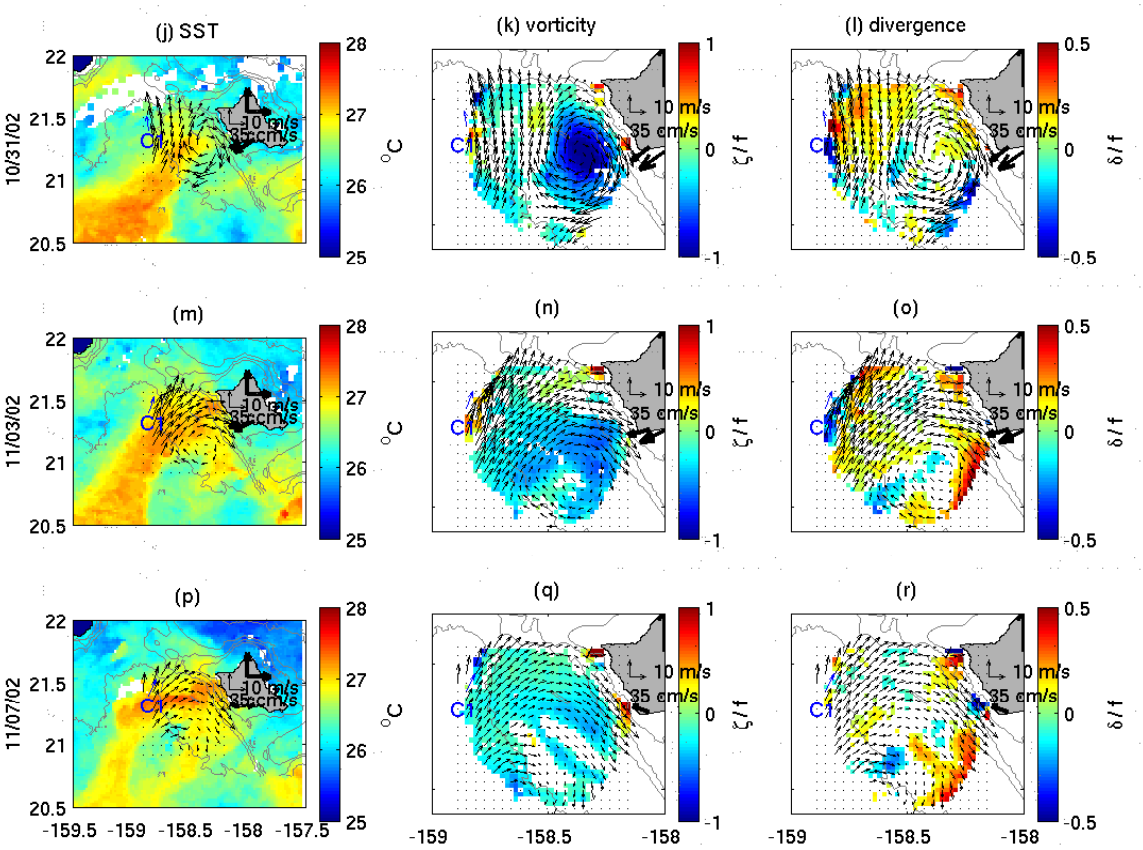

Figure 5.4: Fig. 5.3 continued.

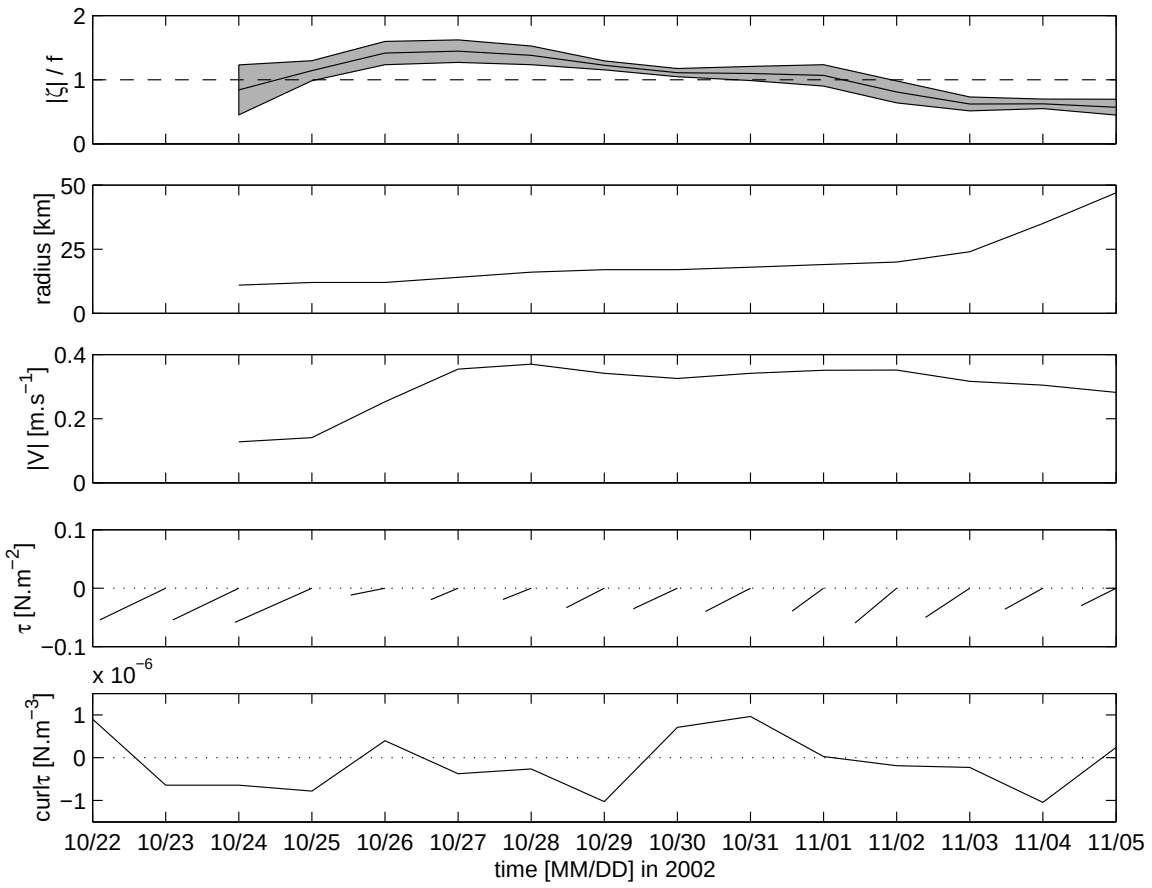

Figure 5.5: Time-series of (a) maximum core vorticity (in absolute value) normalized by f (solid line) and 95% confidence intervals (gray shading), (b) core radius, (c) maximum azimuthal velocity (in absolute value), (d) wind stress interpolated from QuikSCAT observations at vortex center, and (e) wind stress curl estimated by least-square fit at vortex center.

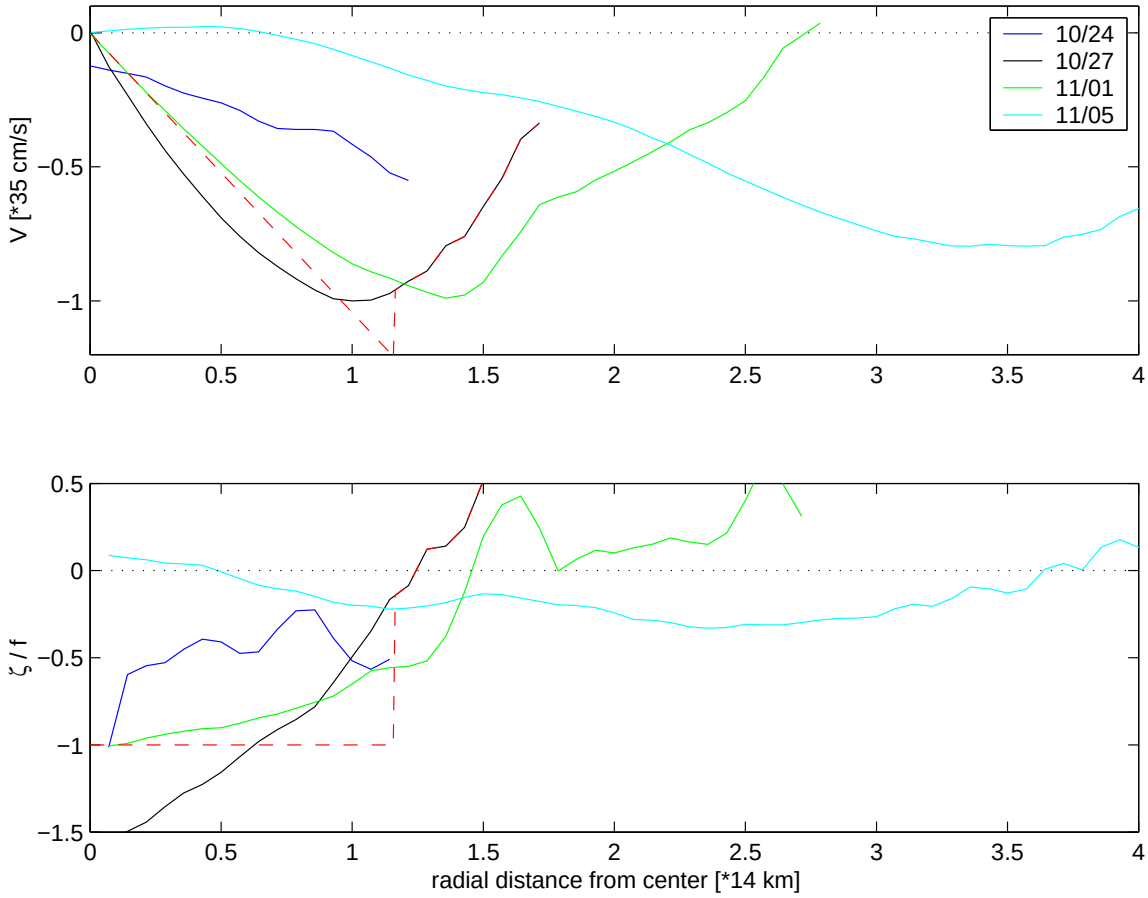

Figure 5.6: Evolution of azimuthally-averaged radial profiles of (a) azimuthal velocity, and (b) vorticity normalized by f. The model of Kloosterziel et al. (2007) is shown as red dashed lines.

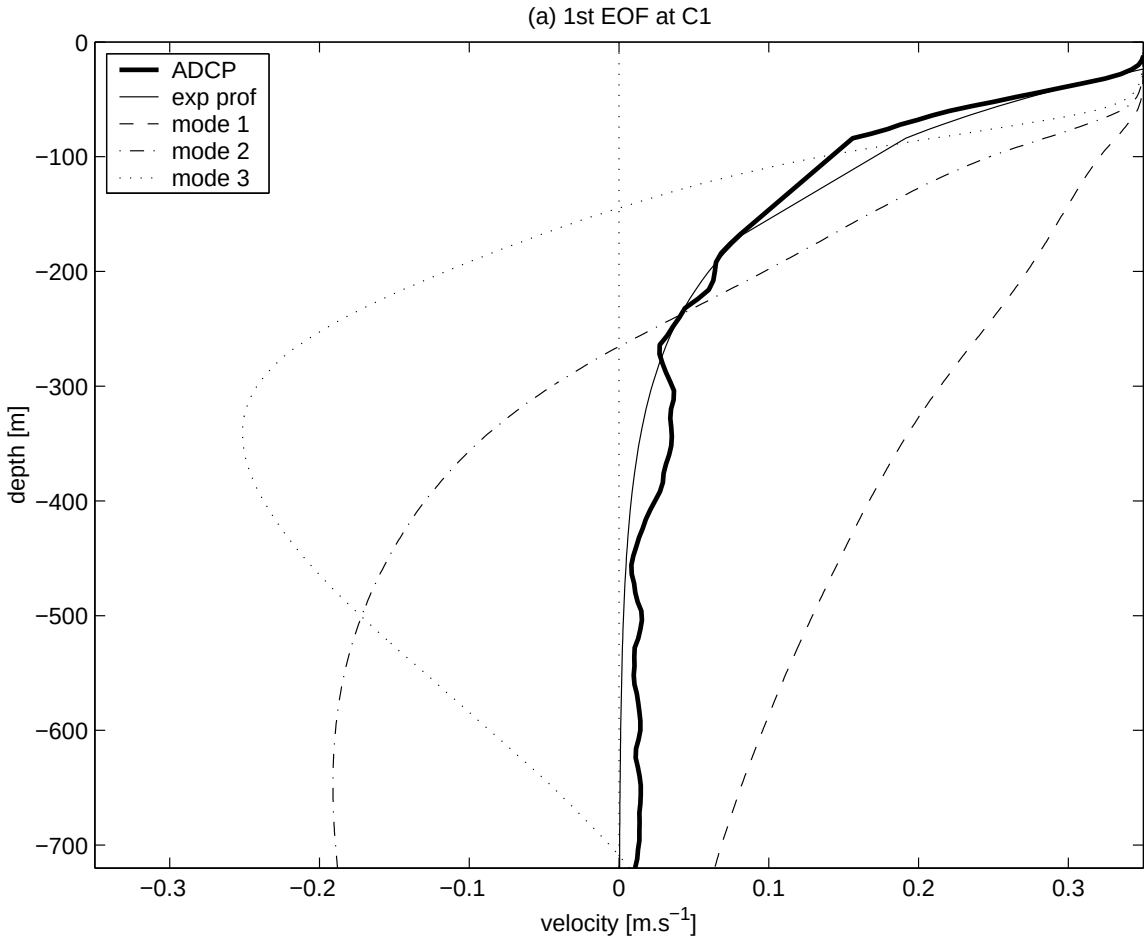

Figure 5.7: Vertical profile of the first EOF amplitude of horizontal currents at C1 (thick line), exponential fit (thin solid line), and first three normal modes (discontinuous lines, computed from HOT climatological stratification for Sep-Nov).

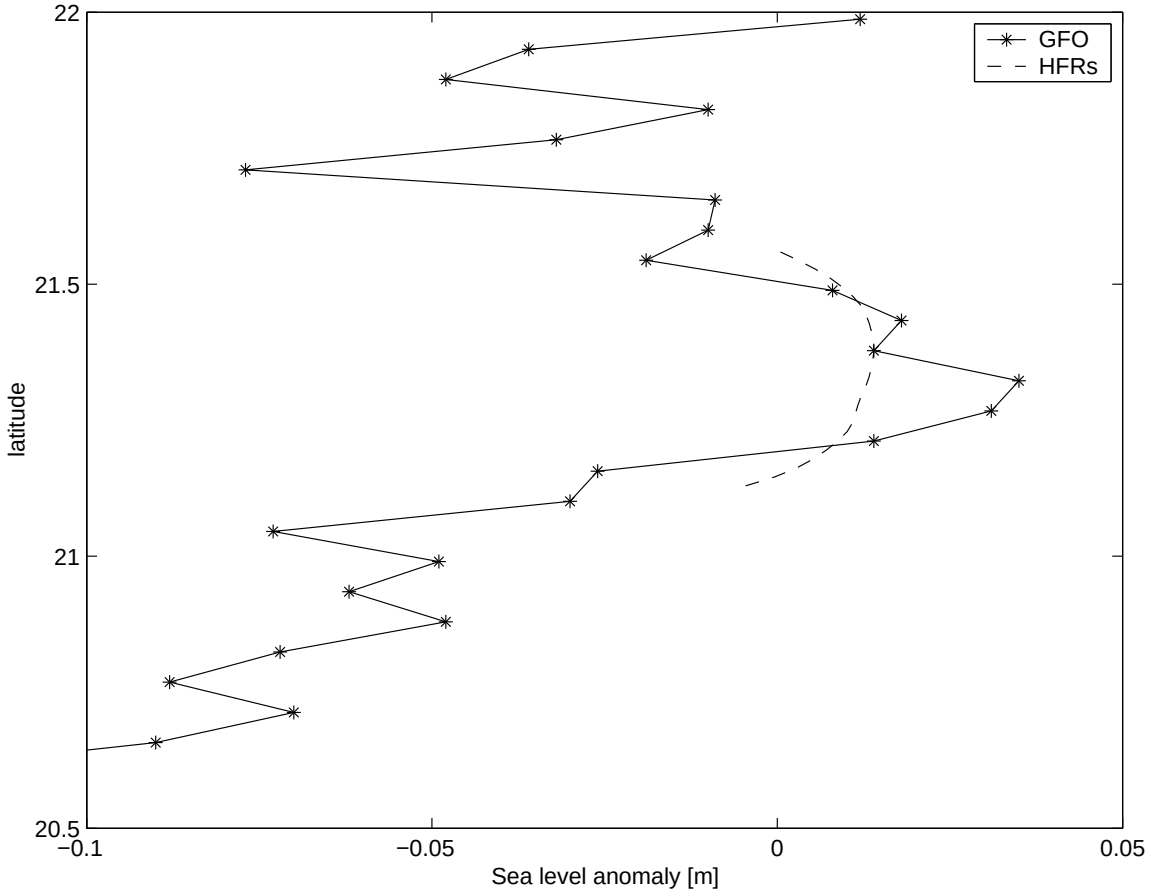

Figure 5.8: Sea Level Anomaly (in m) along GFO track 13, on Oct 27 at 5 UTC (solid line) and computed from the HFRs currents assuming cyclo-geostrophic balance (dashed line, reference height arbitrary).

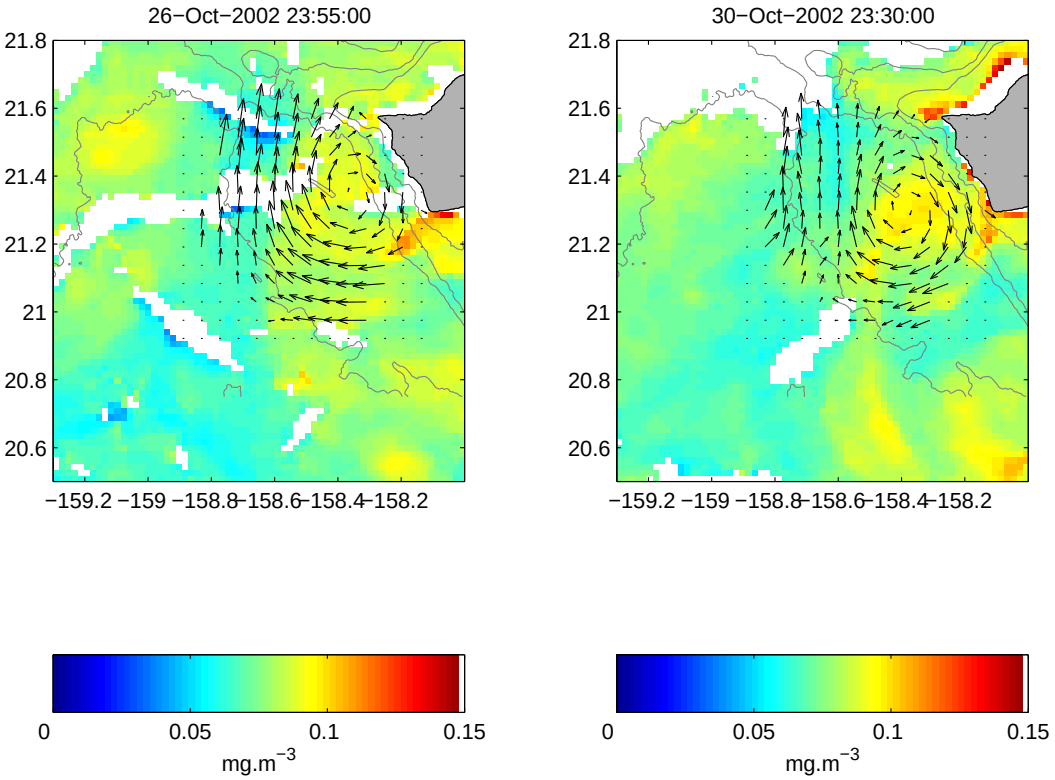

Figure 5.9: Chlorophyll a concentration (in $mg.m^{-3}$) from MODIS onboard Aqua, on (a) Oct 26 at 23:55 UTC, and (b) Oct 30 at 23:30 UTC. Overlaid are the corresponding lowpass-filtered surface currents.

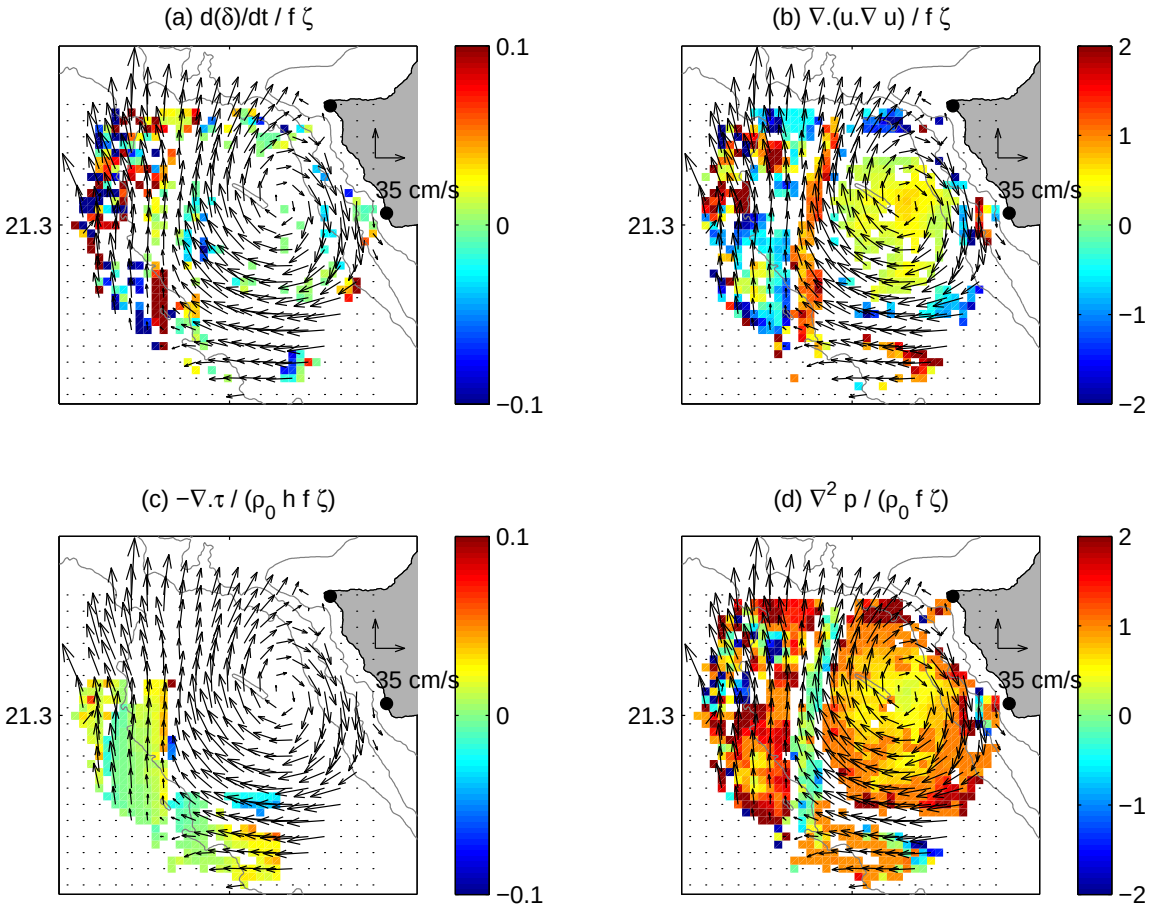

Figure 5.10: Magnitudes of the divergence equation (5.4.6) relative to the Coriolis term $f\zeta$, shown only when above the 95% confidence intervals.

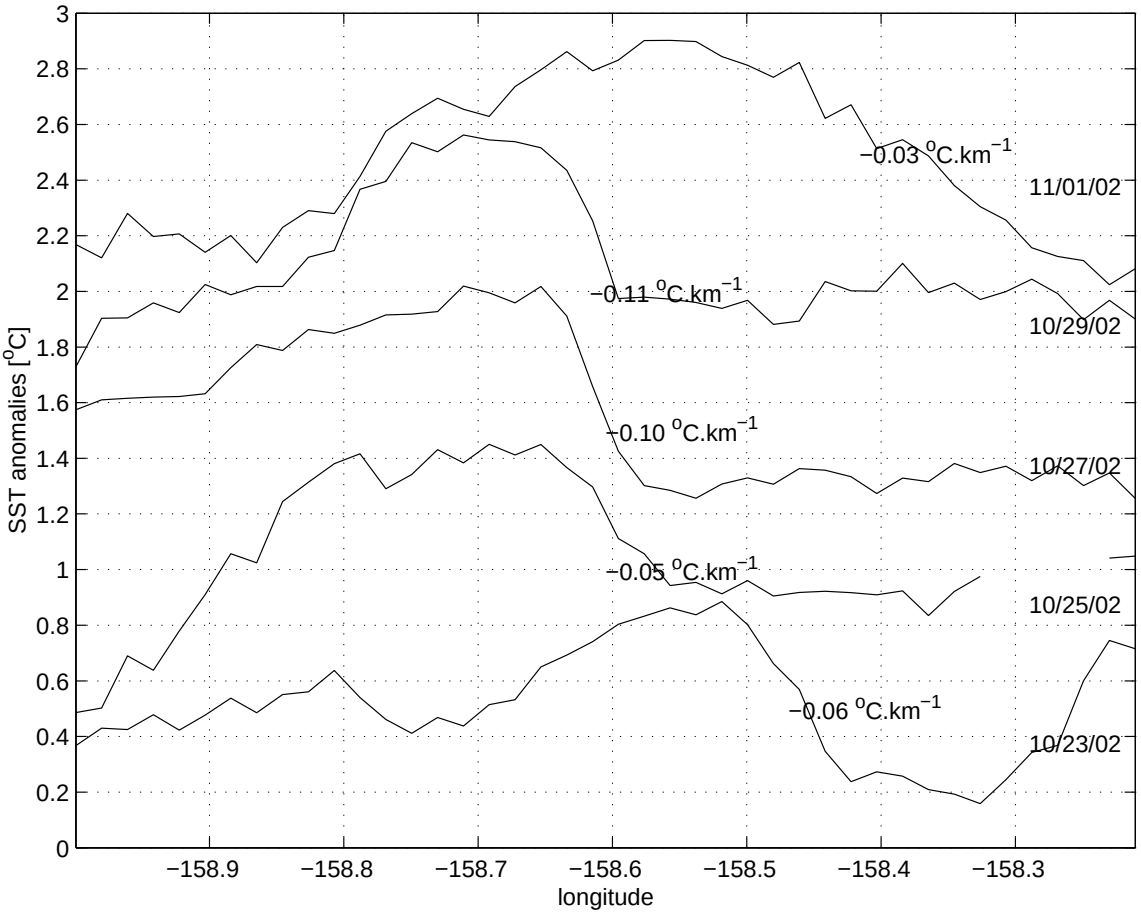

Figure 5.11: Evolution of the SST front along zonal sections averaged between 21.2N and 21.4N. Zonal averages have been removed, and the profiles have been shifted by 0.5^oC for clarity.

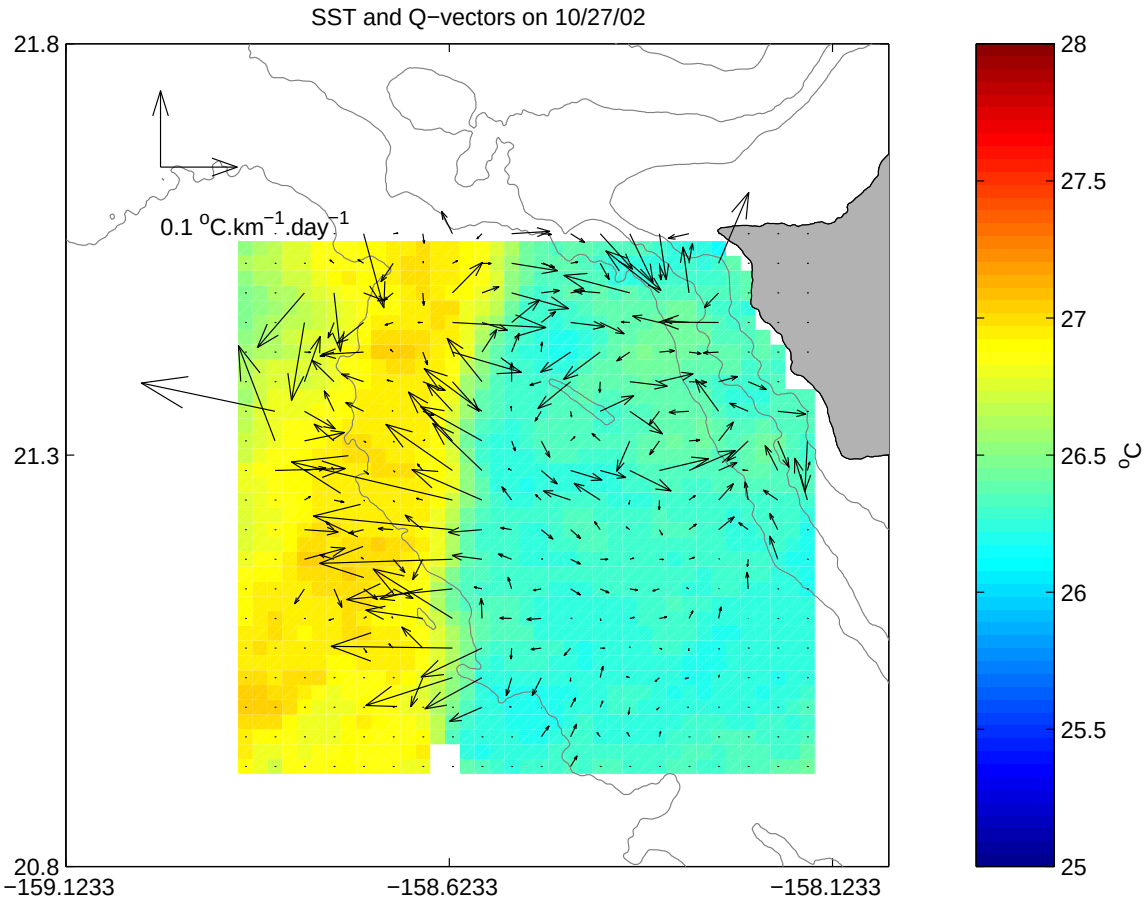

Figure 5.12: Q-vectors overlain on SST on Oct 27.

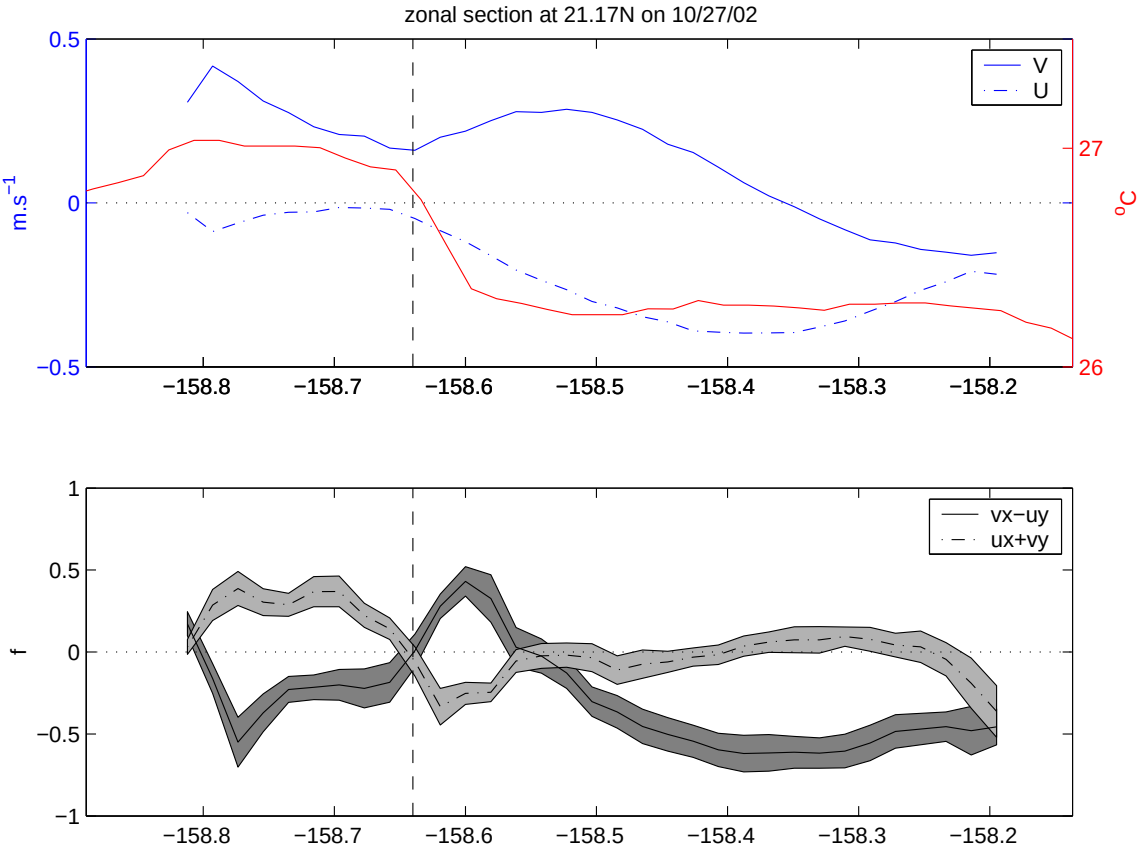

Figure 5.13: Zonal section at $21.17N$ of (a) zonal (dash-dot blue line) and meridional (solid blue line) current and SST (red line), and (b) vorticity (solid line) and divergence (dash-dot line), with 95% confidence intervals (gray shadings).

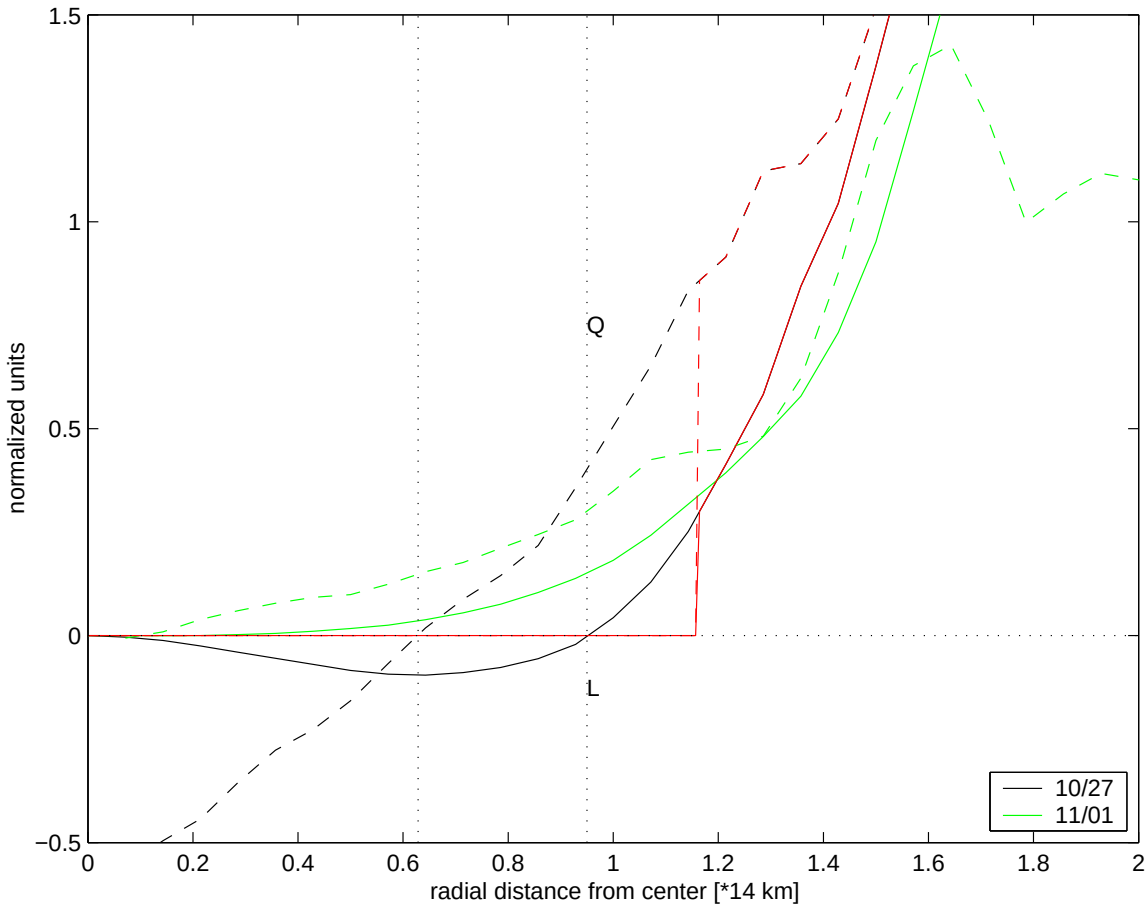

Figure 5.14: Radial profile of absolute angular momentum (solid lines) and absolute vorticity (dashed lines), in normalized units, for Oct 27 (black) and Nov 1 (green). The model of Kloosterziel et al. (2007) is shown in red. The vertical lines indicate the range satisfying the modified Rayleigh criterion of instability.

Chapter 6

Conclusions

When internal tides propagate through energetic inhomogeneous background currents, their amplitude, phase and trajectories are modulated by horizontal and vertical refraction, Doppler shifting, and energy exchange with the background currents. Recent studies have started to document these interactions in particular areas such as the South China Sea (Park and Watts, 2006), the Hawaiian archipelago (Rainville and Pinkel, 2006b), or the South Brazil Bight (Pereira et al., 2007). Our observations document another area, the northwestern Adriatic Sea, and revisit the Hawaiian archipelago at finer scales than previously studied, by focusing on an area of strong internal tides generation, the Kauai Channel. We complement the results of Rainville and Pinkel (2006b) by showing that the tides are significantly affected by the surface intensified mesoscale variability already at the first surface reflexion of internal tidal beams. The net effect of mesoscale variability over long periods of time is to low-pass filter the vertical modes of internal tides, the resulting surface pattern resembling that one would obtain from the summation of only the first few lowest vertical modes.

What are the implications of these results on tidal energy budgets ? The fast barotropic tide is not affected by mesoscale variability, therefore the barotropic energy loss is well constrained by models assimilating satellite observations (Egbert and Ray, 2000, 2001). Zaron and Egbert (2007) have shown that internal tides have a negligible impact on the barotropic tidal fields inferred from those assimilations. The latest estimation for the Hawaiian Ridge (Zaron and Egbert, 2006a) finds that $17^{+5}_{-1.5} GW$ of M_2 barotropic tidal energy are lost within 250 km of the ridge.

The slower internal tides, however, are affected by mesoscale variability, therefore estimations from satellite observations assimilation should be considered as lower bounds, due in part to the non-phase-locked energy not captured by the altimeters (Ray and Mitchum, 1997; Ray and Cartwright, 2001). However, since the baroclinic energy fluxes radiating away from the Hawaiian ridge are dominated by the lower modes (St. Laurent and Nash, 2004), which are not affected much by the mesoscale variability close to the ridge (Rainville and Pinkel, 2006b), estimates of the energy radiated away from the ridge as low mode internal tides should not be too sensitive to mesoscale variability. Zaron et al. (2008) finds that assimilating the phase-locked M_2 HF-radio observations into PEZHAT decreases the energy fluxes radiating away from the Kauai Channel ridge by only $\sim 10\%$. Ray and Cartwright (2001) estimate that ~ 6 GW are radiated from the Hawaiian Ridge into M_2 mode-1 internal tides, a value similar to that from the non-assimilating model of Merrifield and Holloway (2002), who found that ~ 10 GW were radiated for all modes, 60% of which was accounted for by mode 1. However, Carter et al. (2007) recently found that increasing the resolution from 4 km to 1 km over a smaller area encompassing the main Hawaiian islands (excluding the Island of Hawai‘i) lead to an increase of $\sim 40\%$ in energy converted to M_2 internal tides, as compared to Merrifield and Holloway (2002) estimation, which would give ~ 14 GW if extrapolated to the entire ridge. It is not known whether further increase in resolution would lead to higher estimates, therefore this part of the energy budget is still poorly known.

What about the remainder of the budget, usually attributed to local dissipation ? The present study shows that interactions of internal tides with mesoscale currents cannot be neglected if one wants to quantify how much energy not radiated away from the ridge as low-mode internal tides is locally dissipated, and what is the distribution of dissipation in the water column. Energy transfers occur between internal tides and mesoscale currents near the surface, which could provide another source or sink of local energy. Also, the strong increase of internal tide energy near the surface in the presence of mesoscale currents such as the cyclone observed in October 2002, could lead to breaking and dissipation near the surface. Althaus et al. (2003) observed strong dissipation near the surface close to the first surface reflexion of a tidal beam to the north of the Mendocino Escarpment. They attributed it to the energy amplification by the strong stratification near the surface,

which was particularly strong during their experiment due to the 1997 El Niño. Near-surface stratification increases due to mesoscale currents should also be taken into account. Furthermore, intrinsic frequency Doppler-shifting and effective Coriolis frequency modulation by mesoscale currents (Kunze, 1985) could lead to absorption of internal tides at critical layers near the surface, transferring energy to the mesoscale currents and increasing local dissipation by wave breaking. At the latitude of Hawai‘i, this is not likely to happen for semi-diurnal tides, but could happen for diurnal tides in the presence of strongly sheared mesoscale currents. If parametric subharmonic instability transfers some energy from M_2 to $M_2/2$, as observed by Carter and Gregg (2006) within a tidal beam emanating from the northern edge of Ka‘ena Ridge, then shifts of the effective Coriolis frequency to $M_2/2$ could lead to rapid dissipation of energy, as observed by phase-locked altimetry observations (Kantha and Tierney, 1997) and predicted in the absence of mesoscale currents (MacKinnon and Winters, 2005) around 29^o of latitude, where $f = M_2/2$.

All these phenomena could increase the local sinks of energy in the surface layer, leaving less energy to be dissipated at depth near the ridge, as shown schematically in Fig. 6.1. Estimations of energy dissipated at depth (ie below the first 100m) over the Hawaiian Ridge could indeed be too low to close the energy budget: Klymak et al. (2006) estimate $3^{+1.5}_{-1.5}$ GW to be dissipated within 60 km of the ridge, and Martin and Rudnick (2007) find an upper limit of $6^{+3}_{-2} GW$ within 50 km of the ridge. Using Zaron and Egbert (2006a) estimate of barotropic M_2 energy loss and $10 - 14$ GW of energy radiated into M_2 internal tides, we have $1.5 - 12$ GW of M_2 energy available for mixing. Adding the contributions from the other tidal constituents, as well as from inertial and mesoscale energy, we see that the observed dissipation could be insufficient. Closing the energy budget will require to reduce the uncertainties, and to include the effects of inertial, submesoscale and mesoscale currents onto internal tides propagation.

The challenge is to adequately reproduce the energetic mesoscale and submesoscale circulation in the vicinity of the Hawaiian islands. Our observations show that the variability is much richer than what altimetric observations can resolve. High resolution will be required to accurately model the background circulation in which the tides propagate, both for the ocean model itself and for the atmospheric forcing used, since details in the wind field are important to reproduce the observed circulation features in the Hawaiian

archipelago (Chavanne et al., 2002). As a first step, one could simply put a balanced vortex as background state into a numerical model of the tides, to study its effect on tides propagation, especially to check whether parametric subharmonic instabilities and critical layers can occur, and quantify their effect on local dissipation. Then, the net effect of mesoscale currents onto the tidal energy budget could be addressed statistically by using numerical simulations resolving both the tides and the mesoscale dynamics. For example, Horsburgh and Hill (2003) used a modified version of POM to study the mesoscale circulation and the interactions with tides in the Irish Sea. Recently, Pereira et al. (2007) studied observationally and numerically the effect of the Brazil Current on internal tides in the South Brazil Bight. They concluded that "in regions of strong baroclinic flows, internal tides may not be investigated independently of the background flows if the internal tide field and associated mixing are to be properly accounted for". Our results reinforce their conclusion, and show that the western boundary currents are not the only places where background flows may matter for internal tides.

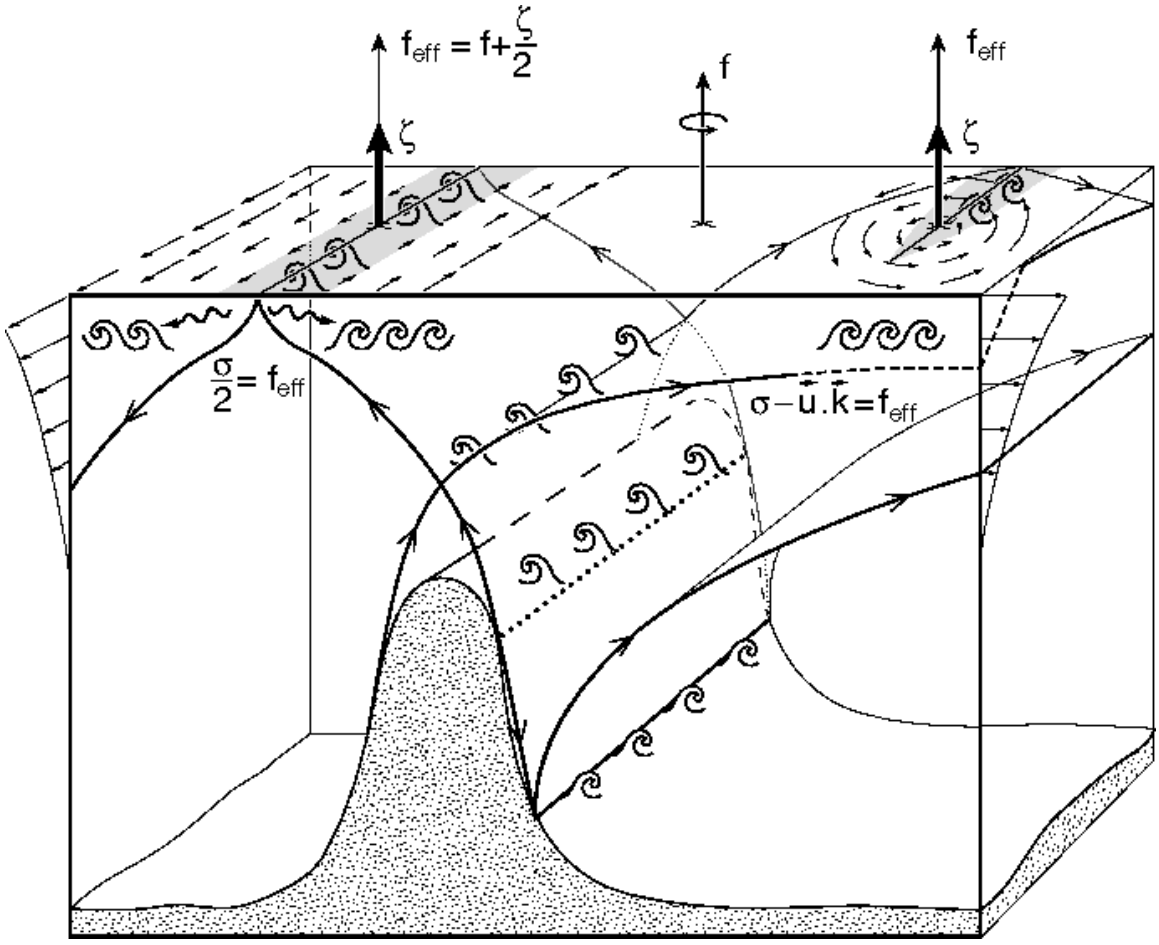

Figure 6.1: Schematic representation of possible mixing locations (indicated by breaking waves) for internal tide beams generated on the flanks of an ocean ridge, in the presence of horizontally and vertically sheared mesoscale currents. Mixing can occur at depth: at the generation location, at the bottom reflexions, at beams crossings (where energy increases); and near the surface: at the surface reflexions (indicated by shaded areas), at critical levels where the intrinsic frequency is Doppler-shifted low to the effective Coriolis frequency value, or at critical levels for half-frequency waves generated by parametric subharmonic instability.

Appendix A

Data processing

A.1 Radial currents processing

For the linear arrays, beam-forming is performed by adding the antenna signals with appropriate phase shifts, to steer the beam in the desired direction, and Hamming windowing to reduce side lobes, (Gurgel et al., 1999). The azimuthal resolution depends on the aperture of the receive array, which is $\frac{2cos(\theta)}{(N-1)}$ for N antennas linearly spaced at half the electromagnetic wavelength, and a steering angle θ relative to the normal to the array. For 16 antennas, it varies from 7^o for $\theta = 0^o$ to 15^o for $\theta = 60^o$. For a given direction and range, the energy spectrum of the echoes contains two peaks due to Bragg waves advancing to and receeding from the receiver. The radial current is determined from the offset of the peak frequencies from the theoretical Doppler shift for the deepwater waves (Paduan and Graber, 1997). Spectral lines around the peak frequencies, weighted by their signal-to-noise ratio, are used to compute the average radial current and its standard deviation, a measure of accuracy. A threshold of 4 cm/s on the accuracy was used to eliminate outliers.

For the square arrays, direction-finding is performed for each spectral line by comparing the phases of the signals from the 4 receive antennas (Essen et al., 2000). This requires that the radial speed uniquely depends on the azimuth (Gurgel et al., 1999), which is satisfied for uniform coastal currents flowing parallel to the coast, but could be violated for spatially variable flows. For a given range, a mapping between radial current values and directions results. The radial current values are then sorted by azimuth, and the average radial current and its standard deviation are computed for each azimuthal bin. The number

of available current estimates differs for various azimuths, therefore the standard deviation of radial currents is not a reliable estimate of accuracy. A threshold of 3 cm/s was used to eliminate some outliers, but further statistical filtering was required.

Spatio-temporal intervals, 6 km in range, 6 degrees in azimuth, and 4 hours in time (a compromise between statistical robustness and M_2 retrieval) were defined for each direction finding site. The median and standard deviation of the radial currents were computed for each interval, providing a robust estimate of the radial current. A threshold of 15 cm/s was used on the radial current standard deviation to remove remaining outliers, and intervals with too few data were discarded. In addition, there were groups of ranges contaminated by 50 Hz interferences and their harmonics in the Doppler spectra. Those ranges have been completely masked. Finally, each radial current map was bilinearly spatially interpolated.

To assess the azimuthal accuracy of the radars, calibrations were conducted in July 2003 by transmitting a fixed frequency signal from a boat following circles of 5km radius around each radar. The received signals were processed with beam-forming or direction-finding algorithms to infer the incoming direction, and compared with the true direction from GPS positions of the boat. Errors in azimuth were smaller than 5 degrees with a median offset of 2 degrees for the beam-forming site, and smaller than 10 degrees with a median offset of 2 to 4 degrees for the direction-finding sites. Corrections did not lead to significant improvement of the correlation of radial currents between pairs of sites (see Appendix B), and therefore were not applied.

A.2 Vector currents processing

Vector currents were estimated on a 5-km (and 2-km in Chapter 5) Cartesian grid by least-square fitting zonal and meridional components to all radial measurements from at least two sites within a 5-km (3-km in Chapter 5) search radius (Lipa and Barrick, 1983; Paduan and Cook, 2004). The normal component is poorly constrained near the baseline between two sites and the azimuthal component is poorly constrained far from the sites, yielding a Geometric Dilution Of Precision (GDOP, Chapman et al. (1997)). It can be estimated as follows (Gurgel, 1994; Barrick, 2002).

The current is assumed to be constant within the search radius, where N radial measurements are available:

$$m_i = n_{ix}u + n_{iy}v + e_i \qquad i = 1, ..., N \tag{A.2.1}$$

or

$$\mathbf{m} = \mathbf{N}\mathbf{w} + \mathbf{e} \tag{A.2.2}$$

where **m** is the $N \times 1$ vector of radial measurements, **N** the $N \times 2$ matrix of the unit radial vectors, $\mathbf{w} = [u, v]^T$ the current vector, and **e** the $N \times 1$ vector of measurements noise and model errors.

An estimate of **w** can be obtained by minimizing the sum of squared errors:

$$J = \sum_{i=1}^{N} e_i^2 = \mathbf{e}^T\mathbf{e} \tag{A.2.3}$$

The solution is (e.g. Wunsch (2006), pp. 43-46):

$$\tilde{\mathbf{w}} = \left(\mathbf{N}^T\mathbf{N}\right)^{-1}\mathbf{N}^T\mathbf{m} \tag{A.2.4}$$

provided that $\left(\mathbf{N}^T\mathbf{N}\right)^{-1}$ exists.

The covariance of $\tilde{\mathbf{w}}$ is:

$$\begin{aligned} \mathbf{C}_{\tilde{\mathbf{w}}\tilde{\mathbf{w}}} &= \left\langle (\tilde{\mathbf{w}} - \langle\tilde{\mathbf{w}}\rangle)(\tilde{\mathbf{w}} - \langle\tilde{\mathbf{w}}\rangle)^T \right\rangle \\ &= \left(\mathbf{N}^T\mathbf{N}\right)^{-1}\mathbf{N}^T\mathbf{C}_{\mathbf{ee}}\mathbf{N}\left(\mathbf{N}^T\mathbf{N}\right)^{-1} \end{aligned} \tag{A.2.5}$$

where brackets indicate ensemble averaging, and $\mathbf{C}_{\mathbf{ee}} = \left\langle (\mathbf{e} - \langle\mathbf{e}\rangle)(\mathbf{e} - \langle\mathbf{e}\rangle)^T \right\rangle$ is the covariance of **e**.

If the errors are independent of each other and have the same variance σ^2, then:

$$\mathbf{C}_{\mathbf{ee}} = \sigma^2\mathbf{I} \tag{A.2.6}$$

where **I** is the unit matrix.

The covariance of $\tilde{\mathbf{w}}$ becomes:

$$\mathbf{C}_{\tilde{\mathbf{w}}\tilde{\mathbf{w}}} = \sigma^2\left(\mathbf{N}^T\mathbf{N}\right)^{-1} \tag{A.2.7}$$

This expression for $\sigma = 1$ is the GDOP. The principal axes of $\mathbf{C}_{\tilde{\mathbf{w}}\tilde{\mathbf{w}}}$ are shown in Fig. 2.2 for different geometric configurations in the Adriatic, and in Fig. 3.2 for Hawai'i. In the Adriatic, with only two sites, the vector currents cannot be estimated reliably over large areas. A third site is then needed to improve vector currents estimation.

In the present processing, currents were discarded when the largest eigenvalue of $\mathbf{C}_{\tilde{\mathbf{w}}\tilde{\mathbf{w}}}$ exceeded 0.5 in the Adriatic and 1 in Hawai'i, and were instead bilinearly interpolated from neighboring grid points. These rather restrictive values were chosen because the errors of neighboring measurements from the same radar are not truly independent.

A.3 Temporal interpolation

The diurnal modulation of data coverage biases the estimation of power spectra and least-square analysis of constituents synchronized with or not separable from S_1, such as S_2 and K_1, which differs from S_1 by only 1 cycle per year (see Table 2.1). A formal attempt at demodulating the estimated spectra is attempted in Appendix F. The major flaw of the method is that the resulting spectra can have negative values at some frequencies. Therefore, an ad-hoc method was followed instead, as described below.

Most missing data segments are shorter than a day, but long enough to preclude linear interpolation. The main variability for periods shorter than a day is tidal (M_2 and K_1) and inertial with a period of 33 hours at 21N and 17 hours at 44.5N. A constant and sinusoids at M_2, K_1 and inertial frequencies were least-square fitted to the observations available in a 3-day window centered on each missing data segment shorter than 16 hours. The fit was performed only if more than 24 observations were available. A linear trend was added to match the interpolation with the observations on the edges of each segment. This interpolation was carried out on the radial and vector currents separately. Vector currents were not estimated from the interpolated radial currents, to avoid spurious tidal variability arising from geometric dilution of precision. The least-square analysis was carried on the interpolated time series.

To estimate the power spectra of the time series, their mean was removed and the remaining missing data segments were replaced by zeros. This amounts to multiplying the uninterrupted signal by a missing data function (1 for data and 0 for no data). In

the frequency domain, the Fourier transform of the uninterrupted signal is convoluted with the Fourier transform of the missing data function, resulting in spectral smearing (see Appendix F). To minimize such smearing, continuous data segments shorter than 36 hours were replaced by zeros, and the spectrum was estimated only when data return was greater than 75%. Time series were multiplied by a Blackman window prior to computing their Fourier transform. The spectrum shown in Fig. 2.5 is an average of the spectra at $N = 61$ grid points, and those shown in Fig. 3.5 are averages over $N = 156$ grid points. The 95% confidence intervals are based on an effective number of degrees of freedom of $N/4$, since adjacent grid points are not independent of each other. The number of degrees of freedom was increased for higher frequencies, by splitting the time series into half-overlapping segments. Each segment was demeaned and multiplied by a Blackman window.

Appendix B

Data validation

B.1 Radial currents cross-correlation

Since each HF Radio is an independent instrument, the quality of the radial currents can be assessed by the correlation between radial currents from both sites, which should approach -1 along the baseline joining the two sites, where the radials are in opposite directions, and +1 far offshore, where the radials are almost collinear. If along-baseline and across-baseline current components were uncorrelated with equal variance, the correlation pattern would follow that of the cosine of the angle between the two sites, as shown below.

The components u and v of vector current along and normal to the baseline between two sites (line joining the two sites) are:

$$\begin{cases} u(t) = V(t)cos\theta(t) \\ v(t) = V(t)sin\theta(t) \end{cases} \tag{B.1.1}$$

where V and θ are the vector current magnitude and angle relative to the baseline.

Radial currents in the directions from the sites can be expressed at a particular location by:

$$\begin{cases} v_1(t) = V(t)cos(\theta(t) - \theta_1) \\ v_2(t) = V(t)cos(\theta(t) - \theta_2) \end{cases} \tag{B.1.2}$$

where θ_1 and θ_2 are the directions of the radial components relative to the baseline.

The radial currents cross-correlation coefficient is:

$$r_{12} = \frac{\langle v_1 v_2 \rangle}{\sqrt{\langle v_1^2 \rangle \langle v_2^2 \rangle}} \tag{B.1.3}$$

where brackets indicate time averaging.

The covariance and variances of the radial currents can be expressed in terms of the covariance and variances of u and v:

$$\begin{aligned} \langle v_i v_j \rangle &= \frac{1}{2}\langle u^2 + v^2 \rangle cos(\theta_i - \theta_j) \\ &+ \langle uv \rangle sin(\theta_i + \theta_j) \\ &+ \frac{1}{2}\langle u^2 - v^2 \rangle cos(\theta_i + \theta_j) \qquad (i,j) = (1,2) \end{aligned} \tag{B.1.4}$$

Along the baseline, $\theta_1 = 0$ and $\theta_2 = \pi$, yielding $r_{12} = -1$. Far from the radars, $\theta_1 \to \frac{\pi}{2}$ and $\theta_2 \to \frac{\pi}{2}$, yielding $r_{12} \to +1$.

If u and v are uncorrelated and have the same variance, then

$$\langle v_i v_j \rangle = \frac{1}{2}\langle u^2 + v^2 \rangle cos(\theta_i - \theta_j) \qquad (i,j) = (1,2) \tag{B.1.5}$$

yielding

$$r_{12} = cos(\theta_1 - \theta_2) \tag{B.1.6}$$

B.2 Comparisons with ADCPs

Scatterplots of ADCPs 12 m bin and HFRs currents at the closest grid point are shown in Fig. B.1. Correlations are between 0.87 and 0.9 and root-mean-square (rms) differences are between 9.7 and 11.1 cm/s for the radial currents and the zonal currents at C1, but the correlation drops to 0.52 (still significant to 95% confidence) and the rms difference jumps to 19.2 cm/s for the meridional currents at C1, due to geometrical amplification of the errors (see Fig. 3.2). The threshold on GDOP major axis amplitude of 1 was chosen so that the area of vector currents estimation did not extend beyond C1.

Time-series of currents at the moorings locations are shown in Fig. B.2. The HFRs and ADCPs observations are consistent at high frequencies as well as low frequencies. The meridional component at C1 displays periods of good and bad agreement, the latter corresponding to periods of slight differences in the radial currents in the direction from Ka‘ena.

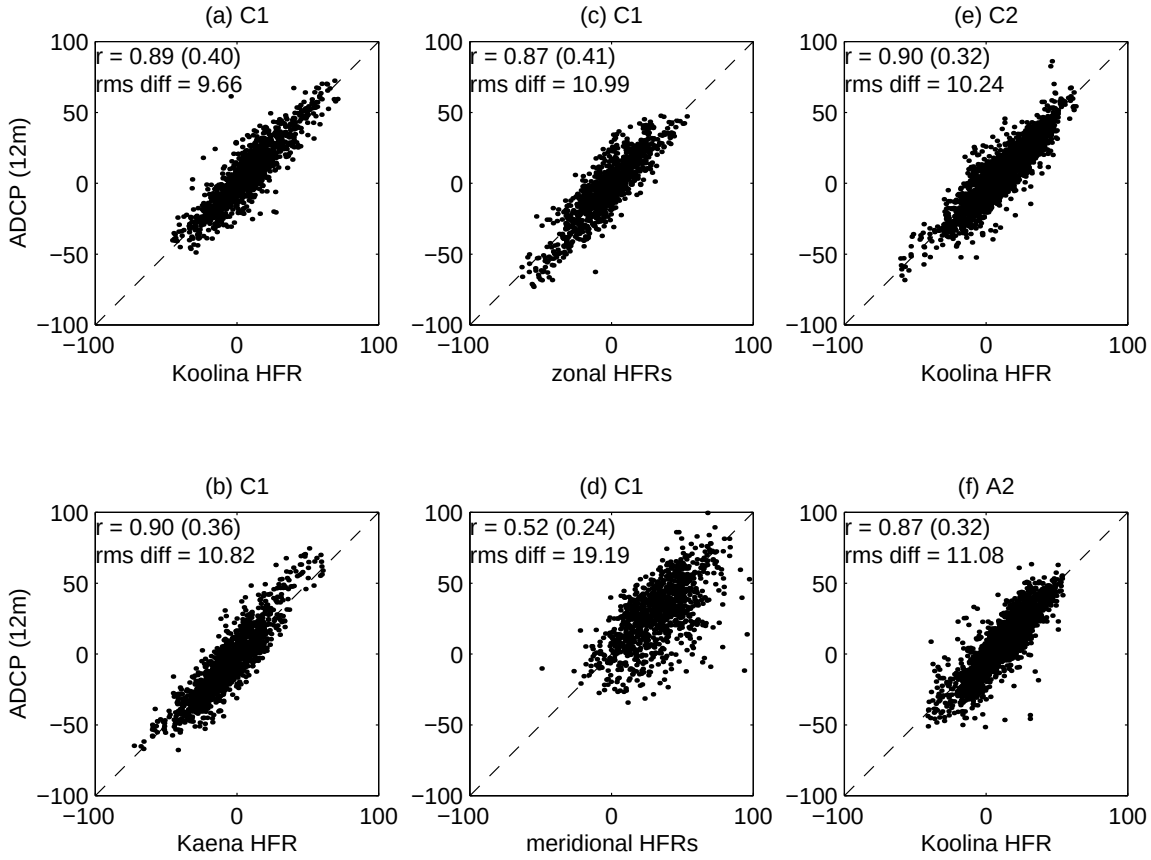

Figure B.1: Scatterplots of ADCPs vs. HFRs currents ($cm.s^{-1}$). ADCPs currents are from the 12 m depth bin. HFRs currents are from the grid points closest to the moorings locations. At C1, ADCPs currents are projected in the directions from Koolina (a) and Kaena (b) and compared with the HFRs radial currents. In addition, the zonal (c) and meridional (d) component of currents are compared. At C2 (e) and A2 (f), ADCPs currents are projected in the directions from Koolina. Correlations (r, the numbers in parentheses indicate the 95% confidence null hypothesis values) and root-mean-square differences (rms diff)are indicated in the top-left corner of each panel.

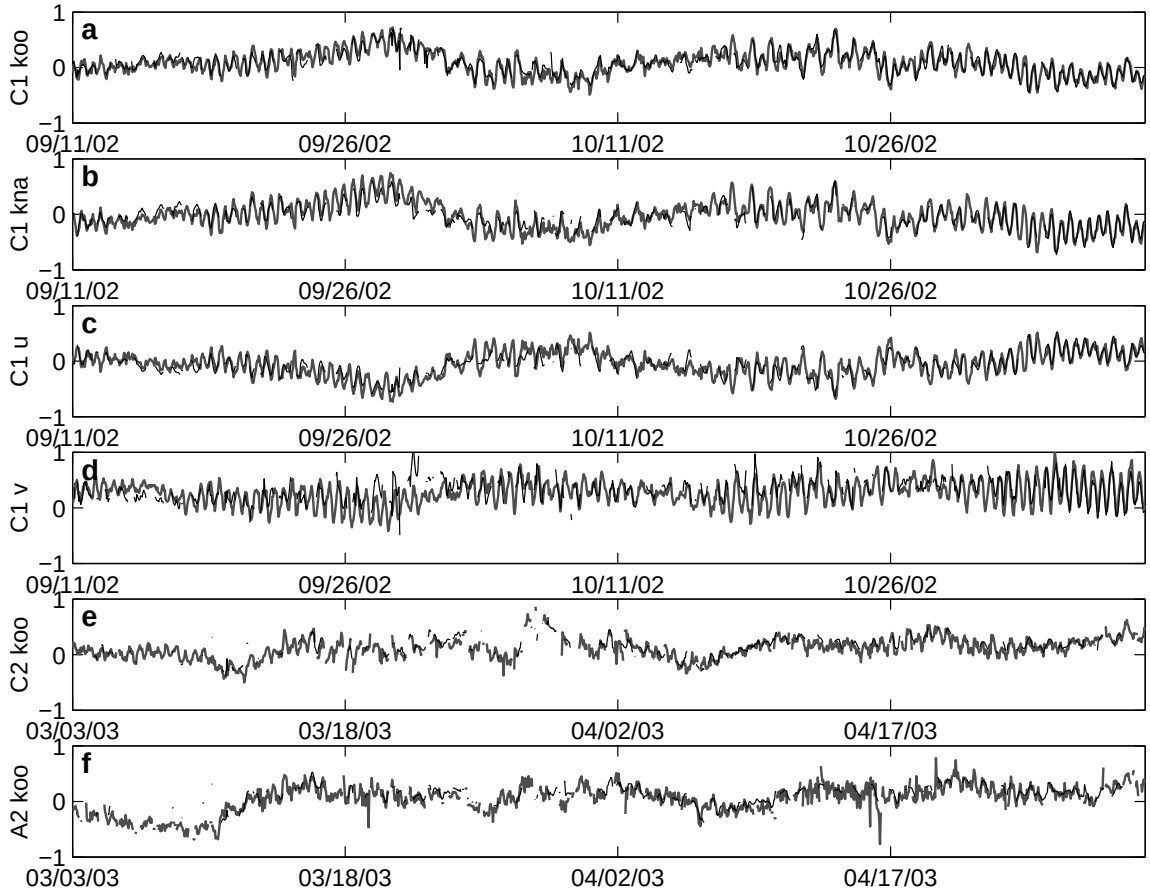

Figure B.2: Same as Fig. B.1, but for the time series. ADCPs data in gray lines, HFRs in black lines.

Appendix C

Ray tracing with hydrostatic approximation

Dispersion relation

Suppose internal waves are governed by the inviscid, hydrostatic, Boussinesq equations linearized around a background state:

$$\frac{Du}{Dt} + u\frac{\partial U}{\partial x} + v\frac{\partial U}{\partial y} + w\frac{\partial U}{\partial z} - fv = -\frac{1}{\rho_0}\frac{\partial p}{\partial x} \quad \text{(C.0.1)}$$

$$\frac{Dv}{Dt} + u\frac{\partial V}{\partial x} + v\frac{\partial V}{\partial y} + w\frac{\partial V}{\partial z} + fu = -\frac{1}{\rho_0}\frac{\partial p}{\partial y} \quad \text{(C.0.2)}$$

$$0 = -\frac{1}{\rho_0}\frac{\partial p}{\partial z} - b \quad \text{(C.0.3)}$$

$$\frac{\partial u}{\partial x} + \frac{\partial v}{\partial y} + \frac{\partial w}{\partial z} = 0 \quad \text{(C.0.4)}$$

$$\frac{Db}{Dt} + u\frac{\partial B}{\partial x} + v\frac{\partial B}{\partial y} - N^2 w = 0 \quad \text{(C.0.5)}$$

where (u, v, w, p, b) are the zonal, meridional, vertical components of velocity, pressure and buoyancy fields describing the internal waves, (U, V, W, B) are the corresponding fields describing the background state, f is the Coriolis parameter, ρ_0 is a reference density, $N^2 = N_0^2 - \frac{\partial B}{\partial z}$ is the buoyancy frequency squared of the background state, N_0 being the buoyancy frequency of the ocean at rest, and $\frac{D}{Dt} = \frac{\partial}{\partial t} + \mathbf{U}.\nabla$ is the material derivative.

This is a closed system of 5 equations for 5 unknowns, with non-homogeneous coefficients. Following Olbers (1981b), when the background state varies on scales much

larger than the internal wavelength, we can neglect the gradients of the background state (except for the contribution of the vertical gradient of buoyancy to the background buoyancy frequency), and solve for local plane waves solution:

$$(u, v, w, p, b) = Re[(u_0, v_0, w_0, p_0, b_0)e^{i(\mathbf{k}.\mathbf{x}-\omega t)}] \tag{C.0.6}$$

where $\mathbf{k} = (k, l, m)$ is the local wavenumber vector and ω is the local frequency.

One obtains the local dispersion relation:

$$\omega = \Omega(\mathbf{k}, \mathbf{x}, t) = \omega_0 + \mathbf{k}.\mathbf{U} \tag{C.0.7}$$

where the intrinsic frequency $\omega_0 = \Omega_0(\mathbf{k}, \mathbf{x}, t)$ satisfies the classic dispersion relation:

$$\omega_0^2 = f^2 + N^2\frac{k^2 + l^2}{m^2} \tag{C.0.8}$$

Locally, the only effects of the background state is to modify the buoyancy frequency (through $\frac{\partial B}{\partial z}$) and to Doppler-shift the frequency of the wave propagating on the background current (the intrinsic frequency).

Propagation and refraction

As the wave propagates through the varying background state, its wavenumber and frequency adjust to satisfy the dispersion relation, and the wave gets refracted. Its trajectory is governed by the propagation equation:

$$\frac{d\mathbf{x}}{dt} = \mathbf{C_g} = \frac{\partial\Omega}{\partial\mathbf{k}} = \mathbf{C_{g0}} + \mathbf{U} \tag{C.0.9}$$

$\mathbf{C_g}$ is the group velocity, and $\frac{d}{dt} = \frac{\partial}{\partial t} + \mathbf{C_g}.\nabla$. The intrinsic group velocity is:

$$\mathbf{C_{g0}} = \frac{\partial\Omega_0}{\partial\mathbf{k}} = (\frac{N^2k}{\omega_0 m^2}, \frac{N^2l}{\omega_0 m^2}, -\frac{\omega_0^2 - f^2}{\omega_0 m}) \tag{C.0.10}$$

Its wavenumber evolution is governed by the refraction equation:

$$\frac{d\mathbf{k}}{dt} = \mathbf{r} = -\frac{\partial\Omega}{\partial\mathbf{x}} = \mathbf{r_0} - k\frac{\partial U}{\partial\mathbf{x}} - l\frac{\partial V}{\partial\mathbf{x}} - m\frac{\partial W}{\partial\mathbf{x}} \tag{C.0.11}$$

$\mathbf{r}$ is the rate of refraction, and the intrinsic rate of refraction is:

$$\mathbf{r_0} = -\frac{\partial\Omega_0}{\partial\mathbf{x}} = -\frac{\omega_0^2 - f^2}{\omega_0 N}\frac{\partial N}{\partial\mathbf{x}} \tag{C.0.12}$$

Finally, the evolution of frequency is governed by:

$$\frac{d\omega}{dt} = \frac{\partial \Omega}{\partial t} \tag{C.0.13}$$

and is zero when we assume that the background flow is steady, or varies on time scales much longer than the time it takes for the waves to propagate through it. These equations are integrated numerically using the fourth-order Runge-Kutta finite differences scheme. The intrinsic frequency evolution can be obtained through Eq. C.0.8 or Eqs. C.0.7 and C.0.13, providing a way to check the accuracy of the numerical scheme. Discrepancies remained below 1%.

Energy evolution

In the hydrostatic approximation ($f^2, \omega_0^2 \ll N^2$), the kinetic energy is well approximated by the horizontal kinetic energy:

$$KE \approx HKE = \frac{1}{2}\rho_0 \overline{|u|^2 + |v|^2} \tag{C.0.14}$$

where the overbar denotes time averaging and $||$ the absolute value. The potential energy is given by:

$$PE = \frac{1}{2}\rho_0 \frac{\overline{|b|^2}}{N^2} \tag{C.0.15}$$

The ratio of kinetic energy over total energy $E = KE + PE$ is:

$$\frac{KE}{E} = \frac{1}{2}\frac{\omega_0^2 + f^2}{\omega_0^2} \tag{C.0.16}$$

The evolution of total energy is governed by the conservation of wave action equation:

$$\frac{\partial A}{\partial t} + \nabla.(\mathbf{C_g} A) = 0 \tag{C.0.17}$$

where $A = \frac{E}{\omega_0}$ is the wave action. Eq. C.0.17 means that the action enclosed in a small volume moving along a ray with the group velocity is conserved. Following Edwards and Staquet (2005), we compute the evolution of the action along a ray by computing the volume of a small tetrahedron defined by the ray plus three nearby rays positions.

Eq. C.0.17 can be rewritten as an energy balance equation:

$$\frac{dE}{dt} = -E\nabla.\mathbf{C_g} + \frac{E}{\omega_0}\frac{d\omega_0}{dt} \tag{C.0.18}$$

The first term on the rhs is the ray divergence contribution: when rays diverge, the energy density decreases, while it increases when rays converge. In the absence of background currents, ray divergence is due only to vertical gradients in buoyancy frequency:

$$\nabla.\mathbf{C_{g0}} = -\frac{k^2+l^2}{\omega_0 m^3} N \frac{dN}{dz} \tag{C.0.19}$$

Physically, an increase in buoyancy frequency N results in an increase in vertical wavenumber m (from C.0.8), resulting in a slower vertical group velocity, therefore in a vertical convergence of ray tubes. In the presence of background currents, there are also contributions from the horizontal variations of N and m as well as the 3D variations of k, l and ω_0. This term can be obtained from Eq. C.0.17:

$$\nabla.\mathbf{C_g} = -\frac{1}{A}\frac{dA}{dt} \tag{C.0.20}$$

The second term on the rhs of Eq. C.0.18 is the energy exchange with the background flow: when the waves propagate upward in the direction of the shear, the Doppler-shifted intrinsic frequency decreases (Eq. C.0.7) and the energy decreases too, corresponding to an energy transfer from the waves to the background flow. Conversely, when the waves propagate upward against the shear, the intrinsic frequency increases, and the energy increases too, corresponding to an energy transfer from the background flow to the waves. The opposite happens for a downward propagating wave. This term can be expressed explicitly by obtaining the energy equation from Eqs. C.0.1-C.0.5, and comparing to Eq. C.0.18:

$$\frac{E}{\omega_0}\frac{d\omega_0}{dt} = \rho_0 Re\left[\overline{u^* u_i}\frac{\partial U}{\partial x_i} + \overline{v^* u_i}\frac{\partial V}{\partial x_i} - \frac{\overline{|b|^2}}{2N^4}\left(\frac{\partial U}{\partial z}\frac{\partial B}{\partial x} + \frac{\partial V}{\partial z}\frac{\partial B}{\partial y}\right) + \frac{\overline{u^* b}}{N^2}\frac{\partial B}{\partial x} + \frac{\overline{v^* b}}{N^2}\frac{\partial B}{\partial y}\right] \tag{C.0.21}$$

where * denotes the complex conjugate and the repeated indices i are implicitly summed from 1 to 3. The first two terms on the rhs of Eq. C.0.21 are the rate of working of the radiation stress tensor of the waves against the rate of strain of the background flow (Garrett (1968)). Additional terms appear due to the horizontal gradients of stratification.

Appendix D

Idealized mesoscale features

Eddies

Consider axisymmetric vortices $(U, V, W) = (0, V(r, z), 0)$ in gradient-wind balance:

$$\frac{g}{\rho_0}\frac{\partial \rho}{\partial r} = -(f + \frac{2V}{r})\frac{\partial V}{\partial z} \tag{D.0.22}$$

Assume an idealized radial profile of the form:

$$V(r, z) = V_0 \frac{r}{R} e^{-\frac{1}{2}\left(\frac{r}{R}\right)^2 + \frac{1}{2}} F(z) \tag{D.0.23}$$

where V_0 is the vortex maximum current (positive for cyclones, negative for anticyclones), R is the vortex radius, and $F(z)$ is an arbitrary function of depth. Using Eq. D.0.23, Eq. D.0.22 can easily be solved for ρ, from which we can obtain the buoyancy frequency squared $N^2 = -\frac{g}{\rho_0}\frac{\partial \rho}{\partial z}$:

$$N^2(r, z) = N_0^2(z) - fRV_0 e^{-\frac{1}{2}\left(\frac{r}{R}\right)^2 + \frac{1}{2}} \frac{\partial^2 F}{\partial z^2} - \frac{1}{2} V_0^2 e^{-\left(\frac{r}{R}\right)^2 + 1} \frac{\partial^2 F^2}{\partial z^2} \tag{D.0.24}$$

where $N_0^2(z)$ is the stratification of the ocean at rest (at infinite radius).

Vorticity waves

Consider rectilinear parallel currents $(U, V, W) = (0, V(x, z), 0)$ in a referential rotated so that the x-axis is aligned in the direction of wave propagation, of the form:

$$V(x, z) = V_0 cos(kx + \phi) F(z) \tag{D.0.25}$$

where k is the wavenumber and ϕ the phase at a particular time.

Such parallel flows are in thermal-wind balance:

$$\frac{g}{\rho_0}\frac{\partial \rho}{\partial x} = -f\frac{\partial V}{\partial z} \tag{D.0.26}$$

Using Eq. D.0.25, Eq. D.0.26 can be solved easily for ρ, yielding the buoyancy frequency squared:

$$N^2(x,z) = N_0^2(z) + \frac{fV_0}{k} sin(kx+\phi)\frac{\partial^2 F}{\partial z^2} \tag{D.0.27}$$

where $N_0^2(z)$ is the stratification used in PEZHAT, chosen to be that where the currents are extremum, so that the stratification profiles oscillate around it.

Appendix E

Vortex Rossby Waves

From March to April 2003, the low-frequency currents variability south of the Kauai Channel is dominated by vorticity waves, two snapshots of which are shown in Chapter 4 (Fig. 4.3). They are surface intensified, and their vertical structures differ from March to April, 2003 (Figs. 4.5, 4.6 and 4.7), their decay scale decreasing with time. Their horizontal structures are captured by complex EOF (Empirical Orthogonal Function) analyses of the horizontal currents and their vorticity, shown below.

During March 14 to 30, 2003, 91% of variance of currents and vorticity combined are captured by the first EOF (Fig. E.1), which represents the variability associated with the first passage of the waves. The currents are not all aligned in the same direction, as modelized in Chapter 4. In the south, they are almost zonally oriented, with high eccentricity, and turn progressively in the along-shore direction as the coast is approached, becoming more circular. In the northwestern part, the are aligned almost perpendicular to the ridge. The amplitude of vorticity increases toward the 2000-m isobath, close to the shore, possibly as a result of the coastal boundary layer on the current shear. The phase shows a northeastward propagation, with a mean direction of 61^o ccw from east, and a mean wavelength of 147 km. Phase gradients increase near the coast, indicating that the waves are slowed down over shallow topography. The temporal amplitude shows that the wave pattern is strongest around March 22. Instantaneous periods range from 12 to 20 days, with a mean period of 17 days, yielding a mean phase velocity is $10cm.s^{-1}$.

During April 14 to 24, 2003, 92% of variance of currents and vorticity combined are captured again by the first EOF (Fig. E.2), which represents the variability associated

with another passage of the waves. The currents are more aligned in the same direction everywhere, almost perpendicular to the phase propagation direction, which is 77^o ccw from east on average. The mean wavelength is 112 km, and the mean period is 12.5 days, yielding a mean phase velocity of $10.4cm.s^{-1}$.

Due to the eastward component of their phase propagation, these waves cannot be purely planetary Rossby waves. Barotropic and bottom-trapped topographic Rossby waves can have an eastward phase propagation if the bottom slopes downward to the north (opposing the β effect), but the surface intensified baroclinic modes always have a westward phase propagation, isolating themselves from the topographic effect by moving a node in the horizontal velocity to the bottom (Rhines, 1970), as observed at A2 (4.7). They are not Doppler shifted by a mean eastward current neither (Fig. 4.1).

The last possibility for free waves of these frequencies to have an eastward phase propagation is that they propagate thanks to gradients of background currents vorticity (e.g. Pedlosky (2003), pp. 209-210), in the same way as classic Rossby waves propagate thanks to the meridional gradient of planetary vorticity. Figs. E.3 and E.4 show weekly-averaged geostrophic currents from altimetry observations obtained from AVISO (Ducet et al., 2000), centered on March 26 and April 16, respectively. Three-day low-pass filtered currents from the HF-radios are superimposed. Altimetry reveals the presence of a large cyclone south of Kauai, which originated in the lee of the Island of Hawaii in December 2002, over which the vorticity waves are superimposed. Waves propagating thanks to the radial gradient of vorticity of vortices have been called vortex Rossby waves, and were first proposed to describe hurricane spiral bands (MacDonald, 1968). For waves with scales smaller than the vortex scale, Montgomery and Kallenbach (1997) derived their dispersion relation in the WKB approximation:

$$\omega = n\Omega + \frac{n\zeta_r}{R(k^2 + n^2/R^2)} \tag{E.0.28}$$

where ω is the instantaneous wave frequency, n is the azimuthal mode number, k is the radial wavenumber, Ω is the angular velocity of the vortex at the range R where the wave packet is localized, and ζ_r is the radial gradient of the vortex relative vorticity at the range R. The first term on the rhs of Eq. E.0.28 is the Doppler shift by the vortex azimuthal velocity, and the second term is the analog of the beta effect. The frequency is dominated by the first

term, and so is the radial phase speed ω/k, which is outward for positive k (corresponding to a trailing spiral), explaining the eastward component of phase propagation seen in the HF-radios observations.

We infer the vortex characteristics from azimuthal averages of the azimuthal velocity from AVISO, shown in Fig. E.5. The ranges where the wave packets are localized are taken as the average ranges of the HF-radios observations relative to the vortex center, and the vortex characteristics are also averaged over these ranges. Using the wavenumber obtained by the complex EOF analysis, projected onto the radial direction from the vortex center, equation E.0.28 yields a period of 18 days for azimuthal mode number 2 for March 26, close to the 17-day period inferred from the complex EOF analysis of the HF-radios observations. A mode 2 perturbation is also consistent with the elliptic shape of the vortex (Fig. E.3). The period closest to the 12.5 days inferred from the HF-radios observations in April is for mode 6 on April 16, which yields a period of 12 days. However, altimetry still suggests a mode 2 perturbation (Fig. E.4). We note that the WKB approximation should degrade in our case, where the wavelengths are on the same order as the vortex size. Also the results are sensitive to which ranges are chosen as representative of the wave "packet" positions (Fig. E.5). Nevertheless, the results are suggestive that the vorticity waves observed by the HF-radios can be vortex Rossby waves associated with the large cyclone south of Kauai present in the AVISO dataset.

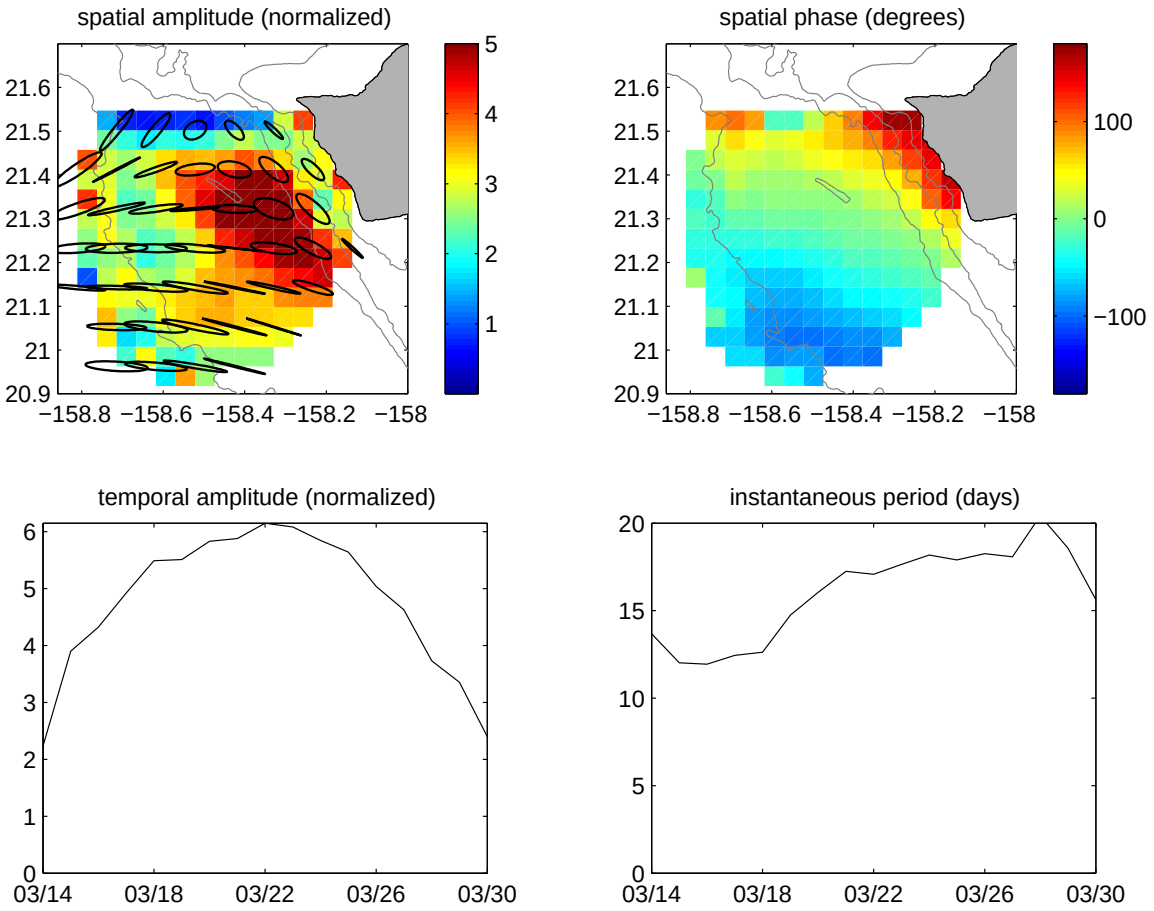

Figure E.1: First complex EOF of currents and vorticity during March 14 to 30, 2003. (a) Spatial amplitude of currents (ellipses) and vorticity (color), (b) spatial phase, (c) temporal amplitude, and (d) instantaneous period (from temporal gradient of temporal phase). Amplitude units are arbitrary.

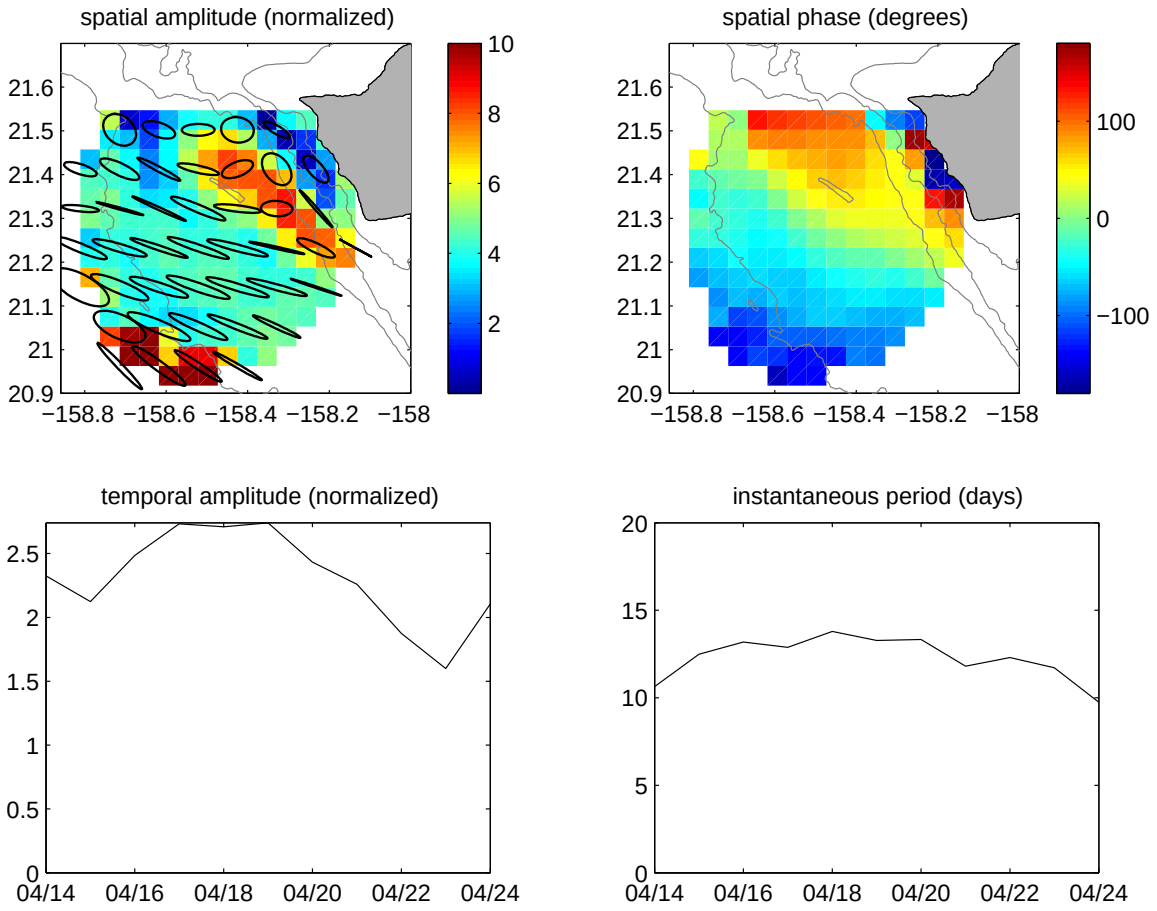

Figure E.2: Same as Fig. E.1, but during April 14 to 24, 2003.

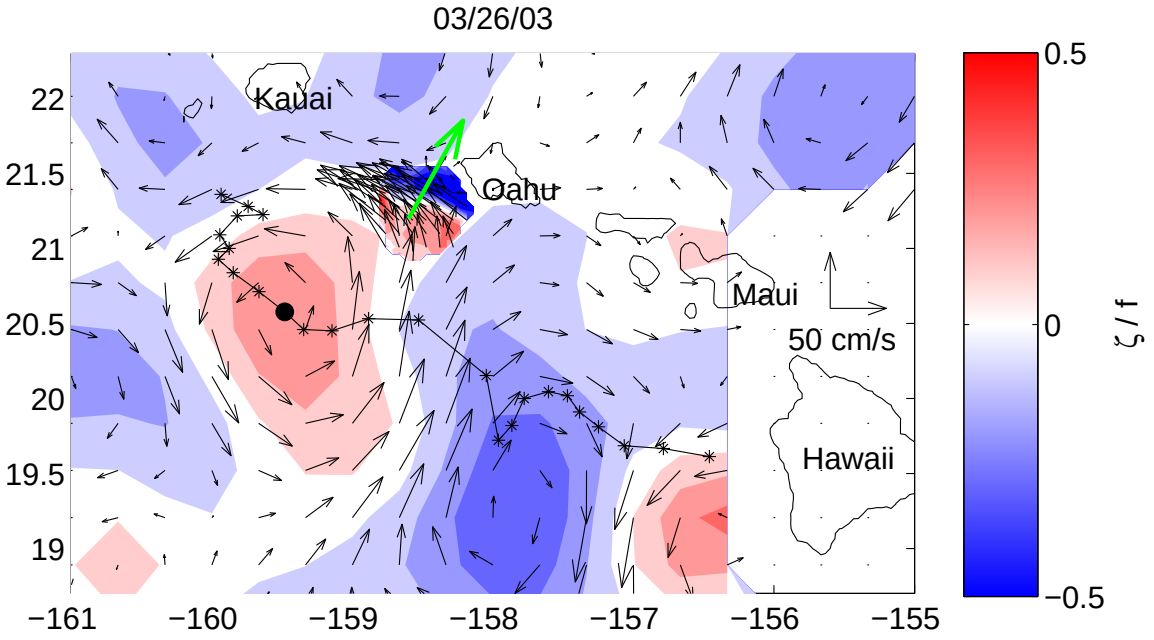

Figure E.3: Weekly-averaged geostrophic currents from altimetry observations obtained from AVISO (Ducet et al., 2000), centered on March 26, 2003. Three-day low-pass filtered currents from the HF-radios are superimposed. Vorticity (color) is normalized by f. The green arrow indicates the direction of phase propagation inferred from Fig. E.1b.

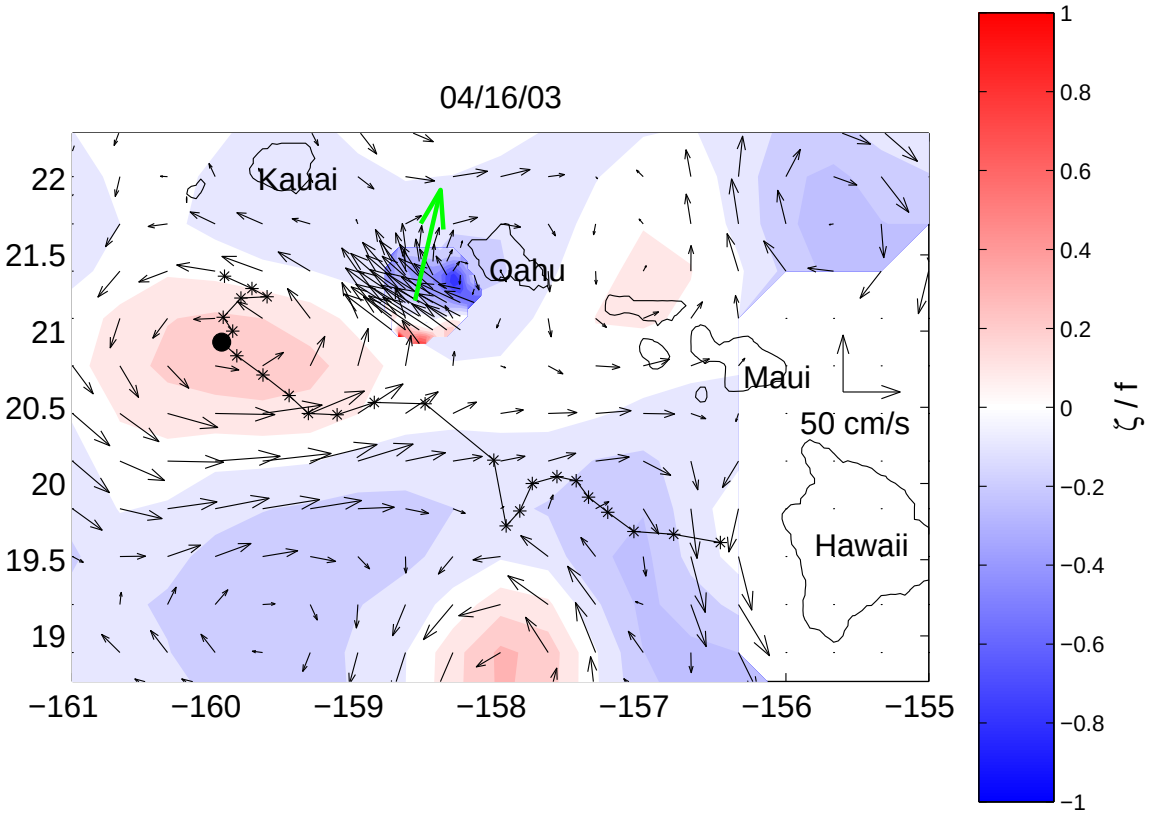

Figure E.4: Same as Fig. E.3, but centered on April 16, 2003 (phase propagation direction inferred from Fig. E.2b).

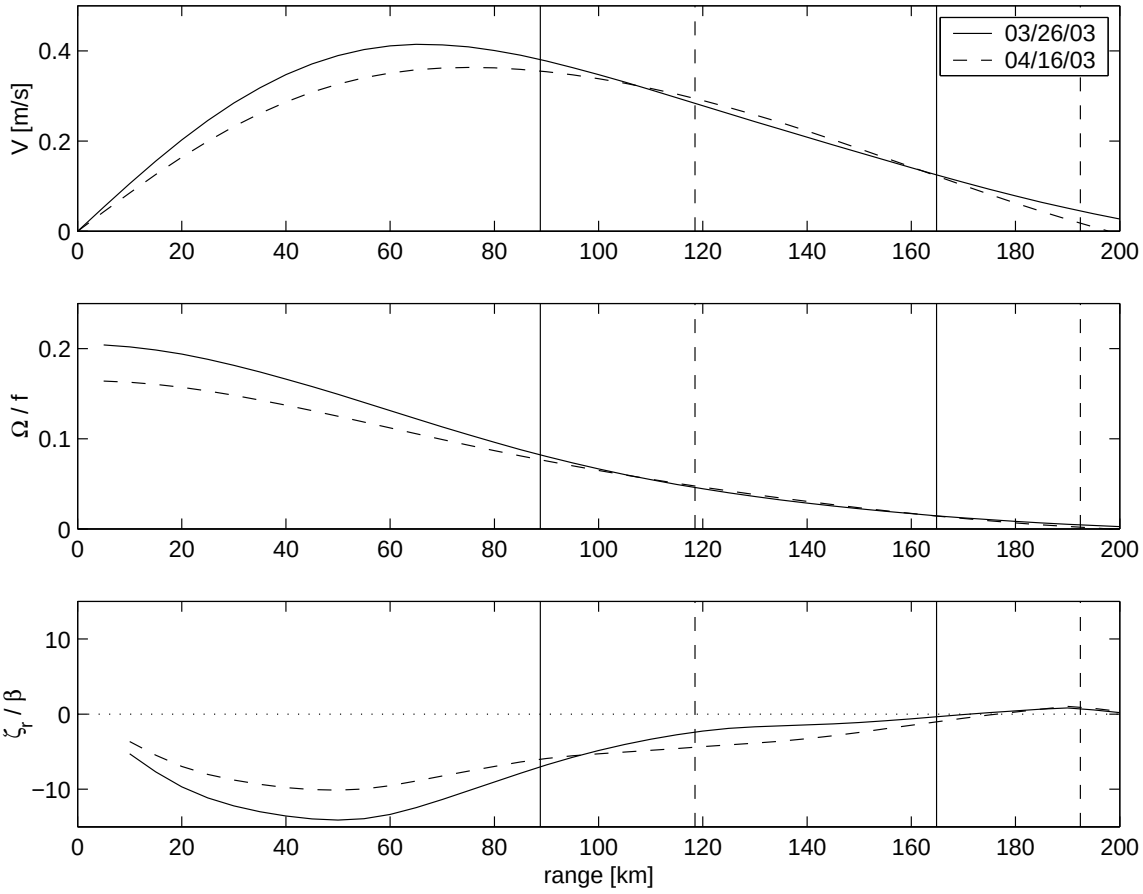

Figure E.5: (a) Azimuthally averaged azimuthal velocity V from weekly AVISO geostrophic currents centered on March 26, 2003 (solid line) and April 16, 2003 (dashed line), as a function of distance r from the vortex center (where velocity is zero). (b) Angular velocity $\Omega = V/r$, normalized by f. (c) Radial gradient of vorticity $d\zeta/dr$, where $\zeta = 1/rd(rV)/dr$, normalized by $\beta = df/dy$. Vertical lines indicate the range of the HF-radios observations relative to the vortex center.

Appendix F

Fourier analysis on gappy time series

F.1 Least-square fitting of one sinusoid

This paragraph is based on materials from Bloomfield (1976).

Consider a N-point time series $x_n = x(t_n), n = 0, ..., N-1$; where the t_n's are not necessarily regularly spaced.

We want to fit a sinusoid of a given frequency $f \geq 0$:

$$x_n = Xcos(2\pi f t_n + \phi) + \epsilon_n \qquad\qquad n = 0, ..., N-1 \qquad \text{(F.1.1)}$$

where X is the amplitude, ϕ is the phase, and ϵ_n are the residuals.

The least-square fit approach consists in minimizing the sum of the squared (to get rid of changes in sign) residuals , called the fitting error:

$$E = \sum_{n=0}^{N-1} \epsilon_n^2 = \sum_{n=0}^{N-1} (x_n - Xcos(2\pi f t_n + \phi))^2 \qquad \text{(F.1.2)}$$

Note that since a sinusoid oscillates about 0, we have to fit a mean value to the time series too, so that the residuals can be small. This complicates a lot the algebra, so let's assume for now that our time series has a zero mean.

Least-square problems are simplest to solve when the fitting model is a linear function of the unknown parameters, since then E is quadratic. The model (F.1.1) is non-linear in X and ϕ, but can be rewritten as:

$$x_n = Acos(2\pi f t_n) + Bsin(2\pi f t_n) + \epsilon_n \qquad\qquad n = 0, ..., N-1 \qquad \text{(F.1.3)}$$

where $A = Xcos(\phi)$ and $B = -Xsin(\phi)$.

Now the fitting error E is quadratic in A and B, so to minimize it we have to solve the following 2 equations: $\frac{\partial E}{\partial A} = 0$ and $\frac{\partial E}{\partial B} = 0$, which can be written in matrix form:

$$\begin{bmatrix} \sum cos^2(2\pi f t_n) & \sum cos(2\pi f t_n) sin(2\pi f t_n) \\ \sum cos(2\pi f t_n) sin(2\pi f t_n) & \sum sin^2(2\pi f t_n) \end{bmatrix} \begin{bmatrix} A \\ B \end{bmatrix} = \begin{bmatrix} \sum x_n cos(2\pi f t_n) \\ \sum x_n sin(2\pi f t_n) \end{bmatrix} \tag{F.1.4}$$

Solving this system will give us the least-square estimates of the parameters A and B.

The expressions in the system square matrix of equation (F.1.4) simplify when the time sampling is regularly spaced, say $t_n = n\delta t, n = 0, 1, ..., N-1$, by the use of trigonometric identities:

$$\sum_{n=0}^{N-1} cos^2(2\pi f n\delta t) = \frac{N}{2}(1 + D_N(4\pi f\delta t)cos(2\pi f N\delta t) \tag{F.1.5}$$

$$\sum_{n=0}^{N-1} sin^2(2\pi f n\delta t) = \frac{N}{2}(1 - D_N(4\pi f\delta t)cos(2\pi f N\delta t) \tag{F.1.6}$$

$$\sum_{n=0}^{N-1} cos(2\pi f n\delta t)sin(2\pi f n\delta t) = \frac{N}{2} D_N(4\pi f\delta t)sin(2\pi f N\delta t) \tag{F.1.7}$$

where D_N is the Dirichlet kernel:

$$D_N(a) = \frac{sin(\frac{Na}{2})}{Nsin(\frac{a}{2})} \tag{F.1.8}$$

and is plotted in figure F.1.

Now if

$$f = \frac{k}{2N\delta t} \qquad\qquad k = 1, 2, ..., N-1 \tag{F.1.9}$$

then $D_N(4\pi f\delta t) = 0$, and the square matrix of equation (F.1.4) becomes diagonal, which means that the cosine and sine functions are orthogonal for those particular frequencies.

The coefficients are then given by:

$$A = \frac{2}{N}\sum_{n=0}^{N-1} x_n cos(2\pi f n\delta t) \tag{F.1.10}$$

$$B = \frac{2}{N}\sum_{n=0}^{N-1} x_n sin(2\pi f n\delta t)$$

which are the standard Fourier coefficients.

Therefore **when dealing with regularly spaced time series, the Fourier coefficients are those giving the least-square solution to the problem of fitting a sinusoid of a particular frequency to the data**.

Remark: the frequencies given by (F.1.9) are half the usual Fourier frequencies. This is because we have only fitted one frequency at a time, see later when we fit many frequencies altogether.

F.2 Lomb periodogram

This paragraph is based on materials from Lomb (1976) and Press (1992).

In the case of unequally spaced time series, the non-diagonal terms (left-hand side of equation (F.1.7)) are not zero any more even for the Fourier frequencies, which means that the cosine and sine functions are not orthogonal to each other, hence the coefficients depend on the choice of the time origin.

We can introduce an unknown time shift τ in our fitting model to make the cosine and sine functions orthogonal :

$$x_n = Acos(2\pi f(t_n - \tau)) + Bsin(2\pi f(t_n - \tau)) + \epsilon_n \qquad n = 1, ..., N \quad \text{(F.2.1)}$$

choosing τ such that the non-diagonal terms $\sum cos(2\pi f(t_n - \tau))sin(2\pi f(t_n - \tau)) = 0$, which gives :

$$tan(4\pi f\tau) = \frac{\sum sin(4\pi f t_n)}{\sum cos(4\pi f t_n)} \quad \text{(F.2.2)}$$

The coefficients are now given by :

$$A = \frac{\sum x_n cos(2\pi f(t_n - \tau))}{\sum cos^2(2\pi f(t_n - \tau))} \quad \text{(F.2.3)}$$
$$B = \frac{\sum x_n sin(2\pi f(t_n - \tau))}{\sum sin^2(2\pi f(t_n - \tau))}$$

The constant τ makes the coefficients completely independent of shifting all the t_n's by any constant. Furthermore, it makes the cosine and sine functions orthogonal for any frequency f (not limited to those given by equation (F.1.9). For unequally spaced time series, it gives better results than standard Fourier coefficients (computed as if the time

series was equally spaced) because it weights the data on a "per point" basis instead of on a "per time interval" basis, giving the right least-square solution for the fitting of the sinusoid at any frequency f of interest to the unequally spaced time series.

F.3 Least-square fitting of many sinusoids

All of this works when fitting only one frequency at a time to the data. What if we want to fit many frequencies altogether ? Consider the following model:

$$x_n = \sum_{j=1}^{M} (A_j cos(2\pi f_j t_n) + B_j sin(2\pi f_j t_n)) + \epsilon_n \qquad n = 0, ..., N-1 \qquad \text{(F.3.1)}$$

where $f_j \geq 0$ are M different frequencies.

We will obtain a 2M $\times$ 2M matrix problem, with non-diagonal terms of the form:

$$CC = \sum_{n=0}^{N-1} cos(2\pi f_j t_n) cos(2\pi f_k t_n) \qquad f_j \neq f_k \qquad \text{(F.3.2)}$$

$$SS = \sum_{n=0}^{N-1} sin(2\pi f_j t_n) sin(2\pi f_k t_n) \qquad f_j \neq f_k \qquad \text{(F.3.3)}$$

$$CS = \sum_{n=0}^{N-1} cos(2\pi f_j t_n) sin(2\pi f_k t_n) \qquad \forall f_j, f_k \qquad \text{(F.3.4)}$$

For regularly spaced time series, we get:

$$CC = \frac{N}{2}(D_N(2\pi(f_j + f_k)\delta t)cos(\pi N(f_j + f_k)\delta t) + D_N(2\pi(f_j - f_k)\delta t)cos(\pi N(f_j - f_k)\delta t) \qquad \text{(F.3.5)}$$

$$SS = \frac{N}{2}(D_N(2\pi(f_j - f_k)\delta t)cos(\pi N(f_j - f_k)\delta t) - D_N(2\pi(f_j + f_k)\delta t)cos(\pi N(f_j + f_k)\delta t) \qquad \text{(F.3.6)}$$

$$CS = \frac{N}{2}(D_N(2\pi(f_j + f_k)\delta t)sin(\pi N(f_j + f_k)\delta t) - D_N(2\pi(f_j - f_k)\delta t)sin(\pi N(f_j - f_k)\delta t) \qquad \text{(F.3.7)}$$

Now if:

$$f_j = \frac{j}{N\delta t} \qquad j = 0, 1, 2, ..., N/2 \qquad \text{(F.3.8)}$$

the diagonal terms are zero since $2\pi(f_j \pm f_k)\delta t = 2\pi\frac{i}{N}$, with $i = -N/2, ..., -1, 1, ..., N-1$ for $j \neq k$ (equations (F.3.5) and (F.3.6)), and with $i = -N/2, ..., -1, 0, 1, ..., N$ for all j and k, for which the sines of equation (F.3.7) are 0 when $2\pi(f_j \pm f_k)\delta t = 0$ or 2π (where the Dirichlet kernel is not 0 but 1, see figure F.1).

Now the frequencies given by (F.3.8) are exactly the Fourier frequencies, where

$$f_{N/2} = \frac{1}{2\delta t} \tag{F.3.9}$$

is the Nyquist frequency, the highest frequency resolvable due to the time spacing resolution δt, and

$$f_1 = \frac{1}{N\delta t} = \frac{1}{T} \tag{F.3.10}$$

is the fundamental frequency, the lowest frequency resolvable (aside from the zero-frequency, i.e. the mean) due to the time record period $T = N\delta t$.

So for the Fourier frequencies of a regularly spaced time series, the matrix is diagonal and all the cosines and sines functions are orthogonal. Therefore the results of fitting the frequencies separately are the same as of fitting them altogether. Indeed the coefficients are given by:

$$\begin{aligned} A_j &= \frac{2}{N}\sum_{n=0}^{N-1} x_n cos(2\pi f_j n\delta t) \\ B_j &= \frac{2}{N}\sum_{n=0}^{N-1} x_n sin(2\pi f_j n\delta t) \end{aligned} \tag{F.3.11}$$

which are the same as (F.1.10) for each Fourier frequency.

Notice that for $f = f_0 = 0$, the corresponding Fourier coefficient A gives twice the sample mean of the time series, $A_0 = \frac{2}{N}\sum_{n=0}^{N-1} x_n = 2\bar{x}$, which has been supposed to be 0 up to now, but is not a necessary assumption any more here, since the mean is part of the fitting through the f_0 frequency component.

What about unequally spaced time series ? Can we apply the Lomb method to get orthogonal functions ?

For 2 given different frequencies, f_j and f_k, we dispose of 2 unknowns, τ_j and τ_k, to make the diagonal terms be zero. But there are 4 of them (equations (F.3.2), (F.3.3), (F.3.4), and another (F.3.4) with cos and sin switched), so they cannot be put to zero in general. This means that for unequally spaced time series, the pure sinusoids cannot form an orthogonal basis.

We can always fit by least-squares many sinusoids with different frequencies, but the results will depend on how many frequencies we chose to fit together, since the

functions will not be orthogonal to each other. And the solution may blow up if we try to fit too many frequencies to not enough available data.

Remark: For unequally spaced time series, the result for $f = 0$ (i.e. trying to fit a constant to the time series) does not yield the sample mean $\bar{x}$ any more. So **removing the sample mean before fitting sinusoids is not the same as fitting a constant + sinusoids directly to the time series, which should be the method used when fitting frequencies to a gappy time series**, as is illustrated in figure F.2.

F.4 Fourier spectrum

Consider a time series of N points regularly spaced by δt : (x_n), n=0,...,N-1; spanning the time period $T = N\delta t$.

The discrete Fourier transform of x is defined as :

$$\widehat{x_k} = \hat{x}(f_k) = \sum_{n=0}^{N-1} x_n e^{-i2\pi f_k n\delta t}\delta t \tag{F.4.1}$$

where f_k is one of the Fourier frequencies :

$$f_k = \frac{k}{N\delta t} \qquad\qquad k = 0, 1, ..., N-1 \tag{F.4.2}$$

Notice that k goes up to N-1, while it was restricted to N/2 in the previous paragraph. This is because the range k=N/2+1,...,N-1 corresponds to the negative frequencies range k'=k-N=-N/2+1,...,-1 since $\widehat{x_k} = \widehat{x_{k-N}}$ due to the 2π-periodicity. So the highest frequency resolvable is still the Nyquist frequency given by (F.3.9). Any frequency greater than the Nyquist frequency is folded back into the $[-f_{N/2}, f_{N/2}]$ interval. This is the **aliasing** phenomenon.

How does the Fourier transform relates to the Fourier coefficients obtained in the previous paragraph ?

$$\begin{aligned}
\widehat{x_0} &= \sum_{n=0}^{N-1} x_n\delta t = N\delta t A_0/2 \\
\widehat{x_k} + \widehat{x_{-k}} &= 2\delta t \sum_{n=0}^{N-1} x_n cos(2\pi f_k n\delta t) = N\delta t A_k \\
\widehat{x_k} - \widehat{x_{-k}} &= -2i\delta t \sum_{n=0}^{N-1} x_n sin(2\pi f_k n\delta t) = -Ni\delta t B_k
\end{aligned}$$

The inverse discrete Fourier transform is given by:

$$x_n = \frac{1}{N\delta t} \sum_{k=0}^{N-1} \widehat{x_k} e^{i2\pi f_k n \delta t} \tag{F.4.3}$$

The power (energy per time) of the time series is defined as its variance :

$$P = \frac{1}{N\delta t} \sum_{n=0}^{N-1} x_n^2 \delta t \tag{F.4.4}$$

Parceval's theorem :

$$\sum_{n=0}^{N-1} x_n^2 \delta t = \sum_{k=0}^{N-1} |\widehat{x_k}|^2 \delta f \tag{F.4.5}$$

where $\delta f = 1/(N\delta t)$ is the Fourier frequency resolution, tells us that the energy can be computed also in the frequency domain.

We can then define a power density (i.e. power per unit frequency) :

$$S_{xx}(f_k) = \frac{1}{N\delta t} |\widehat{x_k}|^2 \tag{F.4.6}$$

The distribution of power density with frequency is called the spectrum, and the power density is therefore called power spectral density (PSD). The computation of the PSD using equation (F.4.6) is called the periodogram method.

Ideally, the spectrum of a time series should be computed from an infinite record of the time series. In practice the records are always finite. We can see them as an infinite time series with zeros outside of the record period :

let's x be the original signal (infinite time series), and z be the observations, constructed by replacing values of x outside the record period by zeros :

$$z(t) = \begin{cases} x(t) & \text{if recorded} \\ 0 & \text{otherwise} \end{cases} \tag{F.4.7}$$

whose amplitude-modulating function is :

$$y(t) = \frac{z(t)}{x(t)} = \begin{cases} 1 & \text{if x(t) is recorded} \\ 0 & \text{otherwise} \end{cases} \tag{F.4.8}$$

y is a boxcar function, shown on the top panel of figure (F.3) (black curve).

We have $z(t) = y(t) \times x(t)$. An interesting property of Fourier transforms is that the Fourier transform of $y \times x$ is the convolution of the Fourier transform of y with the Fourier transform of x :

$$\widehat{y \times x} = \hat{y} * \hat{x} \tag{F.4.9}$$

where the convolution operator * is defined by:

$$a * b(f) = \int_{-\infty}^{\infty} a(f')b(f - f')df' \tag{F.4.10}$$

Therefore the Fourier transform of the observations z is the Fourier transform of the original signal x convolved with the Fourier transform of the Boxcar function y, whose squared values are plotted on a logarithmic scale on the lower panel of figure (F.3) (black curve).

The ideal window (1's everywhere) would have a delta function spectrum (zero at all frequencies except the zero frequency in which all the energy is confined), hence not affecting the power spectrum computation. But with the Boxcar window, we see that although a lot of energy is at and around the zero frequency, there are side lobes of energy at higher frequencies, which are going to contaminate the observed spectrum when convoluting the Boxcar Fourier transform with the original signal Fourier transform to obtain the observed spectrum. This is called **spectral leakage**. We notice that there are zeros in the Boxcar Fourier transform at the Fourier frequencies, so if strong signals like tides for example are placed exactly on Fourier frequencies by choosing an adequate time period of observation, spectral leakage can be avoided.

When we cannot avoid having significant energy falling in-between the Fourier frequencies, as is almost always the case, it is necessary to reduce the side lobes of the window, by applying coefficients different than 1 to the observations before computing the Fourier transforms. A commonly used window is the Hanning window, which is plotted in blue in figure (F.3). The side-lobe energy is much weaker than for the Boxcar window, reducing leakage. Note that the central peak of energy is much wider, spanning 3 Fourier frequencies centered around 0, which reduces the frequency resolution of the observed spectrum, or equivalently applies some kind of frequency averaging to the spectrum. We notice also that the energy level of the main lobe is reduced compared to the Boxcar window

case, which means that the global energy level of the spectrum is lowered (it has to be so since we have decreased the amplitude of the signal on the edges of the time series by applying the hanning window).

How to correct for this energy loss ? Following Harris (1978), suppose first that the original signal is a pure sinusoid:

$$x_n = Ae^{i2\pi f_k n\delta t} \qquad n = 0, 1, ..., N-1 \tag{F.4.11}$$

The Fourier transform at the frequency f_k of the windowed signal $z = x.y$, where y is the window, is:

$$\widehat{z_k} = \sum_{n=0}^{N-1} y_n A e^{i2\pi f_k n\delta t} e^{-i2\pi f_k n\delta t}\delta t = A\delta t \sum_{n=0}^{N-1} y_n \tag{F.4.12}$$

For a Boxcar window we would have $z = x$ and $\widehat{x_k} = A\delta tN$, so the ratio of original energy over windowed energy is:

$$(\frac{1}{N}\sum_{n=0}^{N-1} y_n)^2 = \bar{y}^2 \tag{F.4.13}$$

This corrects for the level of the main lobe of the Fourier transform of the window at zero frequency, to get it back to the level of the Boxcar window transform, since the energy of the sinusoid, which is confined to a single frequency, is only affected by the zero frequency component of the window Fourier transform.

The situation is more complicated if the original signal has energy at all frequencies, as is most of the time the case, since then energy at different frequencies are mixed up with energy at the computed frequency when applying the window, due to the widening of the main lobe and due to the sidelobes of the Fourier transform of the window. In general we cannot determine a single correction factor, since the bias will depend on the frequency being computed because of the relative distribution of energy at the other frequencies. But there is a particular case for which we can obtain a single correction factor: if the original signal x is white noise with zero mean and variance (i.e. energy) σ^2. Then the Fourier transform of the windowed signal is:

$$\widehat{z_k} = \sum_{n=0}^{N-1} y_n x_n e^{-i\omega_k n\delta t}\delta t \tag{F.4.14}$$

and the statistical expected value of the PSD is:

$$\begin{aligned} E[\frac{1}{N\delta t}|\widehat{z_k}|^2] &= \frac{1}{N\delta t}\sum_{n=0}^{N-1}\sum_{m=0}^{N-1} y_n y_m E[x_n x_m] e^{-i\omega_k n\delta t} e^{i\omega_k m\delta t}\delta t^2 \\ &= \sigma^2\frac{\delta t}{N}\sum_{n=0}^{N-1} y_n^2 \end{aligned}$$

For a Boxcar window we would have $z = x$ and $E[\frac{1}{N\delta t}|\widehat{x_k}|^2] = \sigma^2\delta t$, so the ratio of original energy over windowed energy is:

$$\frac{1}{N}\sum_{n=0}^{N-1} y_n^2 \tag{F.4.15}$$

This is the sample window variance, hence energy, which is the amount by which energy is biased for a white noise signal. It is the correction factor usually used, but keep in mind that it works only for a white noise signal. If you are trying to estimate the energy of a tidal peak for example, you should use the factor given by (F.4.13) instead. Now if your signal is composed of peaks plus white or red noise, as is the case for geophysical data, there is no universal correction factor.

Remark: If we add a non-zero mean to the original white noise signal, say $x = \bar{x} + x'$, with x' a white noise signal with zero mean, then:

$$E[x_n x_m] = \bar{x}^2 + E[x'_n x'_m]$$

so that its PSD is now given by:

$$S_{zz}(f) = \bar{x}^2 S_{yy}(f) + \sigma^2\frac{\delta t}{N}\sum_{n=0}^{N-1} y_n^2$$

We see that if we don't remove the mean of a time series before applying a window, then the final spectrum is distorted by the window spectrum times $\bar{x}^2$, in addition of having its energy level changed. **That's why it is necessary to remove the mean of the time series before applying windows**.

Now let's look at the case of missing observations, which are replaced by zeros. The window function y is the gap function, which values are 1 when the observation is available, and 0 when it is missing. See figure F.3 (red curves) for an example. Its Fourier transform can be very ugly, depending on the number and structure of the gaps. There

can be high sidelobes whose level is not negligible compared to that of the main lobe. And the Fourier transform is not 0 any more at the Fourier frequencies, which means that those frequencies are not independent of each other any more (indeed they do not form a basis of the ensemble of functions of period T any more). So even by placing spectral peaks onto Fourier frequencies, spectral leakage cannot be avoided. Therefore spectral peaks must be removed from the time series by least-square fitting prior to Fourier analysis. Also the gap function is a window unwillingly applied to the observations, from which the mean was not removed, therefore the spectrum would be distorted by the gap window spectrum. The mean having been modified by the gaps, we cannot remove it directly from the observed time series. We have to remove it by least-square fitting a constant, along with the spectral peaks sinusoids (cf figure F.2). Therefore **it is necessary to remove the sinusoids corresponding to the spectral peaks plus the original mean, by least-square fitting them altogether to the observations, prior to compute the spectrum of a gappy time series**. As for the energy correction, the high sidelobes imply that a lot of other frequencies energy will be mixed up with the one being computed, and a single correction parameter for all frequencies makes even less sense. In fact we are facing the problem of finding an inverse convolution operator, to estimate $\hat{x}$ knowing $\hat{z}$ and $\hat{y}$, which are linked through:

$$\hat{z} = \hat{y} * \hat{x} \tag{F.4.16}$$

Unfortunately such an operator does not exist.

But there is another approach to the spectrum estimation, which uses autocorrelation functions. Those do not depend on time but only on lags (for stationary random processes), therefore they should not be affected much by missing observations, as long as there is enough information available for any given lag. This topic is developed in the next 2 sections.

F.5 Wiener-Khinchin theorem

Consider a time series of N points regularly spaced by δt : (x_n), n=0,...,N-1; spanning the time period T=Nδt.

Its power spectral density, defined in equation (F.4.6), is given by :

$$S_{xx}(f) = \frac{\delta t}{N} \sum_{n=0}^{N-1} \sum_{m=0}^{N-1} x_n x_m e^{-i2\pi f(n-m)\delta t} \tag{F.5.1}$$

Let's $n' = n - m$ replace the variable n. Upper limit: when $n = N-1$, $n' = N-1-m$; lower limit: when $n = 0$, $n' = -m$. It consists in changing the geometry of the parameters domain over which we sum, as sketched in figure F.4.

Let's sum first over m at $n' = cst$, then sum over n' :

$$S_{xx}(f) = \frac{\delta t}{N}\Big(\sum_{n'=-(N-1)}^{-1} \sum_{m=-n'}^{N-1} x_{m+n'} x_m e^{-i2\pi f n' \delta t} + \sum_{n'=0}^{N-1} \sum_{m=0}^{N-1-n'} x_{m+n'} x_m e^{-i2\pi f n' \delta t} \Big) \tag{F.5.2}$$

We can see that a biased estimator of the autocorrelation function R_{xx} of x appears in equation (F.5.2), and is plotted in figure F.5 (in blue):

$$R^b_{xx}(n') = \begin{cases} \frac{1}{N} \sum_{m=0}^{N-1-n'} x_m x_{m+n'} & \text{if } n' \geq 0 \\ \frac{1}{N} \sum_{m=-n'}^{N-1} x_m x_{m+n'} & \text{if } n' < 0 \end{cases} \tag{F.5.3}$$

It is biased since:

$$E[R^b_{xx}(n')] = \frac{N - |n'|}{N} R_{xx}(n') \tag{F.5.4}$$

So we have:

$$S_{xx}(f) = \delta t \sum_{n'=-(N-1)}^{N-1} R^b_{xx}(n') e^{-i2\pi f n' \delta t} \tag{F.5.5}$$

It seems that the spectrum is the Fourier transform of the biased autocorrelation estimator of x, but there is a problem: R^b_{xx} has twice the number of points as x has, hence its Fourier transform would have twice the frequency resolution, which would not lead to the original spectrum.

One way around this would be to use the fact that the autocorrelation is a symmetric function, i.e. $R^b_{xx}(n') = R^b_{xx}(-n')$, so that we have:

$$S_{xx}(f) = \delta t (R^b_{xx}(0) + \sum_{n'=1}^{N-1} 2 R^b_{xx}(n') cos(2\pi f n' \delta t) \tag{F.5.6}$$

The spectrum is then the cosine transform of the one-sided biased autocorrelation, defined by equation (F.5.7) and plotted in figure F.5 (in green):

$$R_{xx}^{b1}(n') = \begin{cases} R_{xx}^{b}(0) & \text{for } n' = 0 \\ 2R_{xx}^{b}(n') & \text{for } n' \geq 1 \end{cases} \tag{F.5.7}$$

Another and better way around would be to get back to equation (F.5.2), and rearrange the first part of the right-hand side, to have only positive lags, by shifting n' by N:

replace n' by p=n'+N, to obtain:

$$\sum_{p=1}^{N-1} \sum_{m=N-p}^{N-1} x_{m+p-N} x_m e^{-i2\pi f(p-N)\delta t}$$

Now,

$$e^{-i2\pi f(p-N)\delta t} = e^{-i2\pi fp\delta t} e^{i2\pi fN\delta t} = e^{-i2\pi fp\delta t} \tag{F.5.8}$$

for the Fourier frequencies given in (F.4.2).

So by replacing p with n', we get for the full equation:

$$S_{xx}(f) = \frac{\delta t}{N}\left(\sum_{n'=1}^{N-1} \sum_{m=N-n'}^{N-1} x_{m+n'-N} x_m e^{-i2\pi fn'\delta t} + \sum_{n'=0}^{N-1} \sum_{m=0}^{N-1-n'} x_{m+n'} x_m e^{-i2\pi fn'\delta t}\right) \tag{F.5.9}$$

Let's define the circular autocorrelation in equation (F.5.10), plotted in figure F.5 (in red):

$$R_{xx}^{c}(n') = \begin{cases} \frac{1}{N}\sum_{m=0}^{N-1} x_m^2 & \text{for } n' = 0 \\ \frac{1}{N}\left(\sum_{m=0}^{N-1-n'} x_m x_{m+n'} + \sum_{m=N-n'}^{N-1} x_m x_{m+n'-N}\right) & \text{for } n' = 1, ..., N-1 \end{cases} \tag{F.5.10}$$

Of course the circular autocorrelation can also be defined for negative lags, but it is a symmetric function, so there is no need for it.

Notice that the summations are always done over N points, so this is an unbiased estimator of the autocorrelation. It is called circular, because as in Fourier transform the time series is considered periodic of period $T = N\delta t$, then $x_{m+n'-N} = x_{m+n'}$ so that the second part of the right-hand side of equation (F.5.10) for $n' \geq 1$ represent the remainder of the autocorrelation terms for indices that go beyond N, for which the beginning of the time series is used again (hence the term "circular").

Finally we have:

$$S_{xx}(f) = \sum_{n'=0}^{N-1} R_{xx}^{c}(n') e^{-i2\pi f n' \delta t} \delta t = \widehat{R_{xx}^{c}}(f) \tag{F.5.11}$$

The spectrum is the Fourier transform of the circular autocorrelation.

Remark 1: we can express the circular autocorrelation in terms of the biased autocorrelation, by making the following variable changes for the second term of the circular autocorelation: let q=m+n'-N replace m , we get:

$$\frac{1}{N} \sum_{q=0}^{n'-1} x_q x_{q+N-n'}$$

then replace n' by r=N-n', we get:

$$\frac{1}{N} \sum_{q=0}^{N-1-r} x_q x_{q+r}$$

which is $R_{xx}^{b}(r) = R_{xx}^{b}(N - n')$ so that:

$$R_{xx}^{c}(n') = R_{xx}^{b}(n') + R_{xx}^{b}(N - n') \tag{F.5.12}$$

This relation is well illustrated in figure F.5.

Remark 2: Looking at equation (F.5.4), some authors have said that the weighting $\frac{N-n}{N}$ acts like a triangular smoothing window to help reduce spectral leakage (e.g. Emery and Thomson (1997)). This is erroneous because the correct autocorrelation function to consider is the circular autocorrelation, which is an unbiased estimator, hence does not have any weighting. We don't see why the autocorrelation method would have an intrinsic weighting while the periodogram method does not have, since they are mathematically equivalent.

Remark 3: Thanks to FFT (Fast Fourier Transform) algorithm, it is more efficient to compute the autocorrelation function of a time series by computing first the spectrum of the time series and then taking its inverse Fourier transform. But in order to obtain the biased autocorrelation function (F.5.3), we need first to pad the time series with N zeros (N being the length of the time series), in order to separate the 2 parts of the circular autocorrelation (cf equation F.5.12). The biased autocorrelation is then the first half of the

inverse Fourier transform of the spectrum of the padded time series (cf figure F.6, from Bendat and Piersol (1986)).

Question: The spectrum, which must be positive for all frequencies, is the simple Fourier transform (not squared) of the circular autocorrelation function. So the latter must have a peculiar property that guarantees its Fourier transform is positive for all frequencies. In fact the circular autocorrelation function is a positive definite operator, in the sense that:

$$\forall (a_j)_{j=1,\dots,N} \in (\mathbb{C})^N, \qquad \sum_{k=1}^{N}\sum_{l=1}^{N} a_k R^c_{xx}(k-l)a_l \geq 0 \tag{F.5.13}$$

(and that it is 0 only when all the coefficients a_j are 0). If this is true, we immediately see why the Fourier transform of the circular autocorrelation is always positive for all Fourier frequencies.

Because of the circularity of the function, this property is better derived using a matrix notation rather than using indices. Let's define the circular matrix of x:

$$\mathcal{X} = \begin{pmatrix} x_0 & x_1 & \cdots & x_{N-1} \\ x_{N-1} & x_0 & \cdots & x_{N-2} \\ \vdots & \vdots & \ddots & \vdots \\ x_1 & x_2 & \cdots & x_0 \end{pmatrix}$$

The matrix form of the circular autocorrelation function is then:

$$\mathcal{R} = \frac{1}{N}\mathcal{X}\mathcal{X}' = \begin{pmatrix} r_0 & r_1 & \cdots & r_{N-1} \\ r_1 & r_0 & \cdots & r_{N-2} \\ \vdots & \vdots & \ddots & \vdots \\ r_{N-1} & r_{N-2} & \cdots & r_0 \end{pmatrix}$$

where $r_j = R^c_{xx}(j)$. This is called a Toeplitz matrix.

Now for any vector $A = [a_1 a_2 ... a_N]$, let define a vector $Y = A\mathcal{X}$, and compute its variance:

$$\begin{aligned} Var(Y) &= YY' \\ &= A\mathcal{X}(A\mathcal{X})' \\ &= A\mathcal{X}\mathcal{X}'A' \\ &= NA\mathcal{R}A' \end{aligned}$$

Since $VarY \geq 0$ (and is 0 only if Y is a vector full of zeros, which happens only if A is a vector full of zeros itself, for an arbitrary time series x), $\mathcal{R}$ is then positive definite.

F.6 Unbiased autocovariance method

This paragraph is based on materials from Bloomfield (1970) and Bendat and Piersol (1986).

We immediately see an application for computing the spectrum of gappy time series. The simple method of replacing missing data by zeros and computing the FFT is equivalent to using only the available data points but still dividing by N when computing the circular autocorrelation function. Then the estimator is biased, and so is the energy. Therefore we can use an unbiased estimator instead, by dividing by the number of pair of points available for each lag for the computation of the circular autocorrelation.

Let's formalize the previous discussion. Let's x be the observed signal, and z be the observations, constructed by replacing missing observations by zeros (cf equations (F.4.7) and (F.4.8)).

For a given lag n, the number of observations available for computing the circular autocorrelation function is given by the non-normalized circular autocorrelation function of the gap function:

$$N_0(n) = NR^c_{yy}(n) \text{ for } n \geq 0 \tag{F.6.1}$$

Therefore the unbiased circular autocorrelation estimator for z is:

$$\tilde{R}^c_{zz}(n) = \begin{cases} \frac{1}{N_0(0)} \sum_{m=0}^{N-1} z_m^2 & \text{for } n = 0 \\ \frac{1}{N_0(n)} (\sum_{m=0}^{N-1-n} z_m z_{m+n} + \sum_{m=N-n}^{N-1} z_m z_{m+n-N}) & \text{for } n = 1, ..., N-1 \end{cases} \tag{F.6.2}$$

so that now

$$\tilde{R}^c_{zz}(n) = \frac{N}{N_0(n)} R^c_{zz}(n)$$

The unbiased spectrum is thus the convolution of the Fourier transform of the weighting coefficients $\frac{N}{N_0(n)}$ with the Fourier transform of the biased autocorrelation function, which gave the biased spectrum (always positive due to the definite positivity of the biased autocorrelation function). Since the Fourier transform of the weighting coefficients can have

negative values, the unbiased spectrum can have negative values for some frequencies, which is a major flaw of this method. This is because the unbiased autocorrelation function (F.6.2) is not a valid autocorrelation function any more (Claerbout, 1985) in the sense that it is not positive definite, because of the lag-dependent weighting $N_0(n)$ which invalidates the proof of the previous paragraph.

Remark: If we want to keep positive values for all frequencies, we can correct the biased autocorrelation function so that the estimator for lag 0 is unbiased, by dividing by $N_0(0) = \sum_{m=0}^{N-1} y_m^2$, which is not lag-dependent hence does not destroy the definite positivity of the autocorrelation function. We see that $N_0(0)/N$ is the energy loss correction factor defined in equation (F.4.15).

Finally, an interpretation of why we obtain negative values for some frequencies when using the unbiased autocorrelation function is obtained in the light of nonstationary random processes theory (Bendat and Piersol, 1986).
The adequate model for our case if the product model:

$$\{z(t)\} = y(t)\{x(t)\} \tag{F.6.3}$$

where $\{x(t)\}$ is the original stationary random process being observed, $y(t)$ is a deterministic signal (the gap function), and $\{z(t)\}$ is a nonstationary random process, of which the observations are one realization. The nonstationary autocorrelation function of $\{z(t)\}$ is:

$$\begin{aligned} R_{zz}(\tau, t) &= E[z(t)z(t+\tau)] \\ &= y(t)y(t+\tau)E[x(t)x(t+\tau)] \\ &= R_{yy}(\tau, t)R_{xx}(\tau) \end{aligned}$$

Now with a single experiment (i.e. a single realization of $\{z(t)\}$), the only way to estimate expected values is to do a time average, which supposes that the random process at hand is ergodic, which is not the case for the nonstationary random process $\{z(t)\}$. We obtain nonetheless:

$$\begin{aligned} \bar{R}_{zz}(\tau) &= \frac{1}{N\delta t} \sum_{n=0}^{N-1} R_{zz}(\tau, n\delta t)\delta t \\ &= \bar{R}_{yy}(\tau)R_{xx}(\tau) \end{aligned}$$

where for $\tau = m\delta t$

$$\bar{R}_{yy}(m) = \frac{1}{N}\sum_{n=0}^{N-1} y_n y_{n+m} \tag{F.6.4}$$

which is the circular autocorrelation function of the gap function. So $\frac{\bar{R}_{zz}(m)}{R_{yy}(m)}$ is the unbiased autocorrelation function, an estimator of the original autocorrelation function $R_{xx}(m)$.

Now a necessary and sufficient condition that $R_{xx}(\tau)$ be the autocorrelation function of a weakly stationary random process $\{x(t)\}$ is that $R_{xx}(\tau)$ be a symmetric and positive definite function. The fact that the unbiased autocorrelation function is not positive definite reflects the fact that the observations are not a stationary random process any more due to the deterministic gap function which kills the stationarity characteristics (the means and variances depend on the time around which they are computed, due to the non-homogeneous structure of the missing observations).

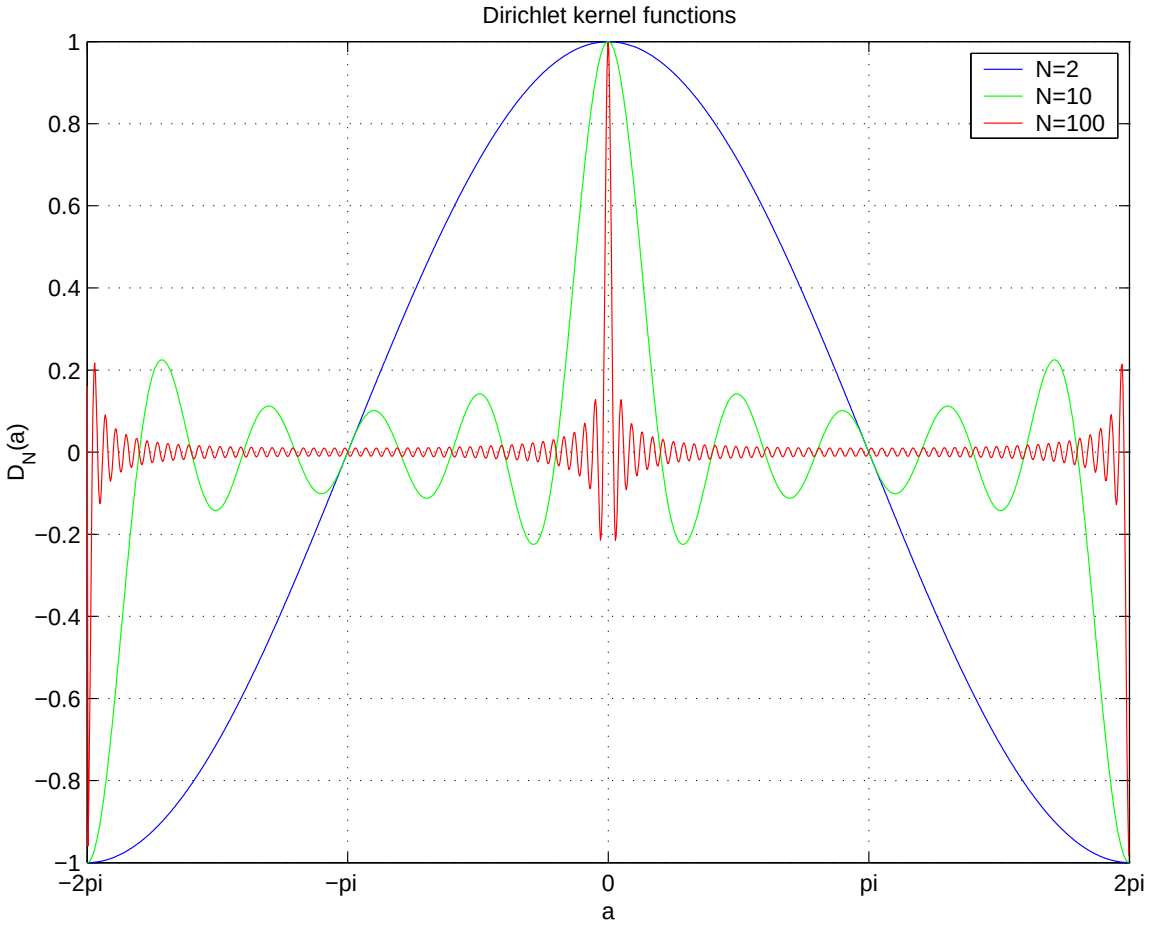

Figure F.1: Dirichlet kernel functions for different values of N

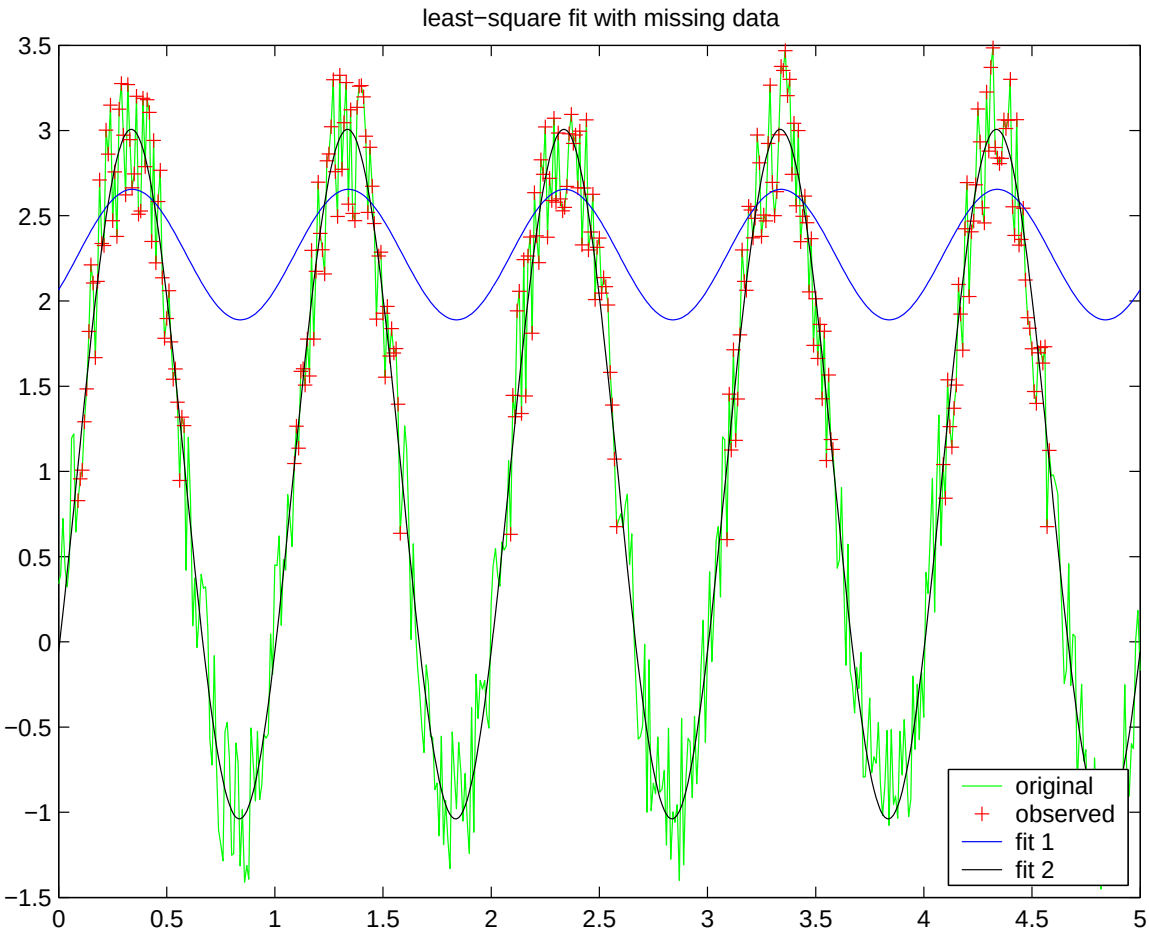

Figure F.2: Test of different least-square fit methods on a noisy sinusoidal signal with missing observations: fit 1 is when the sample mean is removed before the fit, fit 2 is when a constant + sinusoid is fitted directly to the data

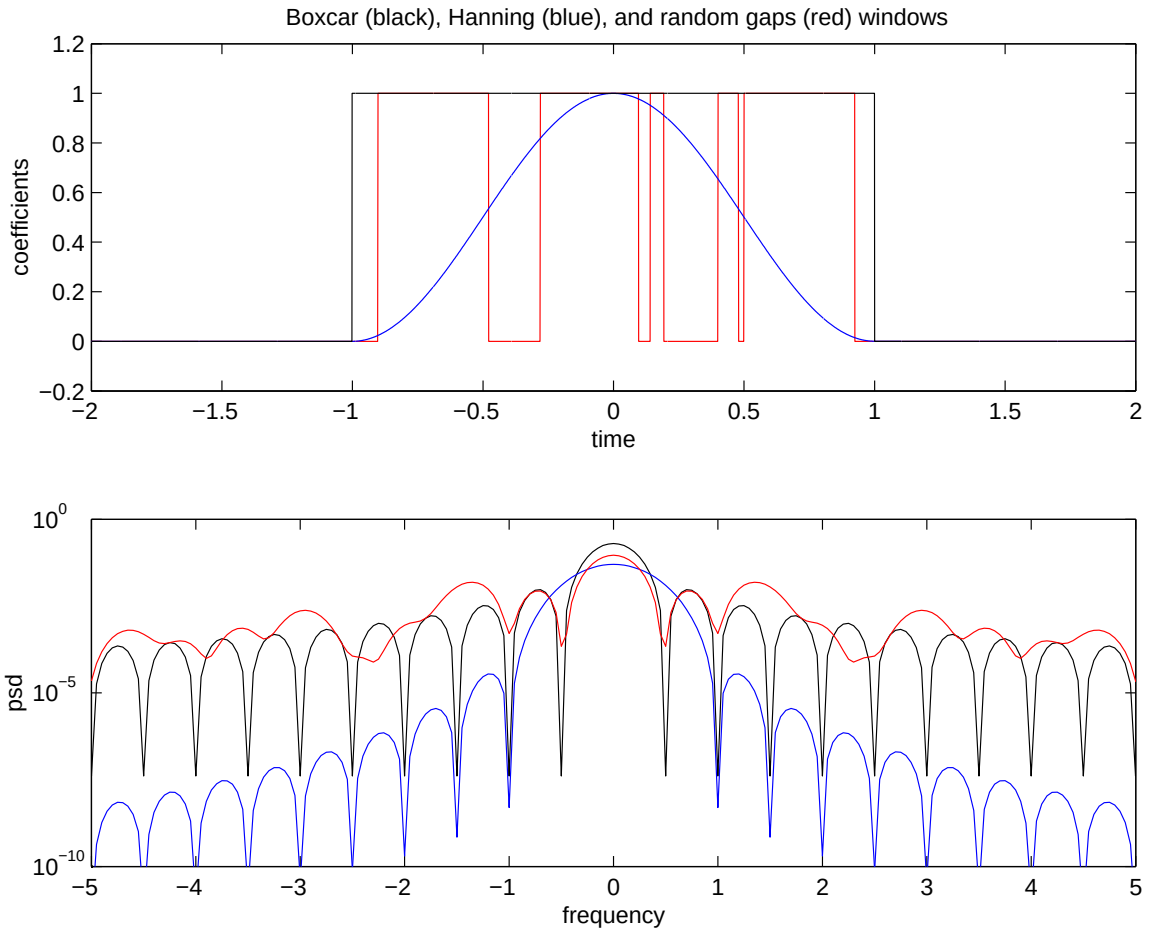

Figure F.3: Boxcar (black), Hamming (blue) and random gap function (red) window coefficients (upper panel) and spectrum (lower panel)

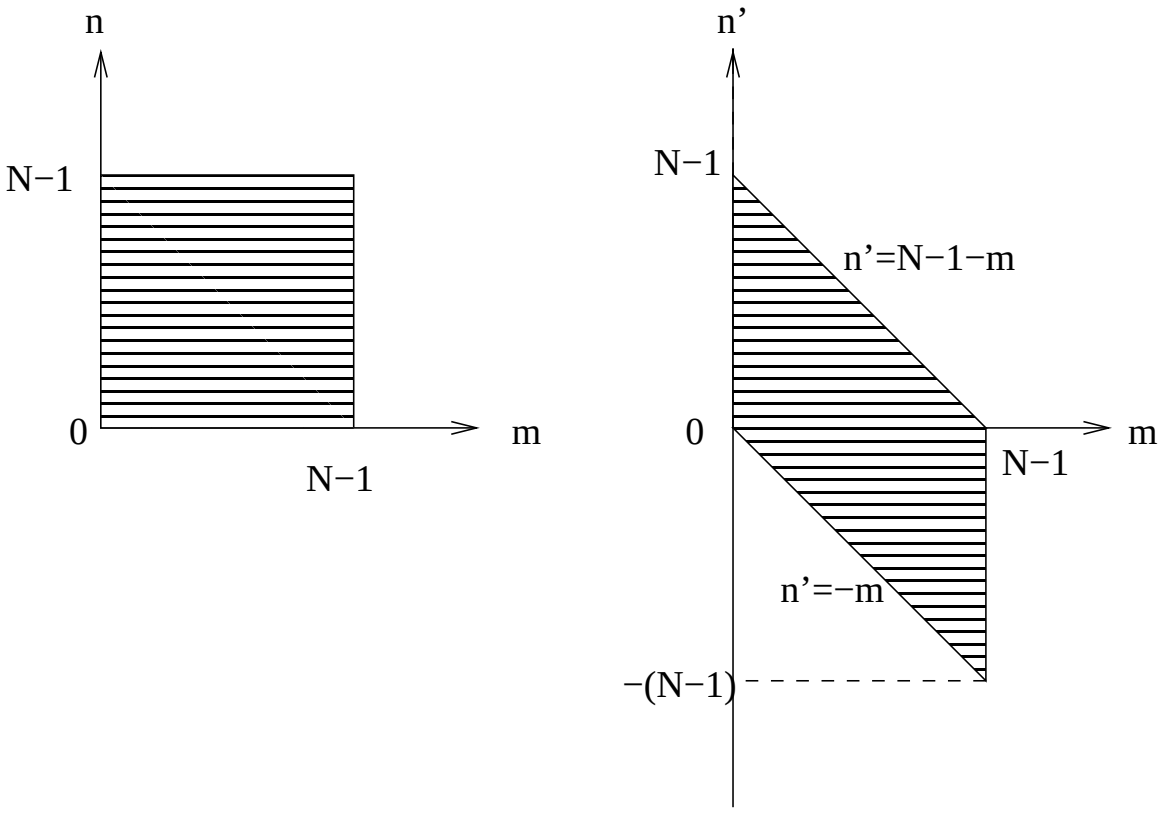

Figure F.4: Variable change for the derivation of the Wiener-Khinchin theorem

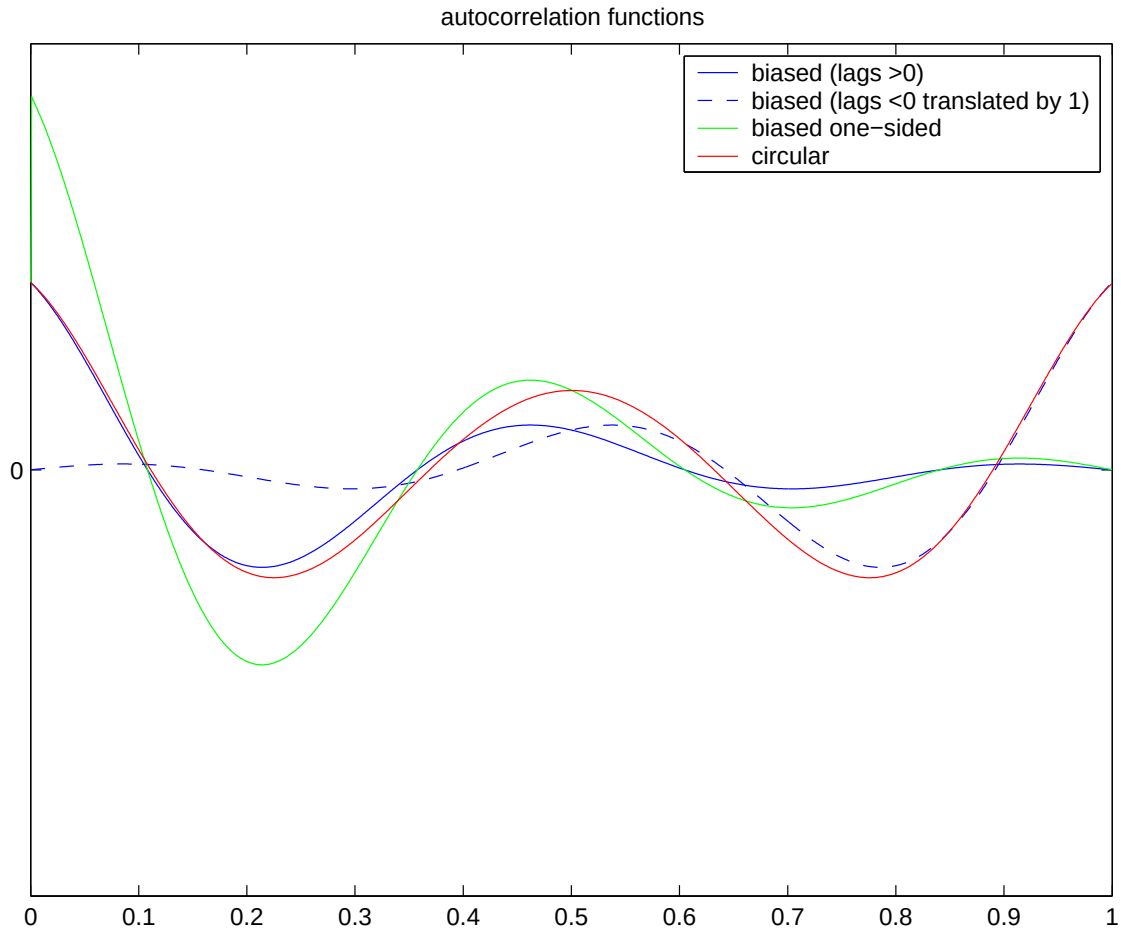

Figure F.5: Autocorrelation functions of a cosine-exponential signal: two-sided biased (blue, the dashed line represent the symmetric negative lag part translated by one observation period), one-sided biased (green), and circular (red). Cf text for definitions.

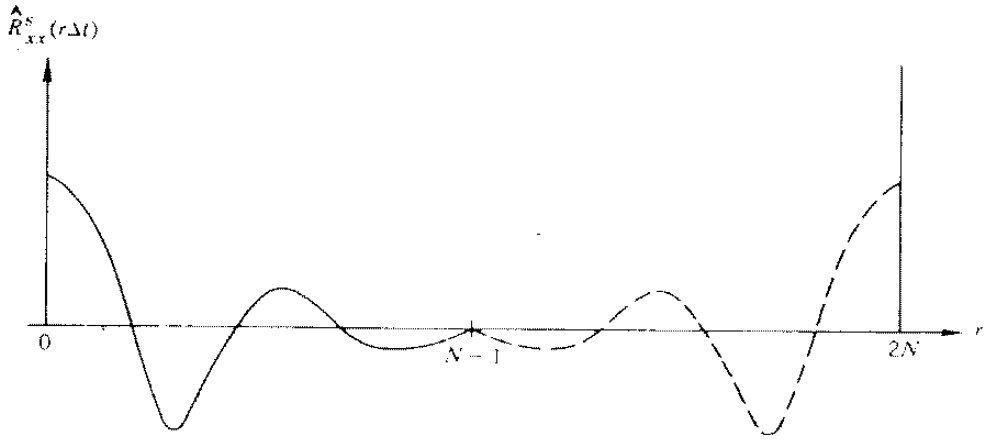

Figure F.6: Illustration of the separation of the two parts of the circular autocorrelation function for a N-zero padded time series.

Bibliography

Alford, M. H., M. C. Gregg, and M. A. Merrifield, 2006: Structure, propagation, and mixing of energetic baroclinic tides in Mamala Bay, Oahu, Hawaii. *J. Phys. Oceanogr.*, **36**, 997–1,018.

Althaus, A. M., E. Kunze, and T. B. Sanford, 2003: Internal tide radiation from the Mendocino Escarpment. *J. Phys. Oceanogr.*, **33**, 1510–1527.

Barrick, D., 2002: Geometrical dilution of statistical accuracy (GDOSA) in multi-static HF radar networks, unpublished note.

Barton, E. D., G. Basterretxea, P. Flament, E. G. Mitchelson-Jacob, B. Jones, J. Aristegui, and F. Herrera, 2000: Lee region of Gran Canaria. *J. Geophys. Res.*, **105**, 17173–17193.

Bendat, J. and A. Piersol, 1986: *Random Data: Analysis and Measurement Procedures*. Wiley-Interscience.

Bloomfield, P., 1970: Spectral analysis with randomly missing observations. *J. R. Stat. Soc.*, **32**, 369–380.

— 1976: *Fourier Analysis of Time Series: an Introduction*. Wiley, New York.

Brambati, A., 1990: Origin and evolution of the Adriatic Sea. *Papers presented at the 25th European Marine Biology Symposium*, University of Ferrara, 5–23.

Bretherton, F. P., 1966: The propagation of groups of internal gravity waves in a shear flow. *Quart. J. Roy. Meteor. Soc.*, **92**, 466–??

Capet, X., J. C. McWilliams, M. J. Molemaker, and A. F. Shchepetkin, 2007: Mesoscale to submesoscale transition in the California Current system: frontal processes. *J. Phys. Oceanogr.*, in press.

Carter, G. S. and M. C. Gregg, 2006: Persistent near-diurnal internal waves observed above a site of m_2 barotropic-to-baroclinic conversion. *J. Phys. Oceanogr.*, **36**, 1136–1147.

Carter, G. S., M. C. Gregg, and M. A. Merrifield, 2006: Flow and mixing around a small seamount on Kaena Ridge, Hawaii. *J. Phys. Oceanogr.*, **36**, 1036–1052.

Carter, G. S., M. A. Merrifield, J. Becker, K. Katsumata, M. C. Gregg, and Y. L. Firing, 2007: Energetics of m_2 barotropic to baroclinic tidal conversion at the Hawaiian islands, submitted to J. Phys. Oceanogr.

Cavallini, F., 1985: A three-dimensional numerical model of tidal circulation in the northern Adriatic sea. *Boll. Oceanol. Teor. Appl.*, **III**, 205–218.

Chapman, R. D., L. K. Shay, H. C. Graber, J. B. Edson, A. Karachintsev, C. L. Trump, and D. B. Ross, 1997: On the accuracy of HF radar surface current measurements: Intercomparisons with ship-based sensors. *J. Geophys. Res.*, **102**, 18,737–18,748.

Chavanne, C., P. Flament, R. Lumpkin, B. Dousset, and A. Bentamy, 2002: Scatterometer observations of wind variations induced by oceanic islands: implications for wind-driven ocean circulation. *Can. J. Remote Sensing*, **28**, 466–474.

Chelton, D. B., R. A. deSzoeke, M. G. Schlax, K. E. Naggar, and N. Siwertz, 1998: Geographical variability of the first baroclinic Rossby radius of deformation. *J. Phys. Oceanogr.*, **28**, 433–460.

Chiswell, S. M., 2002: Energy levels, phase, and amplitude modulation of the baroclinic tide off Hawaii. *J. Phys. Oceanogr.*, **32**, 2,640–2,651.

Claerbout, J., 1985: *Fundamentals of Geophysical Data Processing, With Applications to Petroleum Prospecting*. Blackwell Scientific Publications.

Colosi, J. A. and W. Munk, 2006: Tales of the venerable Honolulu tide gauge. *J. Phys. Oceanogr.*, **36**, 967–996.

Cushman-Roisin, B., V. Malačič, and M. Gačić, 2001: *The Physical Oceanography of the Adriatic Sea. Past, Present and Future*, Kluwer Academic Publishers, chapter Tides, seiches and low-frequency oscillations. 217–240.

Cushman-Roisin, B. and C. E. Naimie, 2002: A 3d finite-element model of the Adriatic tides. *J. Marine Systems*, **37**, 279–297.

D'Asaro, E. A., 1988: Generation of submesoscale vortices: a new mechanism. *J. Geophys. Res.*, **93**, 6685–6693.

Defant, A., 1914: Zur theorie der gezeiten im adriatischen meere. *Ann. Hydr. Mar. Met.*, **42**, 270–281.

Dong, C. and J. C. McWilliams, 2007: A numerical study of island wakes in the Southern California Bight. *Cont. Shelf Res.*, **27**, 1233–1248.

Ducet, N., P. Y. L. Traon, and G. Reverdin, 2000: Global high-resolution mapping of ocean circulation from TOPEX/Poseidon and ERS-1 and -2. *J. Geophys. Res.*, **105**, 19,477–19,498.

Eakins, B. W., J. E. Robinson, T. Kanamatsu, J. Naka, J. R. Smith, E. Takahashi, and D. A. Clague, 2003: Hawaii's volcanoes revealed. U.S. Geological Survey, Geological Investigations Series Map I-2809.

Edwards, N. R. and C. Staquet, 2005: Focusing of an inertia-gravity wave packet by a baroclinic shear flow. *Dyn. Atmos. Oceans*, **40**, 91–113.

Egbert, G. D. and S. Y. Erofeeva, 2002: Efficient inverse modeling of barotropic ocean tides. *J. Atmos. Oceanogr. Tech.*, **19**, 183–204.

Egbert, G. D. and R. D. Ray, 2000: Significant dissipation of tidal energy in the deep ocean inferred from satellite altimeter data. *Nature*, **405**, 775–778.

— 2001: Estimates of m_2 tidal energy dissipation from TOPEX/Poseidon altimeter data. *J. Geophys. Res.*, **106**, 22,475–22,502.

Emery, W. and R. Thomson, 1997: *Data Analysis Methods in Physical Oceanography*. Pergamon.

Essen, H.-H., K.-W. Gurgel, and T. Schlick, 2000: On the accuracy of current measurements by means of HF radar. *IEEE Journal of Oceanic Engineering*, **25**, 472–480.

Flament, P., L. Armi, and L. Washburn, 1985: The evolving structure of an upwelling filament. *J. Geophys. Res.*, **90**, 11,765–11,778.

Flament, P., R. Lumpkin, J. Tournadre, and L. Armi, 2001: Vortex pairing in an unstable anticyclonic shear flow : discrete subharmonics of one pendulum day. *J. Fluid Mech.*, **440**, 401–409.

Fratantoni, D. M., A. S. Bower, W. E. Johns, and H. Peters, 2006: Somali current rings in the eastern Gulf of Aden. *J. Geophys. Res.*, **111**, C09039.

Galperin, B., L. H. Kantha, S. Hassid, and A. Rosati, 1988: A quasi-equilibrium turbulent energy model for geophysical flows. *J. Atmos. Sci*, **45**, 55–62.

Garrett, C. J. R., 1968: On the interaction between internal gravity waves and a shear flow. *J. Fluid Mech.*, **34**, 711–720.

Gerkema, T., 2001: Internal and interfacial tides: beam scattering and local generation of solitary waves. *J. Marine Res.*, **59**, 227–255.

Griffiths, S. D. and R. H. J. Grimshaw, 2007: Internal tide generation at the continental shelf modeled using a modal decomposition: two-dimensional results. *J. Phys. Oceanogr.*, **37**, 428–451.

Gurgel, K.-W., 1994: Shipborne measurement of surface current fields by HF radar. *L'Onde Électrique*, **74**, 54–59.

Gurgel, K.-W., G. Antonischki, H.-H. Essen, and T. Schlick, 1999: Wellen Radar (WERA): a new ground-wave HF radar for ocean remote sensing. *Coastal Engineering*, **37**, 219–234.

Harris, F., 1978: On the use of windows for harmonic analysis with the discrete fourier transform. *Proceedings of the IEEE,* **66**, 51–83.

Hendershott, M. C. and A. Speranza, 1971: Co-oscillating tides in long, narrow bays; the Taylor problem revisited. *Deep-Sea Res.*, **18**, 959–980.

Hogg, N. G., 1980: Observations of internal Kelvin waves trapped round Bermuda. *J. Phys. Oceanogr.*, **10**, 1353–1376.

Holloway, P. E. and M. A. Merrifield, 1999: Internal tide generation by seamounts, ridges, and islands. *J. Geophys. Res.*, **104**, 25,937–25,951.

Horsburgh, K. J. and A. E. Hill, 2003: A three-dimensional model of density-driven circulation in the Irish Sea. *J. Phys. Oceanogr.*, **33**, 343–365.

Hoskins, B. J., I. Draghici, and H. C. Davies, 1978: A new look at the ω-equation. *Quart. J. Roy. Meteor. Soc.*, **104**, 31–38.

Janeković, I., J. Bobanović, and M. Kuzmić, 2003: The Adriatic sea M2 and K1 tides by 3D model and data assimilation. *Est. Coast. Shelf Sci.*, **57**, 873–885.

Janeković, I. and M. Kuzmić, 2005: Numerical simulation of the Adriatic sea principal tidal constituents. *Annales Geophysicae,* **23**, 1–12.

Jones, R. M., 2001: The dispersion relation for internal acoustic-gravity waves in a baroclinic fluid. *Phys. Fluids*, **13**, 1274–1280.

Jones, W. L., 1969: Ray tracing for internal gravity waves. *J. Geophys. Res.*, **74**, 2028–2033.

Kantha, L. and C. Tierney, 1997: Global baroclinic tides. *Prog. Oceanogr.*, **40**, 163–178.

Karl, D. M. and R. Lukas, 1996: The Hawaii Ocean Time-series (HOT) program: Background, rationale and field implementation. *Deep-Sea Res.*, **43**, 129–156.

Kloosterziel, R. C., G. F. Carnevale, and P. Orlandi, 2007: Inertial instability in rotating and stratified fluids: barotropic vortices. *J. Fluid Mech.*, **583**, 379–412.

— 2008: Inertial instability in rotating and stratified fluids: baroclinic vortices. In preparation.

Kloosterziel, R. C. and G. J. F. van Heijst, 1991: An experimental study of unstable barotropic vortices in a rotating fluid. *J. Fluid Mech.*, **223**, 1–24.

Klymak, J. M., J. N. Moum, J. D. Nash, E. Kunze, J. B. Girton, G. S. Carter, C. M. Lee, T. B. Sanford, and M. C. Gregg, 2006: An estimate of tidal energy lost to turbulence at the Hawaian Ridge. *J. Phys. Oceanogr.*, **36**, 1148–1164.

Kuhlbrodt, T., A. Griesel, M. Montoya, A. Levermann, M. Hofmann, and S. Rahmstorf, 2007: On the driving processes of the Atlantic Meridional Overturning Circulation. *Rev. Geophys.*, **45**, 32.

Kunze, E., 1985: Near-inertial wave propagation in geostrophic shear. *J. Phys. Oceanogr.*, **15**, 544–565.

Lapeyre, G. and P. Klein, 2006: Impact of the small-scale elongated filaments on the oceanic vertical pump. *J. Marine Res.*, **64**, 835–851.

Lapeyre, G., P. Klein, and B. L. Hua, 2006: Oceanic restratification forced by surface frontogenesis. *J. Phys. Oceanogr.*, **36**, 1577–1590.

Larsen, J. C., 1977: Cotidal charts for the Pacific Ocean near Hawaii using f-plane solutions. *J. Phys. Oceanogr.*, **7**, 100–109.

Lee, C. M., F. Askari, J. Book, S. Carniel, B. Cushman-Roisin, C. Dorman, J. Doyle, P. Flament, C. K. Harris, B. H. Jones, M. Kuzmić, P. Martin, A. Ogston, M. Orlić, H. Perkins, P.-M. Poulain, J. Pullen, A. Russo, C. Sherwood, R. Signell, and D. T. Detweiler, 2005: Northern Adriatic response to a wintertime bora wind event. *Eos*, **86**, 157,163,165.

Lee, C. M., E. Kunze, T. B. Sanford, J. D. Nash, M. A. Merrifield, and P. E. Holloway, 2006: Internal tides and turbulence along the 3000-m isobath of the Hawaiian ridge. *J. Phys. Oceanogr.*, **36**, 1165–1183.

Lévy, M., P. Klein, and A.-M. Treguier, 2001: Impact of sub-mesoscale physics on production and subduction of phytoplankton in an oligotrophic regime. *J. Marine Res.*, **59**, 535–565.

Lipa, B. J. and D. E. Barrick, 1983: Least-squares methods for the extraction of surface currents from codar crossed-loop data: Application at ARSLOE. *IEEE Journal of Oceanic Engineering*, **8**, 226–253.

Liu, W. T. and W. Tang, 1996: Equivalent neutral wind. Technical Report JPL Pub. 96-17, Jet Propulsion Laboratory, Pasadena.

Lomb, N., 1976: Least-squares frequency analysis of unequally spaced data. *Astrophysics and Space Science*, **39**, 447–462.

Lozano, C. J. and J. Candela, 1995: The M2 tide in the Mediterranean sea: dynamic analysis and data assimilation. *Oceanologica Acta*, **18**, 419–441.

Lumpkin, C., 1998: *Eddies and Currents of the Hawaiian Islands*. Ph.D. thesis, School of Ocean and Earth Sciences and Technology, University of Hawaii at Manoa.

Lumpkin, C. F., 1995: *Resonant Coastal Waves and Superinertial Oscillations*. Master's thesis, School of Ocean and Earth Science and Technology, University of Hawai‘i, Honolulu, USA.

Luther, D. S., 1985: Trapped waves around the Hawaiian islands. *‘Aha Huliko‘a Proceedings*, H. I. of Geophysics, ed., 261–301.

Lynch, D. R., T. C. I. P. Justin, C. E. Naimie, and F. E. Werner, 1996: Comprehensive coastal circulation model with application to the Gulf of Maine. *Cont. Shelf Res.*, **16**, 875–906.

MacDonald, N. J., 1968: The evidence for the existence of Rossby-like waves in the hurricane vortex. *Tellus*, **XX**, 138–150.

MacKinnon, J. A. and K. B. Winters, 2005: Subtropical catastrophe: significant loss of low-mode tidal energy at 28.9^o. *Geophys. Res. Letters*, **32**, 5pp.

Malačič, V., D. Viezzoli, and B. Cushman-Roisin, 2000: Tidal dynamics in the northern Adriatic sea. *J. Geophys. Res.*, **105**, 26,265–26,280.

Martin, J. P. and D. L. Rudnick, 2007: Inferences and observations of turbulent dissipation and mixing in the upper ocean at the Hawaiian Ridge. *J. Phys. Oceanogr.*, **37**, 476–494.

Mauri, E. and P.-M. Poulain, 2001: Northern Adriatic Sea surface circulation and temperature / pigment fields in september and october 1997. *J. Marine Systems*, **29**, 51–67.

McCreary, J. P., H. S. Lee, and D. B. Enfield, 1989: The response of the coastal ocean to strong offshore winds: With application to circulations in the Gulfs of Tehuantepec and Papagayo. *J. Marine Res.*, **47**, 81–109.

McGillicuddy, D. J., A. R. Robinson, D. A. Siegel, H. W. Jannasch, R. Johnson, T. D. Dickey, J. McNeil, A. F. Michaels, and A. H. Knap, 1998: Influence of mesoscale eddies on new production in the Sargasso Sea. *Nature*, **394**, 263–266.

Mellor, G. L. and T. Yamada, 1982: Development of a turbulence closure model for geophysical fluid problems. *Rev. Geophys.*, **20**, 851–875.

Merrifield, M. A. and P. E. Holloway, 2002: Model estimates of m_2 internal tide energetics at the Hawaiian Ridge. *J. Geophys. Res.*, **107**, 5.1–5.12.

Merrifield, M. A., P. E. Holloway, and T. M. S. Johnston, 2001: The generation of internal tides at the Hawaiian Ridge. *Geophys. Res. Letters*, **28**, 559–562.

Merrifield, M. A., L. Yang, and D. S. Luther, 2002: Numerical simulations of a storm-generated island-trapped wave event at the Hawaiian Islands. *J. Geophys. Res.*, **107**, 33.1–33.10.

Michelato, A., 1983: Caratteristiche della circolazione delle acque costiere dell'Emilia-Romagna. *Atti del Convegno "Eutrofizzazione dell'Adriatico-Ricerche e linee di intervento"*, Bologna, 149–168.

Montgomery, M. T. and R. J. Kallenbach, 1997: A theory for vortex rossby-waves and its application to spiral bands and intensity changes in hurricanes. *Quart. J. Roy. Meteor. Soc.*, **123**, 435–465.

Mooers, C. N. K., 1975a: Several effects of a baroclinic current on the cross-stream propagation of inertial-internal waves. *Geophys. Fluid Dynamics*, **6**, 242–275.

— 1975b: Several effects of baroclinic currents on the three-dimensional propagation of inertial-internal waves. *Geophys. Fluid Dynamics*, **6**, 277–284.

Mosetti, R., 1986: Determination of the current structure of the M2 tidal component in the northern Adriatic by applying the rotary analysis to the Taylor problem. *Boll. Oceanol. Teor. Appl.*, **IV**, 165–172.

Moulin, F. Y. and J.-B. Flór, 2006: Vortex-wave interaction in a rotating stratified fluid: WKB simulations. *J. Fluid Mech.*, **563**, 199–222.

Müller, P., 1976: On the diffusion of momentum and mass by internal gravity waves. *J. Fluid Mech.*, **77**, 789–823.

Munk, W., L. Armi, K. Fischer, and F. Zachariasen, 2000: Spirals on the sea. *Proc. Roy. Soc. Lond.*, **456**, 1217–1280.

Munk, W. and C. Wunsch, 1998: Abyssal recipes II: energetics of tidal and wind mixing. *Deep-Sea Res.*, **45**, 1977–2010.

Nash, J. D., E. Kunze, C. M. Lee, and T. B. Sanford, 2006: Structure of the baroclinic tide generated at Kaena Ridge, Hawaii. *J. Phys. Oceanogr.*, **36**, 1123–1135.

Naveira Garabato, A. C., K. L. Polzin, B. A. King, K. J. Heywood, and M. Visbeck, 2004: Widespread intense turbulent mixing in the Southern Ocean. *Science*, **303**, 210–213.

Olbers, D. J., 1981a: A formal theory of internal wave scattering with applications to ocean fronts. *J. Phys. Oceanogr.*, **11**, 1078–1099.

— 1981b: The propagation of internal waves in a geostrophic current. *J. Phys. Oceanogr.*, **11**, 1224–1233.

Orlić, M., M. Gačić, and P. E. L. Violette, 1992: The currents and circulation of the Adriatic sea. *Oceanologica Acta*, **15**, 109–124.

Pacanowski, R. C. and S. M. Griffies, 1999: The MOM3 Manual. Technical report, NOAA/Geophysical Fluid Dynamics Laboratory.

Paduan, J. and M. Cook, 2004: HFRadarmap toolbox for MATLAB. Http://www.oc.nps.navy.mil/ radlab/HFRadarmapToolbox/.

Paduan, J. D. and H. C. Graber, 1997: Introduction to high-frequency radar: Reality and myth. *Oceanography*, **10**.

Park, J.-H. and D. R. Watts, 2006: Internal tides in the southwestern Japan/east sea. *J. Phys. Oceanogr.*, **36**, 22–34.

Patzert, W. C., 1969: Eddies in Hawaiian waters. Technical Report 69-8, Hawaiian Institute of Geophysics, University of Hawaii at Manoa.

Pawlowicz, R. B., B. Beardsley, and S. Lentz, 2002: Classical tidal harmonic analysis including error estimates in MATLAB using T_TIDE. *Computers and Geosciences*, **28**, 929–937.

Pedlosky, J., 2003: *Waves in the ocean and atmosphere. Introduction to wave dynamics*. Springer.

Pereira, A. F., B. M. Castro, L. Calado, and I. C. A. da Silveira, 2007: Numerical simulation of M_2 internal tides in the South Brazil Bight and their interaction with the Brazil Current. *J. Geophys. Res.*, **112**, C04009.

Polzin, K. L., J. M. Toole, J. R. Ledwell, and R. W. Schmitt, 1997: Spatial variability of turbulent mixing in the abyssal ocean. *Science*, **276**, 93–96.

Poulain, P.-M., 2001: Adriatic sea surface circulation as derived from drifter data between 1990 and 1999. *J. Marine Systems*, **29**, 3–32.

Poulain, P.-M., E. Mauri, and L. Ursella, 2004: Unusual upwelling event and current reversal off the Italian Adriatic coast in summer 2003. *Geophys. Res. Letters*, **31**, L05303.

Poulin, F. J. and G. R. Flierl, 2003: The nonlinear evolution of barotropically unstable jets. *J. Phys. Oceanogr.*, **33**, 2173–2192.

Press, W., 1992: *Numerical Recipes*. Cambridge University Press, New York.

Qiu, B. and S. Chen, 2005: Eddy-induced heat transport in the subtropical north Pacific from Argo, TMI, and altimetry measurements. *J. Phys. Oceanogr.*, **35**, 458–473.

Qiu, B., D. A. Koh, C. Lumpkin, and P. Flament, 1997: Existence and formation mechanism for the North Hawaiian Ridge Current. *J. Phys. Oceanogr.*, **27**, 431–444.

Rainville, L. and R. Pinkel, 2006a: Baroclinic energy flux at the Hawaiian Ridge: observations from the R/P FLIP. *J. Phys. Oceanogr.*, **36**, 1104–1122.

— 2006b: Propagation of low-mode internal waves through the ocean. *J. Phys. Oceanogr.*, **36**, 1,220–1,236.

Ray, R. D. and D. E. Cartwright, 2001: Estimates of internal tide energy fluxes from Topex/Poseidon altimetry: Central North Pacific. *Geophys. Res. Letters*, **28**, 1259–1262.

Ray, R. D. and G. T. Mitchum, 1996: Surface manifestation of internal tides generated near Hawaii. *Geophys. Res. Letters*, **23**, 2101–2104.

— 1997: Surface manifestation of internal tides in the deep ocean: observations from altimetry and island gauges. *Prog. Oceanogr.*, **40**, 135–162.

Rhines, P., 1970: Edge-, bottom-, and Rossby waves in a rotating stratified fluid. *Geophys. Fluid Dynamics*, **1**, 273–302.

Rizzoli, P. M. and A. Bergamasco, 1983: The dynamics of the coastal region of the northern Adriatic Sea. *J. Phys. Oceanogr.*, **13**, 1,105–1,130.

Roden, G. I., 1981: Mesoscale thermohaline, sound velocity and baroclinic flow structure of the Pacific Subtropical Front during the winter of 1980. *J. Phys. Oceanogr.*, **11**, 658–675.

Rudnick, D. L., 2001: On the skewness of vorticity in the upper ocean. *Geophys. Res. Letters*, **28**, 2045–2048.

Rudnick, D. L., T. J. Boyd, R. E. Brainard, G. S. Carter, G. D. Egbert, M. C. Gregg, P. E. Holloway, J. M. Klymak, E. Kunze, C. M. Lee, M. D. Levine, D. S. Luther, J. P. Martin, M. A. Merrifield, J. N. Moum, J. D. Nash, R. Pinkel, L. Rainville, and T. B. Sanford, 2003: From tides to mixing along the hawaiian ridge. *Science*, **301**, 355–357.

Shay, L. K., T. M. Cook, B. K. Haus, J. Martinez, H. Peters, A. J. Mariano, J. VanLeer, P. E. An, S. Smith, A. Soloviev, R. Weisberg, and M. Luther, 2000: VHF radar detects oceanic submesoscale vortex along Florida coast. *Eos*, **81**, 209–213.

Siegel, A., J. B. Weiss, J. Toomre, J. C. McWilliams, P. S. Berloff, and I. Yavneh, 2001: Eddies and vortices in ocean basin dynamics. *Geophys. Res. Letters*, **28**, 3183–3186.

Smagorinsky, J., 1963: General circulation experiments with the primitive equations. I: The basic experiment. *Month. Weath. Rev.*, **91**, 99–164.

St. Laurent, L. C. and J. D. Nash, 2004: An examination of the radiative and dissipative properties of deep ocean internal tides. *Deep-Sea Res.*, **51**, 3029–3042.

Stern, M. E., 1965: Interaction of a uniform wind stress with a geostrophic vortex. *Deep-Sea Res.*, **12**, 355–367.

Stewart, R. H. and J. W. Joy, 1974: HF radio measurements of surface currents. *Deep-Sea Res.*, **21**, 1,039–1,049.

Taylor, G. I., 1921: Tidal oscillations in gulfs and rectangular basins. *Proc. Lond. Math. Soc.*, **20**, 193–204.

Thomas, L. N. and P. B. Rhines, 2002: Nonlinear stratified spin-up. *J. Fluid Mech.*, **473**, 211–244.

Ursella, L. and M. Gačić, 2001: Use of the Acoustic Doppler Current Profiler (ADCP) in the study of the circulation of the Adriatic sea. *Annales Geophysicae*, **19**, 1,183–1,193.

Ursella, L., P.-M. Poulain, and R. P. Signell, 2007: Surface drifter derived circulation in the northern and middle Adriatic Sea: Response to wind regime and season. *J. Geophys. Res.*, **112**, C03S04.

Weller, R. A., 1982: The relation of near-inertial motions observed in the mixed layer during the JASIN (1978) experiment to the local wind stress and to the quasi-geostrophic flow field. *J. Phys. Oceanogr.*, **12**, 1,122–1,136.

Wunsch, C., 2006: *Discrete inverse and state estimation problems, with geophysical fluid applications*. Cambridge University Press, Cambridge, UK, 371 pp.

Wunsch, C. and R. Ferrari, 2004: Vertical mixing, energy, and the general circulation of the oceans. *Ann. Rev. Fluid Mech.*, **36**, 281–314.

Young, W. R. and M. Ben Jelloul, 1997: Propagation of near-inertial oscillations through a geostrophic flow. *J. Marine Res.*, **55**, 735–766.

Zaron, E. D., C. Chavanne, G. D. Egbert, and P. Flament, 2008: Baroclinic tidal generation in the Kauai Channel inferred from HF-Radio, in preparation.

Zaron, E. D. and G. D. Egbert, 2006a: Estimating open-ocean barotropic tidal dissipation: the Hawaiian Ridge. *J. Phys. Oceanogr.*, **36**, 1019–1035.

— 2006b: Verification studies for a z-coordinate primitive-equation model: Tidal conversion at a mid-ocean ridge. *Ocean Modelling*, **14**, 257–278, doi:10.1016/j.ocemod.2006.05.007.

— 2007: The impact of the M_2 internal tide on data-assimilative model estimates of the surface tide. *Ocean Modelling*, **18**, 210–216.